Micromechanics of stress corrosion cracking in 304 stainless steel and Ni Alloy 600

The Queen's College

University of Oxford

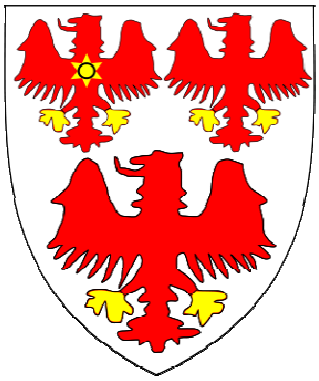



Alisa M. Stratulat

A thesis submitted for the degree of DPhil. in Materials Science

Trinity Term, 2013

ABSTRACT

The current thesis takes a step forward into understanding the intergranular stress corrosion cracking (IGSCC) by applying a relatively new micro-mechanical technique to look at the crack growth rate of individual grain boundaries in 304 stainless steel (SS) and to measure fracture toughness for different grain boundaries in Ni Alloy 600. In addition, a model is tested and proposed that could predict crack initiation in 304 SS. Pentagonal cross-section cantilevers 5 µm wide by 25 µm long were milled at individual grain boundaries in both 304 SS and Ni Alloy 600. The cantilevers milled in 304 SS were tested *in-situ* in a customised stage, using the nanoindenter. Crack growth rate was measured for two different cantilevers to be approximately 40 µm/s ($K = 1.1$ MPa$(m)^{1/2}$) and 120 µm/s ($K = 1.7$ MPa$(m)^{1/2}$). Cantilevers were milled in Ni Alloy 600 for three different samples: samples that were exposed to simulated pressurized water reactors (PWR) environment for 4500 h, for 1500 h and un-oxidised samples. The fracture toughness calculated for the fractured cantilevers in samples that were exposed for 4500 h was measured to be between 0.73 and 1.82 MPa$(m)^{1/2}$. No intergranular fracture occurred in the samples that were exposed for 1500 h and in the un-oxidised samples. The grain boundary misorientation was measured for the tested cantilevers but no direct correlation was observed between the misorientation angle and the fracture toughness.

A Schmid-modified grain boundary stress (SMGBS) model previously used to study the intergranular behaviour of irradiated 316L steel in supercritical water was applied to predict crack initiation in 304 stainless steel. The model was successfully applied and accurately predicted crack initiation. To extend the model, sensitisation was also included. In addition, different areas of the specimen, including the initiation site were

analysed using High resolution electron backscatter diffraction (HR-EBSD) technique to measure the geometrically necessary dislocations (GNDs) density. It was observed that the boundary average GNDs is lower for the intact boundaries and higher for the cracked grain boundaries.

The results presented in this thesis show the potential of using Focused Ion Beam (FIB) manufactured cantilevers to study the behaviour of IGSCC at individual grain boundaries in 304 stainless steel and Ni Alloy 600. This technique proved to give reliable results to study the embrittlement in Ni Alloy 600, and it could be extended to a variety of materials with applications in the nuclear industry. Also, the model proposed to predict crack initiation in 304 stainless steel correctly identified the location of IGSCC initiation.

PUBLICATIONS AND CONFERENCES

The work presented in this thesis has been presented in the following conferences and publications:

- "Micromechanical testing of oxidized grain boundaries in Ni Alloy 600," A. Stratulat and. S. Roberts, Fall MRS Conference, Hynes Convention Center in Boston, MA, United States, Nov. 25-30 (2012)

- "Micromechanical testing of oxidized grain boundaries in Ni Alloy 600," A. Stratulat and. S. Roberts, Thin Film and Small Scale Mechanical Behavior, Colby College in Waterville ME, United States, July 22-27 (2012)

- "Micromechanical testing of stress corrosion cracking behavior at individual grain boundaries in stainless steel and Ni-alloy," A. Stratulat,. S. Roberts and. J. Marrow, The 8th Meeting of TC2 Micromechanisms of the European Structural Integrity Society (ESIS), Mansfield College, University of Oxford, Oxford, UK, April 2-3 (2012)

- "Micromechanical testing of stress corrosion cracking behavior at individual grain boundaries in stainless steel," A. Stratulat and. S. Roberts, Nanomechanical Testing in Materials Research and Development, Lanzarote, Canary Islands, Spain, October 9-14 (2011)

- "Micromechanical testing of oxidised grain boundaries in Ni Alloy 600," A. Stratulat and S. Roberts, MRS Proceedings, 1514, (2013)

AKNOWLEDGEMENTS

I am really grateful to my supervisors, Prof. Steve Roberts and Prof. James Marrow, for their guidance, patience and all the help provided during this journey. I would like to thank them for their support, advice and encouragements. Also, I would like to thank AREVA and The Queen's College for financial support.

I would like to thank Mr. Olivier Calonne and Mr. Marc Foucault from AREVA for providing the Ni Alloy specimens, as well as for the useful discussions and suggestions. Also, I would like to thank to Dr. Jonathan Duff from University of Manchester for providing the DIC analysis as well as the 304 SS sample.

Special thanks go to Dr. Sergio Lozano-Perez for his help on 3D FIB reconstruction, Dr. D.E.J Armstrong for his help on training, advice on micro-mechanical testing and exposing the fracture surface in the Ni specimens, to Dr. Ben Britton and Mr. Jun Jiang for their guidance on HR-EBSD and to Dr. Mahmoud Mostafavi for teaching me ABAQUS.

I would like to thank to the EM Group, to Dr. Dr Gareth Gughes and Steve Lett for their training and FIB support, to Dr. Alex Cock for the nanoindenter support, to Ms. Gabriella Chapman for her help on the EDX analysis, to Mr. Ian Lloyd for his help in the furnace room and to Mr. Laurie Walton for his help in the workshop.

Lastly, I would like to thank the MFFP group, for making Fridays a lot more enjoyable through the very inspiring talks and to Ms. Karen Disney for taking care of all the administrative work.

Thank you!

ABREVIATIONS

BWR	Boiling water reactors
CCD	Charged coupled device
CNS	Critical effective normal stress
CSL	Coincidence site lattice
CSM	Continuous stiffness measurement
DCM	Dynamic contact module
DIC	Digital image correlation
DL-EPR	Double-loop Electro-Potentiokinetic Reactivation
EBSD	Electron backscatter diffraction
EDX	Energy-dispersive X-ray spectroscopy
EPR	Electro-Potentiokinetic Reactivation
FIB	Focussed ion beam
GBE	Grain boundary engineering
GIS	Gas injection system
GND	Geometrically necessary dislocation
HR-EBSD	High resolution electron backscatter diffraction
IGSCC	Intergranular stress corrosion cracking
LMIS	Liquid metal ion source
PWR	Pressurized water reactors
PWSCC	Stress corrosion cracking in pressurized water reactors
SA	Solution annealed
SCC	Stress corrosion cracking

SCE	Saturated calomel electrode
SCW	Supercritical water
SE	Secondary electron
SEM	Scanning electron microscope
SIMS	Secondary ion mass spectrometry
SL-EPR	Single-loop Electro-Potentiokinetic Reactivation
SMGBS	Schmid-modified grain boundary stress
SS	Stainless steel
TEM	Transmission electron microscopy
TMP	Thermo-mechanically processed

TABLE OF CONTENTS

1 INTRODUCTION 1

2 LITERATURE REVIEW 3

2.1 Overview of stress corrosion cracking 3
2.1.1 Stages of stress corrosion cracking 4
2.1.2 Intergranular stress corrosion cracking (IGSCC) 7
2.1.3 Factors that affect SCC 8
2.1.3.1 Stress 8
2.1.3.2 Environment 9
2.1.3.3 Microstructure 13
2.1.4 Models for the effect of microstructure on IGSCC 16
2.1.4.1 Percolation theory and models 18
2.1.4.2 Percolation-like models 20

2.2 SCC in Stainless Steel 24
2.2.1 History and applications of stainless steels 24
2.2.2 Classification and properties of stainless steels 26
2.2.3 Austenitic stainless steels 27
2.2.4 Sensitisation 28
2.2.4.1 Sensitisation tests 30
2.2.4.2 Factors affecting sensitization 36

2.3 IGSCC in 304 stainless steel 38

2.4 SCC Mechanisms in 304 Stainless Steel 45
2.4.1 Slip-dissolution mechanism 45
2.4.2 Hydrogen embrittlement mechanism 47
2.4.3 Film-induced cleavage model 48
2.4.4 Surface mobility model 49

2.5 SCC in Ni Alloy 600 50
2.5.1 Properties of Ni Alloy 600 50
2.5.2 SCC of Ni Alloys in the PWR environment 50
2.5.3 Mechanisms that control SCC in Ni Alloy 600 52

2.6 Micro-mechanical testing using FIB cantilevers 61

2.7 Summary 64

3 EXPERIMENTAL TECHNIQUES 65

3.1 MTS Nano Indenter XP 65

3.2 Electron backscatter diffraction (EBSD) 68

3.3 Focused Ion Beam (FIB) 70
3.3.1 Vacuum system 72
3.3.2 Liquid Metal Ion Source (LMIS) 72
3.3.3 The FIB Column 73
3.3.4 FIB instruments used 74

4 MICROMECHANICAL TESTING OF SCC IN 304 STAINLESS STEEL 77

4.1 Introduction 77

4.2 Sample preparation 82
4.2.1 Annealing treatment 82
4.2.2 Grinding and polishing procedure 84
4.2.3 Sensitisation treatment 84

4.3 Nanoindenter customized stage 85

4.4 Testing cantilevers under fluid using the nanoindenter 85

4.5 Initial bending tests in liquid to determine the upper stress limit of the microcantilevers 87

4.6 Tests applied to control and determine the crack growth in situ 89
4.6.1 In situ method with no voltage applied 89
4.6.1.1 Test conditions and setup 89
4.6.1.2 Results 91
4.6.2 Short *in-situ* method with platinum as the counter electrode 94
4.6.2.1 Test conditions and method 94
4.6.2.2 Results 95
4.6.3 Long in situ method with Pt as the counter electrode 100
4.6.3.1 Tests conditions and method 100
4.6.3.2 Results 101
4.6.4 In situ method with voltage applied (battery – 6 V) with 304 unsensitized SS as the counter-electrode 104
4.6.4.1 Test conditions and method 104
4.6.4.2 Results 106

4.7 Measurement of crack growth rate using micro-cantilevers in 304 SS 111
4.7.1 The use of static stiffness versus harmonic contact stiffness to measure crack growth rate 111
4.7.2 ABAQUS model to determine the relationship between the stiffness of a cantilever and the crack length 114
4.7.3 Crack growth rate results 116

4.8 Summary 122

5 FRACTURE TOUGHNESS OF FIB MICRO-CANTILEVERS IN NI ALLOY 600 125

5.1 Introduction 125

5.2 Sample preparation 126
5.2.1 Determining perpendicular and oxidised grain boundaries 126
5.2.2 Cantilever design and manufacture 128
5.2.3 Pre-notch machining of the cantilevers 130

5.3 Fracture toughness calculation 130

5.4 Cantilever testing 132

5.5 Ni Alloy 600 exposed for 4500 h 133
5.5.1 Sample preparation 133
5.5.2 Stress-strain curves 137
5.5.3 Fracture toughness values 138
5.5.4 Fractography 139
5.5.5 Fracture surfaces 139
5.5.6 Thickness and depth of the oxide 142
5.5.7 Influence of grain boundary misorientation on the fracture toughness 145
5.5.8 3D FIB Reconstruction 145

5.6 Ni-alloy 600 exposed for 1500 h 151
5.6.1 Sample preparation 151
5.6.2 Load vs. displacement curves 152
5.6.3 Micrographs of tested cantilevers 153
5.6.4 Characterising oxidised and unoxidised grain boundaries in terms of misorientation for Ni Alloy 600 samples exposed for 1500 h 153
5.6.5 Oxide depth 156

5.7 Ni Alloy 600 without oxide 159
5.7.1 Sample preparation 159
5.7.2 Stress-strain curves 159
5.7.3 EBSD 161

5.8 Summary 162

6 CHARACTERISATION OF AN IGSCC INITIATION SITE IN 304 SS 165

6.1 Introduction 165
6.1.1 Role of Schmid factor in predicting crack initiation 166
6.1.2 Role of grain boundary inclination to the tensile axis 170
6.1.3 Role of grain boundary misorientation and CSL value 171

6.2 Schmid-Modified Grain Boundary Stress (SMGBS) model 172

6.3 IGSCC Initiation in High-Temperature Oxygenated Water 179

6.4 Autoclave description and DIC technique 180

6.5 High Resolution Electron Back Scatter Diffraction (HR-EBSD) 184

6.6 Testing the SMGBS Model 187
6.6.1 Methodology 187
6.6.1.1 Determining the Schmid factor 187
6.6.1.2 Determining the trace boundary angle 187
6.6.1.3 Determining the grain boundary plane 187
6.6.2 Results 188
6.6.2.1 Simple 2D characterisation 188
6.6.2.2 SMGBS analysis for intact and cracked boundaries 191
6.6.2.3 CSL values of the grain boundaries 198
6.6.2.4 Misorientation and relationship between grain boundaries and low indexed reference planes 200
6.6.2.5 HR-EBSD analysis 204

6.7 Discussion 210

7 FINAL CONCLUSIONS 215

8 APPENDIX: MISORIENTATION DATA FOR EACH GRAIN BOUNDARY 219

9 REFERENCES 237

1 Introduction

The nuclear power industry started to be adopted in many countries in the 1950s, and is now considered to be a solution for a carbon-free power future. In comparison to coal, natural gas or oil, nuclear energy produces almost zero CO_2 [1][2][3][4].

Van Leeuwen [5] reports that in 2005, 66.5% of the world's electricity was generated by fossil-fuel plants, 16% by hydropower, 3% by renewables and 14.8% by nuclear power. According to the Europe's Co-ordination Network on Decommissioning of Nuclear Installations (CND), at the beginning of 2000, there were approximately 433 nuclear power facilities in the world [4]. In France, more than 75% of the generated power is based on nuclear energy [6]. In China, even though nuclear power is not at present as highly used, it is expected that, as the economy will grow, China will shift towards intense use of the nuclear resources [4].

Failure of the structure of components is a major concern in the nuclear power industry and represents not only a safety issue, but also a hazard to economic performance [7]. Corrosion, and especially stress corrosion cracking, has proved to be a significant potential cause of failures in the nuclear industry [8][7] and such a failure first occurred in 1957, at Shippingport Atomic Power Station [10]. It has been estimated that failures caused by stress corrosion cracking (SCC) in the nuclear industry have cost more than $5 billion since 1980 [11]. In order to prevent corrosion and to limit its effect in the nuclear industry, highly corrosion resistant alloys such as Ni-based alloys, stainless steels and Zr alloys have been used. Many of the failures that have been encountered were in components holding radioactive water or gas, made of stainless steel (e.g. piping, pumps, heat exchangers, nuclear systems, welds, valves) [7]. In addition, cases of IGSCC have also been encountered in the components of French Pressurized Water

Reactors [12], where instances of environmentally assisted cracking in high-temperature water of austenitic stainless steels, nickel-base alloys, low-alloy and carbon steels, as well as their weld metals have been reported in several components of steam generators, pressure vessels, piping, pressurizes and deaerators [13].

Stress corrosion cracking involves a highly complex interplay of diffusional, chemical and mechanical factors in a series of related mechanisms. SCC results from a combination of a susceptible alloy in the presence of a tensile stress, in a “corrosive” environment.

Lifetime prediction of components subject to SCC is currently restricted by a lack of understanding of the kinetics of short crack behaviour and complex corrosion mechanisms, as well as by the difficulties of conducting proper experimental observations [14]. The models that predict environmentally assisted cracking of materials in environments such as high-temperature water lack detailed data on crack nucleation and growth and do not take into consideration the various materials or the conditions of the environment that could be present into a system [13]. This is why being able to provide experimental data will be of considerable value for this field.

2 Literature review

2.1 Overview of stress corrosion cracking

The term stress corrosion cracking is associated with failure of stressed alloys produced in a corrosive environment. During SCC, the alloy is unattacked over most of its surface [15], but fine cracks grow progressively. These cracks are produced under the combination of a critical stress (either residual or applied, or a combination of the two), a sensitive microstructure and a corrosive environment [16][17][18]. Cracking can develop into transgranular or intergranular cracking, depending on the environment, and the material can fail from the initial crack that progresses throughout the material or from several cracks branching off the initial crack [15].

SCC requires an electrolyte that transports the flow of electricity between two electrodes. The electrolyte is usually an acid, salt water, water or alkaline solution with different concentrations. The two electrodes may be two different pieces of material or two different areas of the same material. In order for the SCC process to occur, there has to be a potential difference between the two electrodes. The electricity flows such that the positive ions enter the anode, while the negative electrodes travel to the cathode area. At the end of the process, the electrode that is corroded is the anode [19].

Even though this phenomenon was discovered a long time ago and intensive research has been conducted since then, the researchers are only now starting to understand its mechanisms and often the control measures have been unsuccessful [20]. With no accurate methods of predicting failure due to SCC, sophisticated inspections (such as ultrasonic inspection) are the only way to detect corrosion in time. Unless these are employed regularly, cracking due to SCC can produce an unexpected failure [18].

2.1.1 Stages of stress corrosion cracking

The SCC process usually has three different stages: the incubation period, the initiation of the crack and the crack propagation period until the material fails [21] [22]. The incubation period can be broken down into several stages, as illustrated in **Figure 2.1.**: the changes of the environment that constitute the precursor of a pit formation (1), the pit formation (2) and the pit growth (3). The initiation can be divided into: pre-coalescence cracks (4), coalescence (5) and propagation of coalesced crack (6). Lastly, the propagation stage includes: stress intensity factor (K_{ISCC}) criterion (7), the SCC plateau (8) and the rapid crack formation (9).

The 'precursor' (1) is the stage when the conditions for incubation are taking place (e.g. potential changes). Some of these conditions can be: surface abuse, depletion of alloy species or accumulation on superheat surfaces. During this step the surface is not penetrated [23]. The 'micropenetration' (2) is again usually not visible and is the stage during which the surface oxide film breaks. The 'small penetration' (3) period is normally associated with surface pit formation. It has been shown that the pits have not only a mechanical function in starting the SCC via local stress concentrations, but also favour SCC by changing the local chemistry [24].

The incubation period can be from several days to many years. There are also circumstances when SCC is not initiated from pitting, but from weld defects, grooves or laps [26]. Initiation of cracks can also occur through intergranular corrosion (at grain boundaries with favourable chemistry) or through slip-dissolution (when the stacking fault energy of materials is low) [26]. Other mechanisms that can explain the formation of cracks are the hydrogen embrittlement and dealloying.

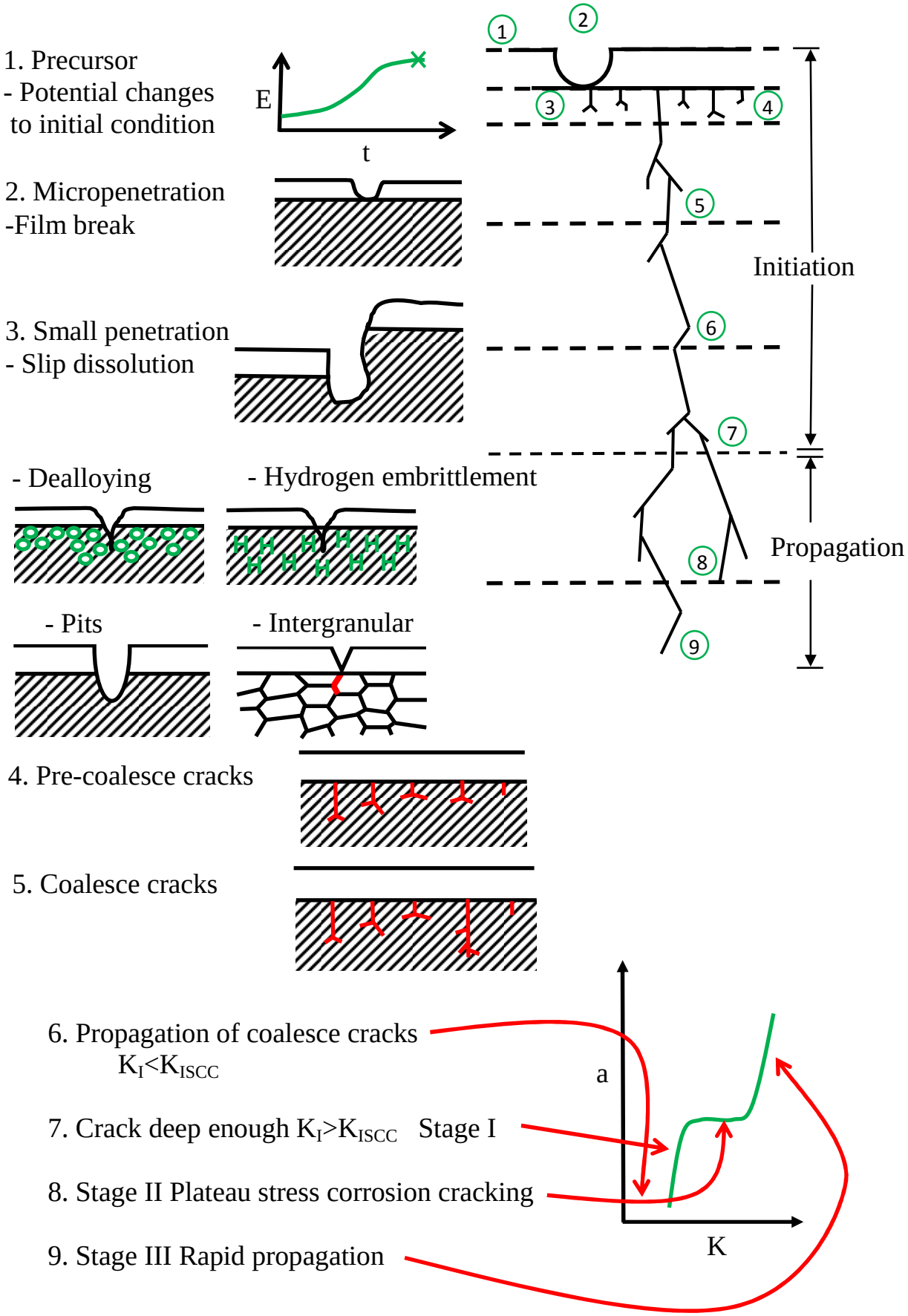

Figure 2.1 Schematic showing the nine different stages of SCC [25].

'Pre-coalescence' (4) is the stage of SCC when cracks start to grow up to 50-500 μm [23] and the number of cracks increases with increasing stress and time [23].

The crack emanates from the pit [27] that was formed during the previous stage, as a result of the summed stress concentrations [24][28]. The rate of cracking during this stage is usually much lower than propagation [23]. The 'coalescence' (5) is the transition from the short cracks to long cracks that take place through coalescence processes, as shown in **Figure 2.2.**

The 'propagation of coalesced crack' (6) is the crack propagation until the stress intensity factor (K_I) reaches a critical threshold stress intensity value, K_{ISCC} [23]. This value makes the distinction between crack initiation and crack propagation. During the 'Stage I '(7), K_I exceeds the critical value K_{ISCC} and the crack propagates until it reaches a plateau region (8). During the 'rapid propagation' (9) stage, the cracks grow very rapidly.

The propagation phase of the SCC process is yet not very well understood. Various mechanisms that have been proposed fall into two categories: electrochemical mechanisms and combined electrochemical-mechanical mechanisms [28]. However, none of them has yet been fully accepted and there is no universal SCC mechanism that can be applied to all the systems [24][29]. Predicting SCC is very difficult since the mechanism is influenced by pH, alloy composition and structure, stress, temperature and electrochemical potential [30] and only models that incorporate two or at most three different factors exist in the literature [24][31].

2.1.2 Intergranular stress corrosion cracking (IGSCC)

Intergranular corrosion or ‘grain boundary attack ’is a non-uniform corrosion process that occurs due to the potential difference between the grain boundaries (that have been chemically changed by precipitation at the grain boundaries) and the rest of the metal [19] [20]. As a result of intergranular corrosion, a narrow band of the material is attacked along the grain boundary [32].

Intergranular stress corrosion cracking appeared for the first time in 304 stainless steel pipe welds in boiling water reactors in the heat-affected zone, after a couple of years in use [33][34] and continued to be a severe problem affecting the large diameter pipes that were used in the coolant recirculation loops [35]. In Ni Alloy 600, IGSCC occurs

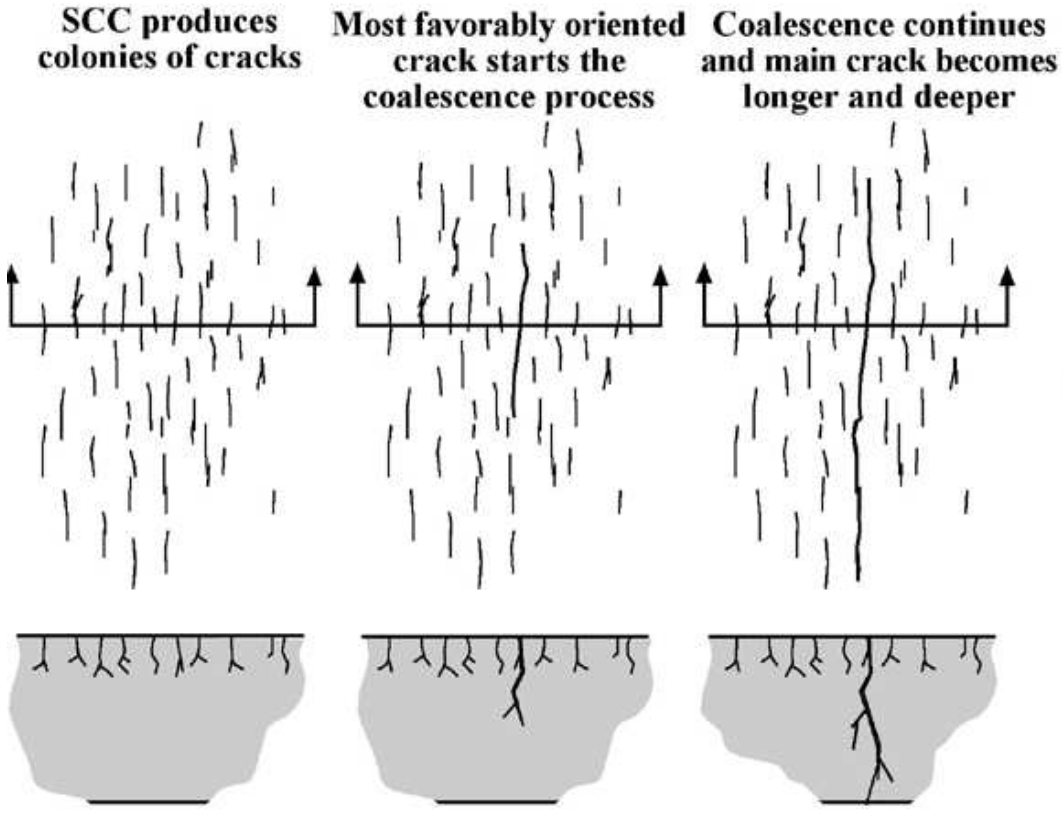

Figure 2.2 Schematic showing the transition from short to long cracks to coalescence processes [23].

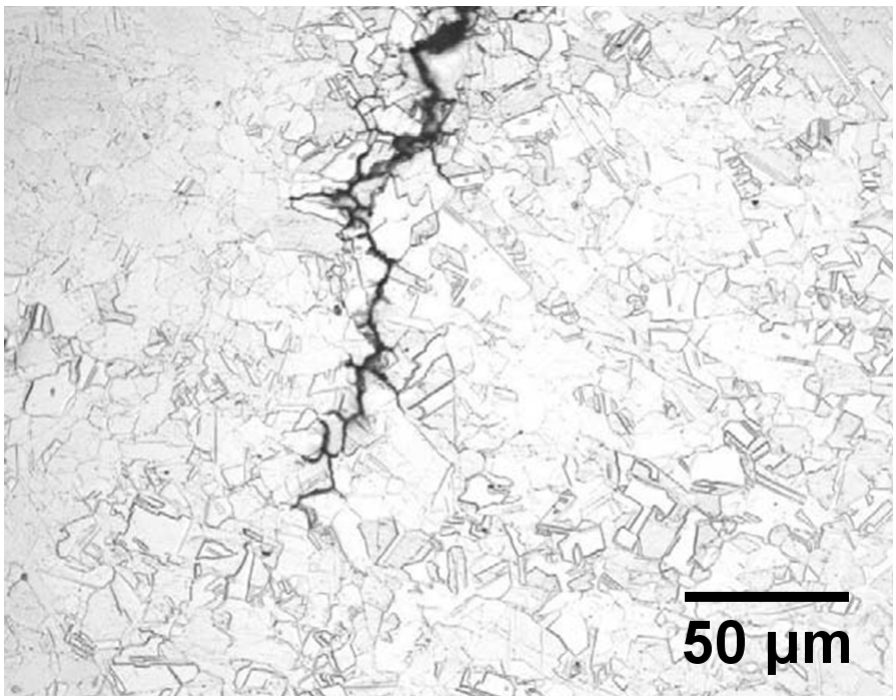

Figure 2.3 Ni Alloy 600 microstructure attacked by IGSCC [36].

mainly in pressurized water reactors, also called PWSCC. An image showing an Alloy 600 affected by IGSCC is shown in **Figure 2.3.**

2.1.3 Factors that affect SCC

There are several factors that influence and add to the complexity of stress corrosion cracking processes. Some of the possible factors that will be described next are: stress, environment and microstructure.

2.1.3.1 Stress

Stresses that enhance SCC in stainless steels are usually caused by external factors (applied load or other corrosion products) or by residual stresses due to welding, forming, cold work, service load, heat treatment or inhomogeneous plastic deformation [13] [24][32][35][37].

The threshold stress at which stress corrosion cracking initiates varies with material and environment from 20% to more than 100% of the yield stress [26]. Even though failure

occurs more rapidly at higher values of the applied stress and cracking takes longer to initiate at lower stress values, there is no minimum value of stress for which SCC will not start [15][26].The level of stress that produces SCC is different for various steel groups [32] and it is highly influenced by the alloy composition, temperature and environmental conditions [15]. For example, it has been observed that, in austenitic stainless steels , in a caustic solution, cracking occurred at stresses that were below the yield stress [38]. In environments such as oxygenated high-temperature water, it was observed that SCC does not occur in austenitic stainless steels when the stresses are below the yield stress [39][40][41][42]. In type 304 SS in boiling $MgCl_2$ at a temperature of 154°C, SCC occurs at stresses between 75 and 100 MPa while in Alloy 600 exposed to PWR primary water, SCC does not occur below 250 MPa [23].

K_{IGCC} is a value below which very small rates of crack growth are present [43] and it usually ranges between 5 and 25 MPa $(m)^{1/2}$ [23]. The influence of the stress intensity factor K on the crack rate of SCC for 304 SS in chloride solution and magnesium chloride is shown in **Figure 2.4.** In 304 SS at a temperature of 153° C in boiling $MgCl_2$ the K_{ISCC} is around 4 to 5 MPa$(m)^{1/2}$ while in Alloy 600 exposed to PWR primary water the K_{ISCC} is around 9 MPa$(m)^{1/2}$ [23].

2.1.3.2 Environment

Temperature is an environmental factor that greatly influences stress corrosion cracking. In stainless steels, SCC is not often observed at temperatures below 60° C [27]. It has been stated by Fontana [15], that by increasing the temperature in an environment where chemical reactions are present, the SCC process is accelerated.

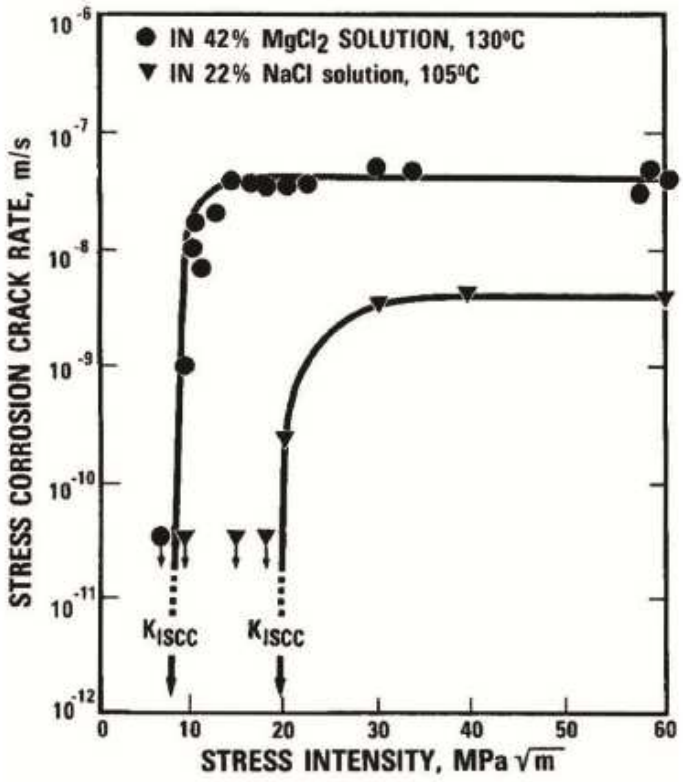

Figure 2.4 SCC crack rate as a function of stress intensity factor for 304 stainless steel in two different environments [44].

Regarding the environments favourable to SCC, it has been shown that in the case of steel 304, intergranular stress corrosion cracking occurs in the water environments in boiling water reactors [32][35].The aggressive environments that favour SCC in metals, besides aqueous corrosive liquids, includes reactive atmospheres (H_2O, I_2, Cl_2), gaseous hydrogen or liquid metals [13]. Several examples of chemical species that can cause SCC of a specific alloy are summarized in **Table 2.1**. These species do not have to be present in large quantities or high concentrations [24]. However, as it has been established by Andresen *et al.* [170] that, given enough time, any aqueous or gaseous environment can produce SCC.

In a review of the influence of the environment on SCC in stainless steels, it has been reported by Engelberg [44] that during the plant shutdowns polythionic acid caused

Table 2.1 Examples of the different environmental conditions under which SCC occurs in different materials [23]

Material	Environment	Temperature
Austenitic Stainless Steels	• Near neutral, diluted aerated chloride solutions • Very acidic chloride solutions • Chloride environment containing H_2S • Caustic solutions	> 60/100 °C ≥ RT ≥ RT ≥ 80/120 °C
Ni-Base Alloys	• Caustic environments	≥ 100/200 °C
Ni-Base Alloys < 25-30 % Cr	• Deaerated, hydrogenated water	≥ 250/280 °C
Sensitized Stainless Steels and Ni-Base Alloys	• Aerated 'pure' water • Solutions containing reactive sulfur species (polythionic acids, thiosulfates, thiosulfates)	≥ 60/100 °C ≥ RT

IGSCC at chromium-depleted boundaries. The acid was formed as a result of the reaction between the sulphide and the moisture present.

It was determined that, in this case, the tetrathionate ion $(S_4O_6)^{2-}$ is the one that causes rapid cracking. In this current thesis, potassium tetrathionate ($K_2S_4O_6$) is used as the active solution to investigate crack initiation and crack growth rate in 304 SS. As shown in **Figure 2.5** both the concentration of the $(S_4O_6)^{2-}$ and the pH influence the IGSCC process in 304 SS such that cracking is accelerated by an increase in acid concentration (decrease in the pH).

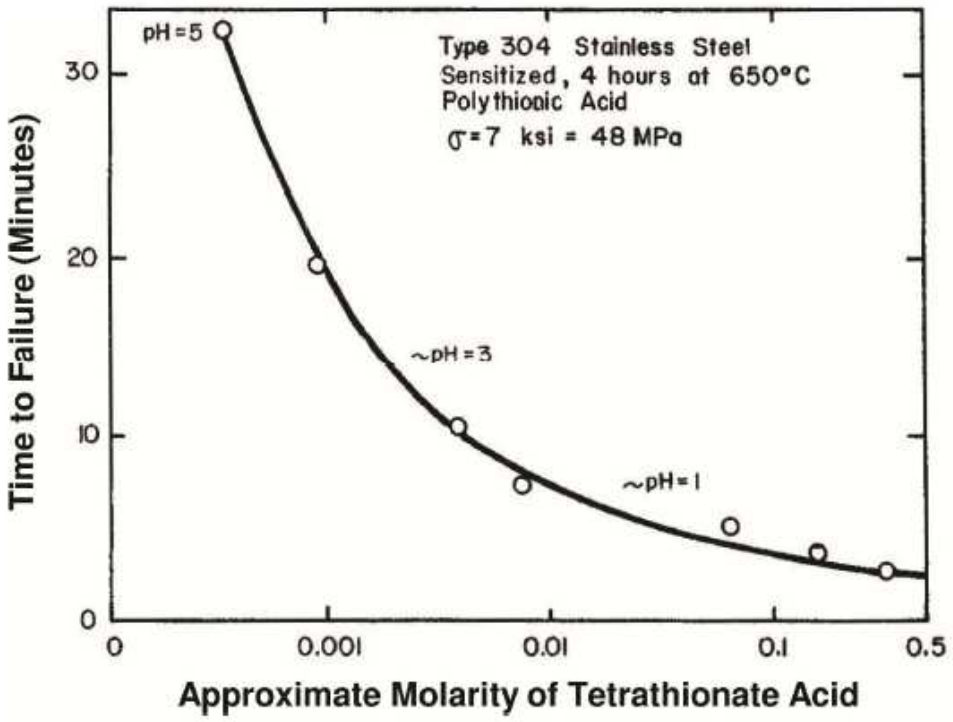

Figure 2.5 Influence of the tetrathionate acid concentration on the time of failure of 304 SS [44].

The tetrathionate solution can be prepared in distilled water and the pH can be varied by diluting the solution with sulphuric acid, the procedure that was used in this thesis. In previous studies [25], IGSCC in stainless steels was observed to occur in $K_2S_4O_6$ in the following situations:

- Concentration > $3.3x10^{-3}$ mol/l and pH<3 caused IGSCC in austenitic steel
- Concentration=0.033 mol/l and pH=5.3 caused IGSCC in 304SS within 18 days
- Concentration=0.033 mol/l and pH=1.5 caused IGSCC in 304SS within 1 hour
- Concentration=0.1 M and pH=2 caused IGSCC in 304 SS (the incubation time was dependent on the level of sensitisation) [45]

It can be concluded from the above observations that tetrathionate is a solution that can be easily used in IGSCC experiments to control the initiation time by changing the concentration of the solution.

2.1.3.3 Microstructure

The "Grain Boundary Engineering" (GBE) concept introduced by Watanabe *et al.* [55] was the first step towards making materials less susceptible to degradation by increasing the fraction of "special" grain boundaries. While lack of experimental data makes defining a "special" grain boundary very difficult, a "special" grain boundary is often classified to have a ∑CSL value lower than ∑29, while a "random" grain boundary has a ∑CSL values above ∑29 and is considered to have a very low resistance. The symbol ∑ represents the ratio between the volume of the CSL unit cell and the volume of the lattice cell of the boundary. The CSL is defined as an array of points in the lattice that coexist for a specific misorientation [148].

Gertsman *et al.* [144] looked at IGSCC in 304 austenitic steel that was sensitized (the time or the temperature of the sensitization treatment is not mentioned) and tested in a high-temperature water environment (PWR simulated environment). It was observed that only ∑3 grain boundaries were "special" non-cracking grain boundaries and even so, they were not always resistant to IGSCC. ∑9 and ∑27 were also found to crack but a conclusion based on the probability of failure with respect to the ∑ value was not possible because of the limited number of grain boundaries in the observed population of 161 boundaries. The study also concluded that the ∑ parameter is not the only one that controls IGSCC susceptibility and that other factors such as segregation and precipitation should be taken into consideration. Rahimi *et al.* [45] also observed that microstructure plays an important role in crack initiation, in an *in-situ* stress corrosion

cracking experiment on thermally sensitized 304 stainless steel, (tested in 0.1 M potassium tetrathionate solution diluted with sulphuric acid with a pH of approximately 2, heat treated at a temperature of 650 ^{o}C for 20 h). While most of the grain boundaries that experienced cracking were 'random' grain boundaries ($\sum$>29), a significantly lower percentage (roughly 10%) of $\sum$3 grain boundaries were observed along the crack path than in the overall microstructure (%). In addition, grain boundaries with $\sum$1, $\sum$9 and $\sum$27 were also observed to have a higher resistance to cracking.

As Randle [151] states, the GBE approach is far from being complete, since these models do not take into consideration the grain boundary plane and the fact that it plays an important role in determining special properties of the grain boundaries. A grain boundary has five degrees of freedom and all define the geometry of a grain boundary. Two degrees of freedom define the crystallographic orientation of the grain boundary plane and the other three degrees of freedom represent the misorientation of a grain boundary [151]. The CSL only takes into account the misorientation of a grain boundary (relative crystal orientations of the adjacent grains), leaving out the grain boundary plane orientation with respect to the grains.

King *et al.* [152] took a step forward into observing the interaction between IGSCC and microstructure in 3D, using diffraction contrast tomography to measure grain orientation and shape in thermally sensitised austenitic steel, combined with tomographic observations of *in-situ* stress corrosion cracking (tested in acidified 1.2 M potassium tetrathionate solution with a pH of approximately 2). It was observed that grain boundaries that have a higher resistance to IGSCC are not necessarily low $\sum$ boundaries, but boundaries that were adjacent to the low {hkl} index planes. Jones and Randle [153] concluded that the carbide precipitation in 316 stainless steel is selective to boundary plane rather than low $\sum$ boundaries; for instance incoherent twins were not

immune to precipitation while no precipitation occurred in coherent twins. Also, the precipitation was more common on boundaries that were not on {111} planes than in twins boundaries on {111}.

Surface condition [46], is also a determining factor in the initiation of SCC, especially in steel 304 [17]. In a study conducted by Kuniya [47], it was observed that, in sensitized type 304 SS, time to failure due to the IGSCC decreases with the presence of roughness and surface tensile stress, when specimens were loaded at 8.3 MPa at 288 °C in 26 ppm oxygenated water. However, type 304L sensitized stainless steel that was ground and sensitised at 621 ^{o}C for 2 h, exposed to the same environment did not show any IGSCC susceptibility [47]. Matsushima *et al.* [48] observed the role of surface condition of 304 SS, at 300 °C, in water containing 600 ppm chloride, under constant load conditions. It was concluded that initiation happened more quickly on mechanically polished surfaces than on chemically or electrochemically polished surfaces. Scott [35] also mentions grinding as being deleterious. Solomon [49] has also observed during some extensions tests that the electropolished samples failed in higher strains and only one crack was formed, while in the mechanically polished samples several cracks were formed. As mentioned by Acharryya *et al.* [50], this effect is due to the fact that, through machining grinding, the residual stresses on the surface can reach values as high as 1100 MPa, work hardened layers can be formed and grains can be fragmented. In addition, the electrochemical behaviour is changed by changing the surface roughness; the groves at the surface are deeper and accelerate the crack initiation process.

Another factor that might influence intergranular corrosion is the grain size. It was observed that in an H_2SO_4 environment, sensitization of stainless steels increases with

increasing grain size [51]. Newell [52] reports that larger grains are more susceptible to intergranular attack. Cihal [53] agrees with Newell and he explains that smaller grains have a smaller grain surface area with less possibilities of developing a network of carbides at the grain boundaries. The bigger grains have a larger grain boundary area with more carbides and so the chromium depleted zone increases. This observation was later on confirmed [53][54].

Cold work also influences SCC and it is believed that the susceptibility of 304 SS to SCC increases with the increase of the degree of cold work. A more detailed review is presented by Garcia *et al.* [169]

Chromium content also affects the IGSCC. The effect of chromium content can be best understood from the polarization curve of Fe-Cr-Ni alloys in the presence of sulphuric acid, given in **Figure 2.6**. By increasing the chromium concentration, the passivation potential becomes wider and moves towards the more active zone. A typical polarization curve showing the active and passive zones is shown in **Figure 2.7**. The influence of chromium concentration is linked to sensitization of the stainless steels that will be described in more detail in **Section 2.2.4**.

2.1.4 Models for the effect of microstructure on IGSCC

Since Watanabe [55] introduced the concept of grain boundary engineering, several models have been developed to predict the relation between the grain boundary properties and the crack propagation. These approaches can be grouped into two categories: a) percolation theory models and b) percolation-like models [44][25]. A classification of the models is given in **Figure 2.8**.

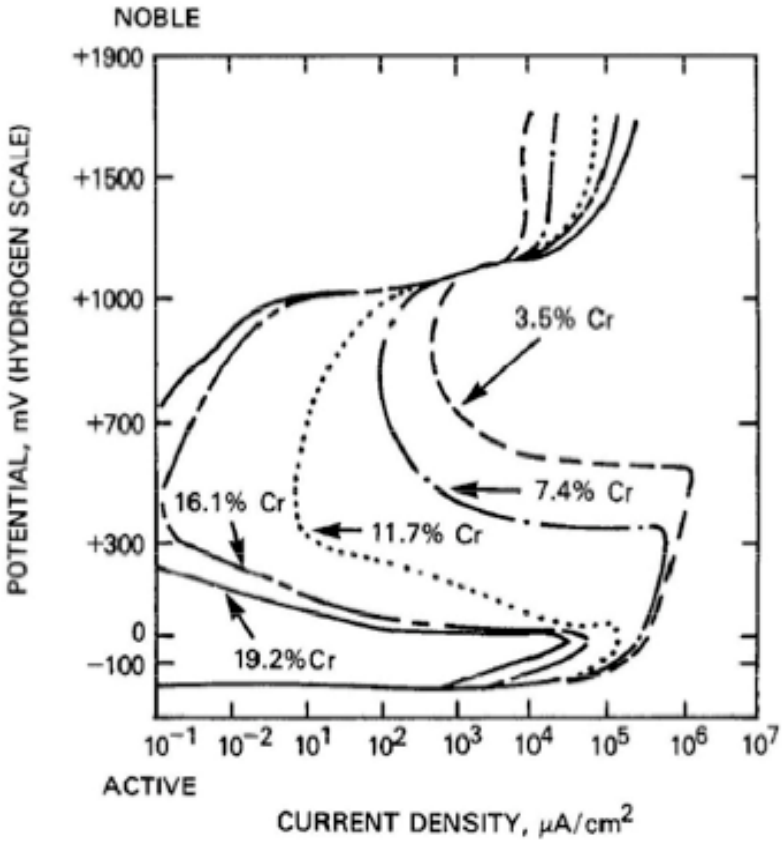

Figure 2.6: Influence of chromium concentration on the polarization curve of Fe-Cr-Ni alloys [16].

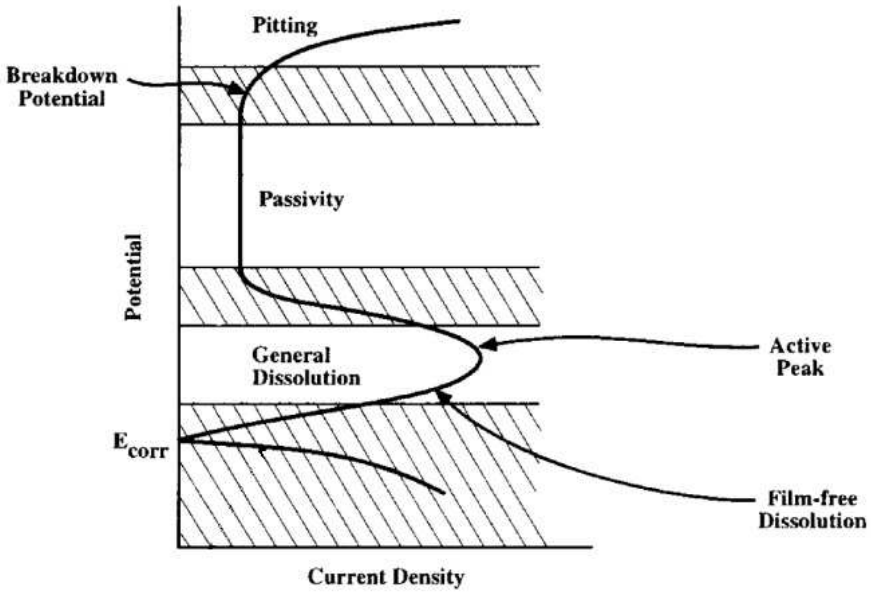

Figure 2.7 Typical polarization curve showing the regions where SCC can occur [26].

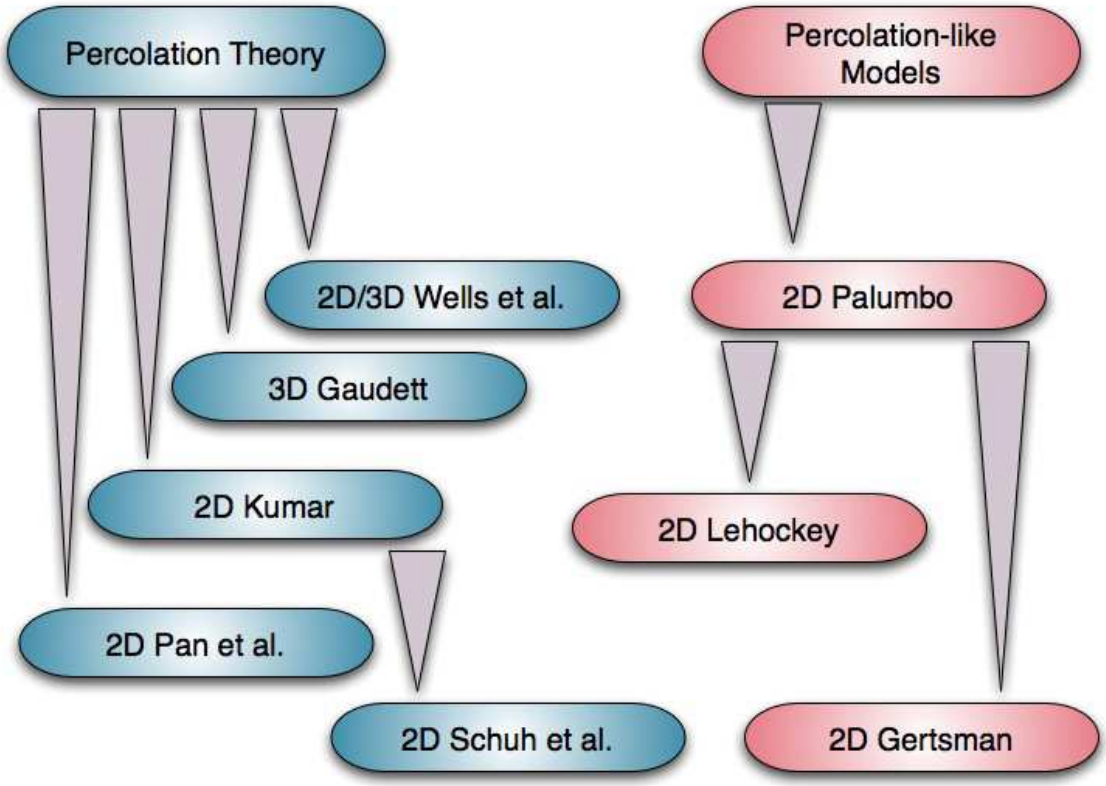

Figure 2.8: Diagram of IGSCC models [Adapted from [25]].

2.1.4.1 Percolation theory and models

Percolation theory is a mathematical concept based on combinatorial elements that are used to define a structure-related critical percolation threshold. A percolation model is defined by a network of points distributed in space, with groups of points that might be linked or adjacent. The criterion of adjacency is established by a mechanism defined in the context of the model [56]. The definition of percolation and clusters is shown in **Figure 2.9.**

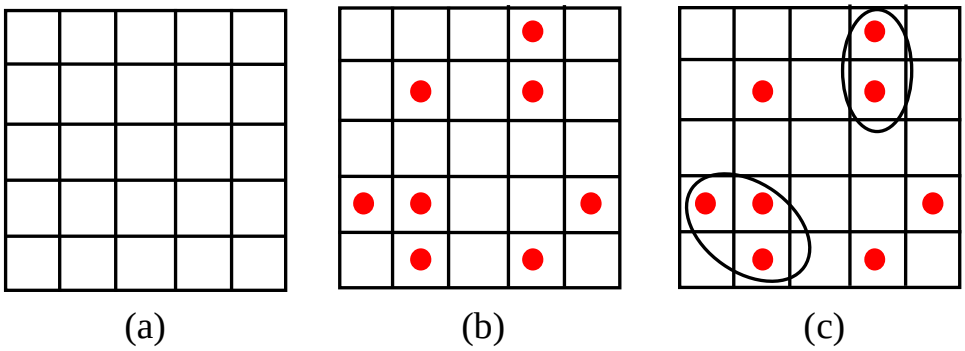

Figure 2.9 Illustration of the percolation theory: (a) representation of a square lattice; (b) dots occupy some squares while others remain empty; (c) clusters are marked [57].

An infinite square lattice is given (a) and it can be randomly occupied by dots (b). Clusters (c) are defined by occupied squares that have one side in common. The percolation theory studies the properties and the number of these clusters [57].

Wells et al. [58] used a percolation theory for 304 stainless steel to determine the susceptibility to IGSCC of grains with different degrees of sensitization. This was implemented using a bond percolation, in which non-sensitized grain boundaries were modelled as inactive while sensitized grain boundaries were modelled as active. The results of the simulations were then compared with the Electro-Potentiokinetic Reactivation (EPR) tests, and it was concluded that samples with a fraction of sensitised boundaries between 23% and 89% fail in both brittle and ductile manner, the ones with a fraction of sensitised boundaries less than 23% are not affected by IGSCC while the ones with a fraction above 89% experience only brittle intergranular fracture.
Gaudett [44] used percolation theory to quantify the level of chromium depletion at the grain boundaries in stainless steel 304. It was established that as the sensitization time increases, the fraction of the grain boundaries which are depleted in chromium increases. Kumar/Schuh improved the previous models by taking into consideration the

limitations of the grain boundary networks [59]. The model used a continuous percolation path, defining the reason of intergranular failure as the triple junctions [44]. The Pan et al. model used for nickel-based alloy 600 observes that twin boundaries improve resistance to corrosion while random grains lower the resistance [59]. These models were a good starting point in understanding the classification of grain boundaries in fully sensitized austenitic stainless steels and nickel alloys and they have been improved by the percolation-like models.

2.1.4.2 Percolation-like models

The percolation-like models are designed for a maximum likely crack length and the material failure depends on finding this length and its relation to the specimen geometry [25] .

The Palumbo model [60] is a 2D model that was first developed to see whether the IGSCC resistance of nickel-based alloys can be improved by considering grain boundary control. This is a geometric model that simulates crack propagation through intergranular paths to determine the effect of different grain boundaries and the average grain size in equiaxed polycrystalline materials. The model is based on the probability of crack propagation through a bulk material when the material is exposed to the combined effect of both stress and corrosive environment. The critical parameter of the model is the critical length: L_{crit} which depends on the wall thickness and on the level of stress applied. If the crack exceeds L_{crit} limit, then failure can occur even though no corrosive environment or active grain boundaries are present. Susceptibility to IGSCC is defined as the probability of finding a crack growth path that exceeds L_{crit}. All the grain boundaries modelled are oriented in such a way that they are in the direction of the applied stress as shown in **Figure 2.10** [60].

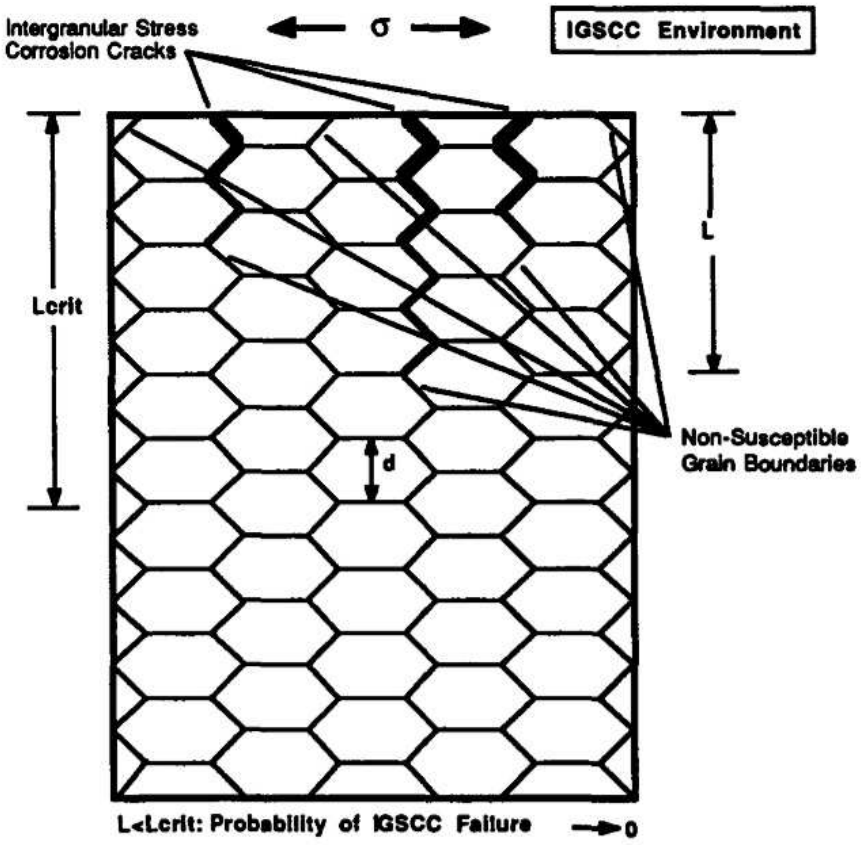

Figure 2.10: Representation of the parameters used in the Palumbo model [60].

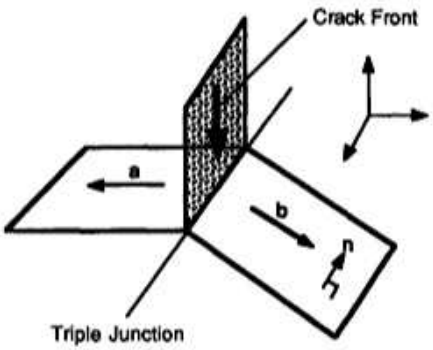

Figure 2.11: Schematic representation of factors causing intergranular attack at a triple junction. IGSCC occurs at a crack front that is part of a triple junction when path (a) and path (b) have an unfavourable orientation to the stress axis (n) [60].

The intergranular crack arrest (or transition to transgranular crack propagation) can occur at triple junction when the other two available intergranular paths (path (a) and path (b)) have a different orientation towards the stress axis or they have a structure and chemistry that is unfavourable, as shown in **Figure 2.11**.

The model considers that the probability of finding more than one unfavourable grain boundary is zero (due to the geometry shown in **Figure 2.10**), so the probability of intergranular crack arrest at a triple junction is given by the following equation:

$$P = f_{sp}^{\ 2} + 2[f_0 f_{sp}(1 - f_{sp})] \quad \textbf{(1)}$$

where f_{sp} is the fraction of grain boundaries that are not susceptible and f_o is the fraction of grain boundaries that do not have the same orientation as the stress axis [44][60]. To calculate the probability (X) of arresting a crack within a length L, where d is the average grain size, the equation below can be used:

$$(1 - X) = (1 - P)^{2L/d} \quad \textbf{(2)}$$

Both **Equation (1)** and **Equation (2)** indicate that the grain size, the grain boundary character distribution and the shape of the grain influence the IGSCC susceptibility. Furthermore, the plot of the probability of arresting a crack (X) versus the fraction of grain boundaries that are not susceptible (f_{sp}) for different ratios of L/d, shown in **Figure 2.12** , indicates that by increasing the non-susceptible boundaries, the IGSCC propagation as well as the number of cracks formed are reduced [60]. The model proposed by Palumbo indicates that increasing the grain size and the fraction of non-susceptible grain boundary should increase the IGSCC resistance.

After the Palumbo model, several similar models have been developed, improving on the initial one. Both the Lehockey and the Gertsman models add a deeper understanding

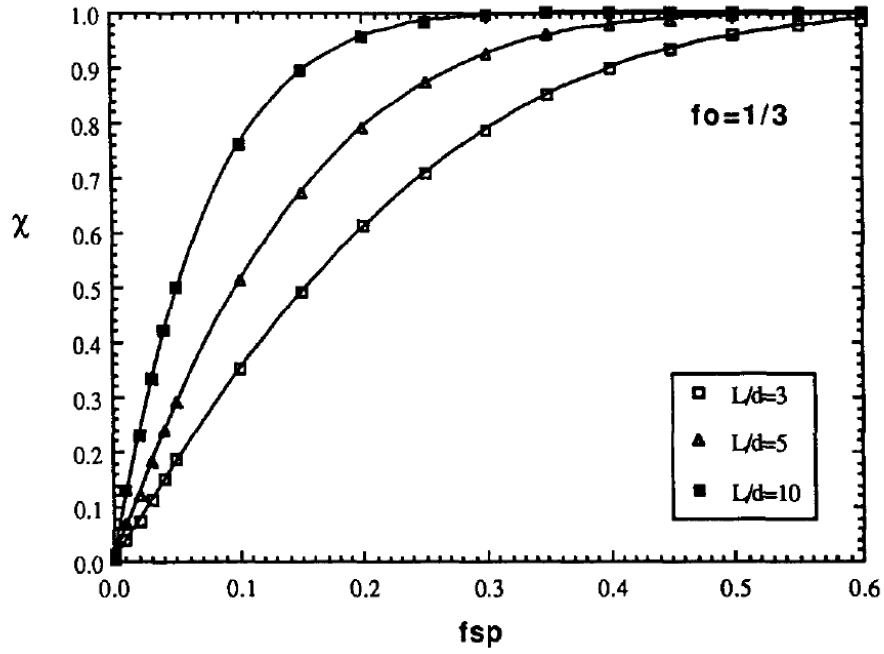

Figure 2.12 Graph of the probability of crack arrest as a function of the fraction of non-susceptible boundaries. As the fraction of resistant boundaries increases, the IGSCC propagation decreases [60].

of the grain boundary character distribution and the grain boundary classification within a microstructure [59]. Gertsman assumed that the only grains that are not susceptible to intergranular corrosion are the twin boundary (sigma 3) and not all the grain boundaries with sigma ≤ 29. Gertsman also noticed that the Palumbo model ignores the orientation correlation of the grains that are next to each other.

So, to take this into consideration, the network that was considered in the model was that of triple junctions and not the individual grain boundaries [44]. In the Lehockey model, the grains that are considered not to be susceptible to corrosion are the twin boundaries and the twin variations. In addition, the higher order twin grains ($\Sigma 9$, Σ 27) are assumed to be formed only after twinning effects [44].

Percolation-like models proved to be improvements on the percolation models (these models considered that some grain boundaries are more resistant to IGSCC than others, and also look at the distribution of grain boundaries), however, these models did not

take into consideration the mechanical component of IGSCC (e.g. crack driving force), that is an important variable in understanding IGSCC [59].

The susceptibility to IGSCC of austenitic stainless steels has been observed to be different for different grains as will be described in more detail in **Chapter 6**. The fact that the grain boundaries properties are connected to the intergranular crack propagation makes it very difficult to understand IGSCC [44] and no quantitative classification of the grains (resistant or susceptible) has been made so far.

2.2 SCC in Stainless Steel

As defined in the British Standards, stainless steels are steels that have at least 10.5% chromium and maximum 1.2% carbon [61]. To extend the definition, the stainless steel group includes iron-chromium alloys and iron-base alloys that have great corrosion, heat and creep resistance. They can withstand concentrated acid environments, they do not scale at temperatures below 1100 °C and they do not rust in sea water [32].

“Stainless” is greatly used in nuclear reactor technology, in the primary side shells of the steam generators (in pressurized water reactors), the pump bowl materials (in the reactor coolant circuits), some main coolant pipes, accumulators and refuelling water storage tanks [17].

2.2.1 History and applications of stainless steels

Vauquelin was the first who studied the properties of iron in the presence of chromium in the year 1797. Later on, in 1821, Berthier worked on a similar material and made several observations regarding the content of iron and chromium. At the end of his study, he managed to produce a 1.5% Cr steel that was used for knife blades which was more resistant to corrosion that the carbon steels [18].

It cannot be stated for sure who is the inventor of stainless steel. The British believe that Brearley produced the first stainless steel while he was trying to discover a material that would be highly resistant to abrasive wear for heavy guns. At that time, chromium was one of the alloying elements that proved to have high corrosive resistance and a stainless steel which contained 0.70% carbon and between 9 and 16% chromium was produced [32]. This steel was the one used for the first stainless cutlery in 1915, in Sheffield [20]. At around the same time as Brearley, Strauss was researching in Essen, Germany to determine a suitable material for protective tubing for thermocouples and pyrometers. His work involved looking at iron-chromium-nickel alloys with a high chromium concentration and at iron-base alloys. Discovering that chromium concentration above 20% protected specimens from rust even after many hours of testing, he developed a steel that contained 0.25% carbon, 20% chromium and 7% nickel. This is known to be the first austenitic stainless steel [20]. In the USA, Becket was also working on steels, trying to discover a scaling-resistant material that would be able to withstand temperatures up to 1200 °C. Strauss discovered that chromium content above 20% was required to resist scaling and oxidation. Strauss initiated the development of the heat-resistant steels [32].

Even though the production of steel has been constant after 1975, the demand for stainless steel has increased by 3-5% annually [16]. More than 180 alloys belong to the stainless steels group [16]. The austenitic stainless steels 300 series (groups where manganese concentration is equal to or lower than 2%) [62] represents the most common and the largest category produced in the United States. The most common steels that are now used are the austenitic 18/9 steels (AISI 304 and 304L); their production represents more than half of the world production of stainless steel [32] and increased from 23,086 tonnes in 1942 to 570,584 tonnes in 1994. Due to their high

corrosion resistance, stainless steels have applicability in numerous industries such as: chemical, petroleum, process and the power industry. In addition, stainless steels are also used in the power generation industry, architecture, chemical pharmaceutical, street furniture as well as domestic appliances [27]. The most common classification of steels is made according to their structure at room temperature, as follows: ferritic, martensitic, precipitation hardening, austenitic and austenitic-ferritic steels [63].

2.2.2 Classification and properties of stainless steels

The composition of the different steel categories is presented in **Table 2.2**. The physical properties of stainless steels are different from the carbon steels, and each stainless steel category has distinctive properties (**Table 2.3**).

Martensitic steels have a high yield and tensile strengths and a low ductility, while the austenitic stainless steels have a low yield strength and high ductility. Between the two extremes, there are the ferritic steels and the ferritic-austenitic steels [32].

Table 2.2: Composition of different categories of stainless steel [32]

Steel category	Composition (wt%)					Hardenable	Ferromagnetism
	C	Cr	Ni	Mo	Others		
Martensitic	>0.10 >0.17	11-14 16-18	0-1 0-2	- 0-2	V	Hardenable	Magnetic
Martensitic-austenitic	>0.10	12-18	4-6	1-2		Hardenable	Magnetic
Precipitation hardening		15-17 12-17	7-8 4-8	0-2 0-2	Al Al,Cu, Ti, Nb	Hardenable	Magnetic
Ferritic	<0.08 <0.25	12-19 24-28	0-5 -	<5 -	Ti	Not hardenable	Magnetic
Ferritic-austenitic (duplex)	<0.05	18-27	4-7	1-4	N,W	Not hardenable	Magnetic
Austenitic	<0.08	16-30	8-35	0-7	N,Cu, Ti,Nb	Not hardenable	Non-magnetic

Table 2.3: Physical properties of different categories of stainless steels [32]

Property	Type of stainless steel			
	Martensitic	**Ferritic**	**Austenitic**	**Ferritic-austenitic**
Density (g/cm^3)	7.6-7.7	7.6-7.8	7.9-8.2	0.8
Young's modulus (GPa)	220	220	195	200
Thermal expansion (x 273 K) 473 - 873 K	12-13	12-13	17-19	13
Thermal conductivity (W/m*K) 293 K	22-24	20-23	12-15	20
Heat capacity (J/kg*K)	460	460	440	400
Resistivity (mΩm) 293 K	600	600-750	850	700-850
Ferromagnetism	Yes	Yes	No	Yes

2.2.3 Austenitic stainless steels

Austenitic stainless steels are the most common stainless steels and they maintain the face centered cubic (fcc) structure of austenite (γ Fe)[18][62]. They are relatively easy to fabricate and they are characterized by a very good toughness, weldability and resistance to corrosion [18][32].

Due to the fcc crystal structure, austenitic stainless steels are ductile (they have a high elongation), non-magnetic, tough and plastic materials [53]. Austenitic stainless steels cannot be hardened by heat treatment or quenching at room temperature. They have a great creep resistance when used at temperatures below 700 °C [18]. Regarding the physical properties, austenitic stainless steels have a considerably higher thermal expansion than other types of stainless steel. In comparison to other types of steels, the austenitic steel has the lowest thermal conductivity [32].

Austenitic stainless steels usually have a low yield stress, of ~300 MPa, and an ultimate tensile strength of ~650 MPa. However, increasing the carbon, nitrogen or molybdenum concentration can increase the strength [32]. Austenitic stainless steels are characterized

by a high ratio of the yield strength to tensile strength;by introducing cold work in the material, it becomes considerably stronger [18][53].

The type of austenitic stainless steels that have the highest resistance to crevice corrosion and pitting are : AISI 304, 304L, 316, 316L, 317L, followed by 904L, 254SMO and 654SMO [32].

The element that is responsible for the high resistance to corrosion is chromium [15]. When chromium is added to a steel, it forms a thin (20-30 nm thick) invisible protective layer of Cr_2O_3, also called a passive film [27], which is very resistive to chemical attack and it is very adherent [27]. This passive layer protects the austenitic stainless steel from attack in an aggressive environment and if the layer is damaged by scratching, the repassivation process (reformation of the layer) occurs immediately [27]. To obtain a uniform passive film, the chromium concentration should be above 11%. As the chromium concentration increases, the passivity increases as well, until the chromium concentration reaches 17%, above which chromium concentration no further increase in passivity is found [32]. Due to this reason, most stainless steels (except “hardenable” ones that have 12% chromium) have in their composition around 17-18% chromium. Besides increasing the corrosion resistance, the increase in chromium content also increases the resistance to oxidation, when the material is exposed to high temperatures [32].

2.2.4 Sensitisation

“Sensitisation” represents the precipitation of chromium carbides at the grain boundary when the specimen is exposed to a temperature between 450-850 ^{o}C [44].

Both ferritic-austenitic steels and austenitic steels are highly affected by intergranular corrosion. Ferritic-austenitic steels are normally not subject to intergranular corrosion at

temperatures below 900-950 °C [32]. Austenitic steels become susceptible to intergranular attack if they are heated to a temperature above 400 °C (especially between 550 °C and 850 °C) or when they are slowly cooled down from a temperature above 1000 °C [32] [53]. Ever since 1930 it has been known that this is caused by the chromium depletion in the grain boundary, as a result of the formation of grain boundary carbide precipitates [64] as shown in **Figure 2. 13**. In the group 300 stainless steels, the precipitates present after sensitization are chromium carbides [16] and the predominant one is $M_{23}C_6$ [16]. The solubility of carbon in austenitic stainless steels is below 0.03%, when the steel is heat treated at a temperature below 850 °C. In this case, the precipitation of $M_{23}C_6$ carbide can occur, if the steel is exposed to a temperature between 450 °C and 800 °C [27].

Because chromium has a very low diffusivity in austenitic steels this precipitation produces a zone of approximately a few tens of nanometres width adjacent to the grain boundary which is depleted in chromium [27][35].

In the case of 304 SS, the carbon content is usually between 0.06 and 0.08%. Carbon promotes the austenitic structure and it also improves the mechanical strength [15]. The chromium concentration profile across a chromium-depleted grain boundary for type 304 SS heat treated at a temperature of 700 °C for 10 hours determined by TEM microanalysis is presented in **Figure 2.14** [65].

Etienne [67] reports in a study of the of $M_{23}C_6$ growth in type 304 stainless steel that for a holding time of more than 10^4 h at a temperature of 600 °C, the predominant precipitation occurred in the grain boundaries. Honeycombe [68] also notes that the critical range of temperature for the nucleation of chromium carbides is usually

between 500-850 °C and mentions that after a stainless steel passes through this heating region, the material becomes susceptible to intergranular corrosion.

The carbon content should be kept below 0.030% to reduce susceptibility to sensitization [62]. An increase in the carbon concentration above 0.030% will increase the intergranular corrosion rate if sensitised [16][20].

2.2.4.1 Sensitisation tests

Several destructive and non-destructive tests have been developed and standardized to detect the susceptibility to intergranular attack in austenitic stainless steels. These tests are listed in **Table 2.4** and described below.

Table 2.4: ASTM standards for detecting sensitization in stainless steels

ASTM Standard Name	Environment	Exposure	Evaluation	Species attacked
A262, Practice A	10%$H_2C_2O_4$, anodic at 1 A/cm^2, ambient temperature	1.5 min	Type of attack	Chromium-depleted area at carbides
A262, Practice B	50% H_2SO_4+2.5 %$Fe_2(SO_4)_3$,boiling	One 120-h period	Weight loss per unit area	Chromium-depleted area at carbides and at twin boundaries in certain alloys
A262, Practice C	65% HNO_3, boiling	Five 48-h periods, fresh solution in each period	Average weight loss per unit area	Chromium-depleted area at sigma and carbides and other phases
A262, Practice E	15.7% H_2SO_4+5.7% $CuSO_4$	One 24-h period	Appearance after bending	Chromium-depleted area at carbides
A262, Practice F	50% H_2SO_4+$CuSO_4$	One 120-h period	Weight loss per unit area	Chromium-depleted area at carbides

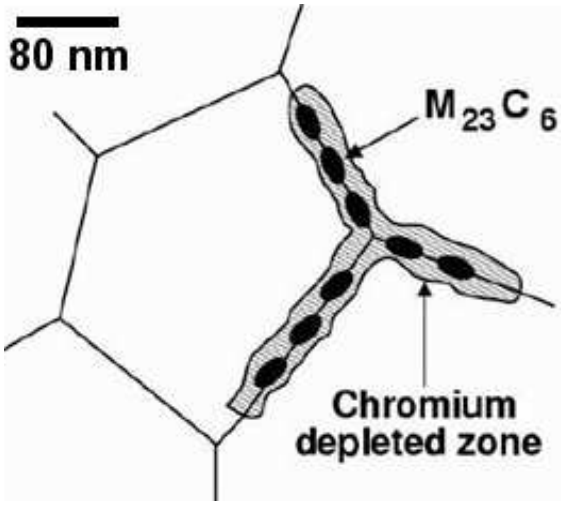

Figure 2.13: Illustration of chromium carbide precipitation at the grain boundaries [66].

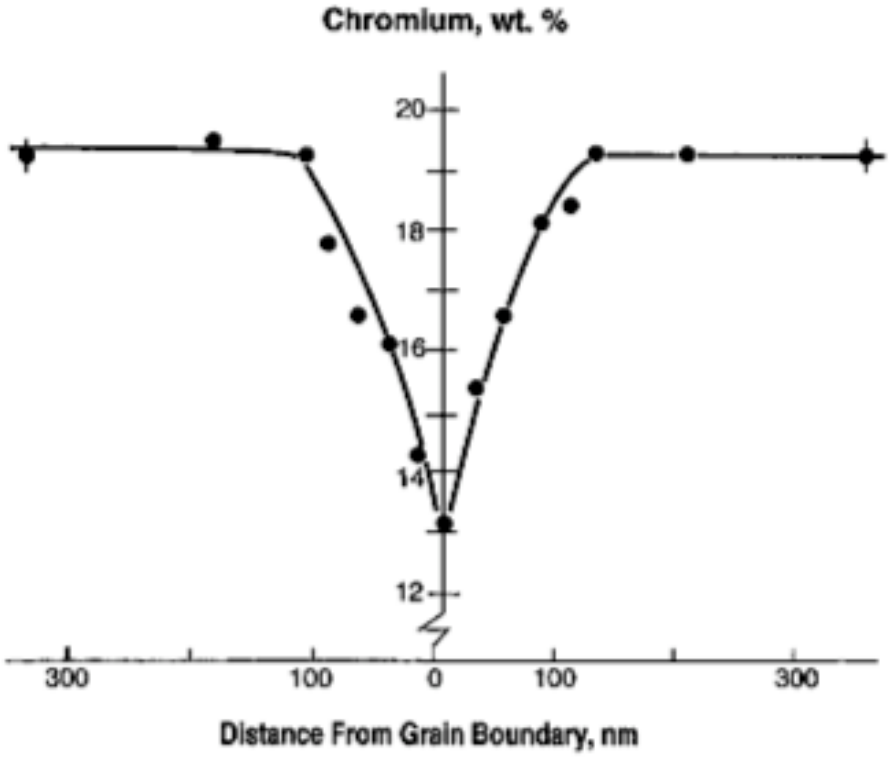

Figure 2.14: Chromium concentration across a sensitised grain boundary in 304 steel [65].

ASTM A262 Practice A or "Oxalic Acid Test"

This test represents a quick method of testing the material. However, it can only be used for the acceptance of the material, but not for the rejection. If a material passes the test, it means that it is sensitised; however, if it does not pass the test it does not mean that is not sensitised. In order to confirm or disprove if a material that fails the test is sensitised other sensitisation tests need to be applied. The sample of austenitic stainless steel needs to be polished first, so that the microstructure can be microscopically examined. The polished specimen is etched electrolytically in a 10% solution of oxalic acid at 1 A/cm^2 for 1.5 min, at room temperature [69].

The etched surface of the specimen is then observed under the optical microscope at a 250-500 x magnification and different levels of susceptibility are indicated by the micrographs (**Figure 2.15)** : (a) the dual structure cannot indicate whether the sample is susceptible to IGSCC or not, so further testing needs to be made; (b) step structure indicates that the sample is free of susceptibility to IGSCC and (c) ditch structure indicates that the sample is susceptible to IGSCC [27][69][70].

ASTM A262 Practice B or "Ferric sulfate-sulphuric acid test"

This test is categorized as a 'weight loss' test and is used to predict sensitization due to the precipitated carbides, without being able to predict other form of corrosion, such as general corrosion, pitting, or stress corrosion cracking [69]. It does not predict the susceptibility to intergranular attack associated with the sigma phase in the molybdenum-containing wrought stainless steels such as types 316,316L, 317 and 317L [69] [72].

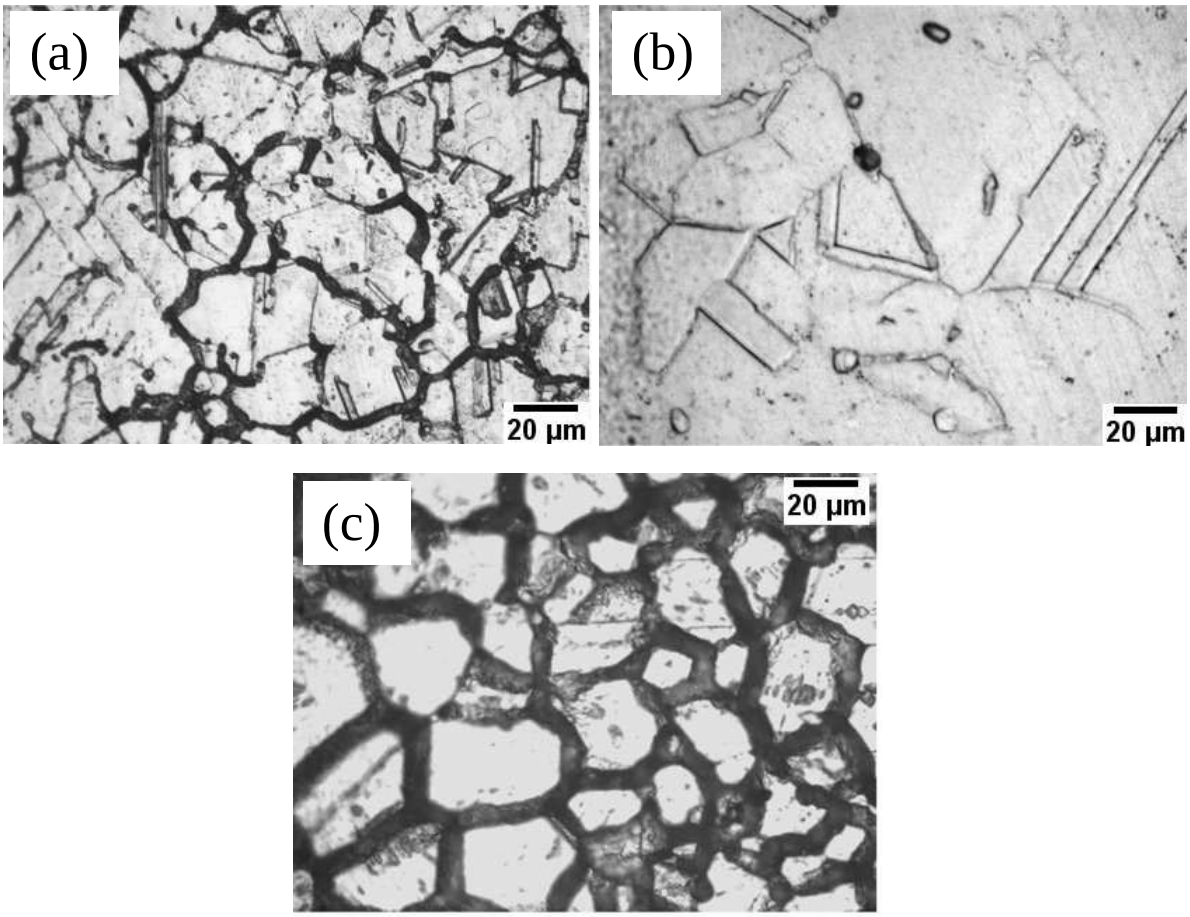

Figure 2.15: Microstructure of stainless steel after "oxalic acid test": a) Dual Structure (x250); b) Step Structure (x500) and c) Ditch Structure (x500) [71].

A sample with a total surface area of 5-20 cm^2 is boiled in

50% H_2SO_4 + 2.5% $Fe_2(SO4)_3$ test solution for 120 hours and the effect of the solution is measured by the loss of weight of the specimen. If the ratio of weight losses of sensitized to annealed conditions is greater than 1.5 to 2.0, then the material is susceptible to intergranular corrosion [73].

ASTM A262 Practice C or "Nitric acid test"

Initially called the Huey test, this test was developed for a nitric acid plant environment. The test involves immersing a sample in boiling 65 % HNO_3, for five boiling periods of 48 hours each, using a fresh solution every time. The shape and weight (usually up to

100 g) of the specimen can vary, however in the case of tubular products or bars, the ratio between the cross-sectional area exposed and the total area of the specimen should not vary between tests. Also, the ration between the cross-sectional areas and the total exposed area of the specimen should not be greater than 0.5. After each boiling period, the sample is weighed and the weight loss is converted into a corrosion rate, usually reported in terms of millimetres per month [69].

ASTM A262 Practice E or "Copper-copper sulphate-16% sulphuric acid test"

This test involves the boiling of a specimen in a 15.7% H_2SO_4 + 5.7% $CuSO_4$ solution for 15 h [27] [69]. Then, the specimen is bent through 180° and over a radius that is equal to twice the thickness of the specimen. The dimensions of the tested specimen are controlled by the specifications of the testing apparatus. The evaluation of the steel specimen is conducted by looking at the presence or absence of fissures or cracks after bending [27].

ASTM A262 Practice F or "Copper-copper sulfate-50% sulphuric acid test"

This test is similar to the *"Copper-copper sulfate-16% sulphuric acid test"* and it involves the boiling of a specimen in a 50% H_2SO_4+5.7% $CuSO_4$ solution for 120 h [69]. To determine the susceptibility to sensitization, weight loss is used [74].

Non-destructive tests

Besides the destructive tests outlined above, there are other, electrochemical tests that do not deteriorate the material and can be used to determine the susceptibility of austenitic stainless steels to intergranular corrosion as well as to quantify the degree of sensitization of the material. The Electro-Potentiokinetic Reactivation (EPR) tests consist of a reactivation process that involves a potentiodynamic sweep from the

passive to the active regions of the specimen's electrochemical potential. The test gives a measurement of the charge that is associated with the corrosion of the chromium-depleted regions that are around the carbide precipitates [75].

To determine the degree of sensitization of types 304 and 304L steels, two different tests have been standardized: the single-loop EPR (SL-EPR) and the double-loop EPR test (DL-EPR) [16].

The single-loop EPR test (standardized as ASTM G 108) uses specimens that are first ground and then polished to a 1-µm diamond paste finish. The solution used contains 0.5M H_2SO_4 + 0.01M KSCN at 30 °C. First, the corrosion potential (~ - 400mV vs. SCE) is established by keeping the sample immersed in the solution for 2 minutes. Then, the potential is raised to +200mV vs. SCE for another 2 minutes. After the passivation potential is reached, the potential is decreased down to the corrosion potential, at a constant rate of 6V/h for approximately 6 minutes. To determine the degree of sensitization, the charge Q (which is given by the time integral of the current density below the reactivation curve) is used [75]. For the nonsensitized steels, no change will have occurred to the passive film, and so the loop is relatively small [16]. A schematic of typical EPR curves is given in **Figure 2.16** [75]. The current density increase is associated with the sensitised grain boundary where chromium is depleted [76].

During the DL- EPR test the same conditions (solution, solution concentration, sample preparation, temperature and scan rate) are used. The specimen is polarized anodically during the first scan as for single-loop, and then the scan is reversed to return to the corrosion potential as shown in **Figure 2.17**. The ratio of the maximum current given by the reactivation scan to the maximum current generated by the anodic scan is a

measurement of the degree of sensitization. Majidi [76] notes that small values for the current produced during the reverse scan (around 10^{-6} A) can be obtained for the annealed specimens. This value increases considerably (around 10^{-2} A) in case of the sensitized specimens.

From all the tests reviewed here that check the sensitization of 304 SS, the EPR test seems to be the most useful one, because it does not deteriorate the material and it also gives the possibility to quantify the degree of sensitization.

2.2.4.2 Factors affecting sensitization

In sensitized stainless steel, the effect of sensitization depends on the character of the grain boundaries and the steel's carbon content as well as the heat treatment [77]. In a transmission electron microscopy study on 304SS, Trillo et al. [78] looked at the density of the $M_{23}C_6$ precipitates as a function of C concentration (for samples with 0.011, 0.025, 0.05 and 0.07% C), grain boundary misorientation, aging time (670 ^{o}C) and strain level in (110)/(110) neighbour grain boundaries. It was observed that an increase in the C content above 0.011% C and an increase in the misorientation result in a higher density of precipitates, while no precipitates were present in the sample with 0.011% C.

The same conclusion was observed when the aging time increased (from 10 to 50 h) and when the straining increased to 20%. The % C also has an effect on the sensitization time, such that an increase in the % C results in a decrease in the sensitisation time, as shown in **Figure 2.18** [79]. Also, the temperature required for the material to get sensitised increases with the addition of C.

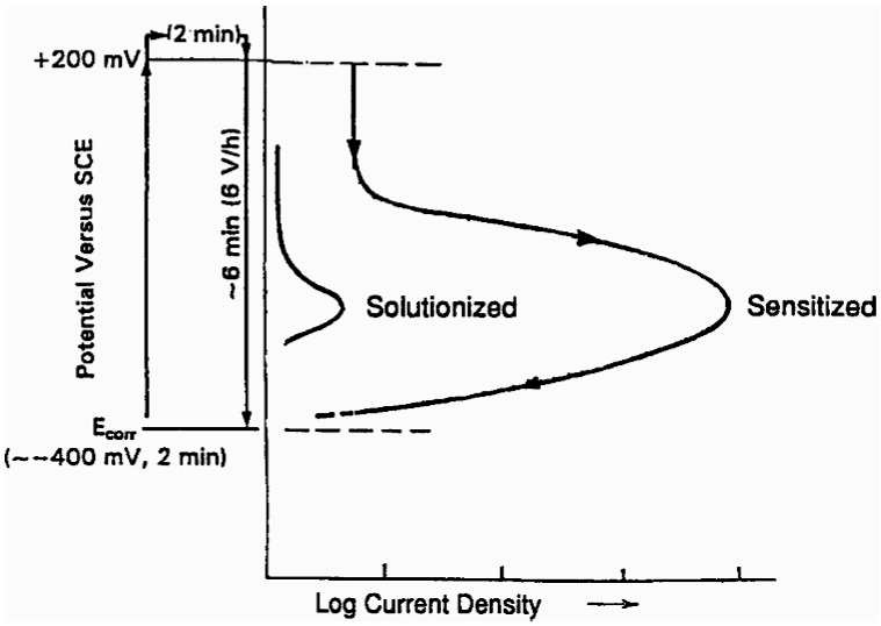

Figure 2.16: Schematic of single-loop EPR curves for sensitised and unsensitised material [75].

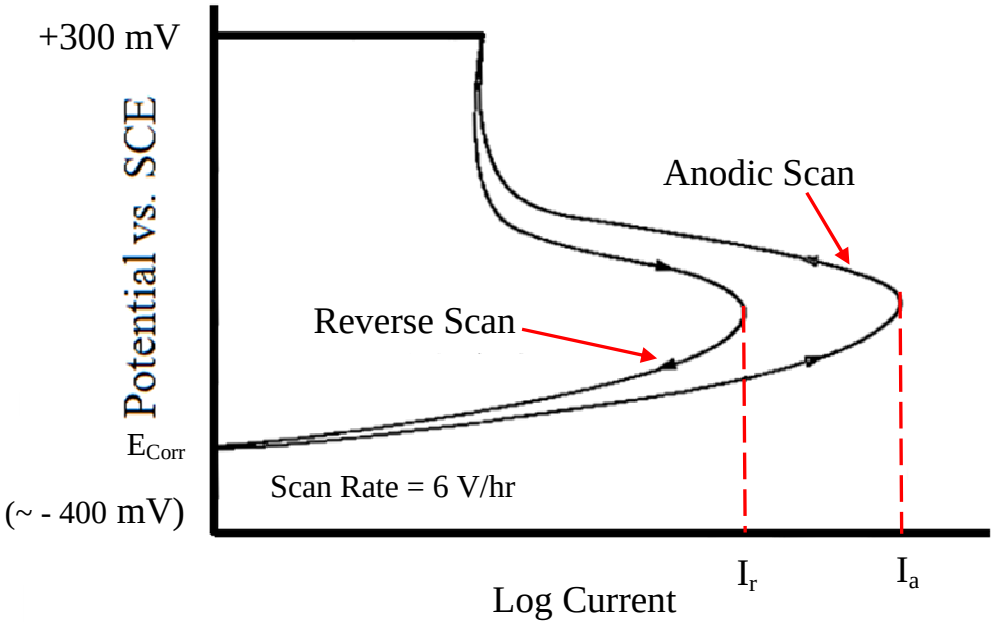

Figure 2.17 Schematic of the double-loop EPR curve [76].

The sensitization temperature is also influenced by cold work, such that in a 304 SS specimen that underwent a cold work treatment the degree of sensitization of the material was found to increase at lower temperature (approximately 400 °C) and decrease at higher temperatures (approximately 600 °C) [16].

Trillo *et al.* [79] observed that the strain applied during the sensitisation accelerates the process and increases the degree of sensitisation in 304 stainless steel.

The influence of the strain applied on the degree of sensitisation is shown for one grain boundary in **Figure 2.19**. The degree of sensitisation of a specimen under 20% strain is greater than of an un-strained sample. This effect is caused by the increase in the dislocation and defect density that result in changes in the thermodynamics of carbide precipitation as well in the kinetics of chromium diffusion [79].

2.3 IGSCC in 304 stainless steel

As presented previously in **Section 2.1.1.1** and **Section 2.1.1.2,** different percolation and percolation-like models were proposed to explain the mechanism of IGSCC in 304 SS by mainly looking at the sensitisation level of the grain boundaries. In addition, several studies were performed to determine the correlation between the susceptibility to IGSCC in 304 SS of grain boundaries and their crystallography, (reviewed in more detail in **Chapter 6**). However, these models do not take into account the effect of applied stress on IGSCC, which is essential in understanding the stress corrosion process.

A 3D computational model applied for 304 austenitic steel has been proposed by Jivkov *et al.* [59] that considers both the bridging effect that has been observed in austenitic steels by Marrow *et al.* [14] and the crack driving force.

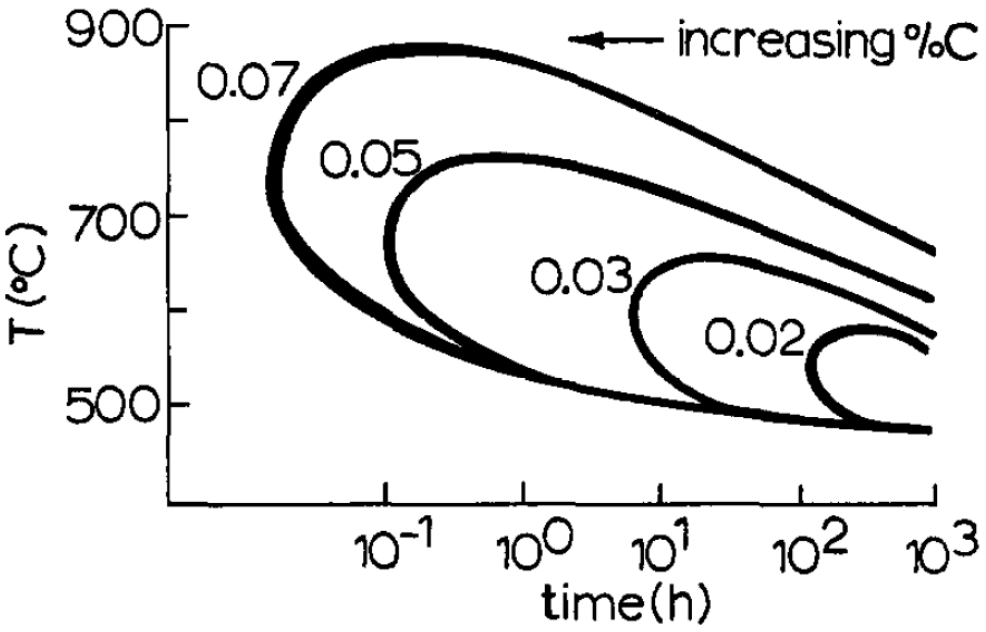

Figure 2.18 Time-temperature-sensitisation curve of stainless steel 304. An increase in the C concentration results in a decrease in sensitisation time. The sensitisation temperature varies from 500 to 900°, depending on the C concentration and is correlated with the sensitisation time [79].

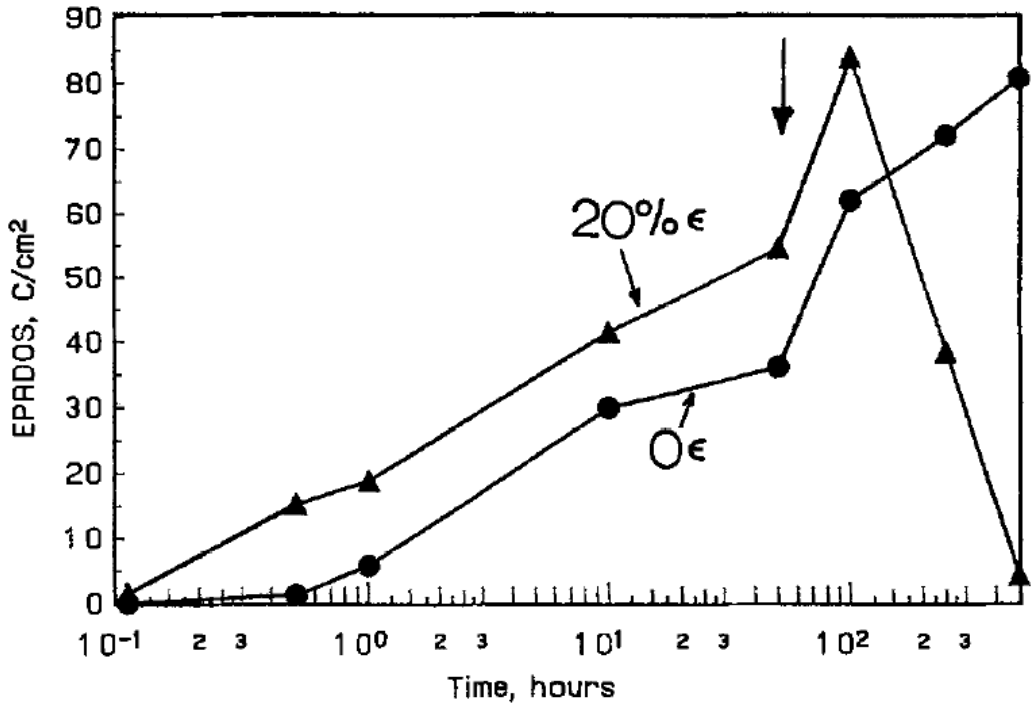

Figure 2.19 Plot of the degree of sensitisation against time for 304 SS in strained and un-strained condition. The 20% level of strain increases the degree of sensitisation [79].

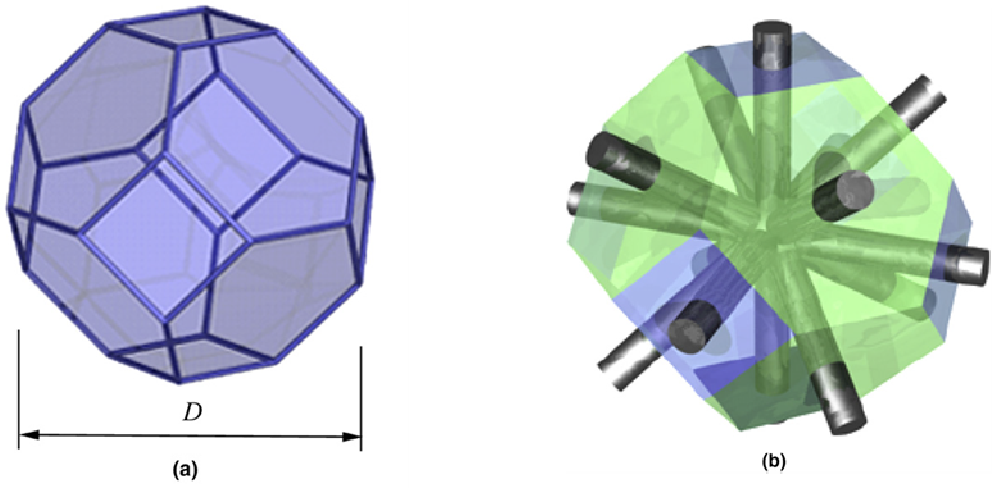

Figure 2.20 Grain geometry used in the 3D simulation: (a) meon or truncated octahedron and (b) cylindrical elements represent the grain boundary plane [59].

The model simplifies a polycrystalline solid as an array of grain structures that have the geometry of a truncated octahedron, as shown in **Figure 2.20.** The model divides grain boundaries into low-angle boundaries (resistant to IGSCC) and high-angle boundaries (susceptible to IGSCC). A parameter f is used to define the ratio between the high-angle boundaries and the total grain boundary population. The distribution of both susceptible and resistant grain boundaries is randomly generated. The failure strain that corresponds to the susceptible boundaries (ε_{sf}) is assumed to be less than the yield strain of the material (ε_y) while the strain that corresponds to the resistant boundaries (ε_{rf}) is assumed to be proportional to the tensile strain (ε_u), as shown in **Figure 2.21.**

The crack advance mechanism is shown in **Figure 2.22.** The strain is calculated for all the boundaries that are depicted in dark black since they are the only ones in contact with the crack. If they reached the strain limit they are eliminated from the array and the procedure is repeated for the remaining grain boundaries. Thus while this model includes a mechanism for crack propagation, it does not consider the kinetics of the IGSCC.

The simulation performed for 304 SS using this model studied the effect of the ratio between susceptible and resistant grain boundaries on the crack growth mechanism. Some results are presented in **Figure 2.23** and **Figure 2.24**. In **Figure 2.23** the plot of stress intensity factor is shown against the area of the crack for a crack without bridges and for a crack with bridges. The difference given by the shielding effect (K_{sh}) is clearly marked. In **Figure 2.24** the stress intensity factor against the crack area is plotted for f = 0.25, 0.35 and 0.45. The stress intensity factor increases with the increase in f.

While this model is considerably improved from the percolation models, by including the driving force, since it does not include the kinetics of SCC, it is still not suitable to determine crack growth rates. A more advanced version of the model [44] used a relationship between the rate of failure and strain energy to simulate crack growth rates. The results obtained for 304 SS are presented in **Figure 2.25**. It can be observed that an increase in f (as defined in the previous model) will increase the incubation time used and will decrease the crack growth rate.

Crack growth rate in 304 SS was also measured experimentally by Rahimi *et al.* [80] in a potassium tetrathionate environment. Digital image correlation techniques (described in more detail in **Section 6.3**) were used to observe the crack growth and nucleation in two different microstructures: a solution annealed (SA) microstructure, that was sensitised for 20 h in argon at a temperature of 650 ^{o}C and a thermo-mechanically processed (TMP) microstructure, that was cold worked at a 20% strain, annealed for 26 h in argon at a temperature of 950 ^{o}C and sensitised as the SA microstructure.

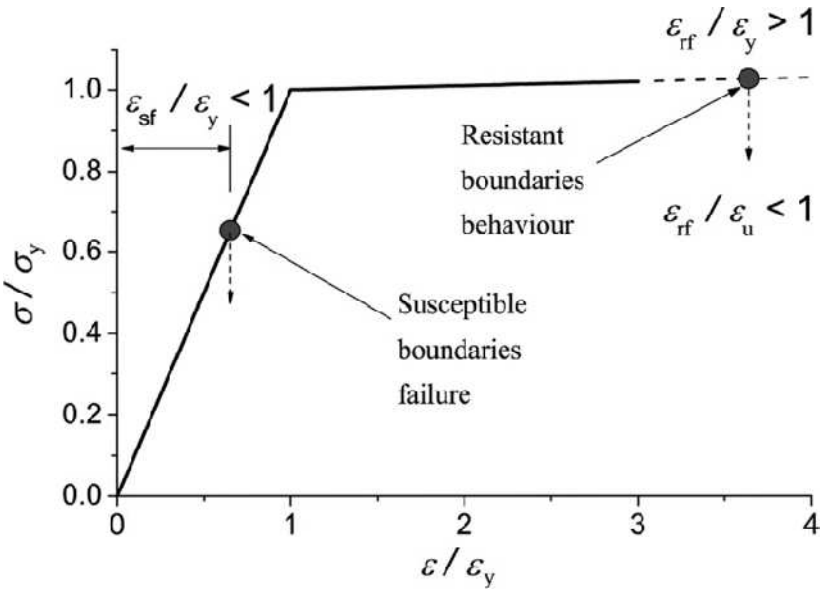

Figure 2.21 Representation of failure behaviour for susceptible and resistant boundaries [59].

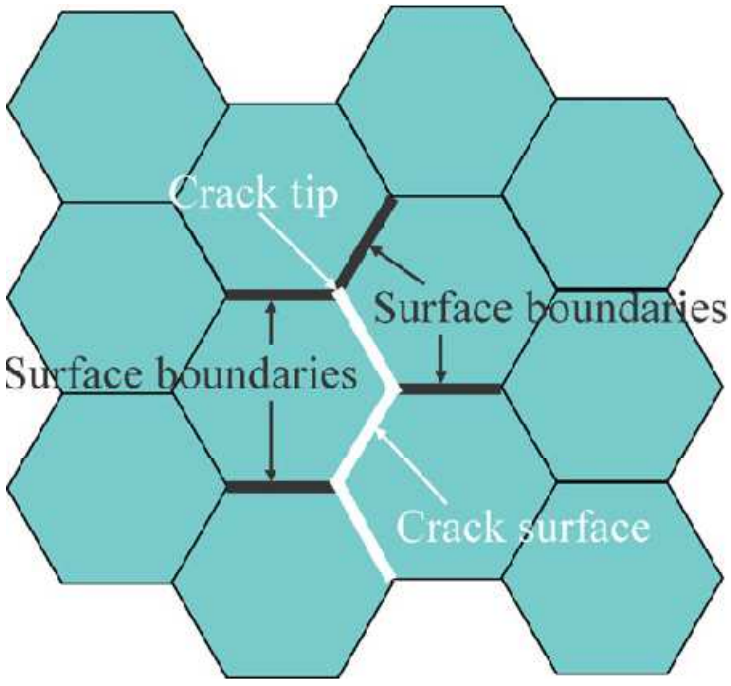

Figure 2.22 Mechanism of crack advance: the crack is represented in white and the neighbouring boundaries that could fail are represented in thick black [59].

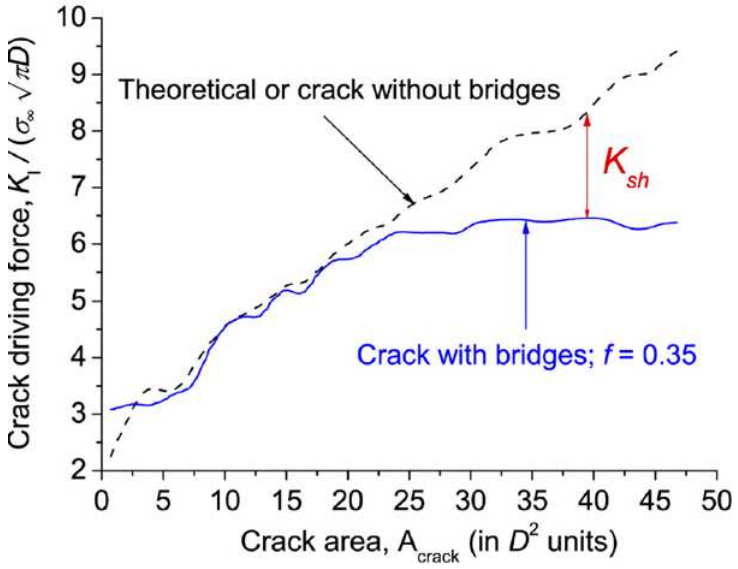

Figure 2.23 Simulation plot of stress intensity factor against the crack area for a crack with and without bridges [59].

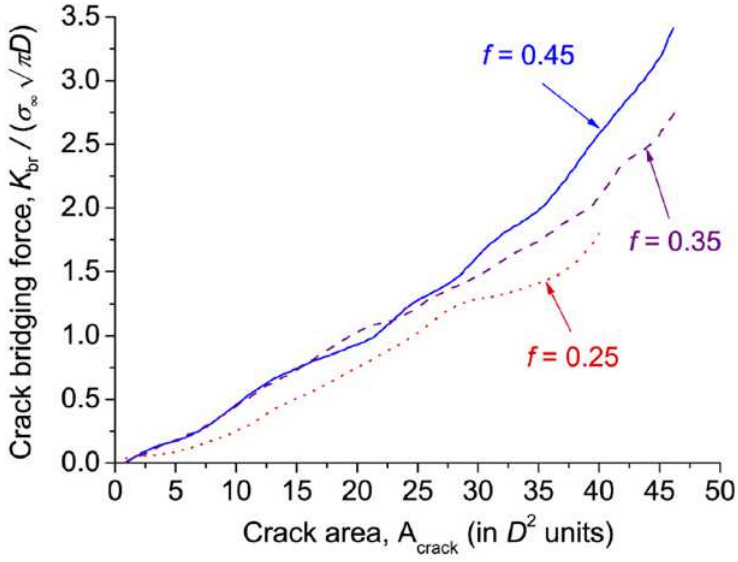

Figure 2.24 Simulation plots of stress intensity factor against the crack area for different fractions of resistant boundaries [59].

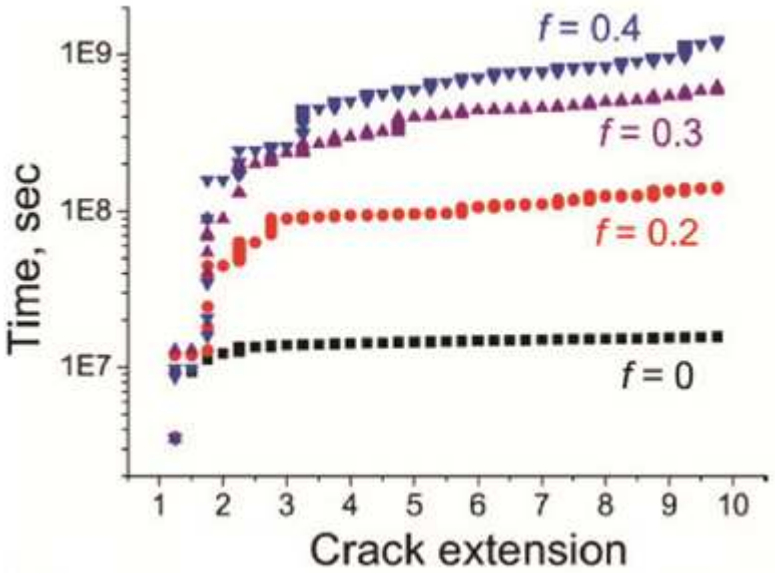

Figure 2.25 Simulations in 304 SS for different fractions of resistant boundaries [44].

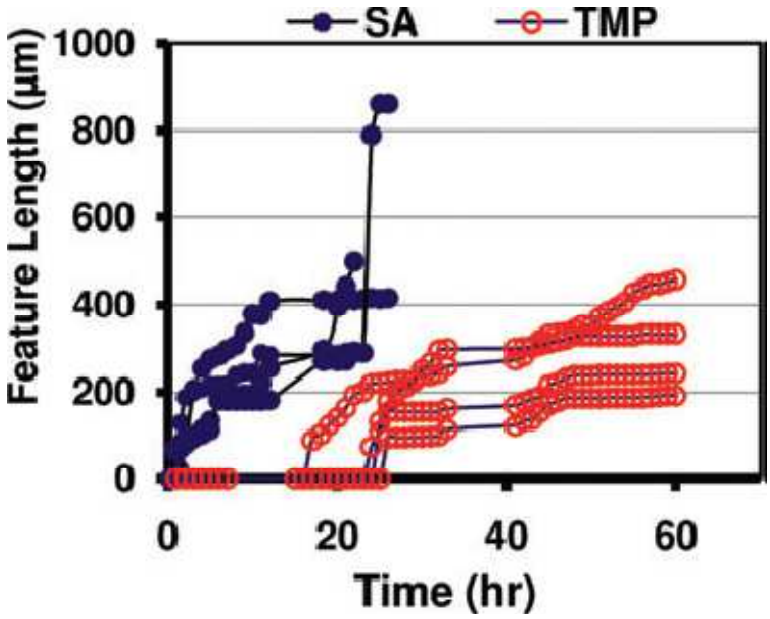

Figure 2.26 Crack length as a function of time obtained during *in-situ* experiments in 304 SS for two different microstructures [80].

The difference between the two was that the TMP microstructure contained more twin grain boundaries that are known to be resistant to IGSCC. The cracks were obtained using an *in-situ* setup in which the specimens were tested using a three-point bending setup. The results obtained are shown in **Figure 2.26.** It can be observed that the crack propagates more rapidly in the samples that have a SA microstructure, in which the proportion of the grain boundaries that are susceptible to IGSCC are higher.

2.4 SCC Mechanisms in 304 Stainless Steel

There are four main mechanisms that can explain SCC in metals: slip-dissolution, hydrogen embrittlement, film-induced cleavage and surface mobility model. However, none of these can be applied universally [13] and their applicability is still questionable [81]. While different mechanisms have been proposed to describe SCC, it is difficult to state which mechanism applies to which system. Often it is challenging to describe quantitatively a SCC process for a specific environment or to state what controls cracking [81]. The mechanisms will be briefly described next.

2.4.1 Slip-dissolution mechanism

The slip-dissolution mechanism is shown schematically in **Figure 2.27.** An oxide film, which protects the crack on both sides, breaks due to the plastic strain accumulated at the tip of the crack. The crack advances through the repetition of the film rupture dissolution and film redevelopment [13]. As reviewed by Turnbull [81], the mechanism was used by Ford and Andresen to model the crack size in 304 SS piping in power plants. The predictions of the model for the depth of the IGSCC cracks in boiling water reactors were in good agreement with the observations. In order to predict the size of the short cracks more work needs to be done to estimate the strain rates at the tip of the crack [81].

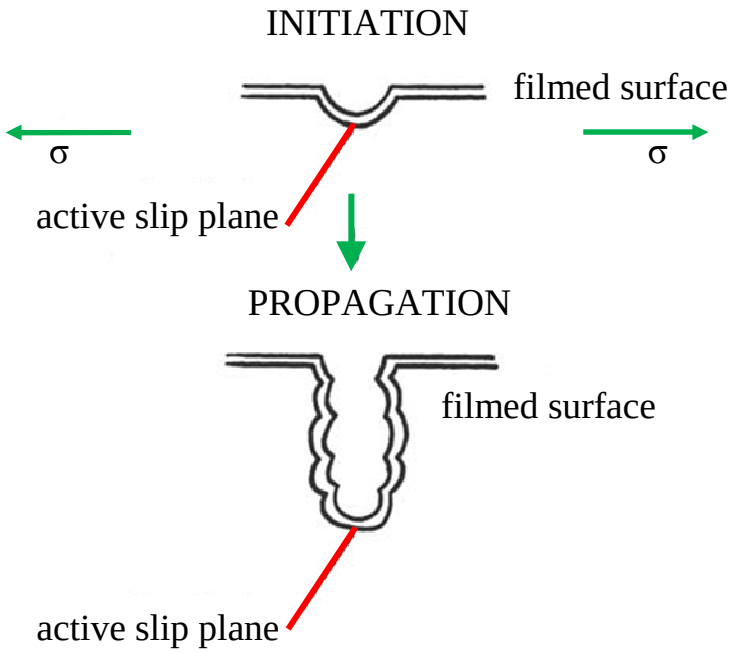

Figure 2.27 Schematic of the slip-dissolution mechanism [13].

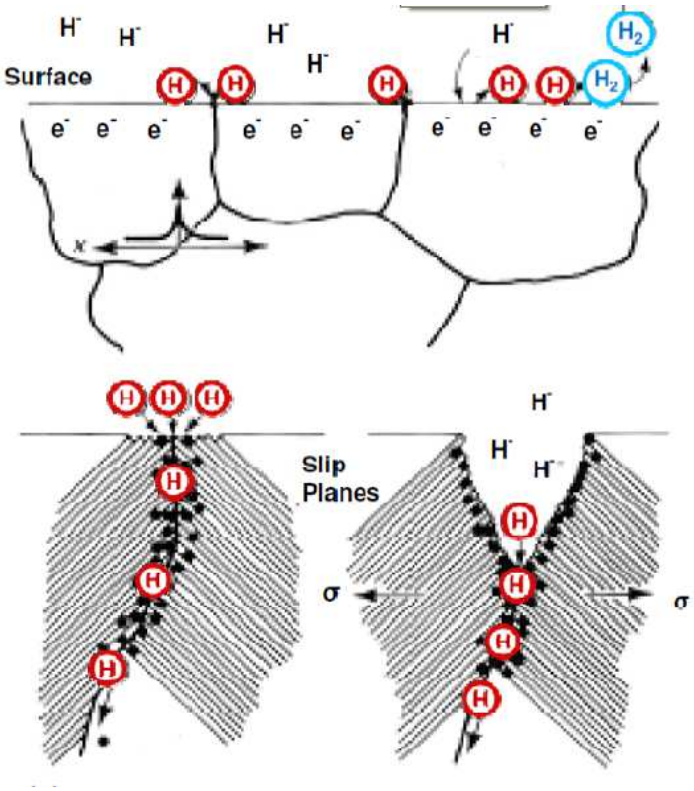

Figure 2.28 Schematic of the hydrogen-embrittlement mechanism [25].

2.4.2 Hydrogen embrittlement mechanism

SCC was believed in 1979 to be caused by the absorption of hydrogen in high-tensile steels in aqueous environments [13][82][83].

The hydrogen absorbed in the metal segregates at the grain boundaries or to dislocations and can cause intergranular separation and cleavage by reducing the force between neighbour grains, as shown in **Figure 2.28** [13][82]. As stated by Turnbull [81], the hydrogen atoms usually come as a result of the following reactions:

$$H^+ + e^- \xrightarrow{yields} H \quad \textbf{(3)}$$

$$H_2O + e^- \xrightarrow{yields} H + OH^- \quad \textbf{(4)}$$

In 304 SS, the influence of hydrogen was observed by Troiano [84]. The experiments conducted on 304 stainless steel charged with hydrogen in a molten salt bath for 5 hours at a temperature of 150 ^{o}C showed that the ductility of steel is lower, the reduction in area decreased from 41% to 78% and the fracture surface of the specimens was brittle [84].

According to Turnbull [81], in order to predict cracking using the hydrogen embrittlement mechanism, several factors need to be taken into account: kinetics of hydrogen atoms, segregation and dissolution of hydrogen and reactions between the material and the hydrogen atoms in different conditions of strain and stress. All these factors are described in more detail elsewhere [81]. Turnbull [81] also reviewed the different mechanisms regarding the role of the hydrogen. However, none of them is universal and each mechanism depends on the environment and the material. Hydrogen cracking models regarding the prediction of crack initiation, threshold and crack growth

rates are also summarized, however, none of the models described applies to 304 SS in particular, the material that makes the subject of this thesis. Regarding prediction of the crack growth rates of materials that fail due to the hydrogen present, Turnbull [81] states that without having a better understanding of the mechanics, chemistry, the hydrogen transport and the interactions between the hydrogen atoms and the material and of how these mechanisms come together, this would not be possible.

2.4.3 Film-induced cleavage model

The film-induced cleavage model was first proposed by Sieradzki and Newman in 1987 [85] to explain transgranular SCC and it states that thin films can produce brittle micro-cracks in ductile materials. Later on, it was also demonstrated that intergranular failure can also be caused in the same way in gold alloys [13]. The model shown schematically in **Figure 2.29** is based on the fact that the oxide/film present at the tip of the crack can initiate cleavage produced by the local plastic deformation [85]. While the basic principles of the mechanism were confirmed experimentally in Cu-Zn and Cu-Al alloys [83] the applicability to other materials (for example 304 SS) is still unknown and more work needs to be done in order to assess its usability in different systems [81].

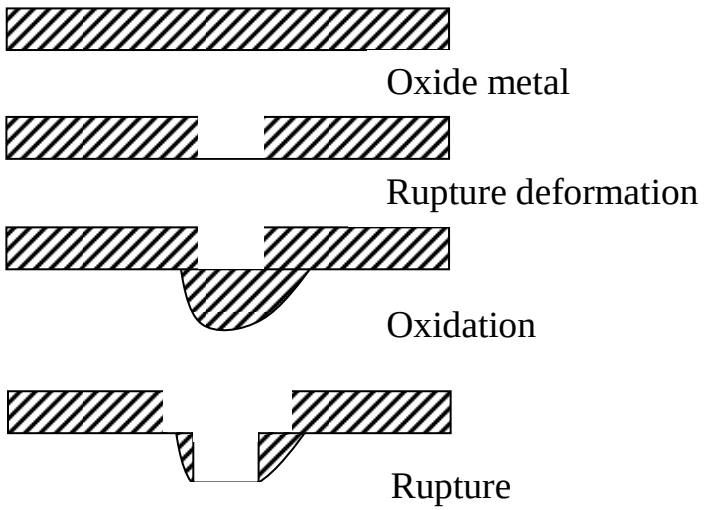

Figure 2.29 Schematic of the film-induced cleavage model [Adapted from [86]].

2.4.4 Surface mobility model

According to Turnbull [81] this model was proposed by Galvele and is based on the crack advancing as vacancies are created at the crack tip. The atoms at the tip of the crack move due to the local stresses, leaving a vacancy at the crack tip, as shown in **Figure 2.30** [81].

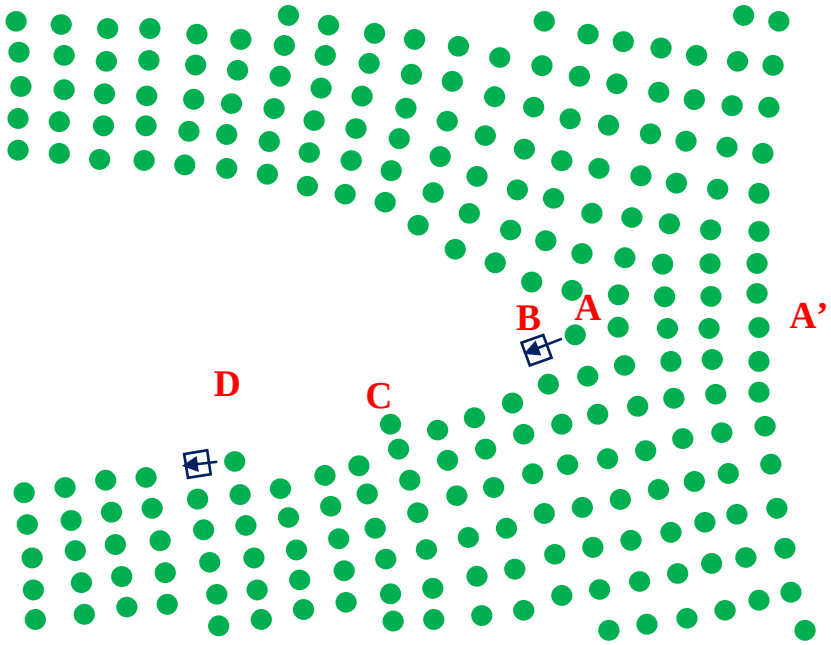

Figure 2.30 Atom A moves to position B, creating a vacancy at the tip of the crack. The atoms that are being replaced (B, C, D) will be moved to other lattices [81].

While Newman [83] affirms that the model has "interesting features," Turnbull [81] mentions that the fact that the assumptions on the surface mass transport are not consistent makes the model impossible to be used quantitatively.

The mechanisms described above are the ones that could explain or predict SCC. However, no model can be universally applied for 304 SS, without more work needed.

2.5 SCC in Ni Alloy 600

2.5.1 Properties of Ni Alloy 600

Ni Alloy 600, (also named INCONEL 600) is a nickel-chromium-iron alloy which was developed by Fraser in 1932, that combines excellent mechanical and corrosion properties [87] . The high concentration of Cr (usually 16%) gives it a high resistance to corrosion and to chloride cracking. The material is susceptible to SCC in high strength caustic alkalis and at high-temperature [88]. The typical chemical composition of such coupons of Ni Alloy 600 is presented in **Table 2.5** [89] and the mechanical properties are summarized in **Table 2.6** [88].

Table 2.5: Chemical composition of Ni Alloy 600 (wt%)

Element	Ni	Cr	Fe	C	Mn	Si	S	P	Co	Al	Ti
	73.8	16.07	8.39	0.034	0.83	0.26	0.001	0.011	0.018	0.23	0.25

Table 2.6: Mechanical properties of Ni Alloy 600

Young's Modulus	214 GPa
Poissons ratio	0.324
Tensile strength	550-690 MPa
Yield strength	205-310 MPa

2.5.2 SCC of Ni Alloys in the PWR environment

Pressurized Water Reactors (PWR) and Boiling Water Reactors (BWR) are two of the most common designs of nuclear steam supply systems that generate electricity. They are water cooled and water moderated, designed and constructed to operate initially for 40 years, though some of them were extended to 60 years. However, as plants reach the

end of their operation, serious corrosion problems occur, the most important one being SCC. The heat in a PWR (shown in **Figure 2.31**) is generated by fission in the core and is transmitted by pressurized water to the steam generators. The pressurized water is pushed through the reactor cooling system by the reactor cooling pumps and it is prevented from boiling by a pressurizer that keeps the pressure at a level of around 15-16 MPa. The generated steam operates the main turbine that is connected to the electric generator, after which it is condensed and the cold water goes through the feedwater pumps back to the steam generators [7].The materials in these systems are exposed to high pressure and high temperatures, the operating temperature reaching between 280 – 320 ^{o}C and up to 343 ^{o}C in the PWR primary circuit [7].

Ni Alloy 600 was selected to be used in the PWRs for steam generator tubes, due to its superiority to chloride cracking, in comparison to stainless steel. Ni Alloy 600 was a material that could be potentially used in the primary circuit components. However, as mentioned before in **Section 2.1.1**, Alloy 600 is affected by IGSCC [7]. PWSCC occurs in different components, such as steam generator tubes, heater sleeves, pressurized instrument penetrations and control rod drive mechanisms [90]. The first failure to IGSCC observed in Alloy 600 was in the early 1970s during operational service in PWR primary water and occurred in the steam generator tubing [7].

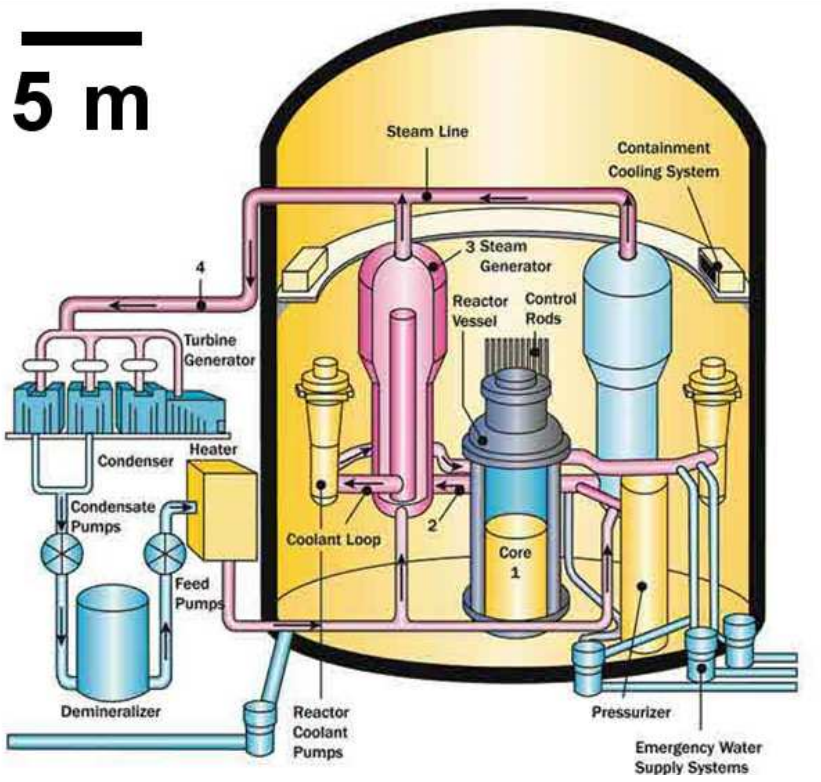

Figure 2.31 Schematic showing a typical PWR [91].

The IGSCC of Alloy 600 in PWR steam generator tubes became a major concern in the 1980s [7] and led to the retirement and replacement of the steam generators. IGSCC failure also occurred in the pressurized nozzles and pressurized vessels of the PWR [7].

The failure occurred due to the very high residual stresses that exceeded the value of the nominal yield strength, along with a roughly machined surface [7]. These high residual stresses might have been induced by rolling operations or by welding operations. In order to predict or prevent the IGSCC failure, extensive research has been made and different SCC mechanisms have been proposed and will be discussed in the next section. However, up until now, there is no agreement into what exactly causes the failure through cracking [7].

2.5.3 Mechanisms that control SCC in Ni Alloy 600

The mechanism of IGSCC in the PWR environment is still unknown, though several mechanisms have been proposed over the years. These mechanisms include: bubble

formation, corrosion-enhanced plasticity at local crack tip, slip oxidation/dissolution and internal oxidation [92]. The three mechanisms that are likely to explain the PWSCC are the slip oxidation model [13][93][94], the hydrogen based model [95] and the internal oxidation model [96]. The slip oxidation model is not fully consistent with PWSCC, for example: it does not explain oxidation when stress is not applied or the selective oxidation present at the tip of the crack [36]. In addition, the predicted length of the tip of the crack is much smaller than predicted by fracture mechanics [36]. The hydrogen based model cannot predict initiation, and also the hydrogen volatility required to explain the model has very high values [36].

The mechanism that has been investigated in this thesis in the context of IGSCC in PWR of Ni Alloy 600 is the widely accepted internal oxidation mechanism that will be described next. Other models are described in more detail in a review by Mohanty *et al.* [97].

Scott and Le Calvar proposed in 1993 a mechanism named “internal oxidation” to study the IGSCC of Ni Alloy 600 in hydrogenated water in PWR. Through internal oxidation, the oxygen diffuses in an alloy and oxidizes the alloying element that is more reactive than the metal. Scott *et al.* studied the applicability of this mechanism in Ni Alloy 600 between temperatures of 300-400 ^{o}C in steam and water [96]. The mechanism of internal oxidation is presented in **Figure 2.32.** The oxygen penetrates the grain boundary causing the material embrittlement. The process happens subsequently, causing crack propagation [98].

This mechanism explains both initiation and propagation and it seems the most likely one to describe IGSCC because, as described by Scott [36] the grain boundary oxidation

and embrittlement correlate well with PWSCC and have the following features, summarised here, and considered in more detail in the sections that follow:

- Observations [99] proved that oxygen is present at grain boundaries
- Carbides present at the grain boundary slow down the intergranular oxidation
- The stress applied increases the depth of the oxidation and influences the initiation time of IGSCC in Alloy 600 [89]
- As in PWSCC, grain boundary embrittlement depends on the value of the hydrogen partial pressure [36]

The presence of the oxygen at grain boundaries has been observed [99] underneath the oxide layer present on the surface of the Alloy 600 sample. It was determined that though all grain boundaries get oxidised, the diffusion of oxygen is deeper and it happens more rapidly at triple junction boundaries [99], as shown in **Figure 2.33.** However, since the technique used by the author lacked 3D and special resolution, the conclusion that oxygen penetration happens without oxidation of several microns might be questionable.

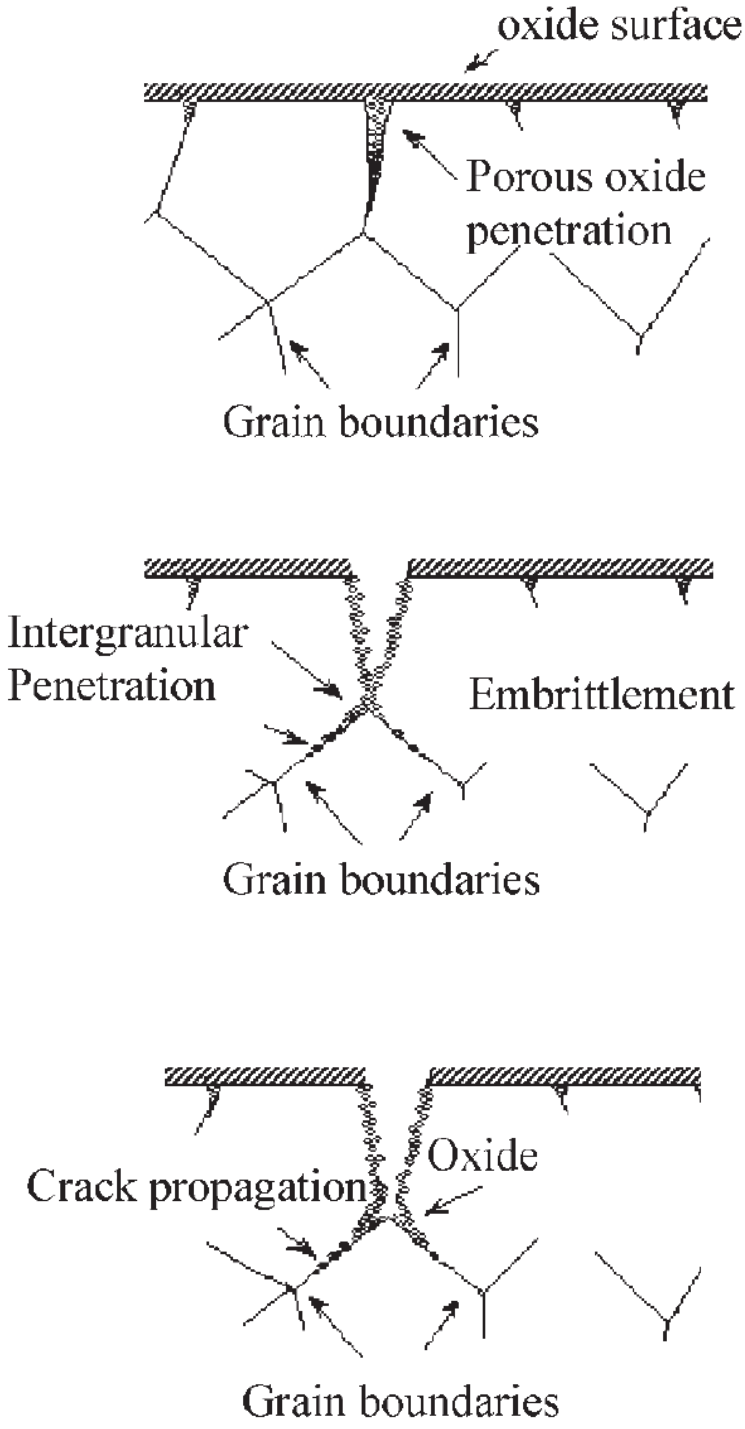

Figure 2.32 Schematic of internal oxidation mechanism [98].

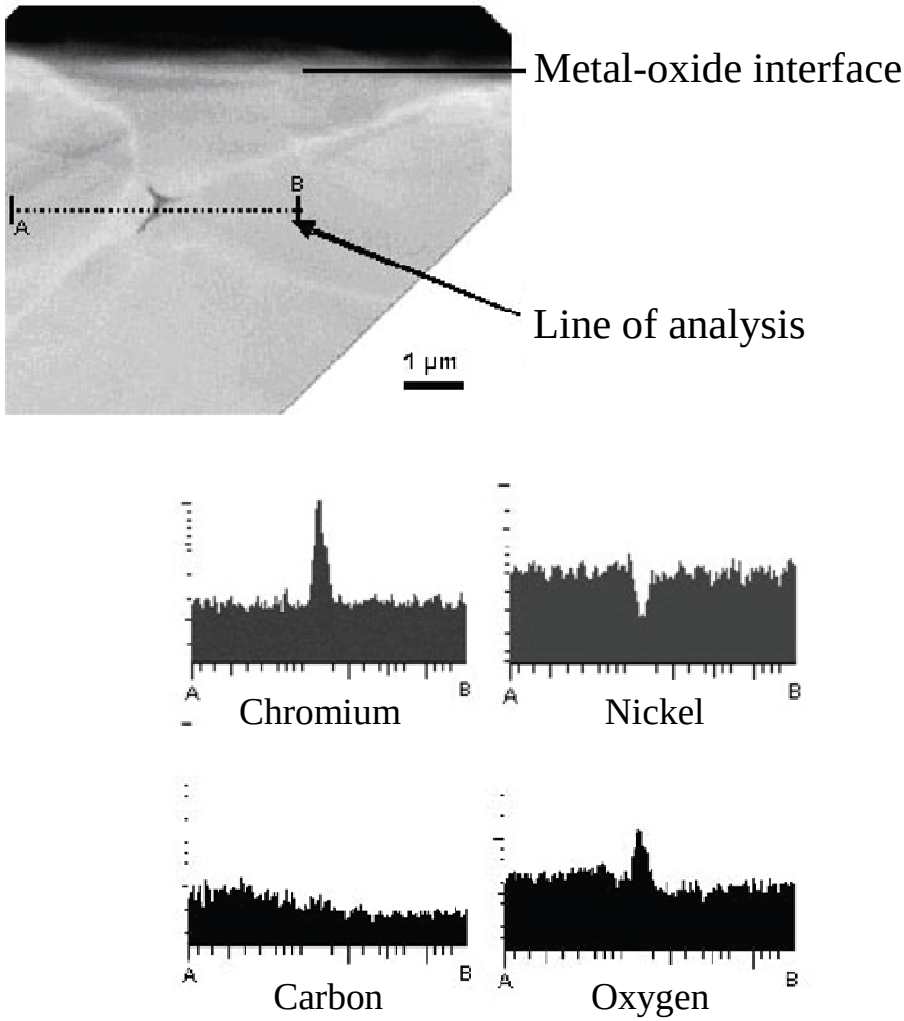

Figure 2.33 Alloy 600 exposed for 300h at 360 ^{o}C in simulated primary water at hydrogen partial pressure of 30 kPa. Oxide is present at a triple junction boundary, approximately 10 µm deep [99].

Also, the penetration depth of oxygen is believed to depend on the chromium concentration such that the depth decreases with the increase in the chromium concentration [99].

In a review of the internal oxidation mechanism, Scott [96] mentions that a Secondary Ion Mass Spectrometry (SIMS) examination of a tube that cracked revealed that intergranular cracks contained high amount of oxygen while no other impurities were present. This might be an indication of internal oxidation. The morphology of the crack

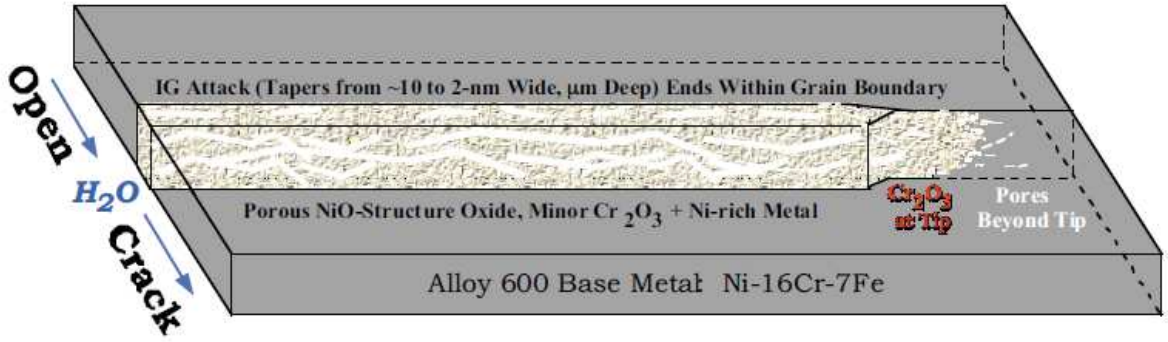

Figure 2.34 Schematic of the crack morphology tip produced by IGSCC in Ni Alloy 600 exposed to PWR [100].

tip of alloy 600 exposed to PWR primary water is consistent with internal oxidation process, as shown in **Figure 2.34.** It can be observed that at the end of the crack tip Cr_2O_3 and porosity are present while Ni-O oxide, metallic nickel and traces of Cr_2O_3 are found on the walls of the crack [96].

In addition, it was observed that in PWR primary water, the oxygen present at the grain boundaries causes embrittlement in Alloy 600 while no embrittlement was observed in Alloy 690 or Alloy 800, which are known to have a higher resistance to IGSCC [36]. Capell and Was [92] also investigated the internal oxidation mechanisms in five different alloys (Ni-5Cr, Ni-5Cr-9Fe, Ni-16Cr-9Fe, Ni-30Cr-9Fe and Ni-9Fe) in a steam environment. Oxides were observed at grain boundaries in both stressed and unstressed specimens and it was found that intergranular cracking as well as the oxidation were influenced by the alloy content. This indicates that the internal oxidation mechanism was the one controlling IGSCC in these alloys.

The oxygen diffused to the grain boundaries causes intergranular embrittlement; the propagation can be either caused by the applied load that allows the oxygen to penetrate deeper at the grain boundaries or it might be caused by the increase in strain caused by the intergranular oxide [99]. While it is known that oxidised grain boundaries are

sources for intergranular embrittlement [99], the crystallographic character of these boundaries and the mechanical conditions in which initiation takes place are still unknown.

Since oxidation might be the cause of IGSCC initiation in Ni Alloy 600 in PWR, various studies [99][101][102] have been performed to better understand the oxidation process, the structure of the oxide and the role of intergranular carbides. The structure of the oxide in Alloy 600 in the PWSCC conditions has been studied extensively [89] [99] and will be described in more detail in **Chapter 5**. The intergranular carbides are chromium rich and have been determined to be $Cr_{23}C_6$ or Cr_7C_3 [101][102].It is known that carbides increase the resistance to IGSCC of Ni Alloy 600 in PWR primary water [103]. As mentioned by Staehle [104], these studies showed that the initiation time is increased by the increase of the amount of carbide at the grain boundary, as shown in **Figure 2.35**. The IAEA concluded that Ni Alloy 600 samples that have carbides on the grain boundaries are more resistant to IGSCC, while the ones where the carbides are present intragranularly are the most susceptible [90]. In addition, the carbides were observed not only to slow the crack initiation, but also to stop the crack propagation [105]. Sennour [101] observed in a study of the influence of intergranular carbide on IGSCC that a high density of intergranular carbides considerably reduced the cracking rate.

TEM observations emphasized that the IGSCC cracks either stop propagating in the presence of carbides or they go around the carbide as shown in **Figure 2.36** [101]. It is believed that the intergranular carbides act as a stress relief and blunt the intergranular cracks, reducing the stress concentration around them [90]. As mentioned by Panter *et al.* [89] the internal oxidation mechanism explains the role of carbides in

reducing the oxidation down the grain boundaries. As illustrated in **Figure 2.37**, the carbides trap the oxygen, preventing the oxygen from diffusing further.

The mechanism presented above shows to have the potential of explaining the IGSCC in Ni Alloy 600 exposed to PWR environment. However, the model is difficult to be used quantitatively because one known problem of the mechanism is that there is no agreement on what the value of the oxygen diffusion specific to IGSCC is [92].

Chapter 5 from this thesis focuses on measuring the fracture toughness of the oxidised grain boundaries in Ni Alloy 600 exposed to simulated PWR conditions using micromechanical testing.

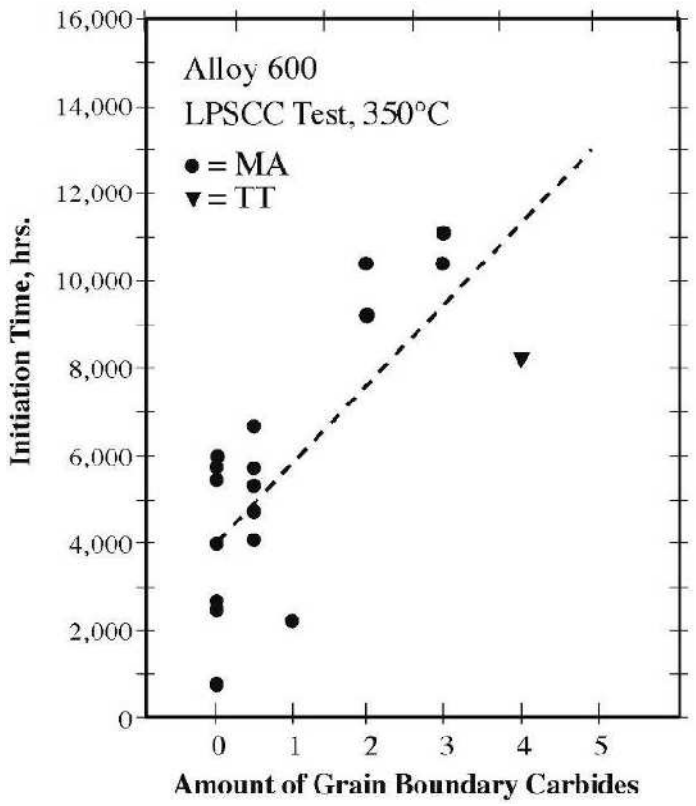

Figure 2.35 Initiation time vs. amount of carbides present at the grain boundaries in Alloy 600. The incubation time is increased at boundaries with high amounts of carbides [104].

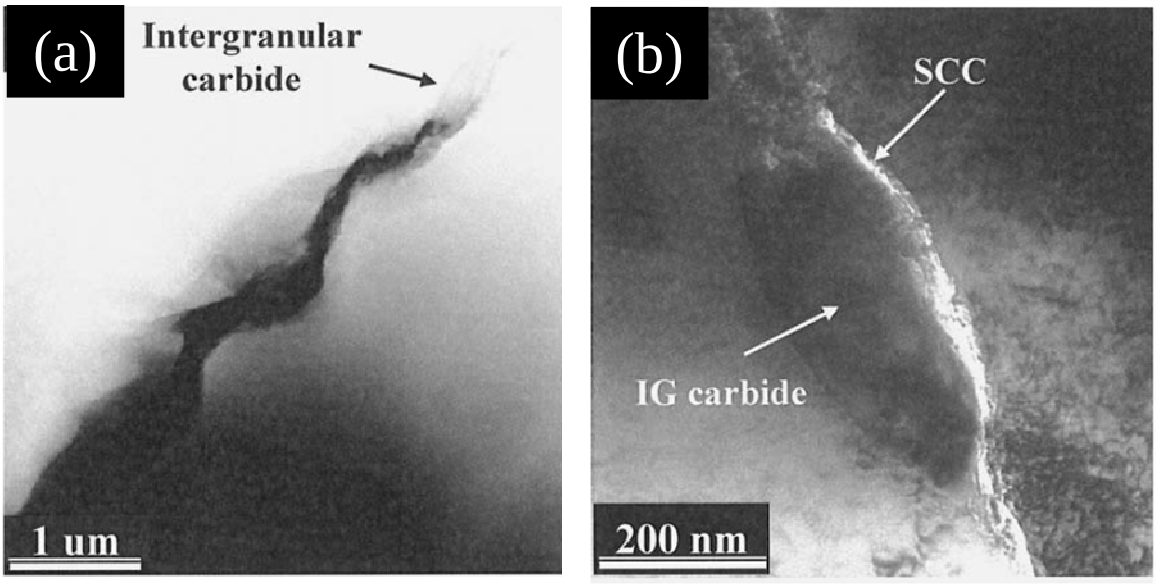

Figure 2.36 Micrographs showing the influence of carbides on IGSCC in Alloy 600: (a) the intergranular crack stops when it reaches an intergranular carbide and (b) the intergranular crack goes around the intergranular carbide [101].

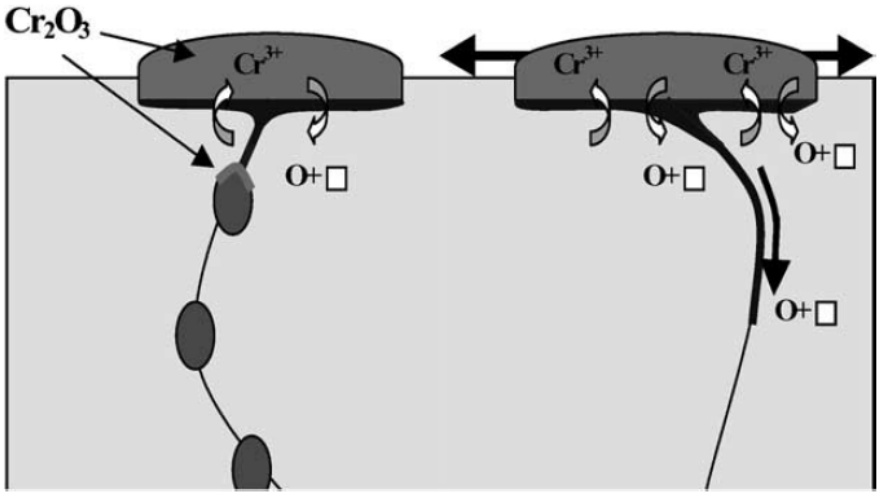

Figure 2.37 Schematic of internal oxidation mechanism illustrating the role of intergranular carbides in preventing the oxygen from diffusion down the grain boundaries [89].

2.6 Micro-mechanical testing using FIB cantilevers

The technique of deflecting cantilever beams using different setups that collected the force-displacement data in real time began in 1988 when Weihs *et al.* [106] and Johansson *et al.* [107] measured the Young's modulus and yield strength of single crystal silicon testing cantilever beams that were fabricated with different lithographic methods. Further similar studies performed on single crystal silicon are described in more detail by Armstrong [108]. The method was extended to test the Young's modulus and residual stress of electroplated gold thin films [109], the Young's modulus of aluminium using aluminium on silicon substrate beams [110] and the compressive stress in boron nitride thin films [111]. This technique has been used to also study the fracture strength of silicon [107][112][113][114] giving results in close agreement with established bulk values.

While this lithographic method proved useful to make microscale test specimens in single crystal silicon and thin films, its application to other materials is limited. In addition, the lithographic technique can only manufacture beams of simple shapes, and it is not suitable for testing beams of complex geometries [108].

McCarthy *et al.* [115] tested single crystal silicon cantilevers manufactured using the dimpler and partially polished with the Focussed Ion Beam (FIB) to measure residual stresses. While it is a more precise method of manufacturing the beams, it still cannot be applied to a wide range of materials (e.g. materials that are more difficult to polish). The first study that presented a method to manufacture cantilever beams using exclusively the FIB is that of Di Maio and Roberts [116]. Cantilevers of 10 μm length and 4 μm width having the geometry presented in **Figure 2.38** were manufactured in chemical vapour deposited WC- based coatings and tested using a nanoindenter to measure the

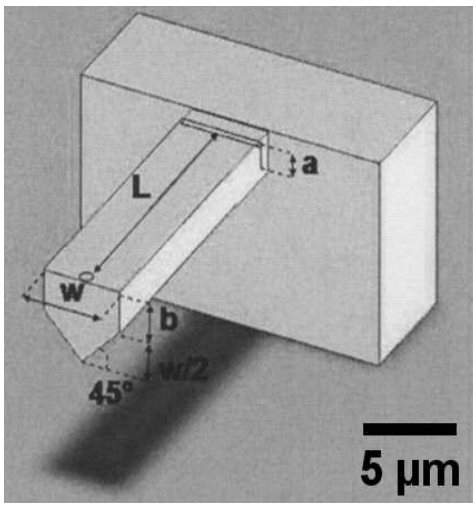

Figure 2.38 Image showing the geometry of the cantilevers produced by Maio and Roberts, where a is de depth of the notch, L is the length from the notch to the loading point and w and b are the width and the height of the pentagonal cross-section [116].

fracture toughness. The beams were pre-notched using the FIB in order to extract values for the fracture toughness.

This method opened the field of using FIB manufactured beams not only to measure the fracture toughness of different materials but also to determine the bending stress or shear strength, using un-notched cantilevers.

Armstrong [108] used FIB-manufactured cantilevers to determine the fracture toughness of electrodeposited nanocrystalline Ni-W alloy films [117] and to calculate the fracture toughness of bismuth embrittled copper grain boundaries [118]. The cantilevers produced in bismuth embrittled copper were milled so that each cantilever contained a grain boundary close to the fixed end. The cantilevers were pre-notched at the grain boundary using a FIB single line of 10 pA.

The values obtained for the fracture toughness were between 2.7 and 7.2 MPa($m^{1/2}$).The misorientation of the grains was also measured using EBSD; however no direct correlation was found between the misorientation of the boundary of the plane normal

and the fracture toughness. This work proved that the fracture toughness of individual grain boundaries can be tested using micro-mechanical testing techniques.

Lozano-Perez *et al.*[119] used a similar method to study the oxide embrittlement of grain boundaries in Ni Alloy 600. Cantilevers of 23x3x4 μm with both triangular and pentagonal cross-section were milled using the FIB and tested using a nanoindenter. The oxidised grain boundary failed in a brittle manner, while the unoxidised ones yielded. The technique was successful in proving the brittle character of the oxide at the grain boundaries. Since the cantilevers were not scanned before the test, the exact location of the loading point of the cantilevers was unknown since post-testing observations of the cantilevers did not show the loading point, information that would be needed to produce an accurate value of fracture toughness. In addition, the data provided by the nanoindenter in terms of the load vs. displacement seems unreliable as well, mainly because of the rather coarse surface of the sample.

The work presented in **Chapter 4** and **Chapter 5** use the technique of manufacturing cantilevers using the FIB and testing them using the nanoindenter to study crack growth rate produced by IGSCC in 304 SS and to determine the fracture toughness of oxidized grain boundaries in Ni Alloy 600.

2.7 Summary

The literature review shows that the problem of corrosion and especially IGSCC affects both 304 SS as well as Ni Alloy 600, two materials that are highly used in the nuclear power industry. Different models have been proposed to either predict the IGSCC or provide a further understanding into the complex mechanism of SCC. However, until now there is no universal model that can be applied for a general system.

This thesis aims to take a step forward into providing some insights on this topic by looking into the grain boundary embrittlement of Ni Alloy 600 and by studying the IGSCC on individual grain boundaries in 304 SS through micro-mechanical techniques. The character of grain boundaries that fail to IGSCC in 304 SS and what makes them susceptible is still unknown. This thesis aims to provide more information on the characteristics of a grain boundary where IGSCC initiates by unique observations of an IGSCC initiation site in 304 SS.

3 Experimental techniques

3.1 MTS Nano Indenter XP

The nanoindenter used during this study was an Agilent MTS Nanoindenter. A schematic of the instrument is presented in **Figure 3.1**.

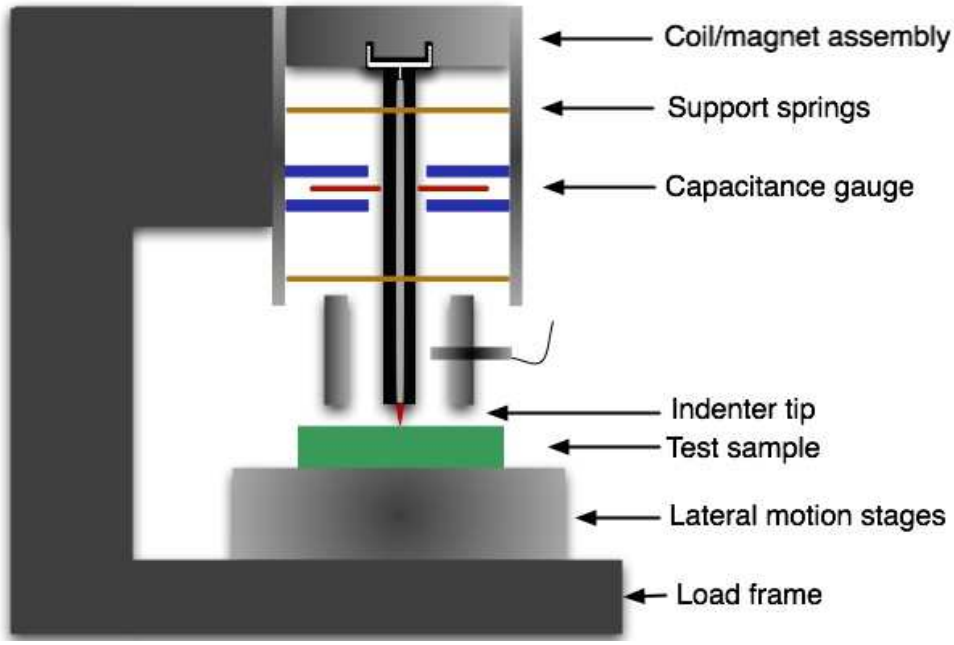

Figure 3.1: Schematic of the Nanoindenter [Adapted from [120]].

The nanoindenter contains a lateral motion stage which is coarse screw-driven with a higher-resolution piezo stage on top, that allows the movement of the sample, an assembly through which the force is applied to the indenter shaft and an assembly that measures the displacement. The force is applied by a current that passes through the coil shown in **Figure 3.1** and so it is proportional to the current applied. The resolution of the force applied is 50 nN. The displacement gauge as shown in **Figure 3.1** consists of a three-plate capacitor; the resolution of the displacement after calibration is 0.01 nm. Though the nanoindenter could be set up to be in a “displacement control” mode

through the software, it is a load-controlled instrument [120]. The software interface is controlled by Test Works 4 which is also Agilent/MTS software.

The instrument presented is mainly used for nanoindentation, however, during this research it has been used to test micro-cantilevers. In order to test micro-cantilevers, several steps need to be followed and they are described next.

First, the sample is mounted on the piezoelectric stage at the right height and the desired objective lens is selected. The height of the sample needs to be lower than the indenter housing; if the set height is too small, the tip will not be able to hit the surface of the sample while if the set height is too high, the tip of the indenter can run into the sample, causing damage to the system. The sample needs to be aligned with the markings of the right height that are indicated on the sample tray. Lenses of various magnifications can be used. To test the Ni Alloy 600 cantilevers, the 20X magnification lens was used, while for the 304 SS cantilevers, the 10X lens was used. The 10X lens was used for the *in-situ* testing to protect the lenses from the active solution. The sample is imaged through the optical microscope. After the sample was loaded, the stage was initialized. For a better accuracy, the microscope was calibrated to the indenter and this procedure was repeated until calibration was done correctly. The calibration of the indenter means the alignment of the microscope with the indenter tip such that the centre of the area observed through the microscope coincides with the position at which indentation is made. This step will assure that indentation is made at the chosen position.

After the calibration, the area with the cantilevers was found and the cantilever of interest was scanned. During scanning, the sample is traversed by the indenter tip similar to an Atomic Force Microscope in contact mode. The height deflections recorded on the surface of the sample (e.g. between the top surface of the cantilever and

the trench) as the sample is being scanned are registered and can be visualized as a 3D map. Before testing, the micro-cantilever that needs to be tested is first scanned to determine a more accurate location of the loading point. The load applied for the scan was 4 μN and the contact time was 2.0 s. Once this was done, the test method was loaded and the test started.

"Methods" are sets of instructions that set different operational parameters during the test. During this research, two different methods were used. For the Ni Alloy 600 cantilevers, a displacement controlled method was used such that the cantilever would be continuously loaded until the displacement reached a set value (1.5 μm). For the 304 SS cantilevers, a load controlled method was used such that the maximum load and the time during which the cantilever was under constant maximum load were inputs given by the user.

The nanoindenter can be used in two different modes: XP Mode and DCM Mode. The Dynamic Contact Module (DCM) mode has a better resolution (displacement resolution of 0.0002 nm) than the XP mode (displacement resolution of 0.01 nm) and it is usually used for smaller indents and smaller loads. The maximum load that can be used with a DCM head is 10 mN and the maximum indenter depth is 15 μm. In the XP mode, the maximum load can be 500 mN and the indentation depth is greater than 0.5 mm [121]. In this study, the tests were performed in the XP mode, using a continuous stiffness measurement (CSM) option. In the CSM option, the nanoindenter applies a monotonically increasing load to the indenter tip, while an oscillation force is superimposed with a force amplitude that is of several orders of magnitude smaller than the applied load. This provides a more accurate measurement of the contact stiffness and the compliance can be calculated as a function of depth. The frequency of this oscillation is approximately 45 Hz [121]. Typically, the contact stiffness (S) is

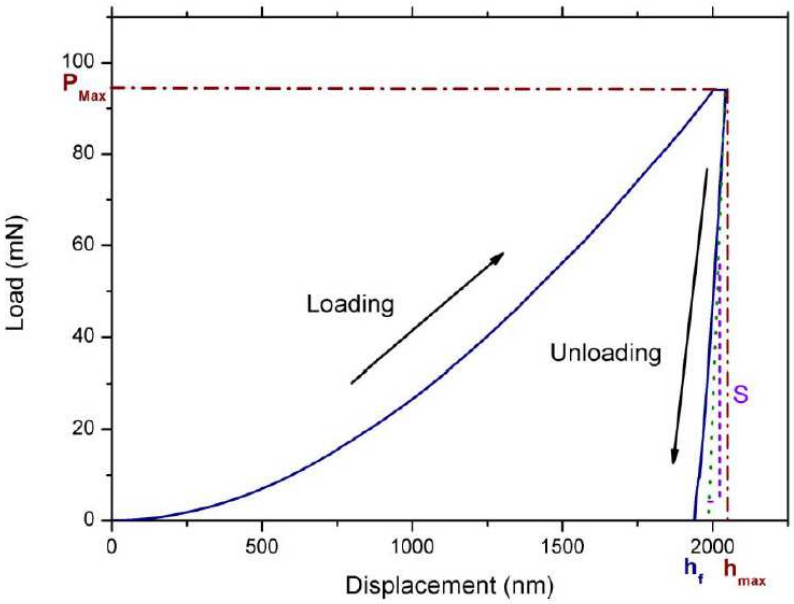

Figure 3.2 Typical load vs. displacement curve produced by the nanoindenter [108].

measured using the slope ($S = \frac{dP}{dh}$) of the unloading data in a typical load vs. displacement curve, as shown in **Figure 3.2.**Using the CSM option, the contact stiffness can be measured continuously during the test and not only from the unloading region [121]. During the tests performed in this thesis, the cantilevers were tested using a diamond Berkovich tip.

3.2 Electron backscatter diffraction (EBSD)

EBSD is a useful characterization technique, which is coupled to a scanning electron microscope (SEM). It determines the grain orientation, local texture, phase or point to point orientation correlations in bulk materials. A schematic of a typical EBSD setup is shown in **Figure 3.3**.

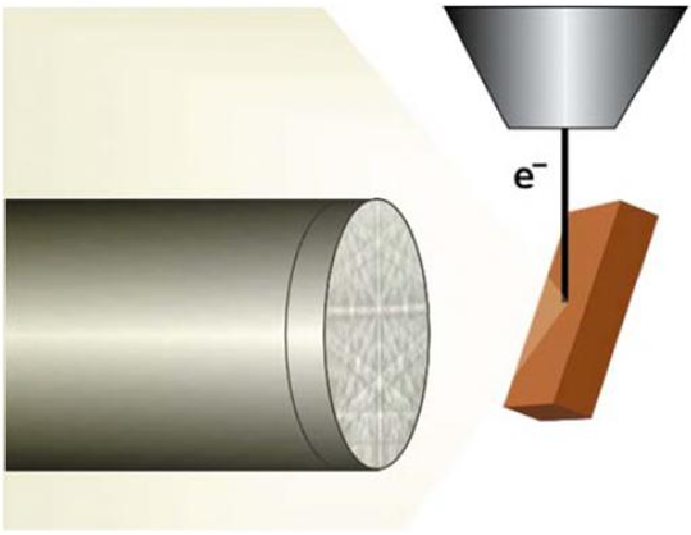

Figure 3.3: Configuration of the EBSD setup [122].

The beam of electrons comes in contact with the sample that is tilted at 70° (to obtain a higher contrast) and the backscatter Kikuchi patterns are projected on the phosphor screen. The Kikuchi pattern appears on the phosphor screen as a projection of the crystal lattice. The diffraction mechanism is shown in **Figure 3.4** where the edges of the diffraction pattern are formed by the two diffracting cones and the middle reflection is the diffraction plane [122]. The waves projected from the crystal lattice cause interference and as a result, diffraction occurs. Interference occurs at a specific Bragg angle (θ_B) given by the Bragg's law:

$$\lambda_e = 2dsin(\theta_B) \quad \textbf{(5)}$$

where $\boldsymbol{\lambda_e}$ is the electron wavelength and $\boldsymbol{d}$ is the atomic spacing. While the incident beam scatters in all directions, the Bragg angle is characteristic to two cones which are about the normal of a diffraction plane, each being on opposite sides of the plane [122].

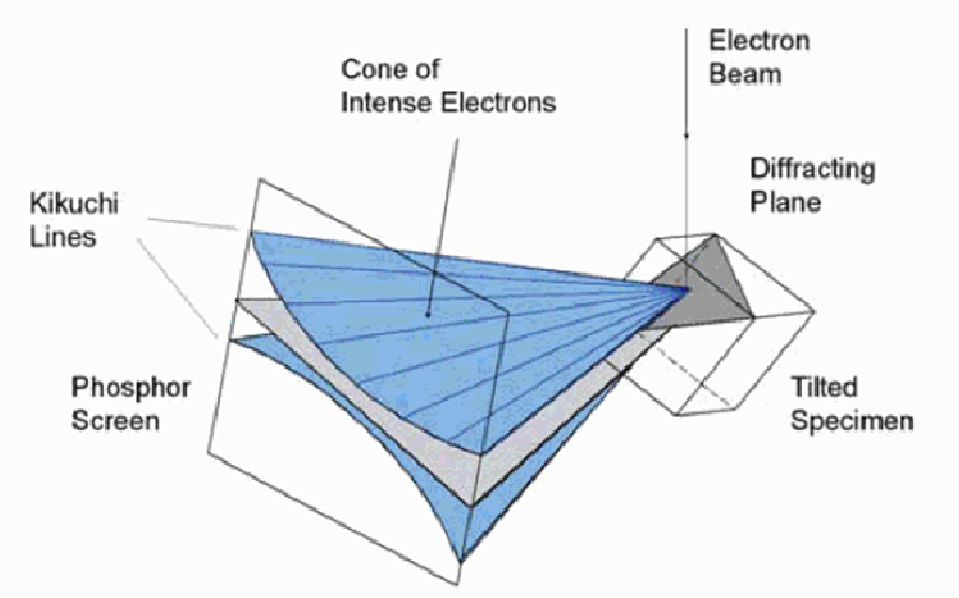

Figure 3.4 Schematic of the diffraction mechanism [122].

In this study, both EBSD and the high resolution EBSD (HR-EBSD) (technique that will be described in more detail in **Section 6.4**) were performed using a JOEL JSM 6500F. The JOEL JSM 6500 F is a low voltage field emission gun SEM that operates between 1 and 30 kV. All the EBSD patterns were collected at 20 kV.

3.3 Focused Ion Beam (FIB)

FIB is very similar to an SEM, but instead of using electrons, it uses the Ga^+ ions from a liquid metal source. The Ga^+ ion source is accelerated down a column and it is focused to a very small point. Imaging can be obtained using the secondary electrons emitted as a result of the impact between the gallium ions and the sample, while milling is obtained as the primary ions replace the atoms on the surface of the specimen. FIB can be set to create complex patterns, lithography or for controlled deposition. Different parameters, such as the milling aperture, time, position on the sample and the dosage of the deposition can be controlled through software. Initially, the FIB was used for the semiconductor industry, to modify the circuits or for failure analysis but nowadays, it

can be used for many more different applications in materials science, such as: TEM sample preparation, microelectronic repair, micro-mechanical cantilever manufacture, atom probe specimen and AFM tip fabrication, cross-sectioning of biomaterials or serial sectioning for 3D reconstruction [123].

An image of a Zeiss Nvision 40 FIB-SEM is shown in **Figure 3.5** and a schematic of the instrument is presented in **Figure 3.6**. As shown in **Figure 3.6**, a FIB consists of a vacuum system, ion optics and ion source, a scan generator, a stage and a computer with control software, each of which is discussed in more detail below.



Figure 3.5: Image of the Zeiss Nvision 40 FIB-SEM instrument at Oxford University.

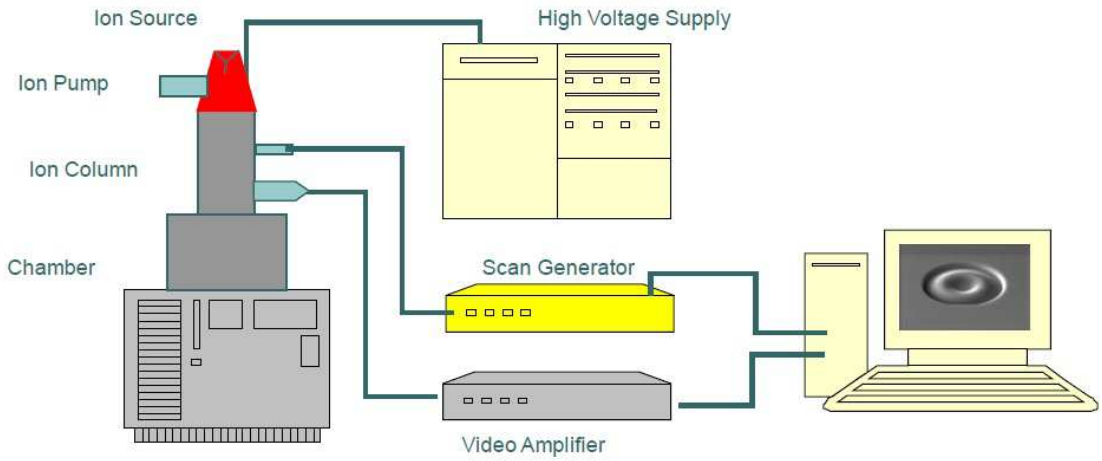

Figure 3.6: Schematic of a FIB instrument [123].

3.3.1 Vacuum system

The instrument needs to be under a high vacuum in order for the ion beam to be used and the samples need to be compatible with these conditions, to prevent the chamber and the instrument contamination. For that, the samples that are not conductive are always coated with either Au, silver dag, Pt or C. The chamber vacuum is required to be around $1x10^{-6}$ torr [124], but the performance of the instrument is increased (e.g. less drift, more milling precision) with a better chamber vacuum.

3.3.2 Liquid Metal Ion Source (LMIS)

The LMIS makes possible the use of FIB for small probe sputtering and it has an emission area of approximately 10 nm and an intensity of approximately 106 A/cm^2. An image of an LMIS is shown in **Figure 3.7.** It contains a reservoir that holds the metal source material, and a tungsten wire. The most commonly used LMIS is Ga^+, because it has a low melting point (29 ^oC), low volatility at melting point and good mechanical and vacuum properties. The life of such an LMIS is around 3000-4000 μA hrs for a common source [123].

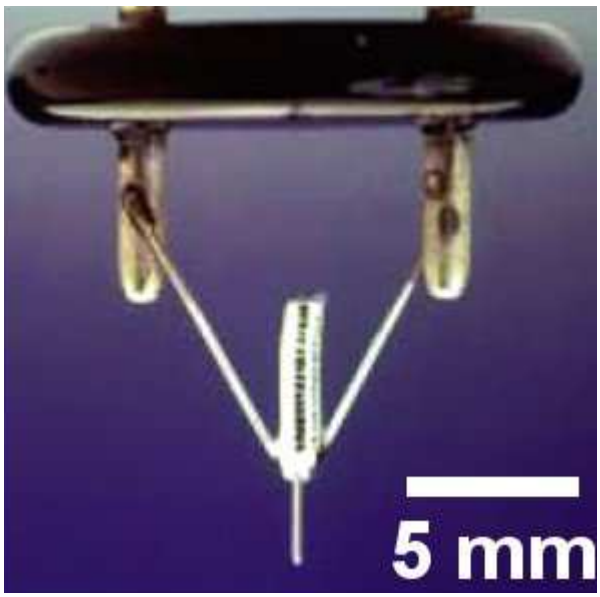

Figure 3.7 Image of an LMIS [123].

3.3.3 The FIB Column

A FIB column is schematically shown in **Figure 3.8**. The beam is generated by an electric field (10^8 V/cm) that is present at the wetted tip of W needle and forms a "Taylor cone" of approximately 2-5 nm in diameter [124]. The emission current of the source is usually 2.2 μA. The beam goes down the column through an aperture that controls the beam current. Then the beam is focused on the sample and astigmatism is corrected through the lenses. The FIB always uses electrostatic lenses and not magnetic ones (as in the case of SEM) because magnetic lenses would be too large to manufacture for the Ga^+ ions.

The stage is 5 axis eucentric and can be used to tilt, rotate or move the sample in the x, y and z directions. The Ga^+ beam can yield secondary electrons, implantation of Ga, sputtered neutral and ions or it can cause damage of the sample. In order to minimize the damage of the sample, small beam currents, usually less than 100 pA are used when in imaging mode.

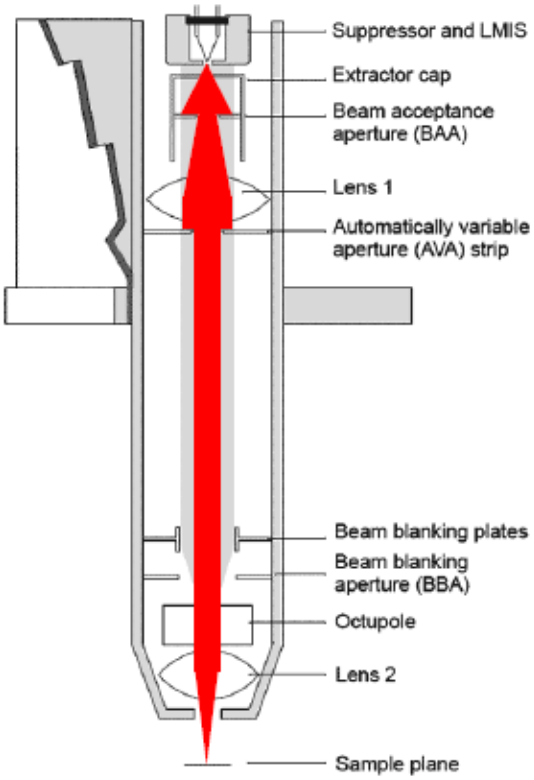

Figure 3.8: Schematic of a FIB column [123].

3.3.4 FIB instruments used

The FEI FIB 200 is an older instrument, installed in 1999. It operates at 5 kV or 30 kV, with milling apertures ranging from 1 pA to 20 nA, and it has a resolution of approximately 10 nm. The instrument was used at the beginning of the project, to manufacture the cantilevers presented in **Chapter 4**.

The Zeiss NVision 40 is a dual beam FIB that also contains a high resolution SEM. The SEM operates between 100 V and 30 kV and it has a resolution 2.5 nm at 1 kV and of 1.1 nm at 2 0kV. The FIB operates between 1 kV and 30 kV with milling apertures from 0.1 pA to 45 nA, and it has a resolution of the ion beam of 4 nm at 1 pA. Deposition can be performed using the gas injection system with W, Pt, C or SiO_2. In addition to the GIS, the instrument is equipped with a dual Kleindiek manipulator that can be used

for *in-situ* specimen lift out. This instrument was used for cantilever manufacturing and imaging in **Chapter 4** as well as for 3D reconstruction in **Chapter 5**.

The Zeiss Auriga, presented in **Figure 3.9** is a dual beam instrument very similar to the Zeiss Nvision 40 instrument. The SEM operates between 100 V and 30 kV, and it has a resolution of 1.9 nm at 1 kV and 1.0 nm at 15 kV. The FIB operates between 1 kV and 30 kV with milling apertures from 1 pA to 20 nA, and it has a resolution up to 2.5 nm. Deposition of C, W and Pt can be performed and it also has a Kleindiek manipulator. This instrument was used for cantilever manufacturing and imaging in **Chapter 4** and **Chapter 5** as well as for determining the grain boundary plane and trace angle in **Chapter 6**.

In contrast to the single-beam instrument, the dual-beam instruments minimize the damage of the sample produced by the gallium while milling, since the specimen is imaged with the SEM beam instead of the FIB beam. In addition, the dual-beam instrument can be used for more complex milling because using the SEM beam, the specimen can be imaged in real time.

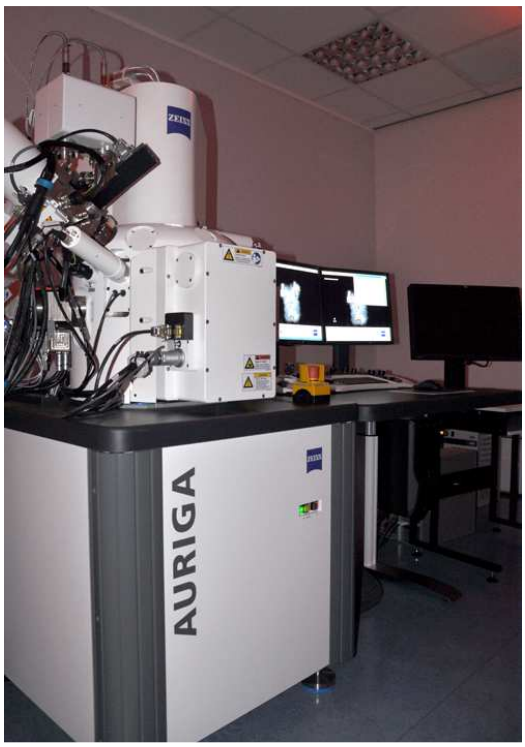

Figure 3.9: The Zeiss Auriga FIB instrument at Oxford University materials.

4 Micromechanical testing of SCC in 304 stainless steel

4.1 Introduction

Rogers [125] and Herbert [126] were the first to develop a setup that could be used to study the stress corrosion crack growth rate of individual boundaries using an *in-situ* micromechanical testing technique. This has been developed further in this work.

Rogers [125] used a focused ion beam machine to produce and a nanoindenter to test micro-cantilevers containing a single grain boundary under an active solution of acidified potassium tetrathionate 0.1 M, with a 2.5 pH [127]. The material tested was stainless steel 304 annealed in argon atmosphere at 1050 °C for 1 h and sensitized at 650 °C for 24 h. To better reveal the grain structure, the samples were anodically etched in 10% oxalic acid at 9 V for 60 s before FIB milling. Micro-cantilevers of approximately 25 μm by 5 μm by 3μm were machined and pre-cracked using the FIB. To perform stress corrosion cracking tests under active solution (potassium tetrathionate diluted with sulphuric acid to a pH of 2.5) using a nanoindenter, a customized stage was built and is shown in **Figure 4.1**.

The cantilever was immersed in the fluid, scanned and then tested using the nanoindenter. Cantilevers were successively stressed to peak loads between 50 and 750 μN in 75 μN increments. The load was held at the peak value for 180 s, then, the micro-cantilever was unloaded. The results are presented in **Figure 4.2** [127]. **Figure 4.2** shows that the displacement continued to increase during the 180 s holding time; this was interpreted as being due to the increase of the cantilever's compliance as the crack grows through the grain boundary.

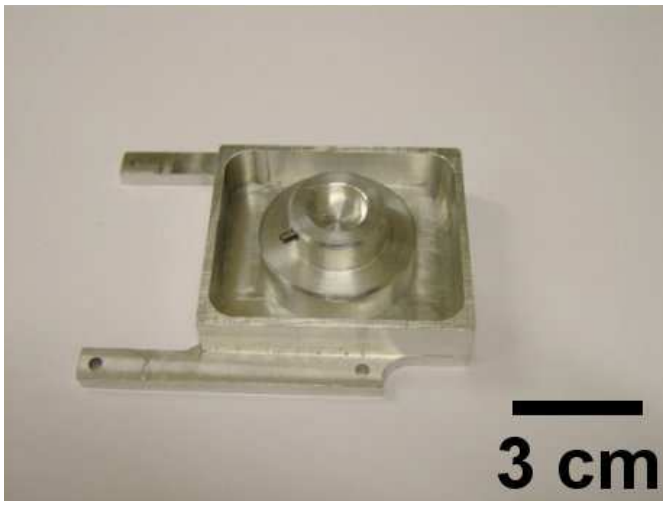

Figure 4.1 Initial stage used by Rogers for micromechanical tests under corrosive environment. The stage contained an aluminium cell where the sample is placed and an overflow tray [125].

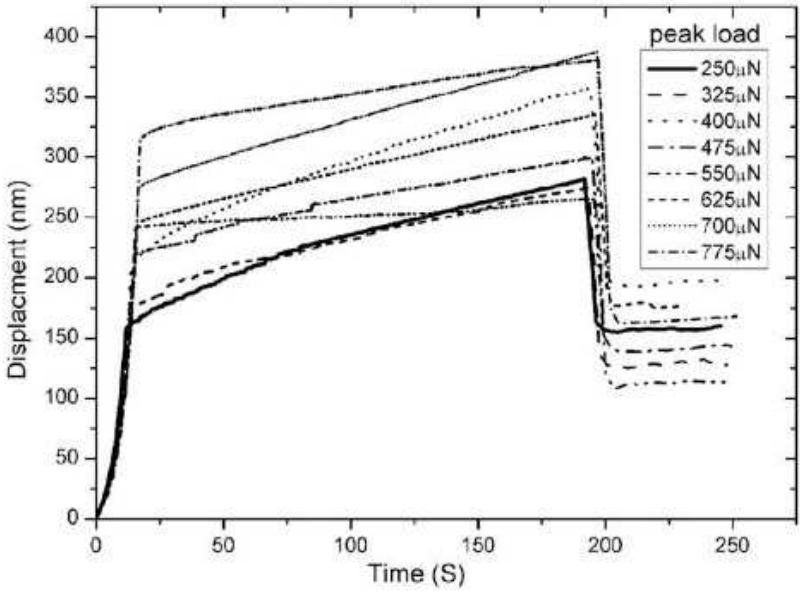

Figure 4.2 Displacement versus time for different micromechanical tests stressed at different loads in corrosive environment, performed by Rogers. The displacement increases with time except for the 550 μN test, when the liquid was removed. The change in displacement is a proof of crack growth rate in liquid [127].

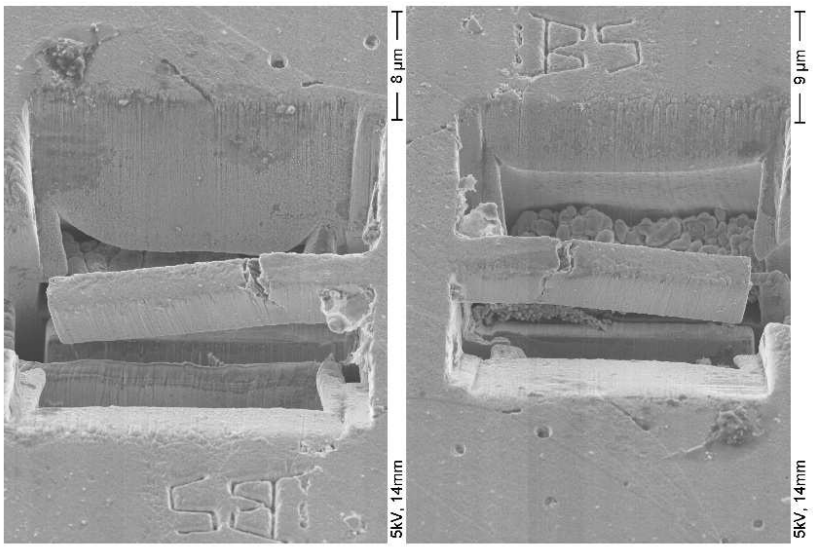

Figure 4.3 SEM micrographs of a fractured cantilever tested by Rogers in active fluid [125].

This was confirmed by the 550 µN test; during the test, the liquid was removed and there was no change in compliance with time in this case. Replacing the liquid and loading to 625 µN resulted in progressive development of displacement with time. SEM observations presented in **Figure 4.3** also confirmed that the sample had fractured.

Roger's work was a proof-of-concept for micromechanical testing of IGSCC in 304 SS, showing that IGSCC in single grain boundaries can be tested using FIB-machined micro-cantilevers [127]. Herbert [126] carried on the work done by Rogers, to develop a method to quantify the crack growth rate. Herbert used the same method of producing the cantilevers and testing as Rogers, but the micro-cantilevers were pre-notched by FIB. The notches were 250 nm deep and 50-100 nm wide and were milled at the grain boundary [128]. The microcantilevers were loaded to 100 µN, held for 300 s and then unloaded. After loading, a 3 V voltage was applied to the sample for 60 s to accelerate the crack initiation, and then the test was continued without an applied voltage. At the end of the tests, the tested beams displayed crack nucleation and growth as shown in **Figure 4.4**.

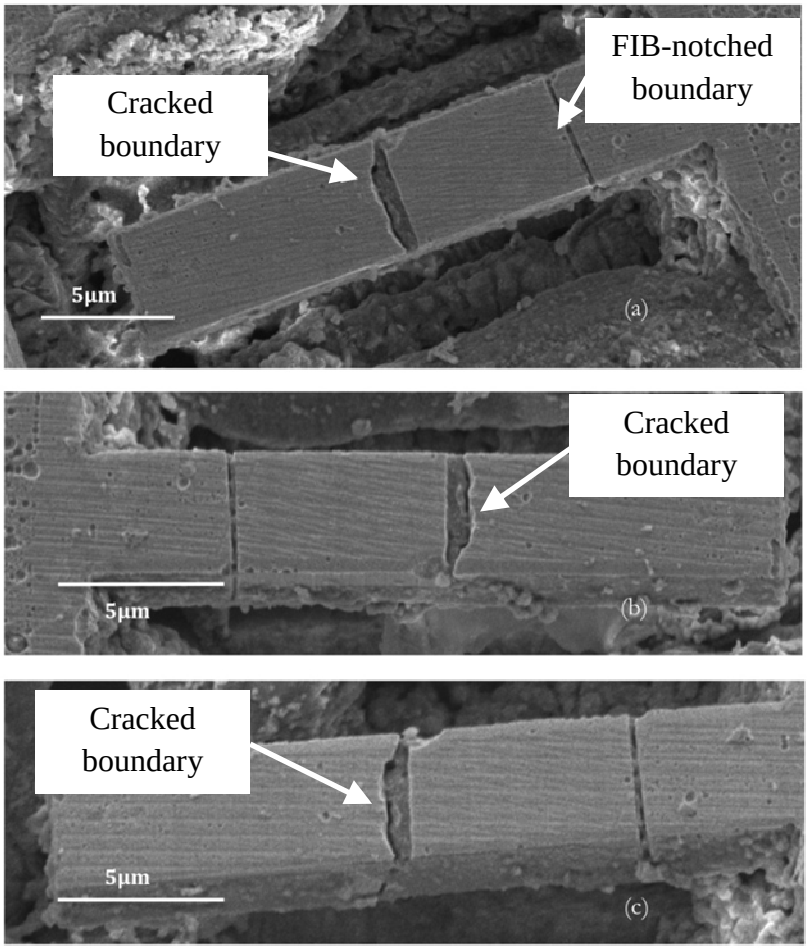

Figure 4.4 SEM micrograph of a tested cantilever in fluid, after the test: a) top view, b) and c) image tilted at 30°. The cantilever fractured at a different grain boundary than the expected FIB pre-notched boundary [126].

It can be observed from **Figure 4.4** that crack growth occurred at an un-notched grain boundary exposed to a lower stress and not at the expected pre-notched grain boundary. This might have happened because the grain boundary that failed was more susceptible to IGSSC.

Regarding data analysis, Herbert noticed the same trend of displacement decreasing a few tens of nm during the hold period, however no crack growth was found to have occurred. It was stated that the decrease in displacement might be due to the plastic flow that occurs in the micro-cantilever or around the cantilever and not necessarily to crack growth. Herbert concluded that using the displacement to determine the crack growth

was rather an unreliable method and developed a new method to measure the crack growth rate using the harmonic contact stiffness measured by the nanoindenter. Using ABAQUS software, the compliance of micro-cantilevers with different notch sizes was modelled and a relationship between the compliance and the crack length was determined. Then, from the harmonic contact stiffness the crack length was calculated and the stress intensity was obtained using simple beam theory. Herbert obtained results on two microcantilevers and found the crack growth rate exponent for the dependence between stress intensity factor and crack growth rate to be approximately 3 as shown in **Figure 4.5**.

Herbert's method demonstrated that intergranular stress-corrosion crack growth could be quantified using the beam compliance method. Limited data were obtained, however.

The study presented in this chapter follows up on Herbert's work by determining whether the IGSCC crack growth rate in 304 SS can be produced and measured in a controllable manner.

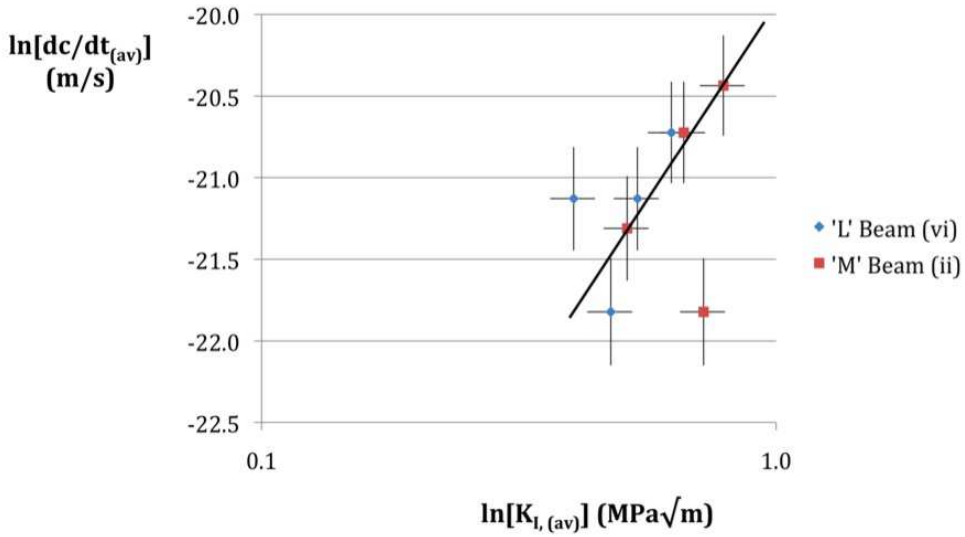

Figure 4.5 Crack growth rate as a function of stress intensity as calculated by Herbert [126].

4.2 Sample preparation

The material used for this study was 304 SS, with the chemical composition presented in **Table 4.1**. The chemical analysis was performed by LSM Analytical Services. The 10 mm diameter 304 SS rod was first machined down to 3 mm in diameter and then ten samples of 3 mm length were sectioned into slices using an Isomet 5000 high-speed rotary saw. For some of the experiments presented in this chapter, the stubs used for FIB, SEM and nanoindentation were not regular aluminium SEM stubs, but stubs made from the same 304 SS material (10 mm diameter and 3 mm height, as-received conditions) so as to have a stub of same electrochemical potential as the specimen. The sample was fixed to the stub using superglue.

Table 4.1 304 Stainless steel chemical composition for the sample used

Chemical analysis (wt%)														
Fe	Cr	Ni	Mn	Cu	Mo	Si	Co	Al	Nb	Sn	Ti	V	W	C
70.91	18.08	8.12	1.34	.50	.40	.19	.13	.05	.05	.05	.05	.05	.05	.03

4.2.1 Annealing treatment

Since the aim of this project was to make and test cantilevers containing one grain boundary, the material was heat treated to increase the size of the grains. To produce grains of approximately 50 μm in size, the sample was annealed at a temperature of 1050 ^{o}C for 1 hr in flowing Ar. To verify that the annealing treatment resulted in achieving the desirable microstructure, specimens were studied by EBSD. An EBSD map is shown in **Figure 4.6**. **Figure 4.7** presents the distribution of the grain size for the

annealed material. The histogram trend shows that most of the grains are of size approximately 50 μm, which will be sufficient for the purpose of this project, as the size of the cantilevers to be used was approximately 30 μm long by 3μm wide.

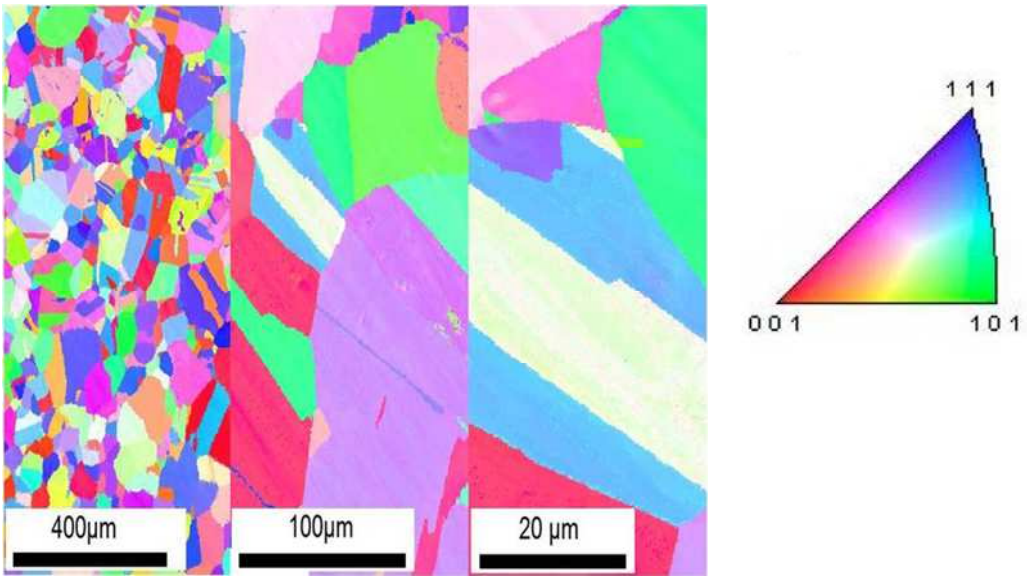

Figure 4.6 EBSD map of annealed 304 SS specimen at different magnifications.

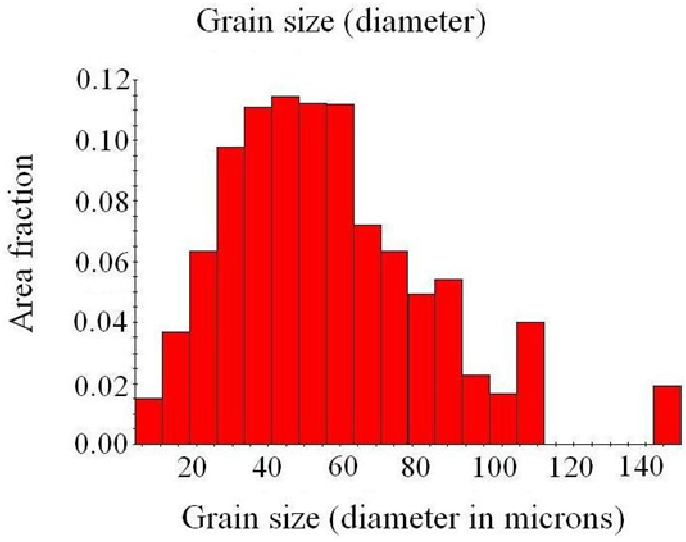

Figure 4.7 Grain size histogram of an annealed 304 SS specimen. The grain size is approximately 50 μm.

4.2.2 Grinding and polishing procedure

Considerable time was dedicated to establish and improve the sample preparation protocols to produce a clean, damage-free surface. Firstly, to be able to obtain a sharp good quality EBSD pattern, the sample was finely polished and the surface was carefully prepared with no scratches. The finalized step by step grinding and polishing procedure is presented in **Table 4.2**.

Table 4.2: Grinding and polishing procedure for stainless steel 304

Step	Procedure	Time (minutes)	Grit Size	Pressure	Lubricant
1	Grinding with grit paper	2	600	applied by hand	Water
2		4	800	applied by hand	
3		6	1200	applied by hand	
4	Polishing with diamond paste	2	9 μm	10 N	Kemet Type OS Fluid
5		4	3 μm	5 N	
6		6	1 μm	None	
7	Polishing with colloidal silica	10	0.05 μm	18 N	Water

4.2.3 Sensitisation treatment

During this project, to ensure that the samples would be susceptible to IGSCC, the samples were treated at 650 ^{o}C for 24 hours in flowing Ar. This sensitization treatment followed the annealing treatment that was described previously in **Section 4.2.1**. To verify that the sensitization had been performed successfully, the DL-EPR test [76], described in more detail in **Section 2.2.4.1**, was used. The environment that was used for the DL-EPR test was 0.5 *M* H_2SO_4 + 0.01 *M* KSCN. During the DL-EPR test, the surface was polarized anodically from -400 mV to 300 mV at a rate of 100 mV/min, and

then the potential was decreased at the same rate. The results from the EPR test on both unsensitised and sensitized 304 SS samples are presented in **Figure 4.8.** The ratio between the reactivation current (I_r) and the activation current (I_a) is called the degree of sensitization and for 304 SS to be susceptible to intergranular corrosion, this value needs to be greater than 0.05 [76]. For the unsensitised material, the DL-EPR result presented in **Figure 4.8a** indicates that the degree of sensitization is 0, which means that the sample is not susceptible to intergranular corrosion, while **Figure 4.8b** indicates a degree of sensitization of 0.06, indicating that the sample is sensitised and susceptible to intergranular corrosion.

4.3 Nanoindenter customized stage

In order to use the nanoindenter under liquid, an aluminium custom stage and a PTFE cell were made after the model used by Rogers [125]. An image of the stage is shown in **Figure 4.9**. The original Rogers stage was not used because the cell was made of aluminium, which has been observed [14] to stop the corrosion process from occurring by causing a cathodic polarisation. The stage underwent several modifications to accommodate the different conditions of the different experiments; these modifications will be described individually for each testing method in the next sections.

4.4 Testing cantilevers under fluid using the nanoindenter

First, the sample was scanned with the nanoindenter using a load of 4 μN and a contact time of 2.0 s to locate the cantilever. Then, acid solution (at a pH between 1.1 and 2.6, for the various experiments performed) was introduced into the PTFE cell. Next, the indenter tip was placed close to the free end of the cantilever, and the cantilever was loaded to a maximum value, held for a certain time and then unloaded.

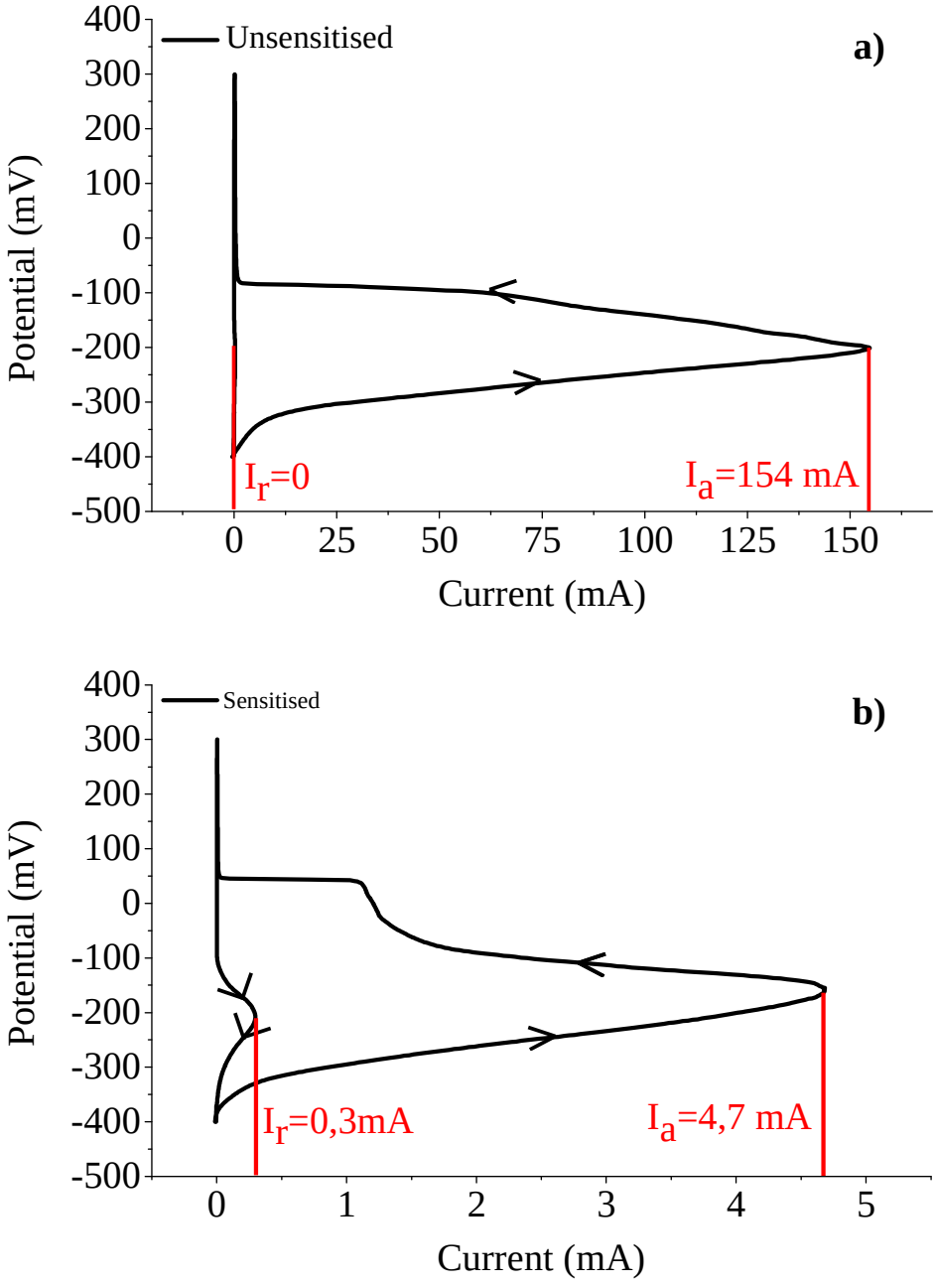

Figure 4.8: EPR result for a) unsensitised; b) sensitised material. The surface was polarized anodically from the corrosion potential of -400 mV to 300 mV, at a rate of 100 mV/min. Then, the direction was reversed and potential decreased at the same rate. The degree of sensitisation is 0 for the unsensitised sample and 0.06 for the sensitised sample.

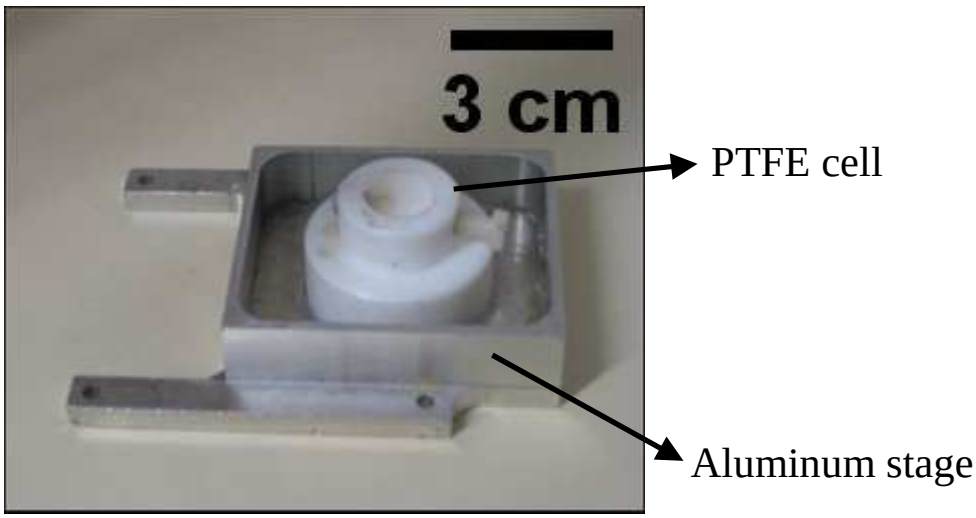

Figure 4.9 Nanoindenter customized stage including a PTFE cell that can accommodate the 304 SS stub and sample emerged in liquid.

4.5 Initial bending tests in liquid to determine the upper stress limit of the microcantilevers

It is important for the SCC experiments to load the cantilevers up to 70-80% of the yield stress so that the corrosion tests can be performed at a high stress, but still in the elastic region. In order to determine the yield stress, two cantilevers of the standard dimensions were milled and tested in solution. The cantilevers were un-notched and a micrograph showing the cantilevers before the test is presented in **Figure 4.10**.

The original load-displacement data obtained during the nanoindenter tests was converted into stress - strain data (both stress and strain being the maximum values in the beams; at the lower surface at the beam root), using simple beam theory (as described in **Section 5.3**) and are presented in **Figure 4.11**. The yield stress of the cantilevers was calculated using a 2% deviation from linear and obtained to be approximately 1300 MPa. The cantilevers were examined by SEM after the tests, and were found to have deformed plastically (**Figure 4.12.**).

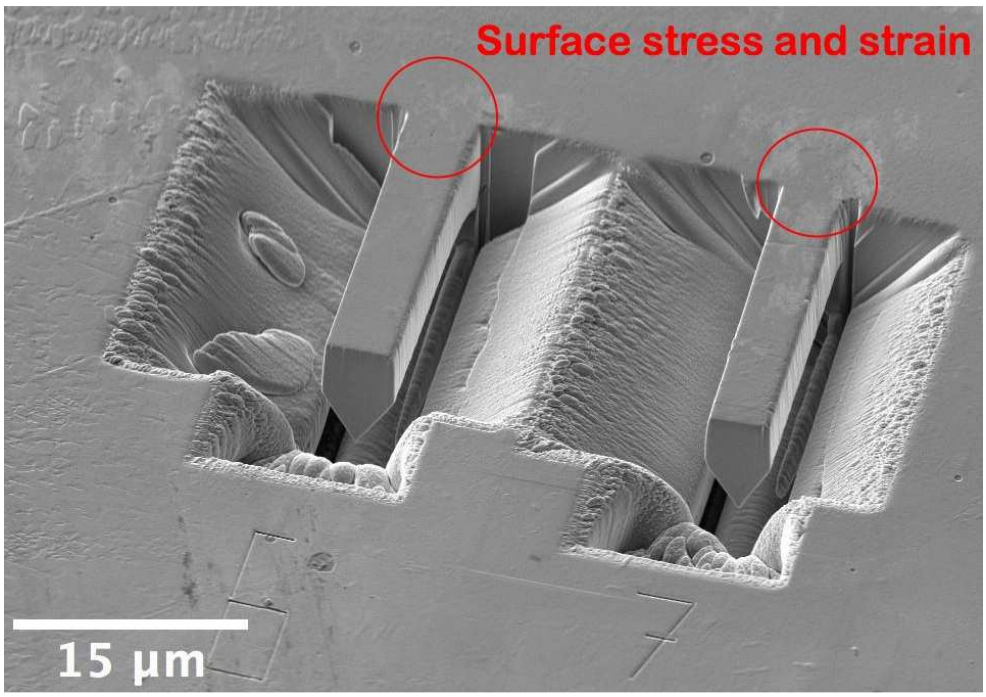

Figure 4.10 Initial micrograph of the cantilevers before testing. The red circles indicate the area of the cantilevers where the stress and strain were calculated.

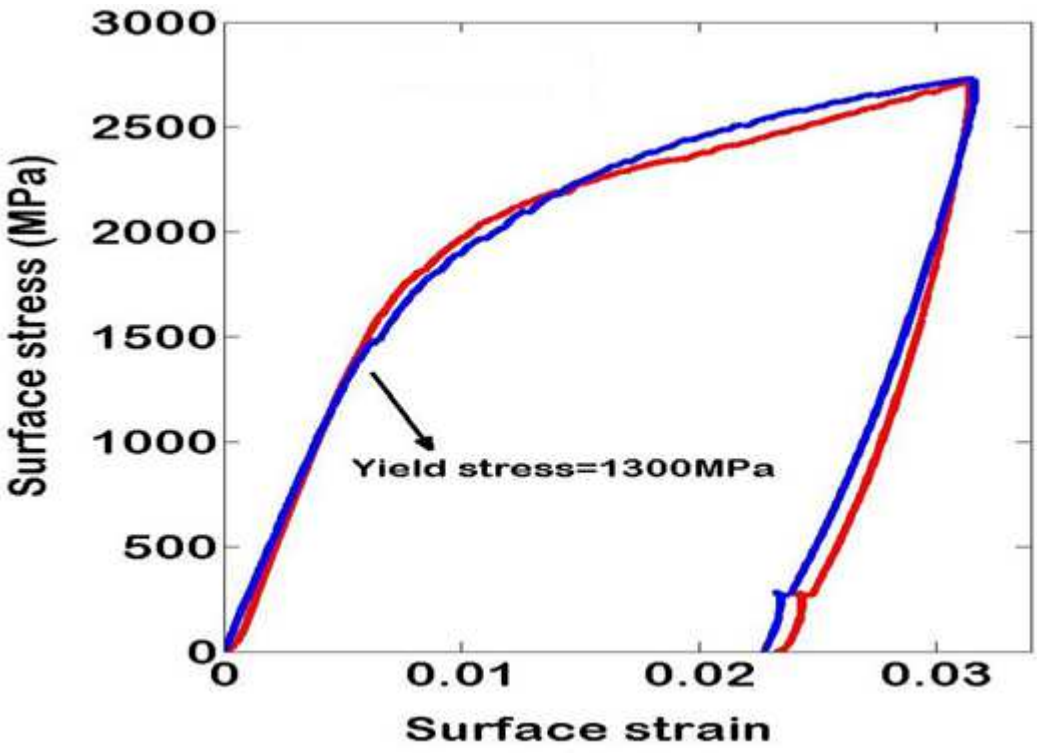

Figure 4.11 Stress vs. strain curves for two tested cantilevers in active solution. The yield stress calculated for these cantilevers is approximately 1300 MPa. The Young's Modulus calculated for these cantilevers is approximately 200 GPa which proves the validity of the stress and strain calculations.

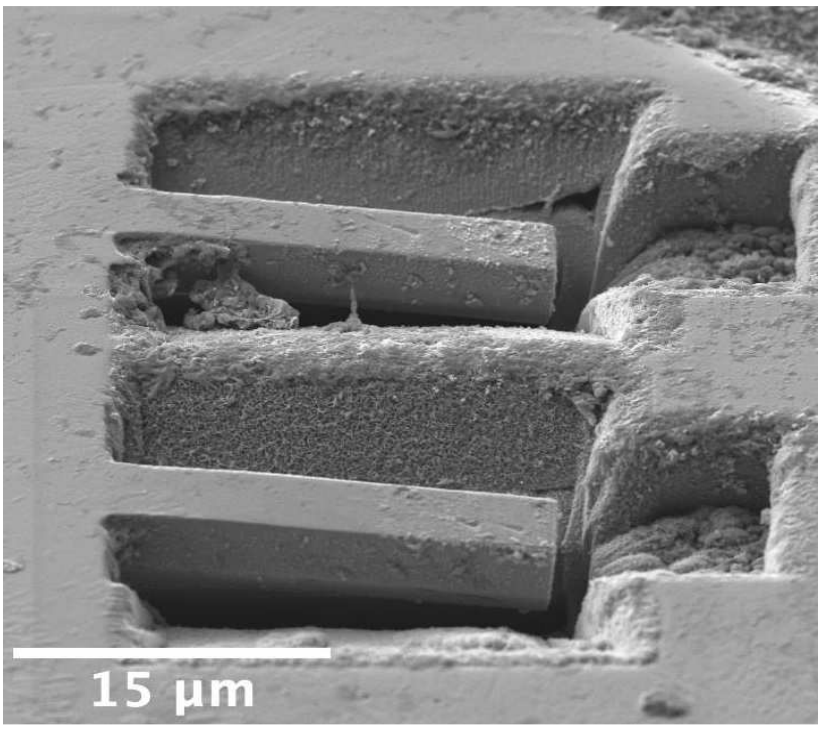

Figure 4.12 Micrograph of two cantilevers tested in fluid after bending test.

4.6 Tests applied to control and determine the crack growth in situ

4.6.1 In situ method with no voltage applied

4.6.1.1 Test conditions and setup

The cantilevers used in this method were milled as described in **Section 5.2.2** and were pre-notched at the grain boundary with a single FIB line for 20 s using a current of 10 pA. An image of a cantilever before the test is shown in **Figure 4.13**.

The solution used for this test was a potassium tetrathionate solution diluted with sulphuric acid, with a pH of 2.6. The schematic of the setup that was used to test cantilevers *in-situ* is presented in **Figure 4.14**. The sensitized 304 SS specimen was glued to the 12 mm aluminium SEM stub using superglue and specimen and stub together were placed in the PTFE cell. The aluminium stub was covered in lacquer to

make sure it does not influence the chemistry of the cell. During the test, the sample surface was covered with a meniscus of tetrathionate solution.

During the test, each cantilever was loaded to three different maximum loads of 400, 600 and 800 μN. The maximum load was held for 180 s and then the cantilever was unloaded.

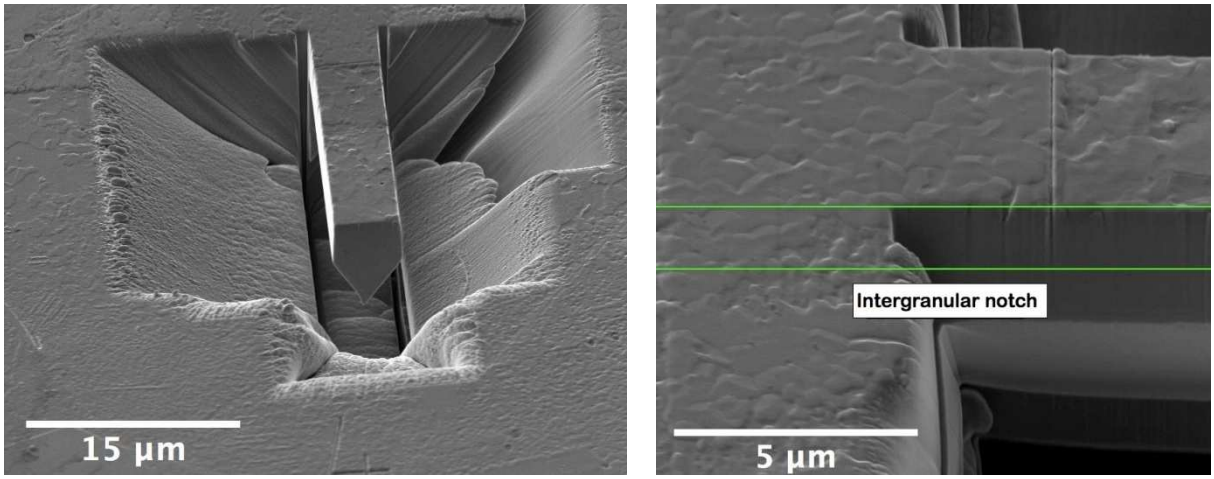

Figure 4.13 FIB pre-notched cantilever milled in 304 SS, before the in-situ test.

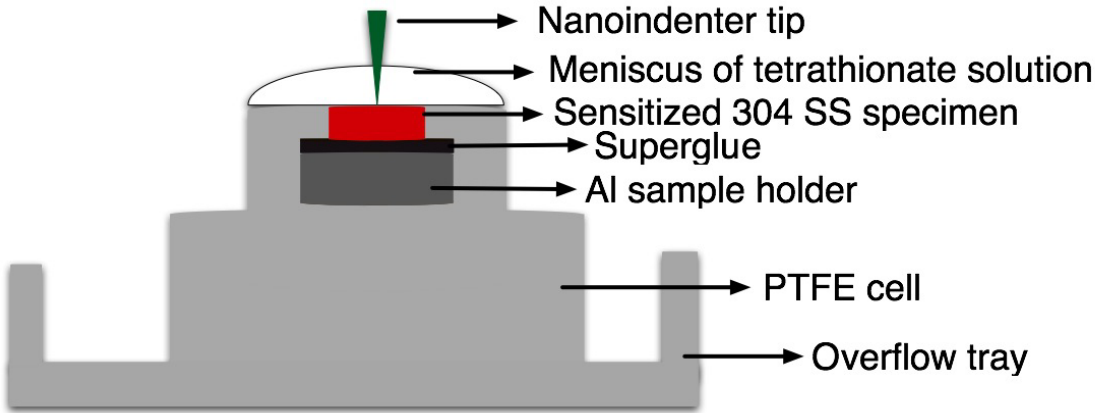

Figure 4.14 Schematic of the setup used for the initial in-situ method with no voltage applied.

4.6.1.2 Results

The data given in terms of the displacement vs. time are presented in **Figure 4.15**. There is no change in the displacement during the test, for any of the three different loads that were used. Since the displacement remains constant for the duration of the test, there is no indication of crack growth. This was also shown by SEM observations after the test. A micrograph of the same cantilever presented in **Figure 4.15** after the test is shown in **Figure 4.16**. In addition, the stiffness data were analysed for the tested cantilever and are plotted against the holding time in **Figure 4.17**. ABAQUS software was used to determine the relationship between the stiffness of a cantilever tested in the experimental conditions presented above and the crack length in a cantilever of similar dimensions. The results are presented in **Figure 4.43** and the model is described in more detail in **Section 4.7.2**. It can be observed from **Figure 4.43** that, for a cantilever of this size, a value in absolute stiffness of less than 1300 N/m would be an indication of crack growth. For the results presented in **Figure 4.17**, even the lowest values of the stiffness observed do not correspond to any crack growth.

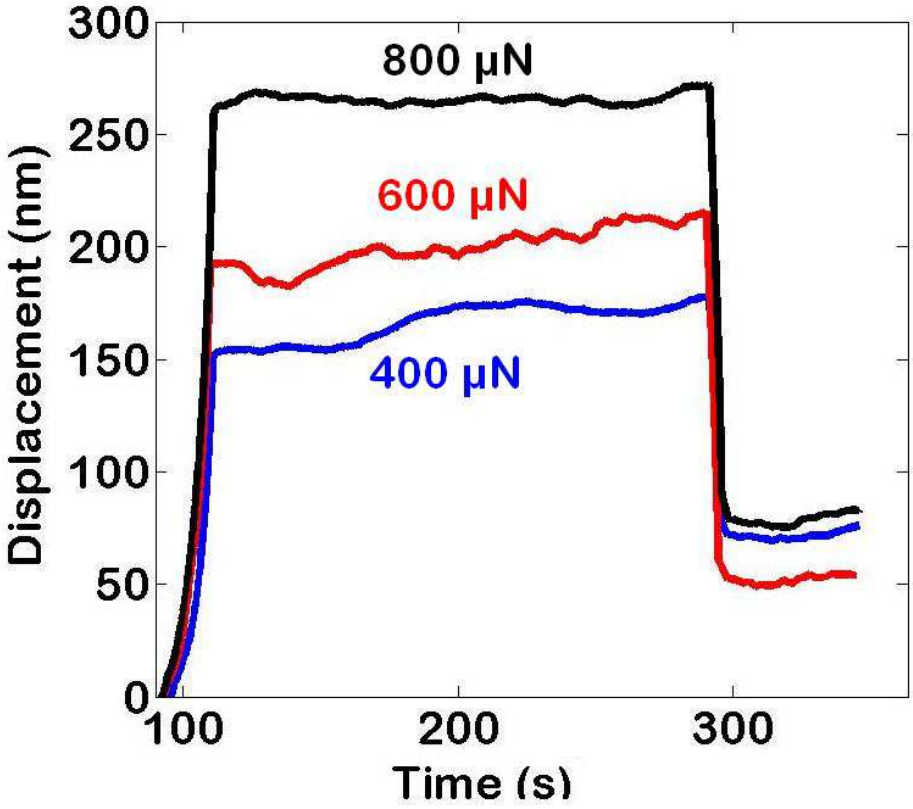

Figure 4.15 Displacement vs. time data for one of the cantilevers tested using the in-situ method with no voltage applied.

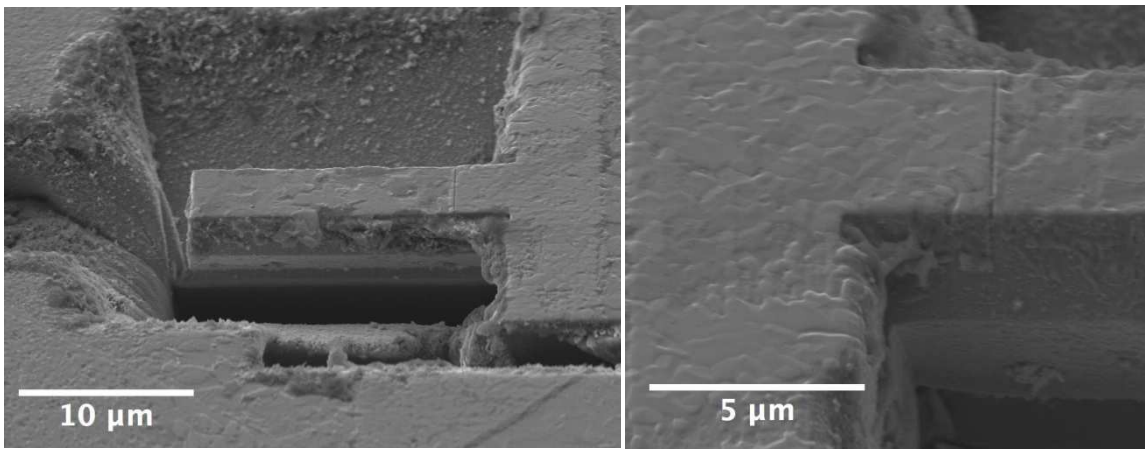

Figure 4.16 Micrograph of a pre-notched 304 SS cantilever after the in-situ test using the method with no voltage applied. No crack growth can be observed.

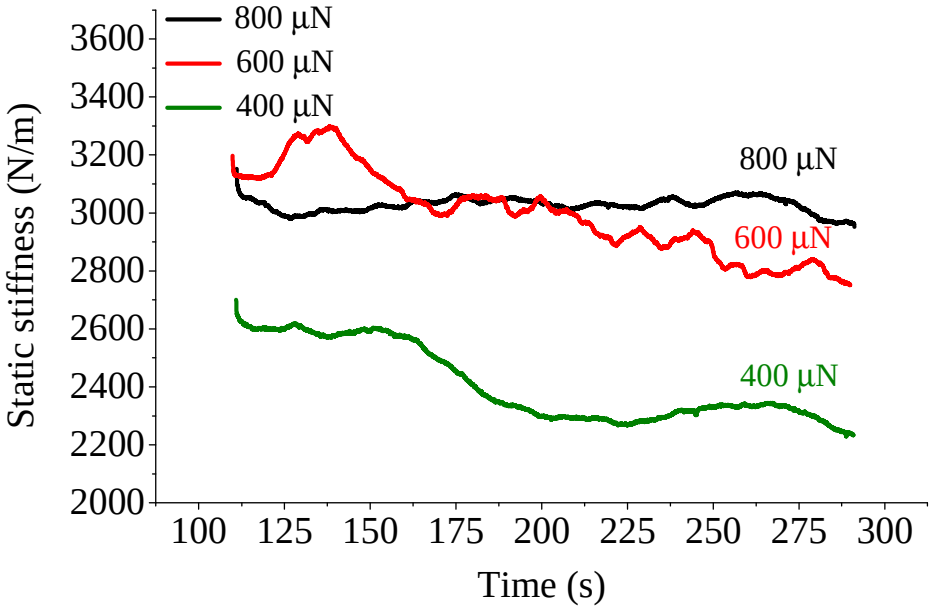

Figure 4.17 Compliance data for one cantilever tested at three different maximum loads against the hold time. The static stiffness values are too high to correspond to a stiffness that will indicate crack growth.

The conditions of the test chosen for this particular method proved to be unsuccessful in producing or measuring any crack growth. This could be due to a variety of factors:

1) the time of the experiment might have been too short;
2) the environment might have been not aggressive enough to initiate a crack during the limited amount of time;
3) the notch that was produced using the FIB might have been not deep enough to start a crack;
4) possibly the grain boundary tested was either not susceptible to IGSCC or it was not sensitized enough.

In successive experiments, these parameters (1-4) were varied in order to attempt to produce crack initiation and growth.

4.6.2 Short *in-situ* method with platinum as the counter electrode

4.6.2.1 Test conditions and method

Three different parameters (2, 3 and 4) mentioned above were varied such that: the pH of the solution was changed from 2.6 to 1.8, the notch was produced by anodically etching the sample in 10% oxalic acid for 60 s at 9 V and the grain boundaries were checked to see whether they were susceptible to intergranular corrosion or not.

The change in the pH of the solution was expected to accelerate the corrosion process by making the environment more aggressive. The etch with oxalic acid not only produced a natural notch at the grain boundary, but it was also indicative of which grain boundaries are susceptible to IGSCC. Some grains etch faster than the others, so some of the grain boundaries had a very deep notch and were unsuitable for cantilever production. Before cantilevers were milled, the depth of the IGSCC attack given by the etch with oxalic acid was checked to ensure that the natural notch was no deeper than a few hundred nm. This was done by milling a trench with the FIB, perpendicular to the grain boundary and by measuring the depth of the notch.

Aluminium in contact with the aggressive liquid has been observed to have the effect of stopping a crack from propagating in austenitic steel while platinum has the opposite effect, accelerating the intergranular corrosion process when used as a counter-electrode [14]. For this reason, the aluminium stub was replaced with an unsensitised 304 SS stub and a platinum wire was used as a counter-electrode. The platinum was introduced in the PTFE cell, in the solution, very close to the area where the cantilevers were milled. The schematic of the setup that was used to test cantilevers *in-situ* is presented in **Figure 4.18**. During the test, the cantilever was loaded to 800 μN, the load was held at the maximum load for 600 s and then the cantilever was unloaded.

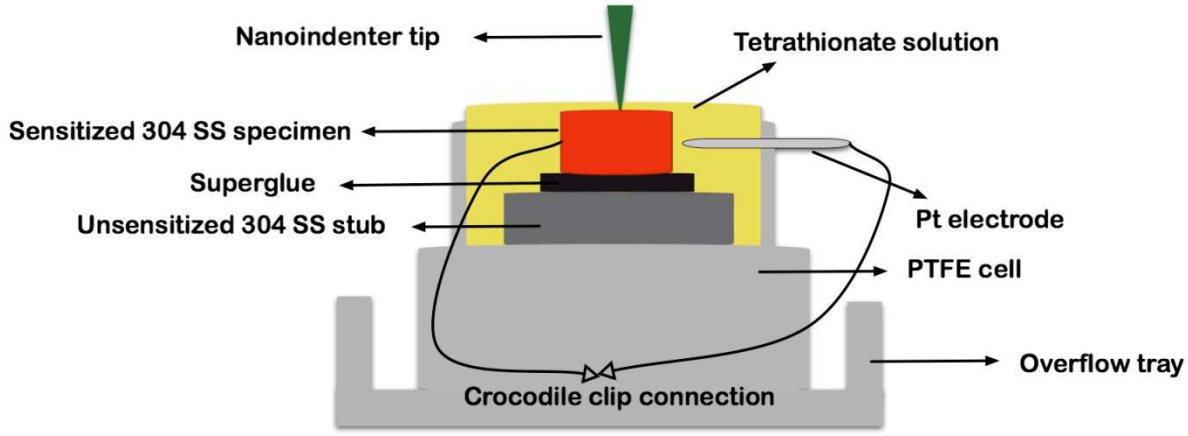

Figure 4.18 Schematic of the setup used for the short (600 s) in-situ method with platinum as a counter-electrode.

4.6.2.2 Results

The data for one of the tested cantilevers are shown in **Figure 4.19** and **Figure 4.20**. The connection between the platinum electrode and the sample was switched on and off during the test, as follows: on at 345 s, off at 441 s, back on at 532 s and off at the end of the test. The experiment was set up so the load was to be kept constant (this was pre-set in the nanoindenter method that was written to use the nanoindenter under load control), and the data shown in **Figure 4.19** indicate that the load was in practice held constant at 800 μN until the connection was turned on. Shortly after that, the load dropped slightly and then it considerably increased to a value of 2300 μN. When the connection was turned off, the load dropped to a value of approximately 1100 μN and increases again up to a value of 1300 μN when the connection is on again until the end of the test. From the graph of the load vs. time there is no indication of crack growth since the load does not decrease appreciably from the maximum value of 800 μN.

Graphs showing the harmonic constant stiffness vs. time data are shown in **Figure 4.21** and **Figure 4.22**. Before the connection was turned on, the harmonic constant stiffness was constant at a value of approximately 2200 N/m. After the connection was turned on, the harmonic constant stiffness oscillated between a minimum value of -570 N/m

and a maximum value of 6900 N/m. After the connection was turned off, the harmonic constant stiffness increased until it reached the initial value of approximately 2200 N/m. Towards the end of the test when the connection was turned on again, the harmonic constant stiffness decreased and then increased considerably to a value of 120000 N/m. The value of the harmonic constant stiffness is around the value that is characteristic to cantilevers of this size, apart from the extreme value at the end of the test that might be due to the indenter hitting the trench or the cantilever hitting the bottom of the trench. From the harmonic constant stiffness data for this particular cantilever it is difficult to determine whether there was crack growth.

Two micrographs of the tested cantilever after the test are shown in **Figure 4.23**. There are some “flower” like crystal structures that initiated on different areas of the specimen, both on the surface of the sample and around the cantilever. One of the crystals seems to initiate from the grain boundary. **Figure 4.23** shows a cross section of the cantilever exposing the grain boundary. It is difficult to determine whether any crack was initiated but it can be observed that the notch opened, allowing the crystal structures to grow inside.

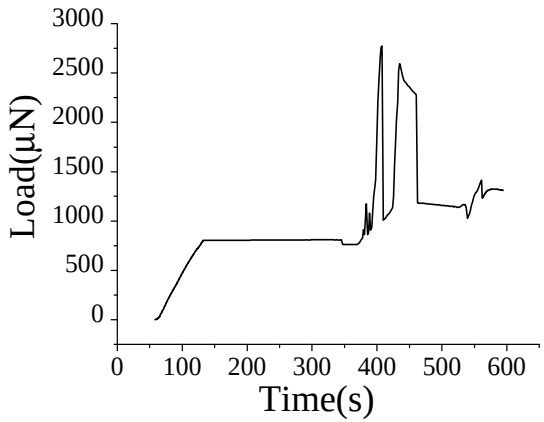

Figure 4.19 Load vs. time data for one of the tested cantilevers using the short *in-situ* method with platinum as a counter electrode.

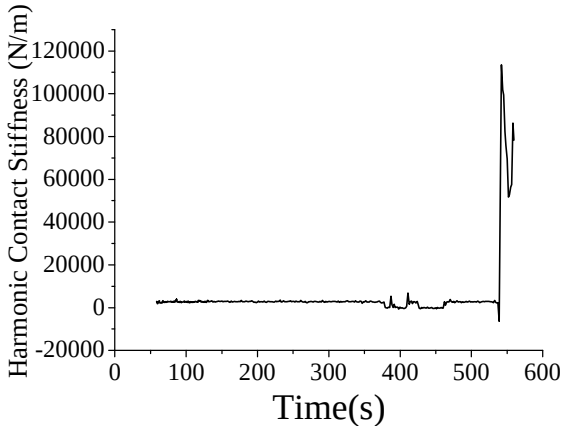

Figure 4.21 HCS vs. time data for one of the cantilevers tested using the short *in-situ* method with platinum as a counter electrode.

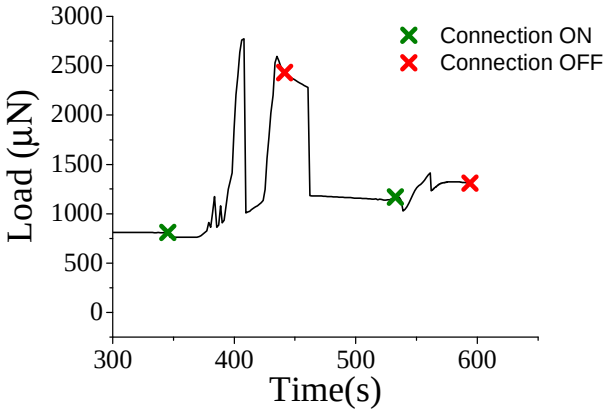

Figure 4.20 Detail of Figure 4.19 showing data from the time when the connection between the counter electrode and the sample was on.

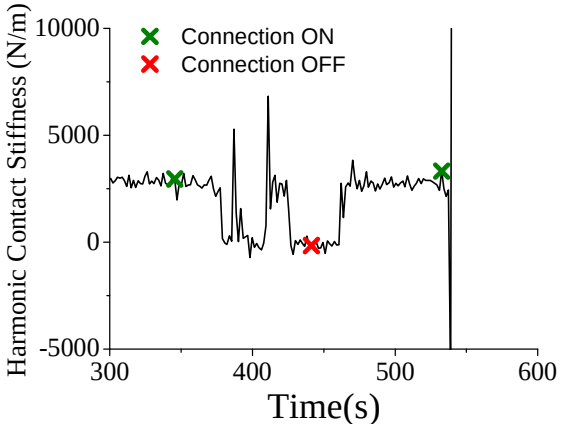

Figure 4.22 Detail of Figure 4.21 showing data from the time when the connection between the counter electrode and the sample was on.

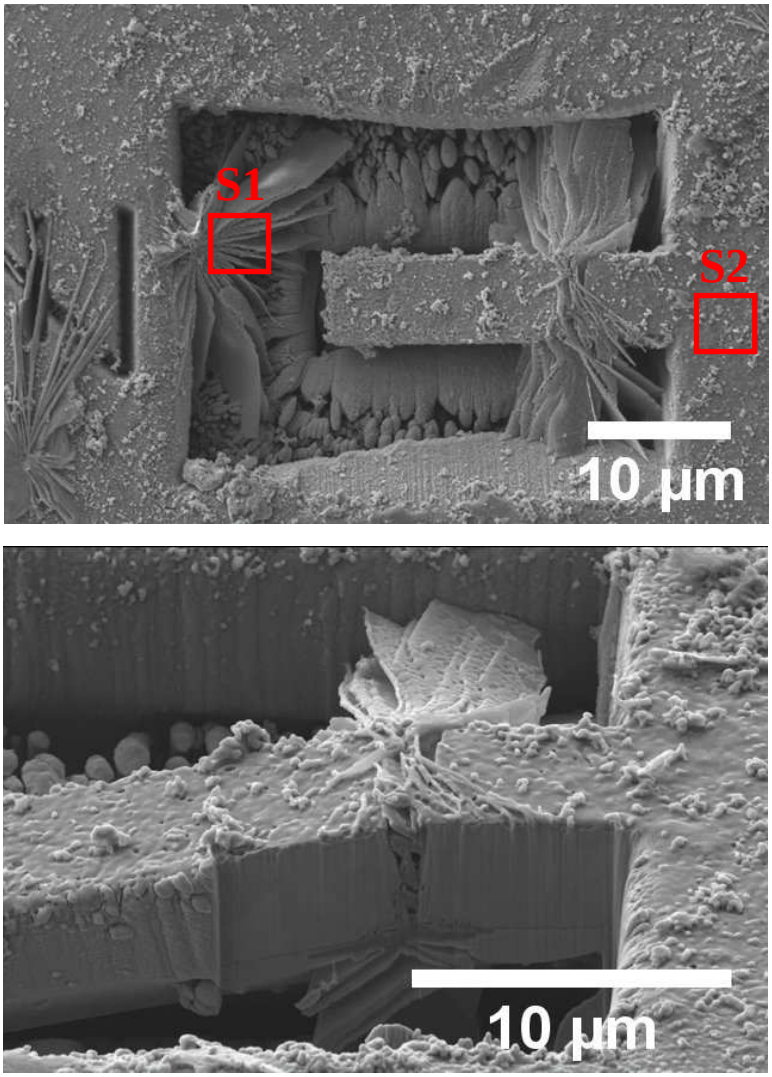

Figure 4.23 Micrograph showing cantilever after test, using the in-situ method with platinum as a counter electrode. The red rectangles marked as S1 and S2 indicate the areas from where the EDX spectra were collected to determine the nature of the "flowers" present after the test.

These "flower" like structures were not observed in any of the previous experiments by Rogers or Herbert. In addition, the surface of the sample seems to have been covered with smaller particles that had not been present before testing. To better understand what happened during the test, energy-dispersive X-ray spectroscopy (EDX) of the crystal structures was performed. Two different areas of the sample were analysed,

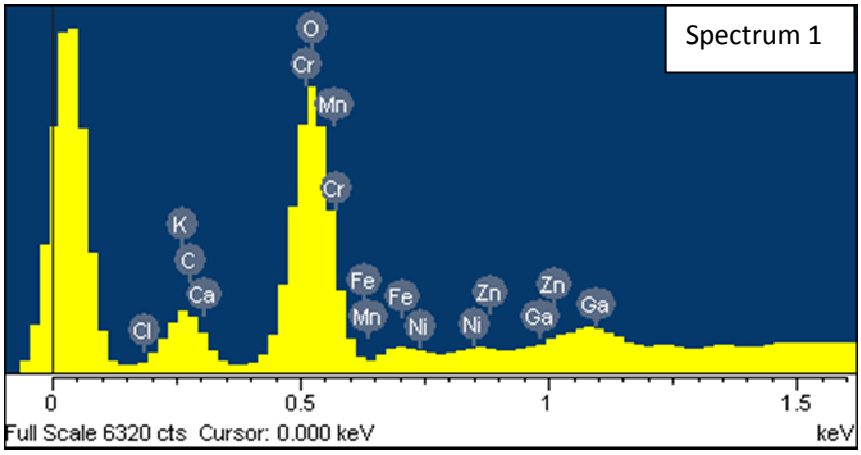

Figure 4.24 EDX spectrum identifying the elements that are present in the "flower" like structures.

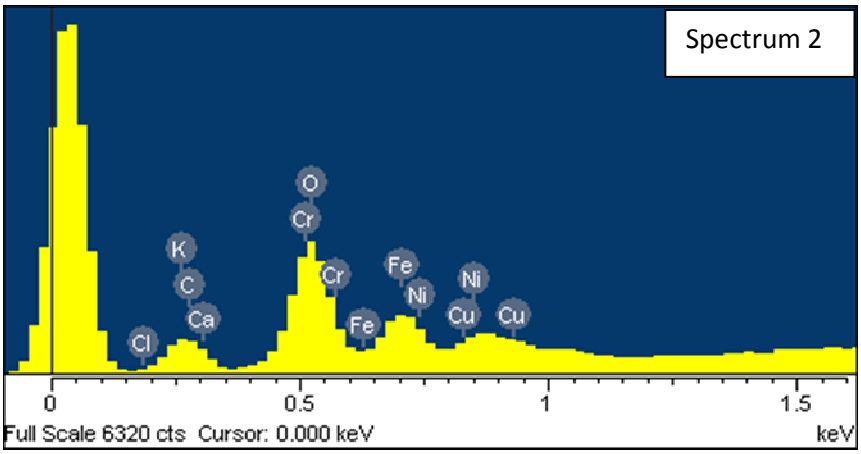

Figure 4.25 EDX spectrum identifying the elements that are present in small particles that are present on the surface of the specimen.

marked as S1 and S2 in **Figure 4.23**. The spectrum that corresponds to area S1 is shown in **Figure 4.24** and the spectrum that corresponds to area S2 is shown in **Figure 4.25**.

In S1 some of the elements that are in the composition of 304 SS were identified: C, Cr, Mn, Fe and Ni. In addition, a Ga peak is present, due to the Ga deposition when using the FIB for cantilever milling. Since K and O are also present, the "flower" like structures are most likely a K compound (e.g. KCl or KOH) that is formed as a result of using the acid solution of potassium tetrathionate. The only elements that were not expected are Zn, Cl and Ca. Zn must have been incorrectly identified by the software.

However, the other elements: Cl and Ca were most probably present in the distilled water that was used to prepare the potassium tetrathionate solution which happened not to be pure from that particular batch. This was due probably because the batch of the distilled water used was contaminated. In S2, the same elements as in S1 were identified except Zn and Ga, excluding the elements that are in the composition of 304 SS.

The use of the platinum electrode in this test did not prove to accelerate the crack growth, possibly because the time of the test was too short. In order to overcome this, the time of the test was increased and the results are presented in the next section.

4.6.3 Long in situ method with Pt as the counter electrode

4.6.3.1 Tests conditions and method

During this method, only one parameter was changed while all the other conditions remained the same as **Section 4.6.2**. The time of the test (1) was increased to allow more time for the crack initiation. As in the previous method, the sample was etched using oxalic acid and the solution used was the same, with a pH of 1.8. The grain boundary that was selected for cantilever manufacturing was susceptible to IGSCC (since oxalic acid attacked it) and pre-notched during the etching procedure. An image of the cantilever before the test is presented in **Figure 4.26**. The setup used was the same as in the previous method, illustrated in **Figure 4.18** except that the sample was all covered in lacquer except the area where the cantilevers were milled.

This way, the exposed surface area of the 304 SS sample was reduced so that it could be smaller than the area of the platinum counter electrode, in order for the local effect of the reaction to increase.

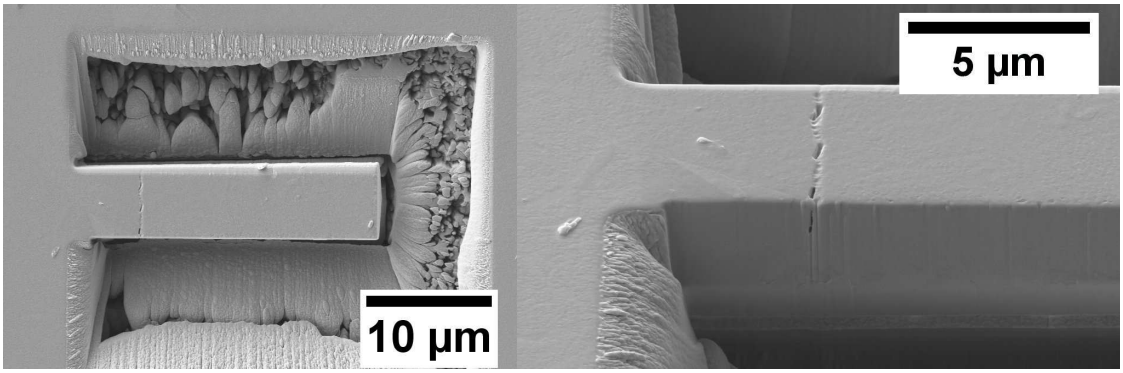

Figure 4.26 Micrograph of a cantilever milled in 304 SS before the test. The grain boundary is etched using oxalic acid.

During the test, the cantilever was loaded to 500 µN and the load was held at the maximum load for a much longer time (2000 s) than in **Section 4.6.2**. The long hold time was intended to give enough time for the crack initiation to occur. The connection between the platinum counter electrode and the sample was on at the beginning of the test.

4.6.3.2 Results

The data for one of the tested cantilevers are shown in **Figure 4.27** and **Figure 4.28**. The load remains constant around the value of 500 µN with a slight tendency to increase. Even though the time of the test was increased, from the data of the load vs. time there is again no indication of crack growth.

The graph showing the harmonic constant stiffness vs. time data is presented in **Figure 4.28**. The harmonic constant stiffness oscillates around the value of 2400 N/m with a slight tendency to decrease to a final value of 2300 N/m. The value of the harmonic constant stiffness is in the correct range for a cantilever of this size, however if compared to the ABAQUS model that will be presented in **Section 4.7.2** this very small level of decrease during the test is not an indication of crack growth. Two

different cantilevers were tested during this method and both of them showed the same results.

A micrograph showing the cantilever after the test is presented in **Figure 4.29** and **Figure 4.30**. A similar crystalline structure to the one shown in **Figure 4.23** has grown on the cantilever from one side to the other. It is difficult to see whether the structure has grown underneath the cantilever or not.

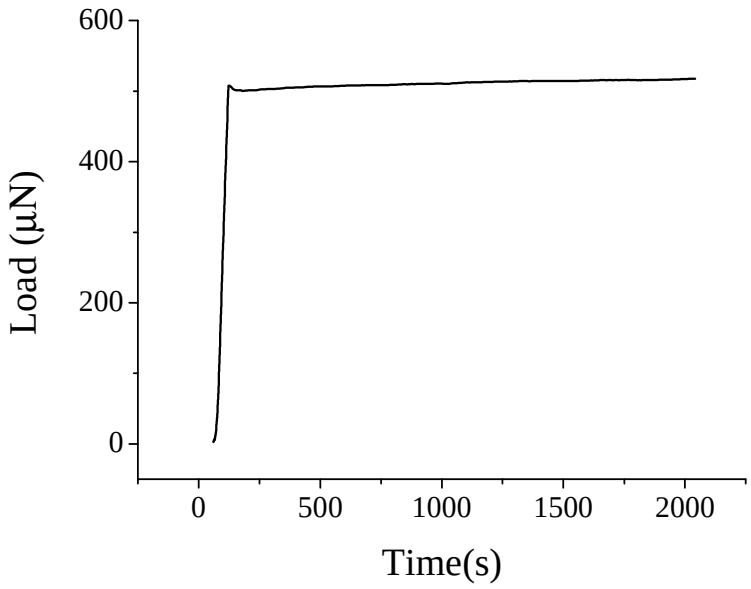

Figure 4.27 Load vs. time data for one of the cantilevers tested using the long in-situ method with platinum as a counter electrode.

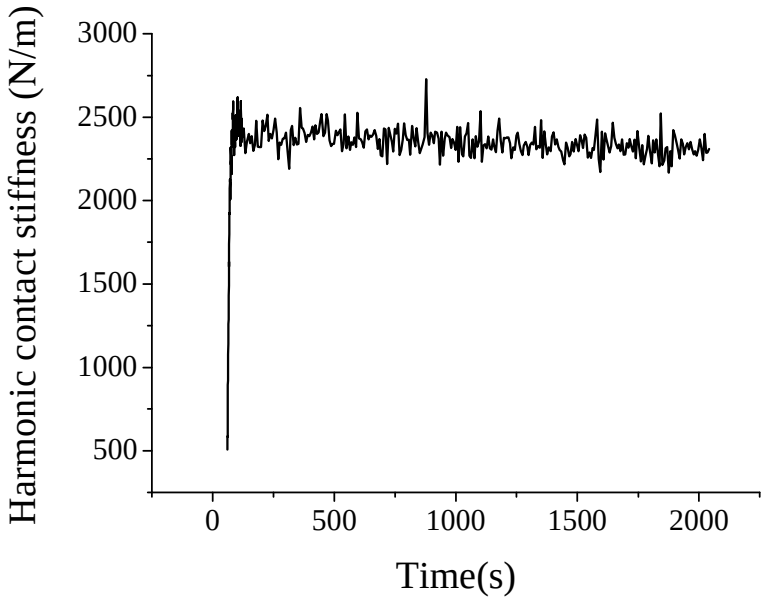

Figure 4.28 Harmonic contact stiffness vs. time data for one of the cantilevers tested using the long in-situ method with platinum as a counter electrode.

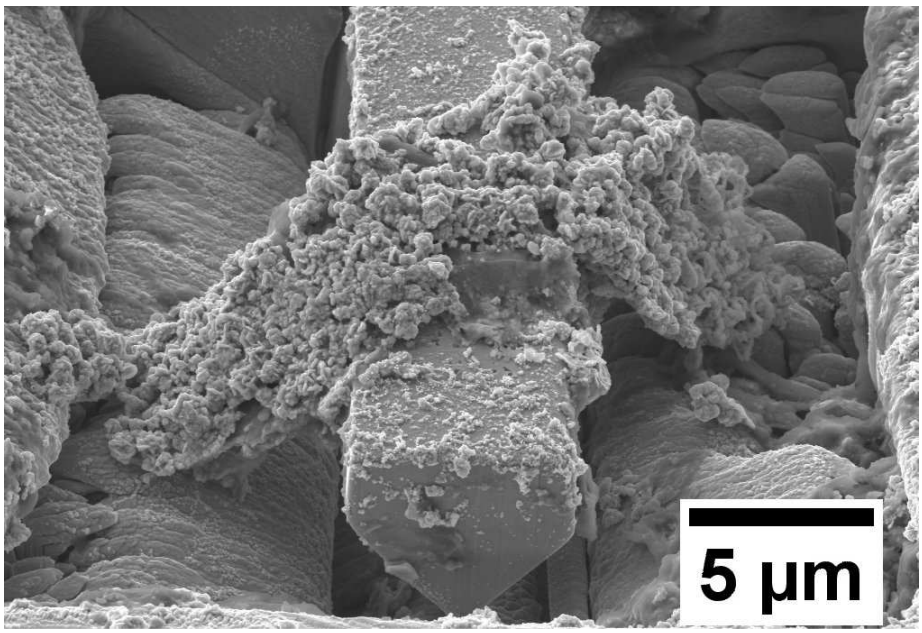

Figure 4.29 Micrograph showing a cantilever after the test using the long in-situ method with platinum as a counter electrode. A crystalline structure has grown over the cantilever.

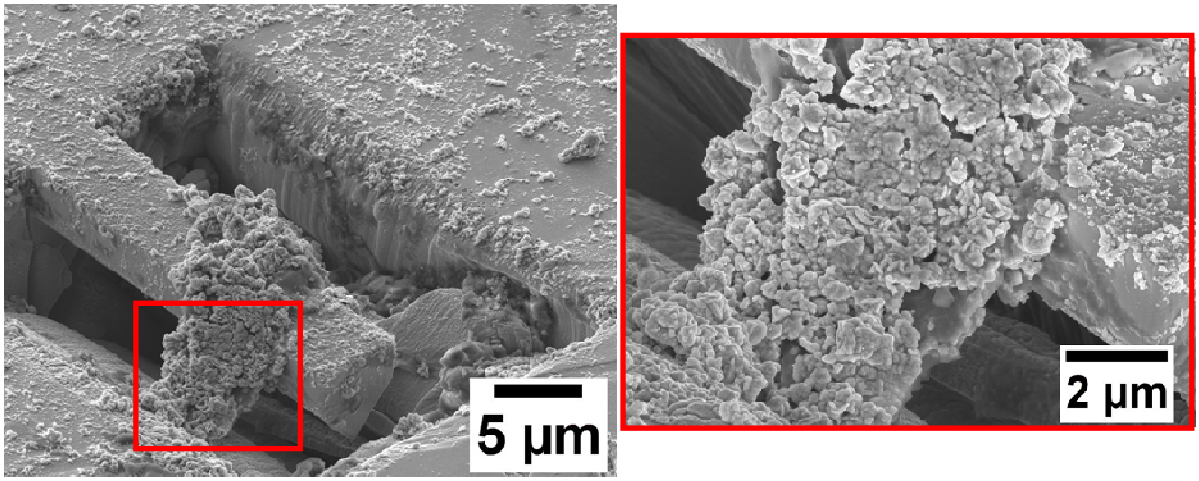

Figure 4.30 Micrograph showing the same cantilever as in Figure 4.29, after the test using the long in-situ method with platinum as a counter electrode. A crystalline structure has grown over the cantilever.

At a closer look, the structure seems to be different from the "flower" like crystals observed previously in **Figure 4.23** and analysed through the spectrum presented in **Figure 4.24**, but looks like a conglomeration of smaller particles that cover the surface, similar to the ones observed previously in **Figure 4.23** and analysed through the spectrum presented in **Figure 4.25** No EDX could be performed on this particular cantilever because the area of the specimen was charging.

4.6.4 In situ method with voltage applied (battery – 6 V) with 304 unsensitized SS as the counter-electrode

4.6.4.1 Test conditions and method

Since using platinum as a counter electrode was not successful to start crack initiation, the setup was modified again to implement a more aggressive method and environment. The sample was prepared as before, etched in oxalic acid, and then cantilevers were milled at grain boundaries that were susceptible to IGSCC., The solution used was the same as the one in the previous method, with a much lower pH of 1.1 and a battery was used that was coupled to the sample and the 304 SS stub, to place the test material into

the “corrosion” regime. The schematic of the setup that was used to test cantilevers *in-situ* is presented in **Figure 4.31**. The sensitized 304 SS specimen was glued to an unsensitised 304 SS stub using superglue and together were placed in the PTFE cell. The sensitized 304 SS sample was connected to a copper wire that was soldered onto the sample. The connection was covered using lacquer to isolate it so it would not interfere with the chemical environment. During this test, the unsensitised 304 SS stub was used as an electrode to accelerate the corrosion process. During the test, the sample surface was covered with a meniscus of tetrathionate solution, while the sample and the stub were connected to the battery to provide an anodic current to the 304 SS sample. The voltage used for this test was 6 V (voltage of the battery used) and it was applied at the beginning of the region when the load was kept constant. During the test, the cantilever was tested at different loads, up to 800 μN, the load was held at the maximum load for 180 s and then the cantilever was unloaded.

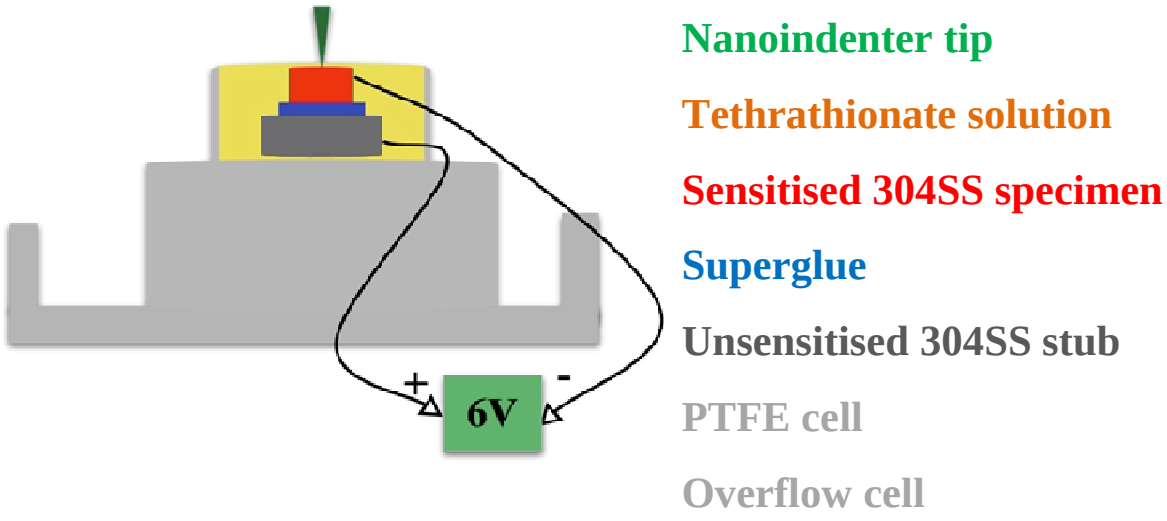

Figure 4.31 Schematic of the setup used for in situ method with voltage applied.

4.6.4.2 Results

Figure 4.32 presents the displacement vs. time data for one of the tested cantilevers. The cantilever was first loaded to 400 μN, then to 500 μN and lastly to 800 μN. The displacement remained constant for the first two tests, when the maximum loads were 400 and 500 μN respectively. However, for the last run there was a jump in displacement of approximately 2.5 μm, 20 s after the voltage was applied. Such a jump in displacement might be associated with the fracture of the cantilever. **Figure 4.33** presents the nanoindenter scans of the cantilever before the test, and after each run. In **Figure 4.33a** the cantilever was intact before the test, as can be also observed in **Figure 4.33b a**nd **Figure 4.33c**. However, after the last run, the scan of the cantilever presented in **Figure 4.33d** indicates that the cantilever had fractured close to the fixed end.

A micrograph of the cantilever at the end of the test is shown in **Figure 4.34**. The cantilever had fractured all the way through at the grain boundary. As is indicated by the nanoindenter scans, the displacement data and the micrograph, the conditions of the method proved to be successful to obtain IGSCC, though at a rather rapid rate.

To verify the method of using the harmonic contact stiffness to measure the crack growth rate and to identify crack propagation, the harmonic constant stiffness, displacement and load against time are shown in **Figure 4.35**. It can be observed that when the displacement jumps, shortly after the current is applied, the load decreases and the harmonic contact stiffness decreases as well.

The same procedure was applied for another cantilever, and a micrograph at the end of the test is shown in **Figure 4.36**. This cantilever also fractured at the grain boundary, but it did not fail all the way across the cantilever, most likely because it hit the bottom

of the trench. The plot of the displacement, harmonic contact stiffness and load vs. time are shown in **Figure 4.37**. The same features as in **Figure 4.35** (an increase in displacement and a decrease in both the load and harmonic contact stiffness) could be observed. The displacement increases shortly after the current is applied and the load decreases, during the same time interval. The harmonic contact stiffness decreases as well after it increases slightly.

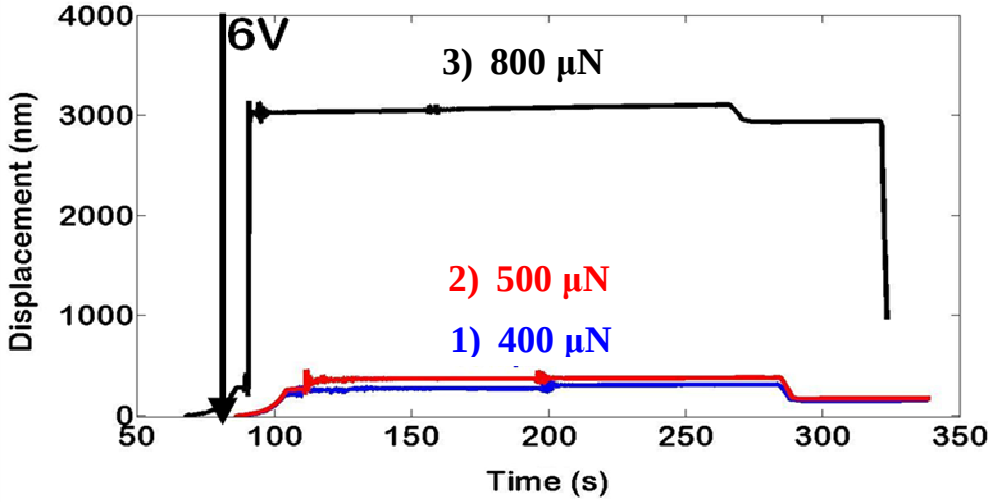

Figure 4.32 Displacement vs. time data for one of the tested cantilevers stressed at different loads using the in-situ method with voltage applied. A change in displacement that might be associated with crack growth can be observed for the run when the cantilever was loaded to 800 µN.

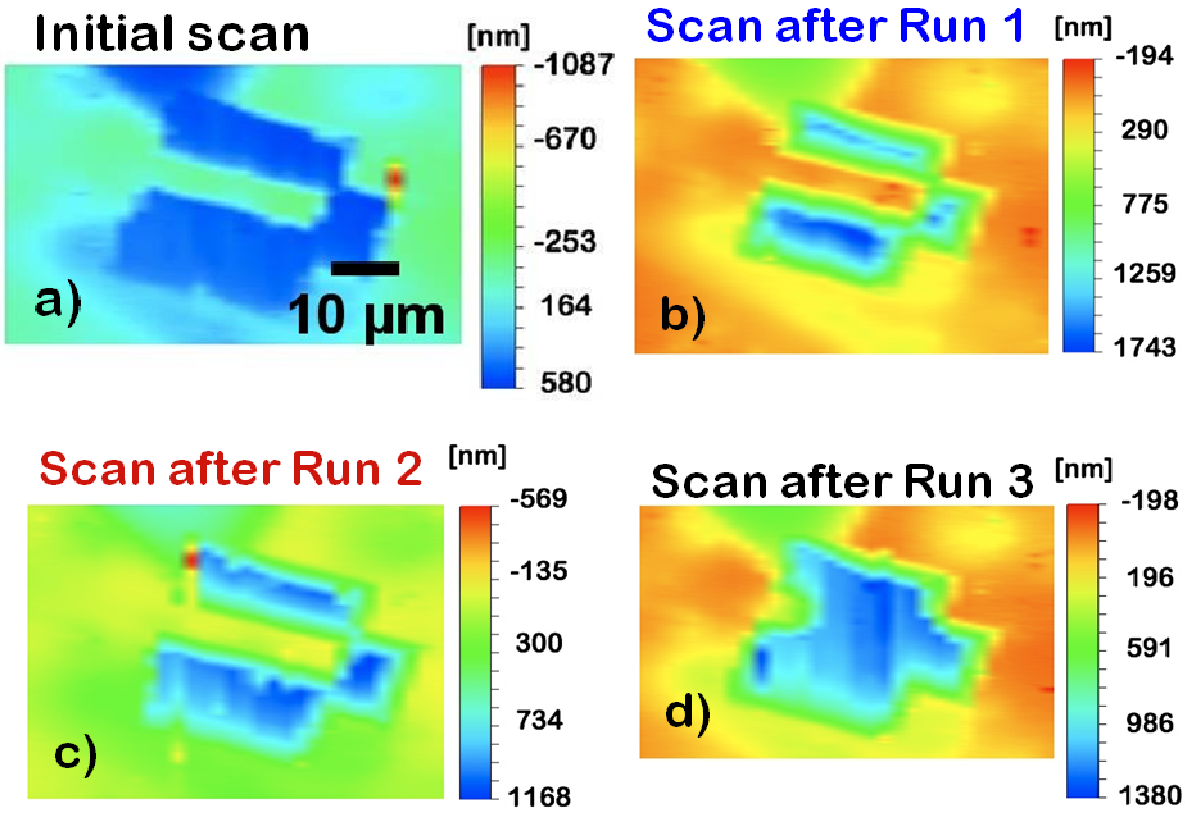

Figure 4.33 Scans of a tested cantilever using the in situ method with voltage applied: a) initial scan, b) scan after run 1 (400 µN), c) scan after run 2 (500 µN) and d) scan after run 3 (800 µN). The cantilever fractured after the last run.

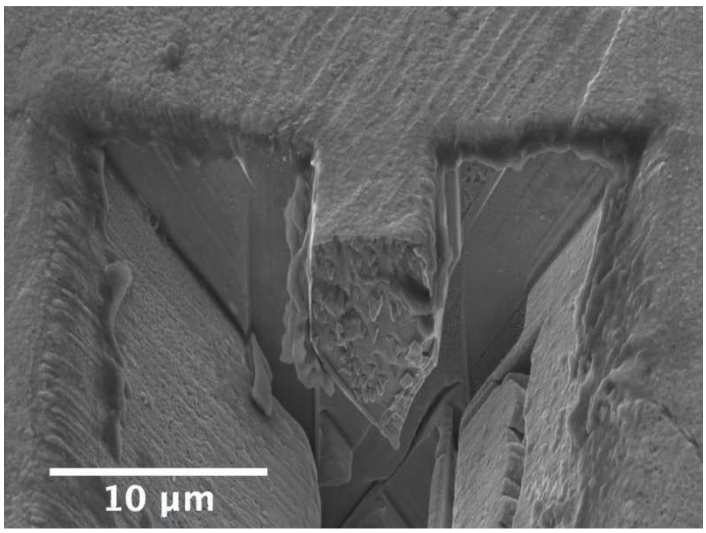

Figure 4.34 First cantilever tested using the in-situ method with voltage applied, showing fracture of the cantilever, at the end of the test.

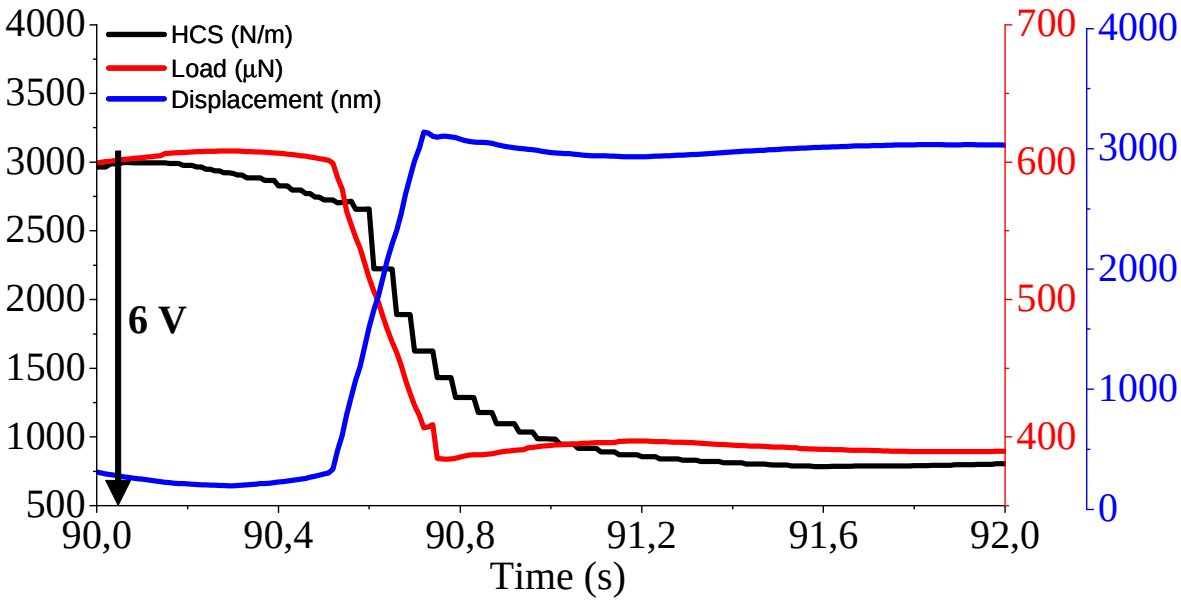

Figure 4.35 Displacement, harmonic contact stiffness and load vs. time for the first cantilever fractured using the *in-situ* method with the voltage applied. Crack propagation region is picked up by an increase in displacement, and a decrease in both the load and the harmonic contact stiffness.

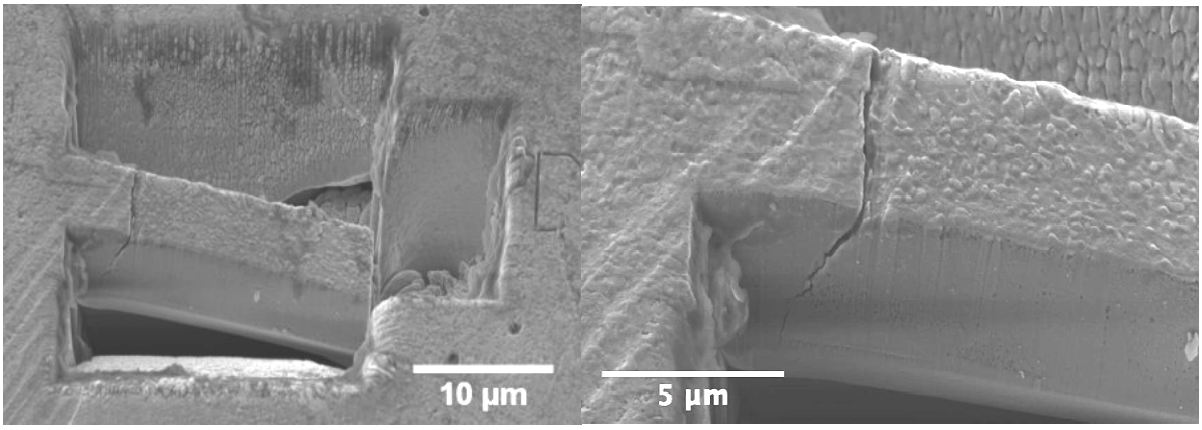

Figure 4.36 Second cantilever tested using the in-situ method with voltage applied showing fracture of the cantilever, at the end of the test.

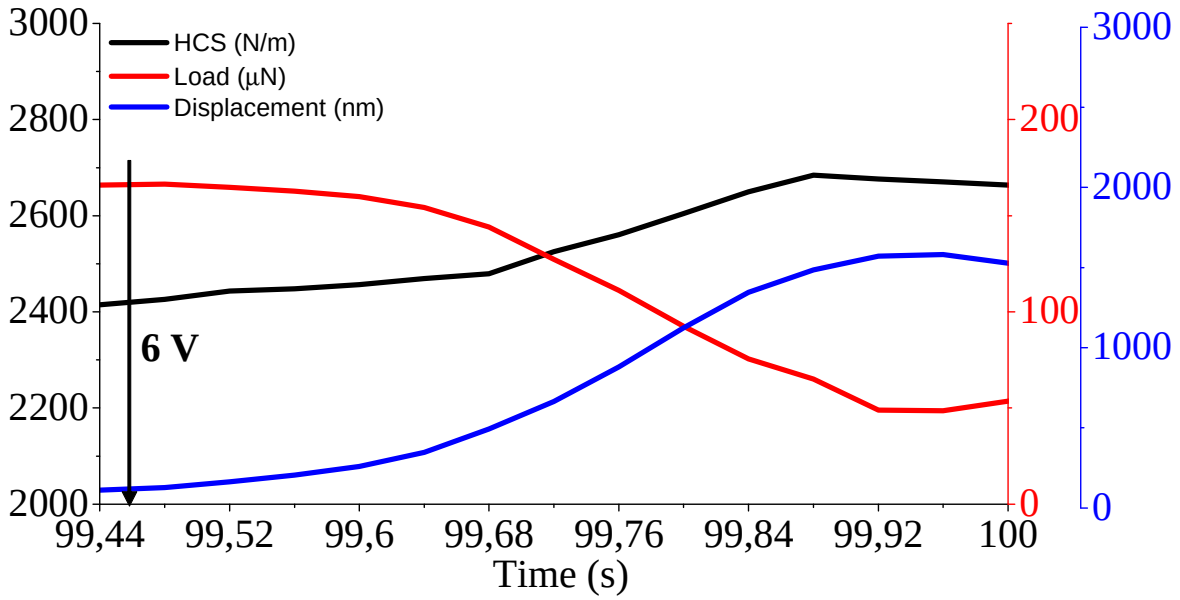

Figure 4.37 Displacement, harmonic contact stiffness and load vs. time for second cantilever tested using the in-situ method with the voltage applied. Crack propagation region is picked up by an increase in displacement, and a decrease in the load.

4.7 Measurement of crack growth rate using micro-cantilevers in 304 SS

4.7.1 The use of static stiffness versus harmonic contact stiffness to measure crack growth rate

In order to determine if the static stiffness measurements could be used instead of the harmonic contact stiffness, the Young's Modulus was calculated for six cantilevers that were used in this study. This was done by fitting a line to the elastic region of the stress vs. strain data. An example is illustrated in **Figure 4.38** and **Figure 4.39.**

The graph of calculated values for Young's Modulus is shown in **Figure 4.40**. The obtained values are around the value of 200 GPa (the Young's Modulus for 304 SS).

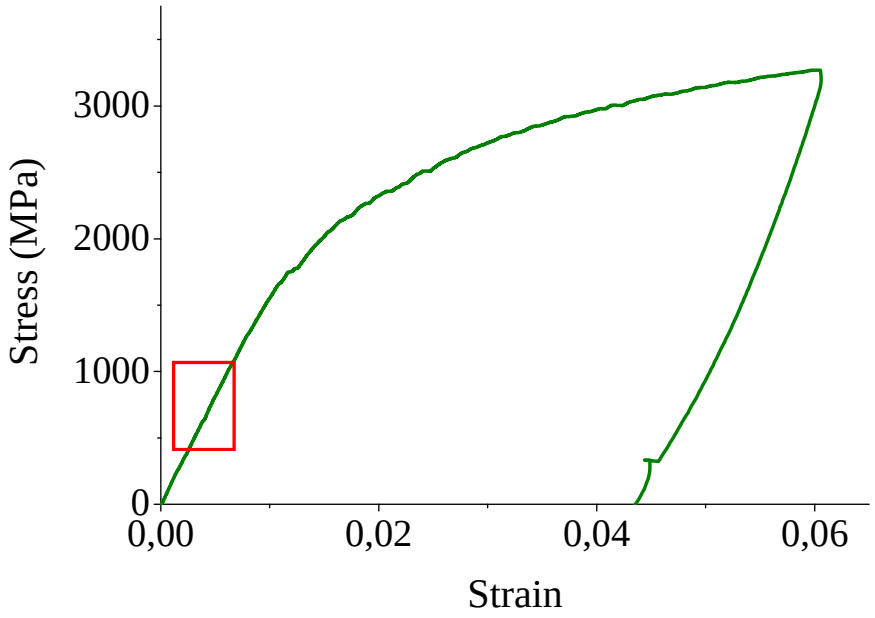

Figure 4.38 Example of stress vs. strain curve from which the value for Young's Modulus was extracted using the static stiffness. The red rectangle indicates the region of the data used.

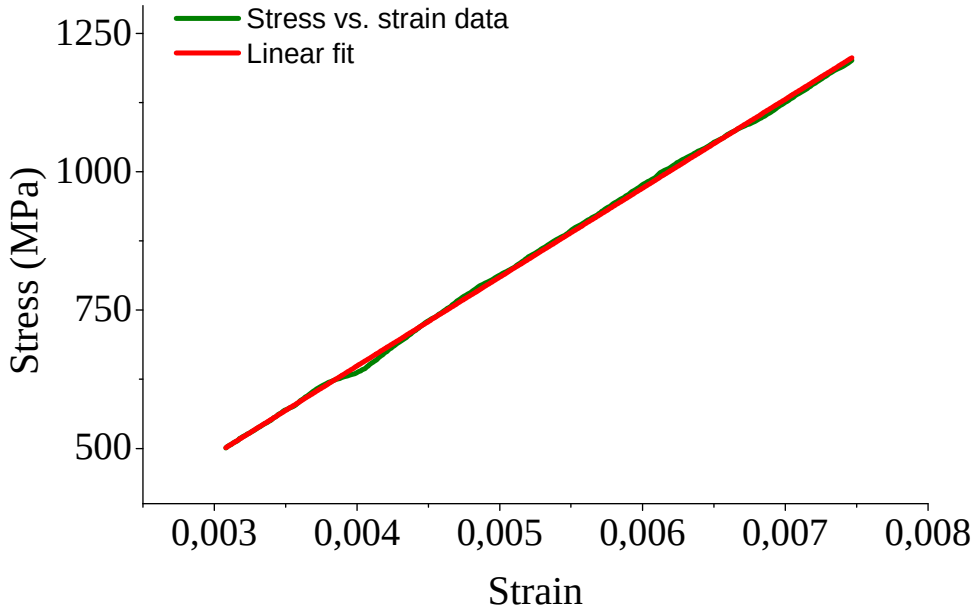

Figure 4.39 Region of data from the stress vs. strain that was used to calculate the value of the Young's Modulus for one of the cantilevers in 304 SS. The Young's Modulus was obtained using a linear fit to the stress vs. strain data from the elastic region.

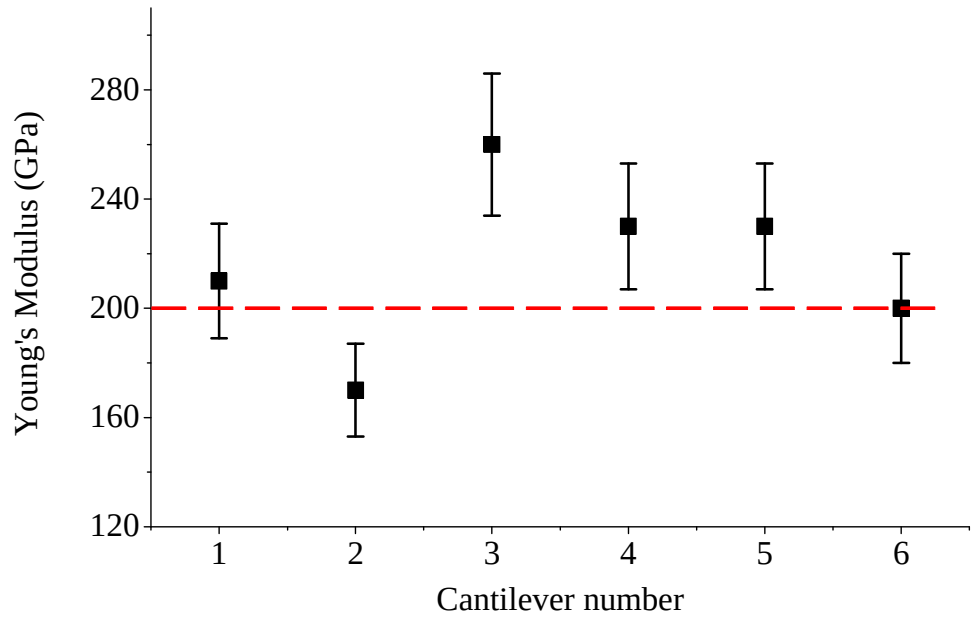

Figure 4.40 Young's Modulus value calculated for six cantilevers using the static stiffness in 304 SS. The red dotted line corresponds to the value of 200 GPa which is known to be the correct value for 304 SS.

It can be observed from **Figure 4.40** that the static stiffness gives moderately accurate results for measuring the Young's Modulus in 304 SS by converting the load vs. displacement data from the nanoindenter to stress vs. strain curve.

To determine how well the HCS from the tests could be used to measure modulus, the average HCS for the same cantilevers was calculated and plotted against the static stiffness. The results are shown in **Figure 4.41.**

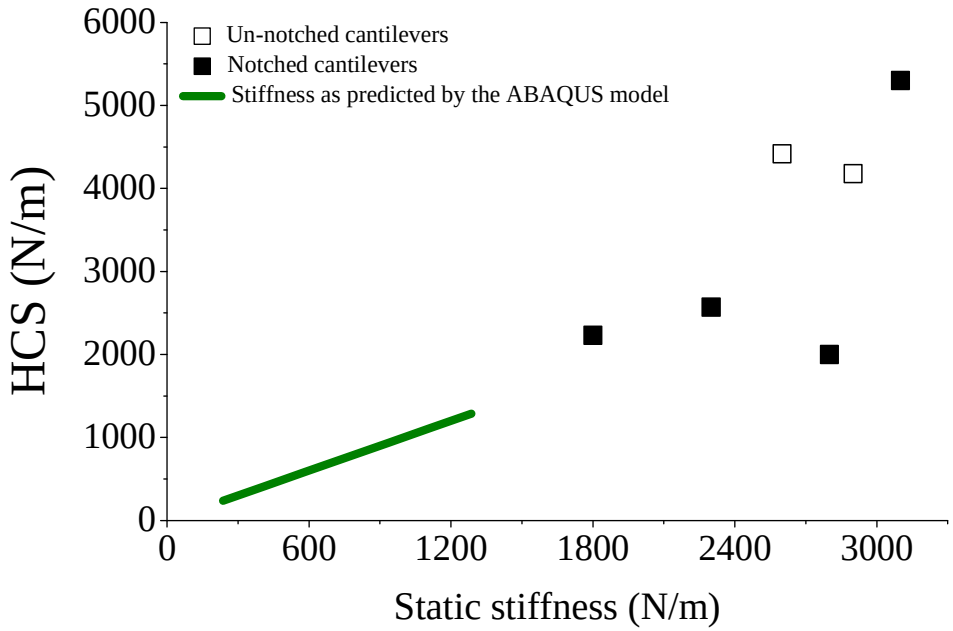

Figure 4.41 Plot of HCS vs. static stiffness calculated for six different cantilevers in 304 SS. The cantilevers were both etched and un-notched such that the empty ones were un-notched and the full ones are the notched cantilevers. It can be observed that the HCS does not go to 0 which means that the use of HCS for measuring crack depth would not be accurate.

From **Figure 4.41** it can be observed that the values for HCS are much higher than the static stiffness and there is also a higher spread in the values obtained. From this graph no relationship between the static stiffness and HCS can be obtained. Since the static stiffness proved before to give good results in the measurement of the Young's Modulus, the static stiffness was used further to determine the crack growth rate for the two fractured cantilevers presented in **Section 4.6.4**.

4.7.2 ABAQUS model to determine the relationship between the stiffness of a cantilever and the crack length

To better determine a relationship between the stiffness and the crack length, an ABAQUS model was implemented. The mesh geometry was of a cantilever with the same dimensions as the ones tested and boundary conditions were set (model was clamped (encastre) at the base) such that the model could replicate exactly the conditions used when a cantilever is tested by a nanoindenter. The properties used by the model were the typical 304 SS ones: 200GPa for Young's modulus and 0.30 for Poisson's ratio. The model used reduced integration with 8-node hexahedral (brick) element (C3D20R) and it had 42138 nodes and 38200 elements. Since only the compliance was to be extracted from the model and the model was purely elastic, crack propagation was simulated by manual node release, so there was not a criterion needed to simulate crack propagation. The mesh size used was 0.5 cubed units in order for the computing time to be short. The stiffness predicted from ABAQUS model for one of the tested cantilevers was 1672 N/m and the static stiffness measured from the nanoindenter for a cantilever of the same size was 1617 N/m. The values are in good agreement which proves the validity of the model.

The results obtained from ABAQUS software after modelling a cantilever with a notch size of approximately 3 μm depth is shown in **Figure 4.42.**

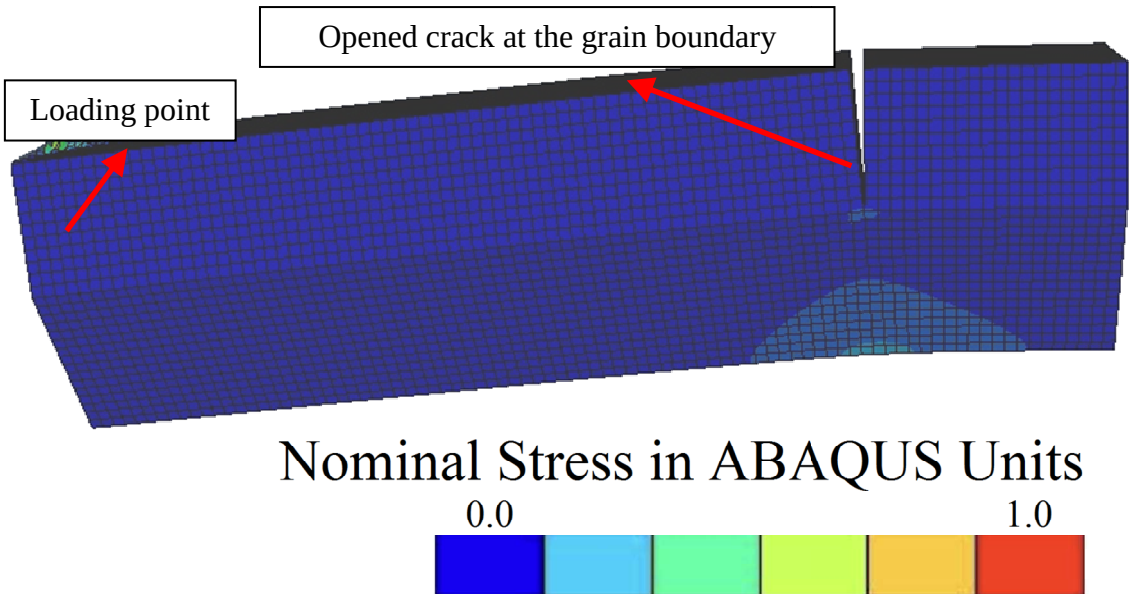

Figure 4.42 Result from ABAQUS model showing a cantilever with a notch size of approximately 3 µm depth, after loading. The crack opened at the grain boundary.

To determine the relationship between the stiffness and the crack length, the model was used to calculate the stiffness for six different notch sizes (between 0.3 µm and 4.5 µm). The results are presented in **Figure 4.43**

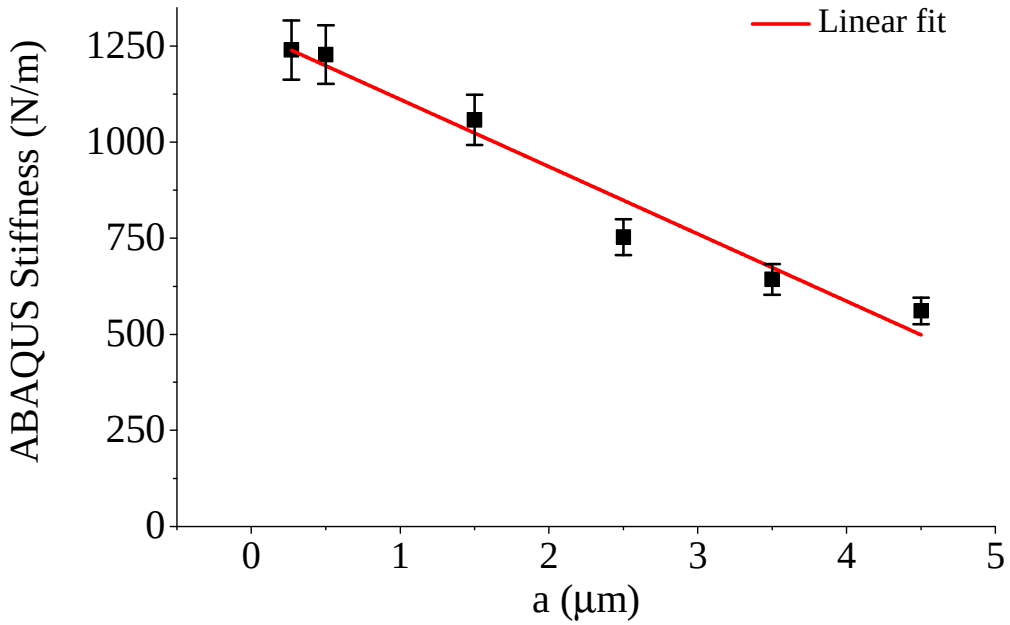

Figure 4.43 Stiffness obtained from the ABAQUS model versus the crack length (a) for the micro-cantilevers tested in 304 SS.

The relationship between the stiffness and crack length (a) was obtained from **Figure 4.43** and is presented in **Equation (6).**

$$Stiffness = -175 \cdot a + 1286.4 \quad \textbf{(6)}$$

4.7.3 Crack growth rate results

The load vs. displacement data from the region when the crack starts to grow for first cantilever (shown in **Figure 4.34**) is given in **Figure 4.44** along with the calculated crack length. The stiffness measured by the nanoindenter against time is shown in **Figure 4.45**. Then, using **Equation (6)**, the crack length was calculated for each data point. The graph of crack length for one cantilever against time is shown in **Figure 4.46**. Similarly, the same set of data was obtained for a second cantilever (shown in **Figure 4.36**) and are presented in **Figure 4.47**, **Figure 4.48** and **Figure 4.49**.

The crack length vs. time for the two cantilevers is plotted in **Figure 4.50** and a best-fit line is applied to calculate the crack growth length. The linear fit was performed only on the first four points, these being the ones that can be trusted since they lay in the square region of the pentagonal cross section of the cantilever. As soon as the crack grows into the triangular region of the cross section, the measurement for the crack length cannot be trusted since the model does not take into account effect of any plasticity in this remaining ligament. The crack growth rates for the two cantilevers are 119 μm/s and 36 μm/s.

The stress intensity factor (*K*) was calculated using the compliance method as described by Knott [129]:

$$K = \sqrt{\frac{G}{E}} \quad \textbf{(7)}$$

where *G* is the energy release rate and *E* is the Young's Modulus. *G* is a function of the load applied, the displacement and the geometry of the micro-cantilever, as described below:

$$\left(\frac{1}{2}P^2\frac{dC}{da}\right)/B \quad \textbf{(8)}$$

where *P* is the load applied on the cantilever, *dC* is the change in compliance that is calculated from the instantaneous load-displacement data, *da* is the change in crack growth and *B* is the thickness of the cantilever that changes as the crack propagates across the cantilever.

This method is good to approximate the stress intensity factor for the micro-cantilevers tested at short crack lengths, when linear elasticity is most likely to apply; however, as the crack grows, because of the plastic deformation that occurs at the crack tip the

calculation will increase the apparent value of *K* while *K* should actually be reduced. The crack growth rates for the two fractured cantilevers as a function of the stress intensity factor are shown in **Figure 4.51.** The shape of the crack growth rate vs. stress intensity curve is not at all what would be expected; the crack growth rate appears to fall as the stress intensity factor increases which is counterintuitive and also different from what was previously observed by Herbert [126]. This effect could be due to the value of the stress intensity factor being overestimated due to the fact that plasticity is not considered.

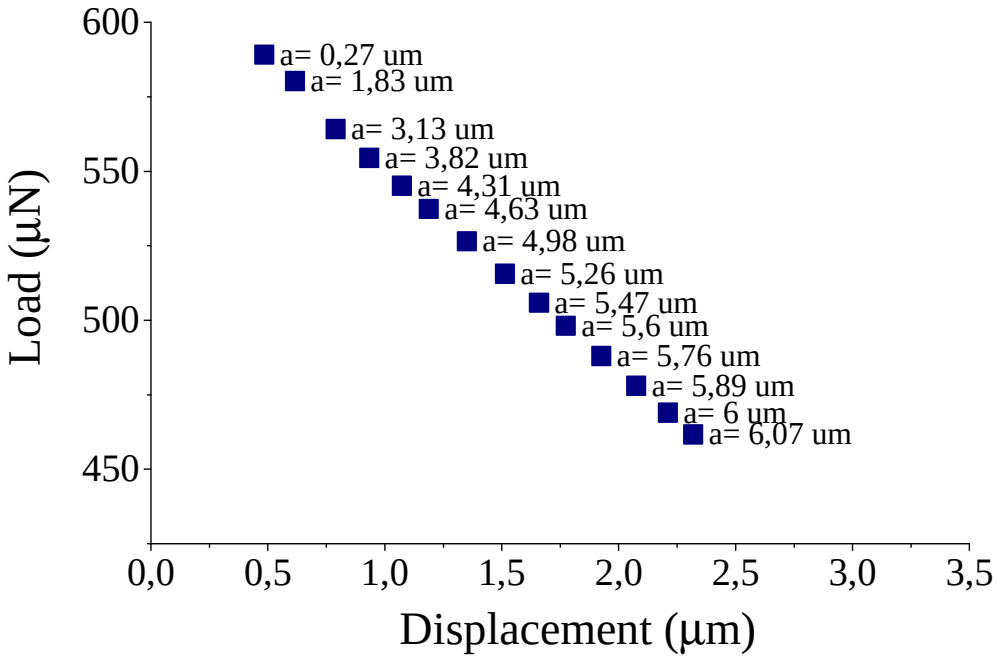

Figure 4.44 Load vs. displacement data from the crack growth region for first cantilever (shown in Figure 4.34) tested in 304 SS. The values for the crack length that correspond to each point of the graph are presented as well.

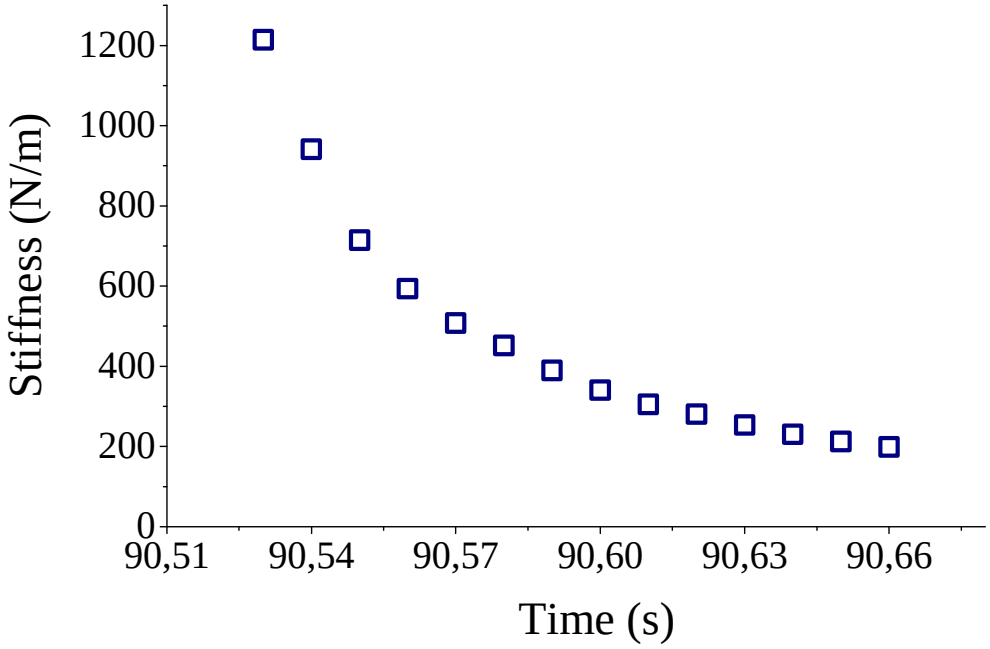

Figure 4.45 Static stiffness against time measured by the nanoindenter for first cantilever (shown in Figure 4.34) tested in 304 SS.

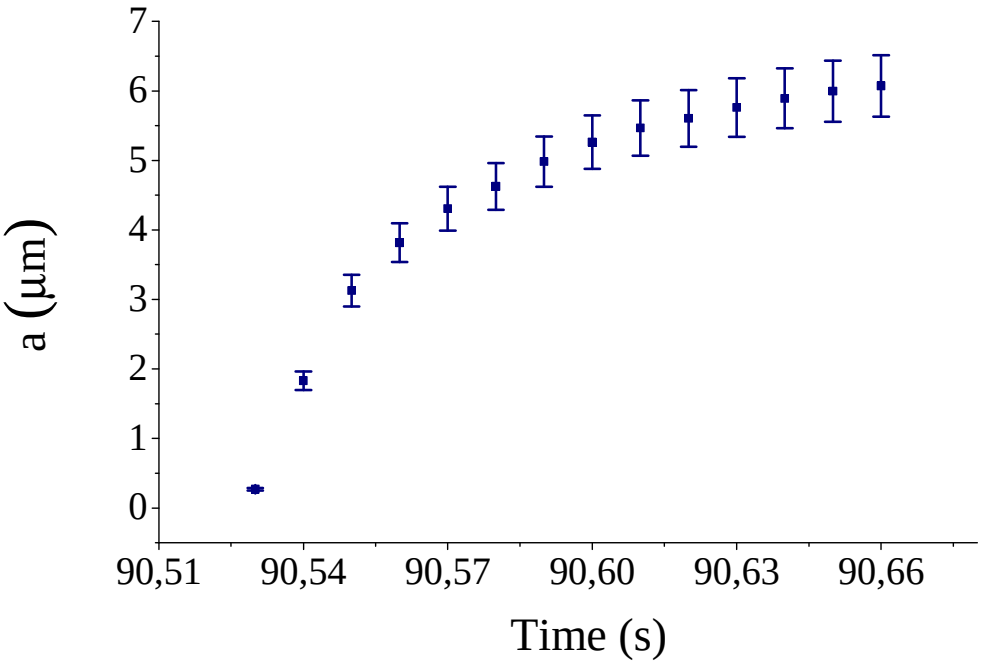

Figure 4.46 Crack length vs. time data from for first cantilever tested (shown in Figure 4.34) in 304 SS.

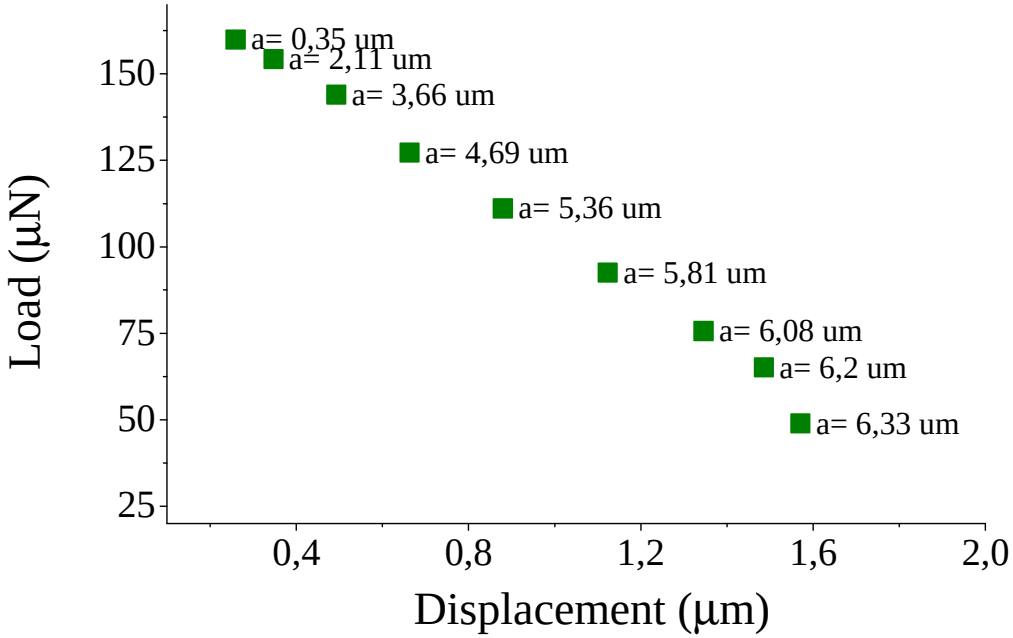

Figure 4.47 Load vs. displacement data from the crack growth region for the second cantilever (shown in Figure 4.36) fractured in 304 SS. The values for the crack length that correspond to each point of the graph is presented as well.

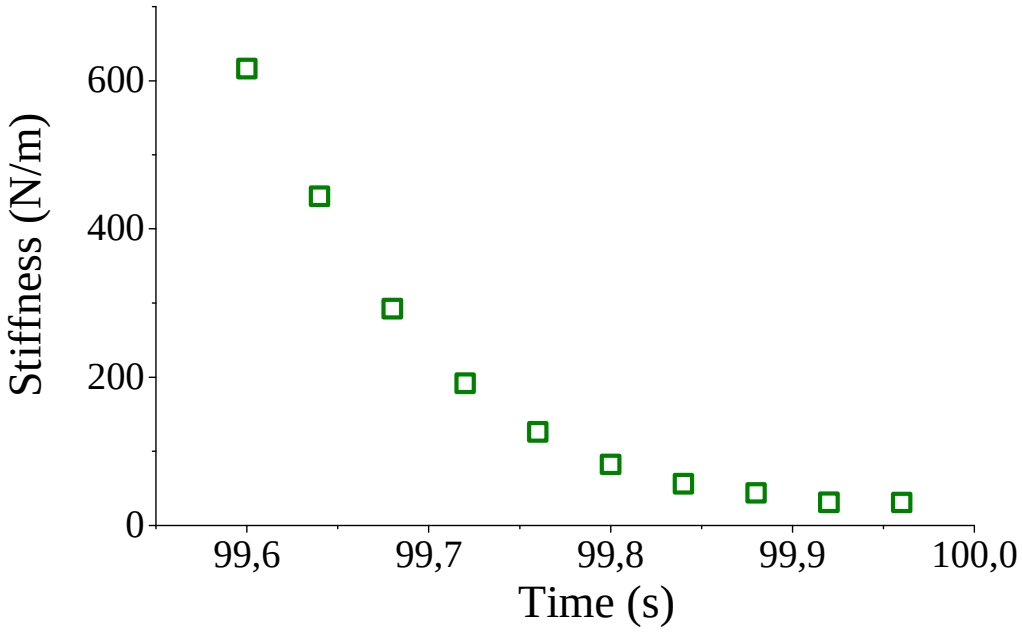

Figure 4.48 Static stiffness against time measured by the nanoindenter for the second (shown in Figure 4.36) cantilever tested in 304 SS.

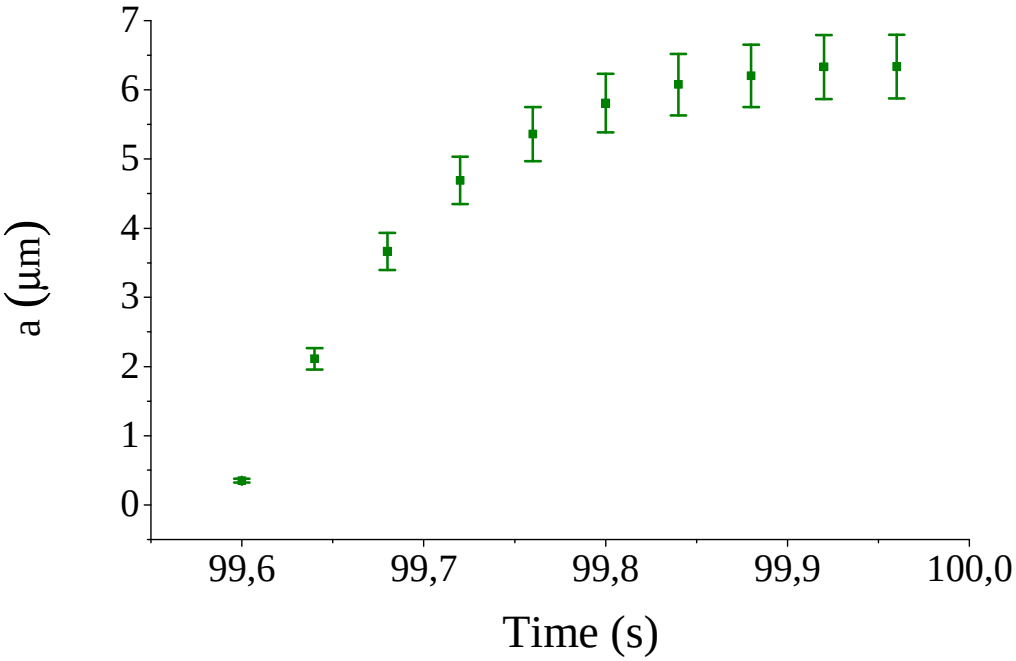

Figure 4.49 Crack length vs. time data from for the second cantilever (shown in Figure 4.36) fractured in 304 SS.

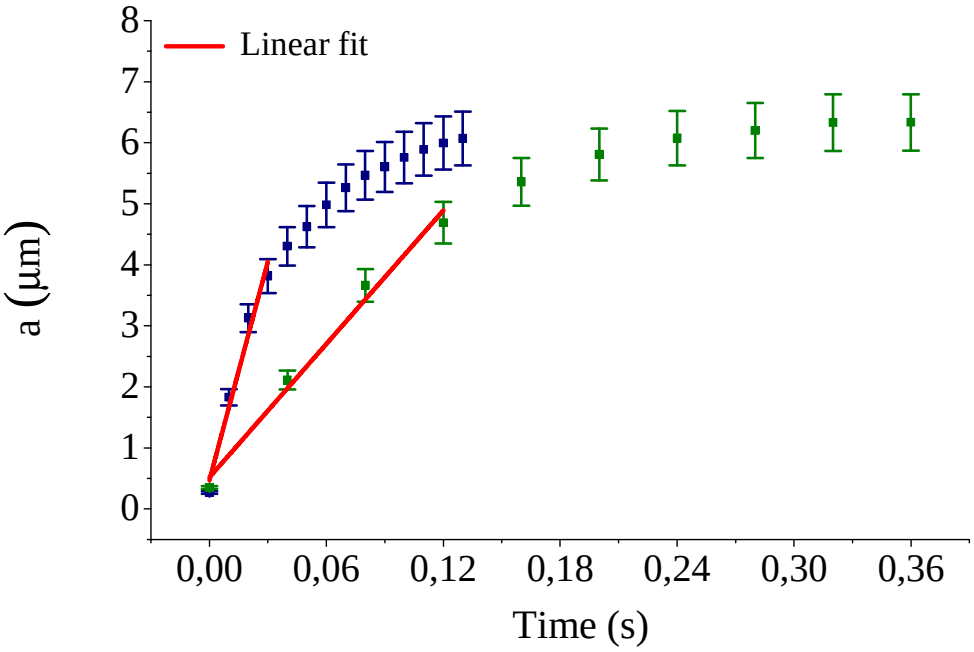

Figure 4.50 Crack length versus time for two fractured cantilevers in 304 SS tested in situ. The linear fit determines the crack growth rate to be: 119 µm/s and 36 µm/s.

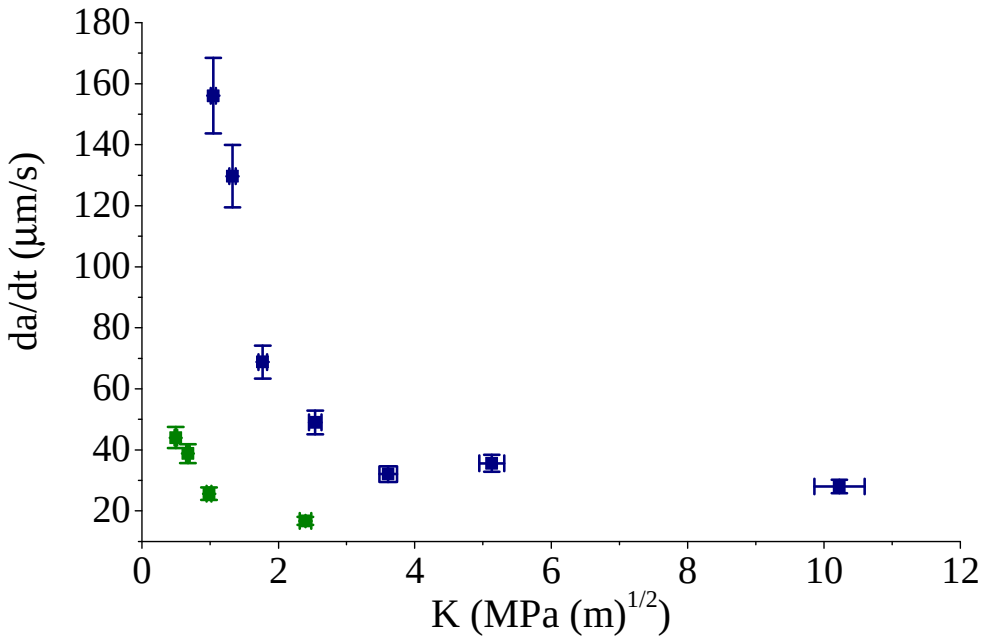

Figure 4.51 Crack growth rate against the stress intensity factor for two cantilevers that fractured *in-situ*.

4.8 Summary

The work presented in this chapter studied the method of obtaining IGSCC in an *in-situ* setup using micro-mechanical testing. First, the method with no voltage applied was studied to determine whether crack initiation can occur without polarizing the sample. This was rather unsuccessful and it might be due to the short duration of the tests. Next, platinum was used as a counter electrode to accelerate the reaction and to initiate cracking. Both short (600 s) and long (2000 s) tests were performed and IGSCC initiated in none of the tests.

The only method that proved to produce IGSCC initiation and growth was the method that used a polarizing current (6 V battery) that connected the sample with the unsensitised stub of 304 SS. The tests performed using this method were done in a very aggressive environment and the crack growth was very rapid.

Crack growth rate was measured for the tested cantilevers and was between approximately 40 μm/s and 120 μm/s. This is a few orders of magnitude higher than the crack growth rate of IGSCC in austenitic steels measured macroscopically. As reported in the literature, the crack growth rate was observed to be approximately 10^{-9}-10^{-8} μm/s for a stress intensity factor of 10-20 MPa$(m)^{1/2}$, 10^{-2}-10^{-1} μm/s for a stress intensity factor of 40-50 MPa$(m)^{1/2}$ [35] and 6-8$\cdot 10^{-3}$ μm/s at an applied stress of 220 MPa [45]. However, a direct comparison between these measurements and the results reported here cannot be done straightforwardly, because the macroscopic scale tests measure the crack growth rate across several grain boundaries, including triple junctions that have been shown before to act as regions of crack arrest [14][130]. The measurements of crack growth rate of single grain boundaries in this context are more analogous to single crystal crack growth rate. In a study of subcritical crack growth in single-crystal silicon [131], micro-machined specimens were tested and the crack growth rate was obtained to be between 10^{-4}-10^{2} μm/s for specimens that had a fracture toughness of approximately 1.15 MPa $(m)^{1/2}$. These values are comparable with the ones obtained for the crack growth rate of FIB machined specimens tested in active solution that are the subject of the current study.

Controlling crack growth rate proved to be a great challenge. While using platinum as a counter electrode proved to accelerate the crack growth in macro tests, this was not the case in the micro tests. In such an environment it might be that the time of the experiments needs to be much longer than 2000 s. However, this would involve modifying the setup so that the solution that covers the sample is refreshed at short time intervals. The solution flow will however be picked up in the nanoindenter data and the noise in the data would somehow needed to be filtered out. Also, platinum might not be a suitable counter electrode because crack growth rate might not be controllable at such

a small scale. In addition, it is quite difficult to determine the best combination of all the variables that are influencing crack initiation that will work for a great population of grain boundaries. Because of these unresolvable problems and shortage of time, this avenue of research was halted.

5 Fracture toughness of FIB micro-cantilevers in Ni Alloy 600

5.1 Introduction

It has been shown in the literature survey that one potential cause for IGSCC initiation in Ni Alloy 600 is grain boundary oxidation. Since this is the case, there is a need to determine methods that could accurately determine the character of the oxide at the grain boundaries and could gather data that could predict failure.

Up until now, to the author's knowledge, Fujii et al. [132] and Dugdale et al [168] have studied the strengths of oxidised grain boundaries in Ni Alloy 600 exposed to a PWR environment. Fujii used a micro tensile testing method in a FIB system to determine the strength of individual grain boundaries. The specimens had been exposed to PWR environment at 360 ^{o}C for 1500 and 2700 h under a bending stress of 200 MPa. Fujii determined that the fracture stress increased from 200 to 300 MPa in the samples that were exposed for 1500 and 2700 h respectively. An unoxidised grain boundary did not fracture even at 900 MPa. TEM observations showed that the fracture occurred between the oxide and the matrix [133].

While Fujii presented a valid method of determining the strength of individual grain boundaries, no method was developed to test the fracture toughness of the oxidised grain boundary or the relationship between the orientation of grain boundaries and the fracture toughness. This chapter presents a valid method of determining fracture toughness for individual oxidised grain boundary and presents results from a range of grain boundary of various orientations in Ni Alloy 600 exposed to a simulated PWR water environment.

5.2 Sample preparation

Coupons of Ni Alloy 600 that had been exposed to the PWR environment were received from AREVA. The received samples were classified for the purpose of this thesis as follows: a) oxidized samples that were exposed for 4500 h; b) oxidized samples that were exposed for 1500 h and c) un-oxidised samples. To prepare the samples, the coupons were cut using the Isomet 500 slow saw to produce six samples, equal in size. The samples were then attached using "superglue" to aluminium SEM stubs that could be used in the FIB and nanoindenter.

5.2.1 Determining perpendicular and oxidised grain boundaries

For the fracture tests in Ni Alloy, it was important before milling the cantilevers to select grain boundaries that were oxidized and perpendicular to the surface. The oxidised grain boundaries could be identified by the contrast of the surface oxide on each side of the grain boundary, as shown in **Figure 5.1.**

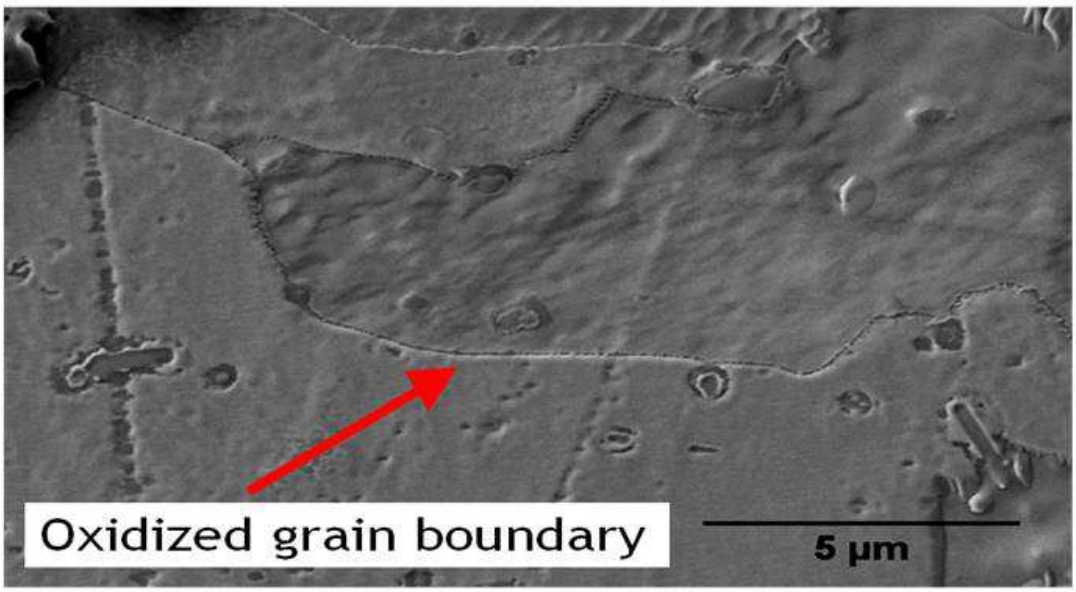

Figure 5.1 Grain boundary revealing intergranular oxide in Ni Alloy 600 sample exposed for 4500 h.

The grooves present between grains, that appear in a dark black colour, are indication of the oxide present at the grain boundary. Only oxidised grain boundaries were characterised by this feature. To determine the oxidized grain boundaries that were perpendicular, the grain boundaries were examined using FIB trenches. Cut-outs were milled using a current of 2000 pA and ion channelling was used to determine the grain boundaries that were normal to the surface. Also, the FIB trenches revealed the oxide at the grain boundaries which could be easily identified by its darker colour in comparison to the bulk material. Because it was difficult to find grain boundaries that had an angle to the surface of exactly 90°, grain boundaries that were within 15° were considered to be acceptably perpendicular to the surface.

Grain boundaries that had an angle to the surface lower than 75°, as the one presented in **Figure 5.2** were not selected. A grain boundary that was suitable for cantilever production is shown in **Figure 5.3.**

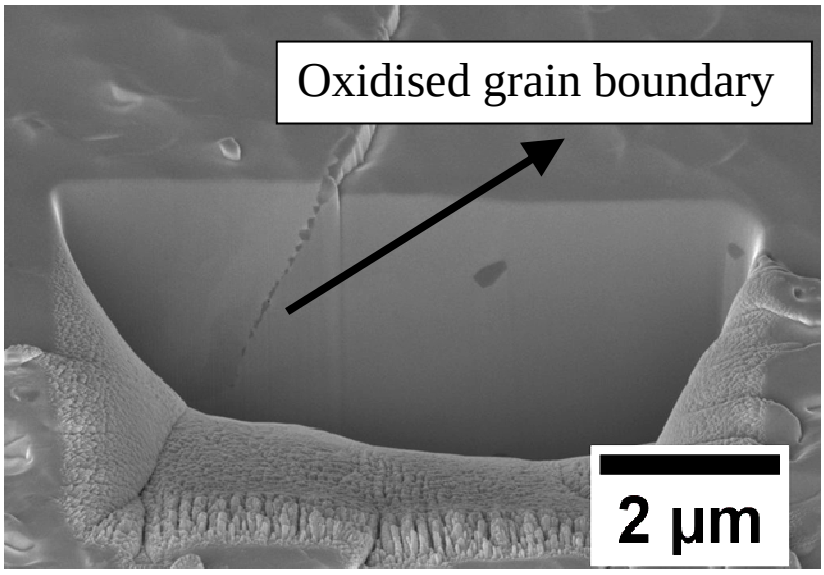

Figure 5.2 FIB cut-out revealing an oxidised grain boundary that is not perpendicular to the surface in a Ni Alloy 600 sample exposed for 4500 h.

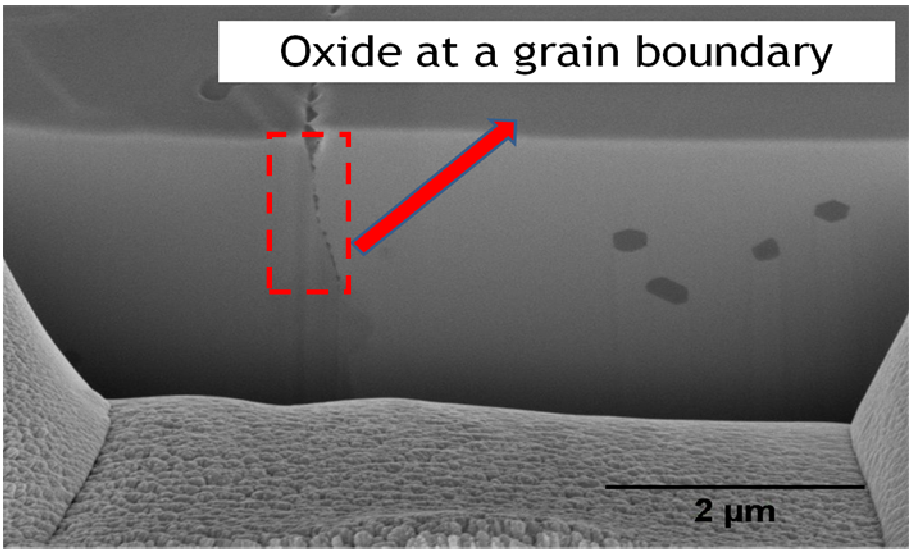

Figure 5.3 FIB cut-out revealing a perpendicular oxidised grain boundary in a Ni Alloy sample exposed for 4500 h.

5.2.2 Cantilever design and manufacture

FIB was used to machine pentagonal cross-section cantilevers 5 µm wide by 25 µm long. To produce the cantilevers, a beam current of 4000 pA was first used to mill rough trenches. Initial rough trenches of four cantilevers are shown in **Figure 5.4**. The cantilevers were milled so that the beam contained, close to the build-in end, a selected grain boundary**.** The beam was milled so that a grain boundary was placed at approximately 3 µm from the fixed end. Then, the sample was tilted by 45° to undercut the beam on one side. The undercutting of the cantilevers was performed using a beam current of 2000 pA. Then, the cantilever was rotated 180° to undercut the cantilever on the other side. To remove any redeposited material, a smaller beam current of 1000 pA was used to "polish" the three sides of the cantilever. Using this manufacturing method, the cantilevers can have triangular or pentagonal cross-section. The pentagonal geometry was chosen over the triangular one to better observe the fracture at the grain boundary. A micrograph of a finished cantilever is shown in **Figure 5.5**.

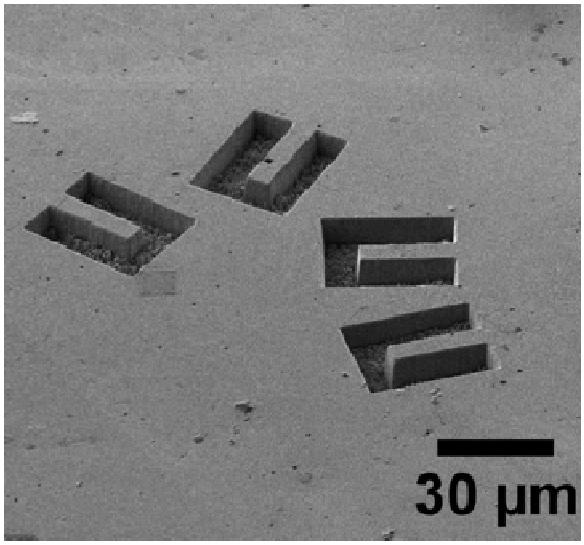

Figure 5.4 SEM image showing four rough trenches milled using the FIB in an un-oxidised sample of Ni Alloy 600.

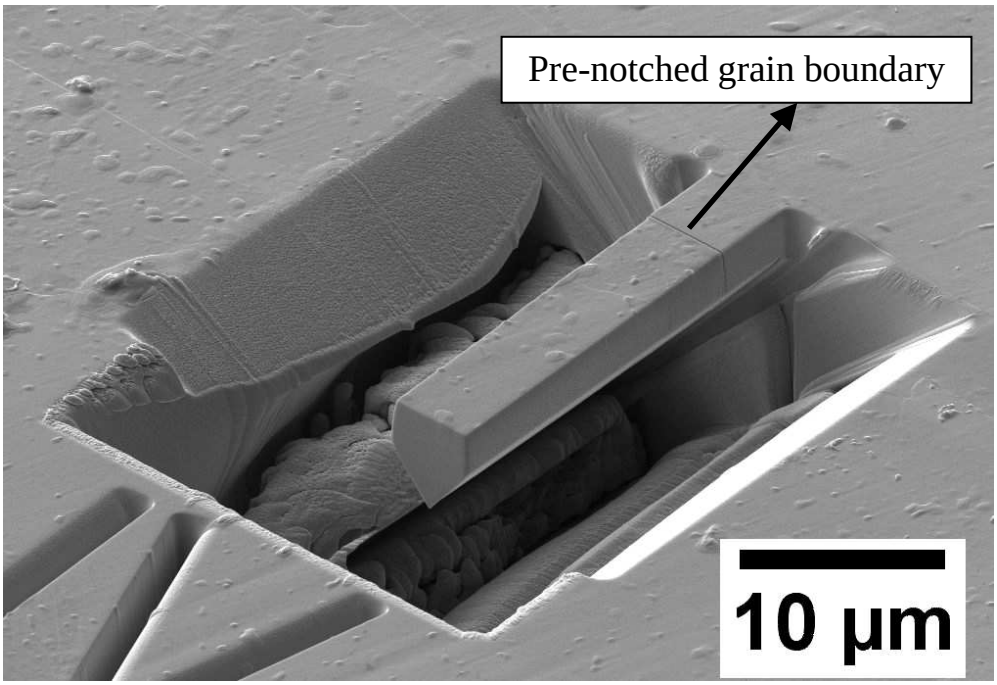

Figure 5.5 SEM image of a finished cantilever milled in an un-oxidised sample of Ni Alloy 600 using the FIB. The arrow indicates the grain boundary that was pre-notched.

5.2.3 Pre-notch machining of the cantilevers

In order to determine the best milling conditions for producing the "pre-crack", a cantilever was pre-notched using single FIB lines of different milling currents. Notches from different milling conditions are presented in **Figure 5.6**.

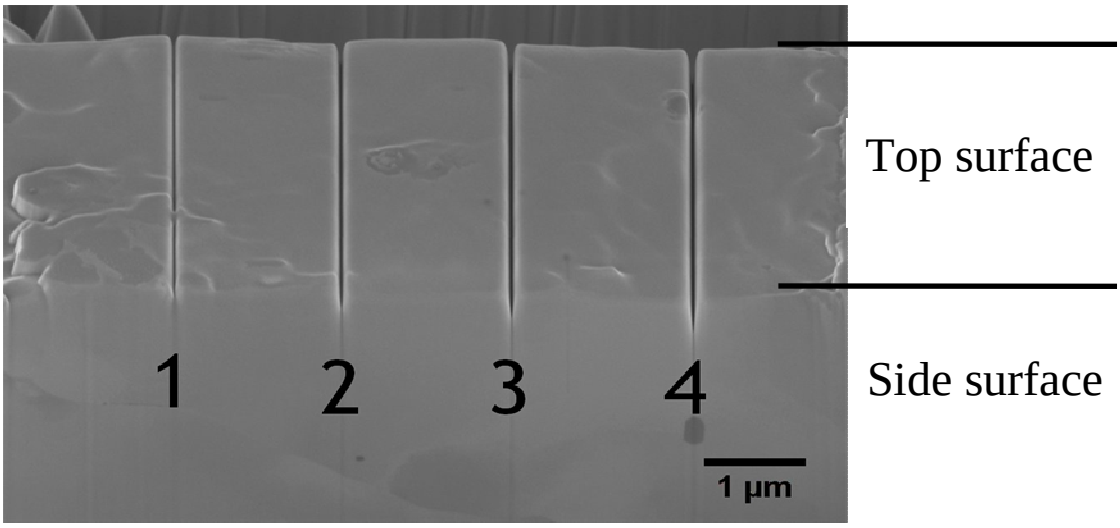

Figure 5.6 Notches milled in Ni Alloy 600 exposed for 4500 h, with the FIB using different conditions: (1)10 pA for 10 s, (2)10 pA for 20 s, (3)10 pA for 40 s and (4)10 pA for 60 s. The different milling conditions produced notches of different depths. The notch milled using condition (4) was used for further tests.

The notch that was selected to be used for all the cantilevers was notch number (4), that was obtained using a milling current of 10 pA for 60 seconds. This was selected because it produced a good size notch, which was deep enough to produce fracture. The depth of the notches varied with the grain boundaries (as some grains mill faster than the others) between 400 nm and 600 nm in depth.

5.3 Fracture toughness calculation

Load vs. displacement data from micro-cantilever tests were used to calculate the fracture toughness of different oxidised grain boundaries.

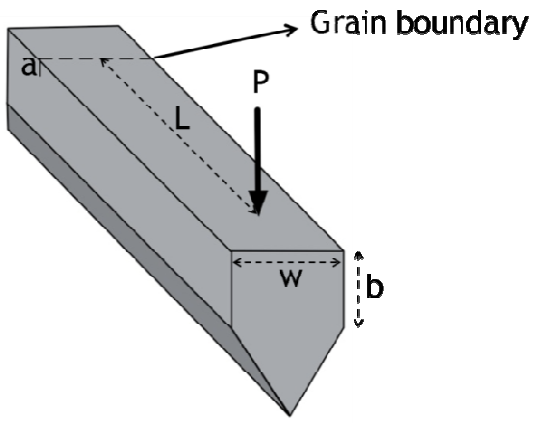

Figure 5.7 Geometry and dimensions of the cantilevers milled in Ni Alloy 600 samples, where a is the depth of the pre-notch (between 400 nm and 600 nm), L is the length between the grain boundary and the loading point (approximately 20 µm), w is the width of the cantilever (approximately 5 µm), b is the height (approximately 3 µm) of the rectangular cross section and P is the load applied on the cantilever (a few hundreds µN).

Using simple beam theory (as by Di Maio [116]), assuming that there are only small amounts of plasticity, the fracture stress can be determined using the following equation:

$$\sigma = \frac{PLy}{I} \tag{9}$$

where P is the load applied by the nanoindenter, L is the length from the grain boundary to the loading point (**Figure 5.7)**, I is the moment of inertia of the beam cross section and y is defined as:

$$y = \frac{\frac{b^2 w}{2} + \frac{w^2}{4}\left(b + \frac{w}{6}\right)}{bw + \frac{w^2}{4}} \tag{10}$$

where w and b are the dimensions shown in **Figure 5.7**. I is calculated as given in [116]:

$$I = \frac{wb^3}{12} + \left(y - \frac{b}{2}\right)^2 bw + \frac{w^4}{288} + \left[\frac{b}{6} - (b - y)\right]^2 \frac{w^2}{4}, \quad \textbf{(11)}$$

Fracture toughness was calculated using the dimensions of the cantilever and the load at which the cantilever failed, via the following equation:

$$K_{I_c} = \sigma\sqrt{\pi a}F\left(\frac{a}{b}\right) \ , \quad \textbf{(12)}$$

where a is the depth of the notch.

F given in **Equation (12)** is approximated by Di Maio [116] to be:

$$F\left(\frac{a}{b}\right) = 1.85 - 3.38\left(\frac{a}{b}\right) + 13.24\left(\frac{a}{b}\right)^2 - 23.26\left(\frac{a}{b}\right)^3 + 16.8\left(\frac{a}{b}\right)^4 \quad \textbf{(13)}$$

The formula for F can only be applied for a pentagonal cross-section, as shown in **Figure 5.7.**

5.4 Cantilever testing

The cantilevers were tested using an MTS Nanoindenter XP System. First, an AFM-type scan was performed to image the cantilever. Then, the cantilever was loaded close to the free end. The cantilevers were tested at constant displacement rate of 5 nm/s to a maximum displacement of 1500 nm. The results were obtained in the form of force versus displacement.

5.5 Ni Alloy 600 exposed for 4500 h

5.5.1 Sample preparation

The Ni Alloy 600 sample was first polished down to a 1µm diamond finish and then exposed in PWR primary water at 325 ^{o}C for 4500 h with a hydrogen partial pressure of 30 kPa. The surface of the as-received samples is presented in **Figure 5.8.**

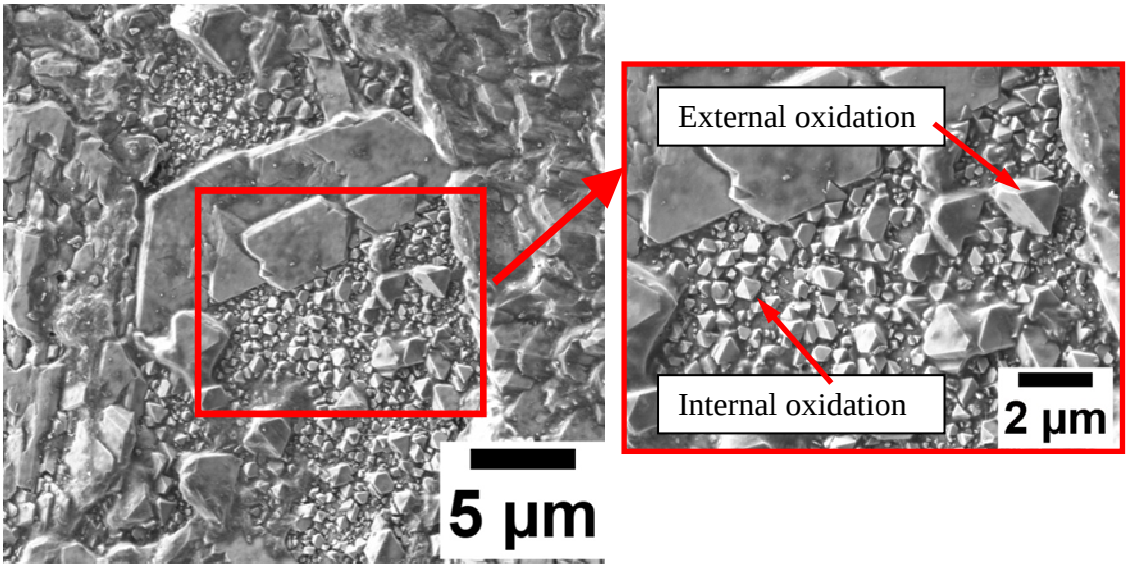

Figure 5.8 SEM image showing the initial rough surface of the Ni Alloy 600 sample exposed for 4500 h.

According to Combrade *et al.*[99], the oxide layer in Ni Alloy 600 in primary PWR water at a temperature of 360° is made of two layers: a Cr-free external layer and a Cr-rich inner layer. Panter *et al.*[89] classified the external crystallites into two families: the first one is constituted of small crystallites of approximately 50 nm in size and covers most of the specimen and the second one is made of larger crystallites of approximately 200 nm or greater in size and covers the specimen sporadically. The analysis of a Ni Alloy 600 sample that was exposed to the PWR water environment at a temperature of 325 ^{o}C and a partial pressure of 30kPa, identified the large crystallites to be oxide of type (Ni,Fe)Fe_2O_4 and the smaller ones to be a mixed oxide of nickel,

chromium and iron of type $(Fe,Ni)(Fe,Cr)_2O_4$. The Cr rich inner layer is believed to be formed by two sublayers: the oxide layer of type of type $(Fe,Ni)(Fe,Cr)_2O_4$ and a barrier layer which is believed to be Cr_2O_3. While it is not possible to see it with the SEM, underneath the barrier layer, there is a Cr depleted metal layer that has been characterized through TEM observations [99].

The microstructure shown in **Figure 5.8** is in accordance with this. While the internal oxide seems to be compact and uniform, the external oxide is made of separated crystallites. The material studied by Combrade *et al.* and the material used for the research conducted during this thesis are the same and they have been exposed to the same conditions. Hence, the cross section of the material used in this thesis, shown in **Figure 5.9** has been labelled according to the structure found by Combrade *et al.*

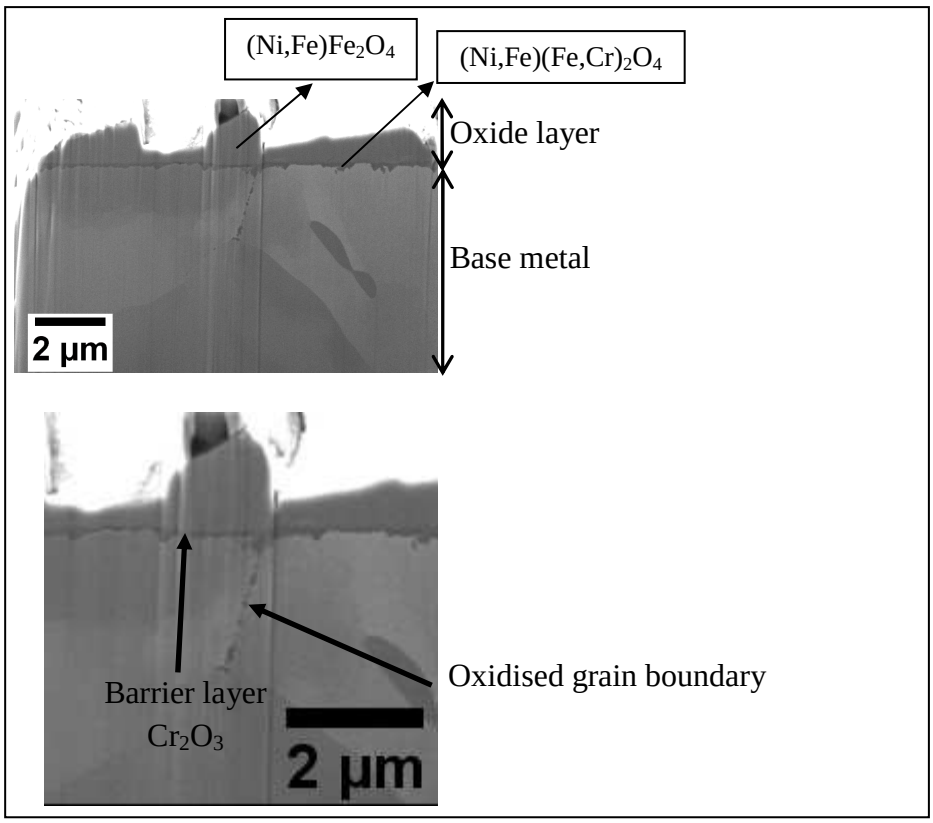

Figure 5.9 General oxide structure presenting the oxide layer and the base metal in a Ni Alloy 600 exposed to PWR environment [Labelled according to [99]].

Both the external and the internal oxide particles on the surface made scanning of the cantilevers very difficult as the surface of the sample was very rough. As can be seen from **Figure 5.10** the scan of the cantilever does not depict a clear image of the cantilever, hence without further mechanical polishing, it was not possible to test the cantilevers milled in the as-received sample.

In order to obtain a smoother surface polish, the samples were further polished with colloidal silica to remove the external oxide layer and part of the internal oxide layer, without removing the barrier layer, so that the oxidised grain boundary would not be removed. This was done by periodically checking the roughness of the surface. The surface that was obtained after the final polishing is presented in **Figure 5.11** and a scan of a cantilever milled in this new sample is shown in **Figure 5.10b**. Several cantilevers (23 in total) were made at grain boundaries in this type of surface, where the oxidised and perpendicular boundaries were selected as presented in **Section 5.2.1**. All the cantilevers milled were apparently the same, with similar dimensions. **Figure 5.12** shows an example of one cantilever before the test.

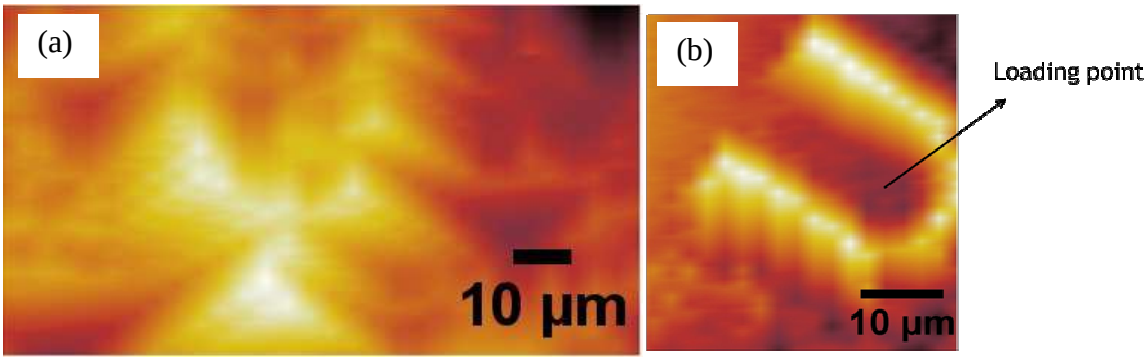

Figure 5.10 AFM type scans performed using the nanoindenter on Ni Alloy 600 sample exposed for 4500 h: (a) on the initial rough surface; (b) on the final polished surface.

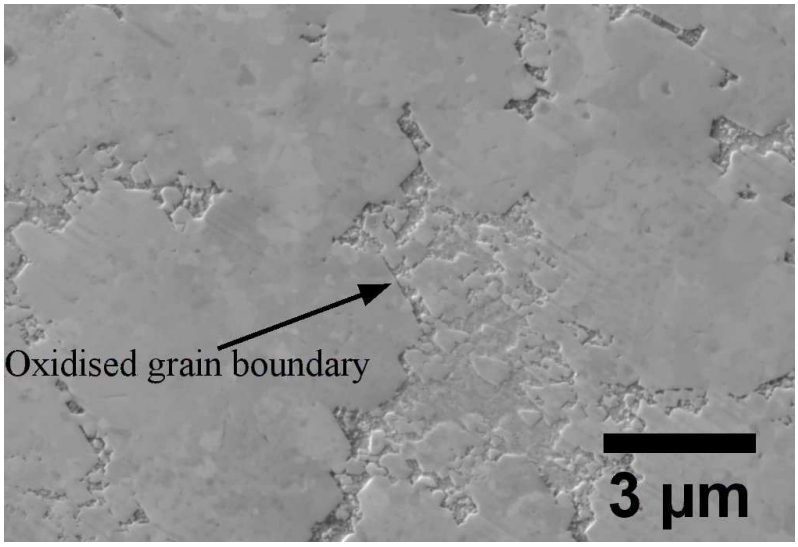

Figure 5.11 SEM image showing the final polished surface of the Ni Alloy 600 sample exposed for 4500 h.

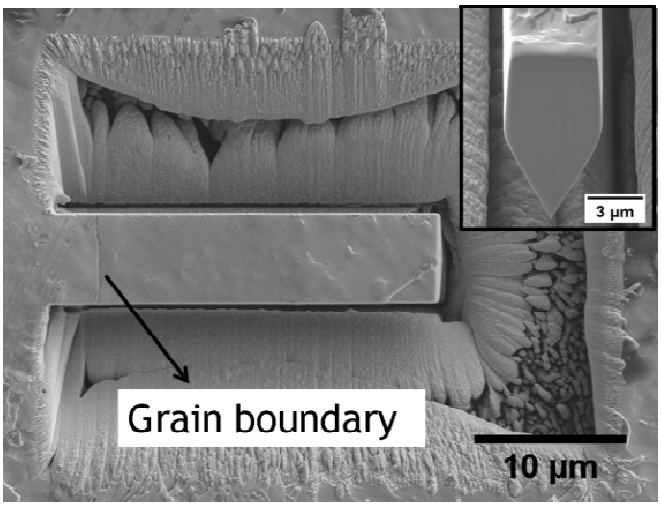

Figure 5.12 FIB machined cantilever with a pentagonal cross section in Ni Alloy 600 exposed for 4500 h before the test. The grain boundary is indicated by the arrow.

5.5.2 Stress-strain curves

Load vs. displacement curves for two different cantilevers from the polished surface of oxidised Ni Alloy sample exposed for 4500 h are presented in **Figure 5.13**. The load vs. displacement curve indicates fracture of the cantilevers, without any amount of plasticity. The linear segment of the curve represents the loading segment and it stops at the point of fracture. After fracture, the nanoindenter continues to load the beam, until the displacement reaches the maximum displacement value (e.g 1500 nm). The load vs. displacement curves for all the 23 tested cantilevers were similar, showing the same features.

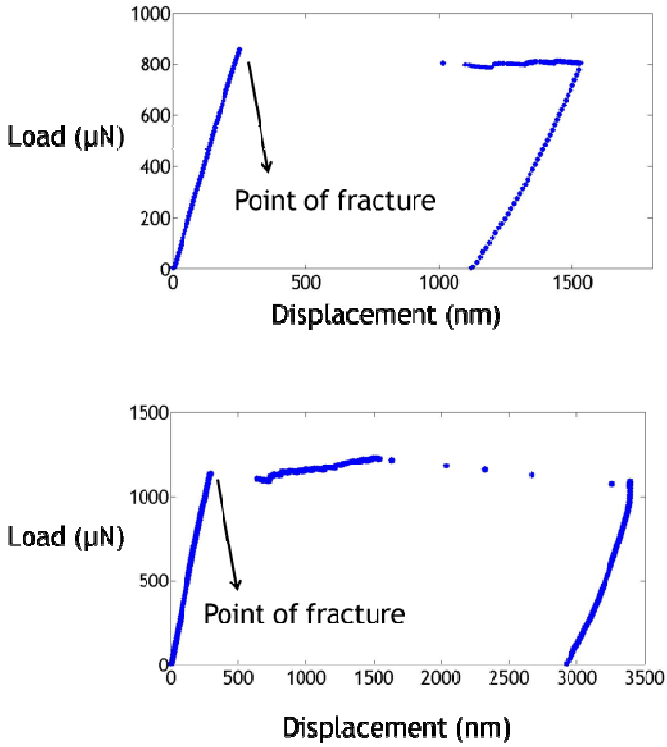

Figure 5.13. Load vs. displacement data for oxidised grain boundaries in Ni Alloy 600 exposed for 4500 h, showing fracture, a rapid displacement increase at a critical load.

5.5.3 Fracture toughness values

Fracture toughness values for each micro-cantilever were calculated using **Equation (12)** and the results for the 23 tested cantilevers are presented in **Figure 5.14.** The plot is similar to a Weibull plot and it was obtained by first ranking the fracture toughness values in ascending order and calculating P (P=1-rank order/(number of specimens+1)) for each value. The fracture toughness associated with fracture of grain boundary in Ni Alloy 600 sample exposed for 4500 h was in the range of 0.73 -1.82 MPa $(m)^{1/2}$.

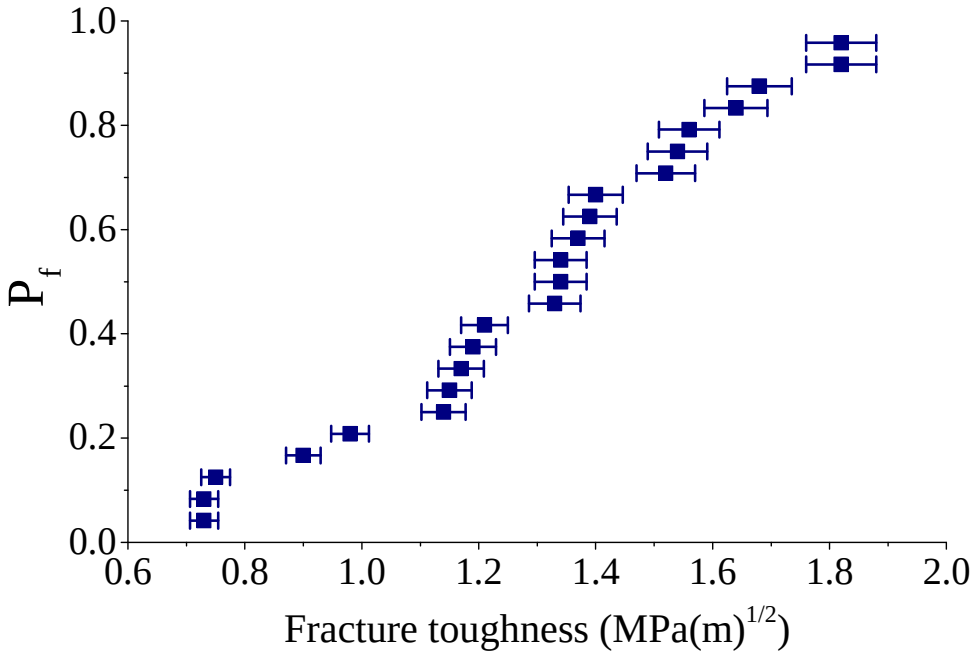

Figure 5.14 Fracture toughness results for the tested cantilevers in Ni Alloy 600 exposed for 4500 h.

5.5.4 Fractography

The 23 tested cantilevers all failed in a similar manner to the one shown in **Figure 5.15.** The cantilevers failed at the oxidized grain boundary, starting from the FIB notch.

5.5.5 Fracture surfaces

To study the fracture surfaces, since the cantilevers did not fracture all the way, the manipulator needle in the FIB was used to push down on the cantilever, so that the crack opened fully. First, to reduce the size of the cantilever the free end of the cantilever was milled away using the FIB. Then, the manipulator needle was used several times to push down on the cantilever, until the cantilever opened. The steps followed to expose the fracture surface of the tested cantilevers are shown in **Figure 5.16.** The cantilevers were then imaged using the SEM and the fracture surfaces were observed. The fracture surfaces for three different cantilevers are presented in **Figure 5.17.**

It can be observed from the fracture surface micrographs that not all the cracks propagated perpendicular to the surface. To see whether the angle at which the crack propagates influences the value of the fracture toughness, the angle was measured with ImageJ software from the SEM images that were previously corrected for tilt. A schematic showing how the angle was measured is presented in **Figure 5.18**. A plot presenting the fracture toughness values against the crack propagation angle is shown in **Figure 5.19.**

As can be seen from **Figure 5.19** there is no strong correlation between the fracture toughness values and the angle at which the crack propagates. However, the fracture toughness values seem to decrease with increasing crack propagation angle up to 100° and then to increase with the increasing crack propagation angle.

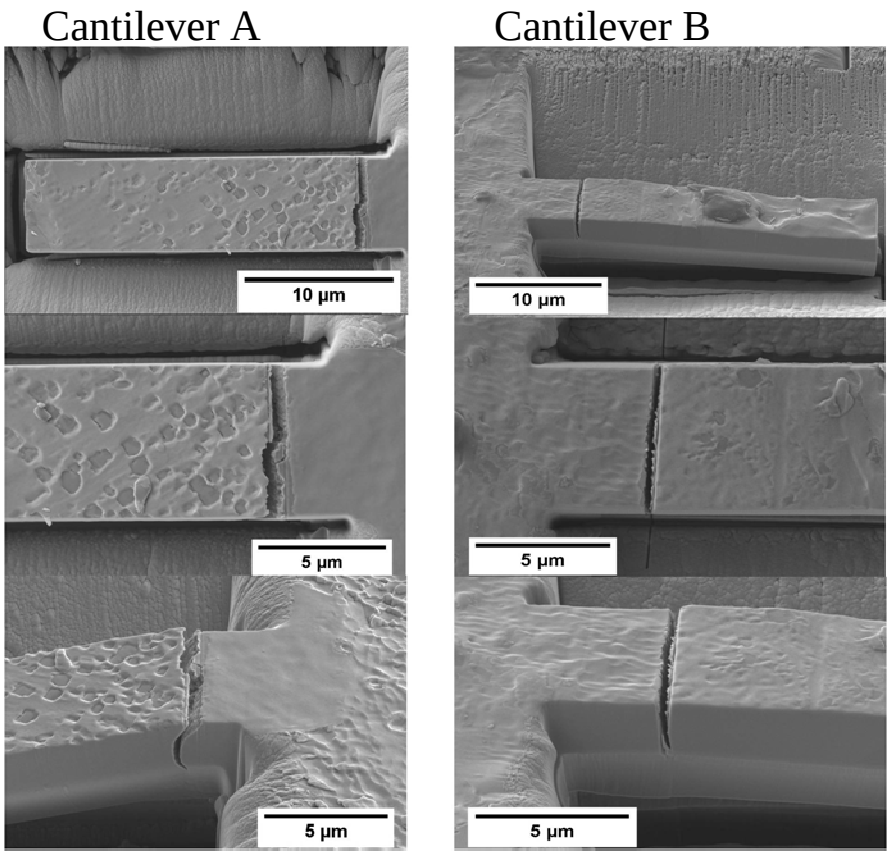

Figure 5.15 Two cantilevers in oxidized Ni Aalloy, after testing, showing fracture at the grain boundary. The images show the cantilevers from above and from both sides.

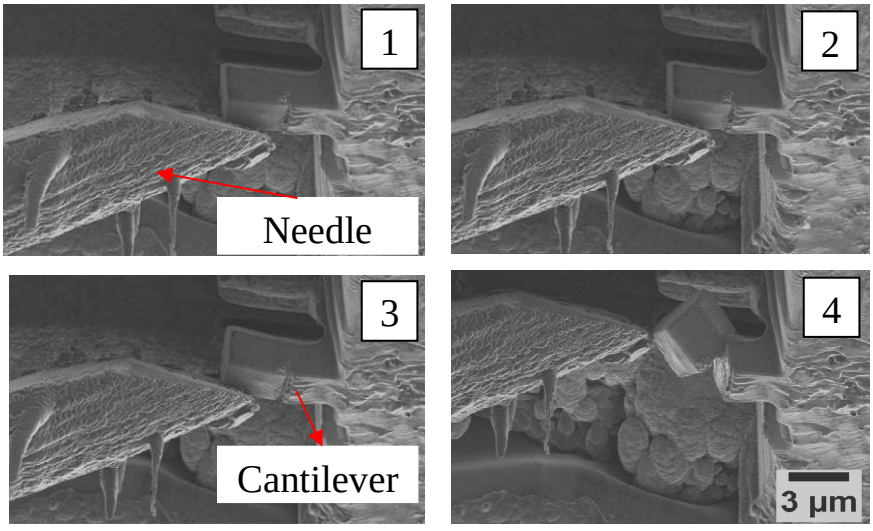

Figure 5.16 SEM images showing the steps followed to expose the fracture surface for one cantilever tested in Ni Alloy 600 exposed for 4500 h. (1) needle comes in contact with the cantilever; (2) needle starts to push down on the cantilever; (3) cantilever is partially opened and (4) cantilever is fully opened.

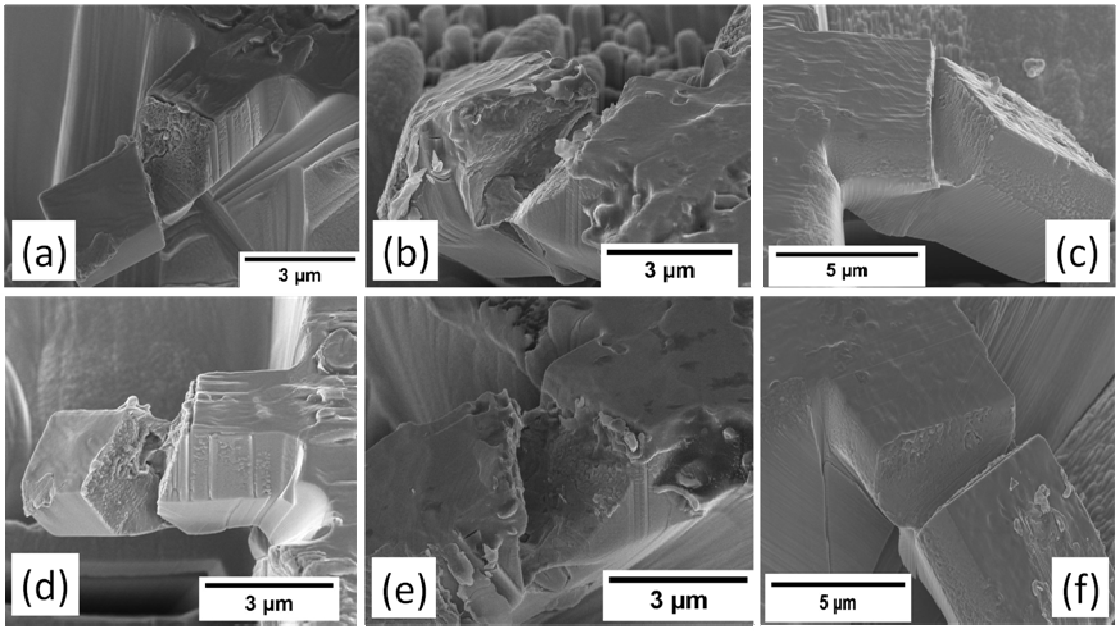

Figure 5.17. Fracture surfaces shown for three different cantilevers milled in Ni Alloy sample exposed for 4500 h, after testing. The fracture toughness values for these cantilevers are: (a, d) 0.73 MPa $(m)^{1/2}$, (b, e) 1.64 MPa $(m)^{1/2}$ and (c, f) 1.82 MPa $(m)^{1/2}$. The pairs (a, d) , (b, e) and (c, f) each correspond to one cantilever and show the fracture surface of the two sides separated by the fracture.

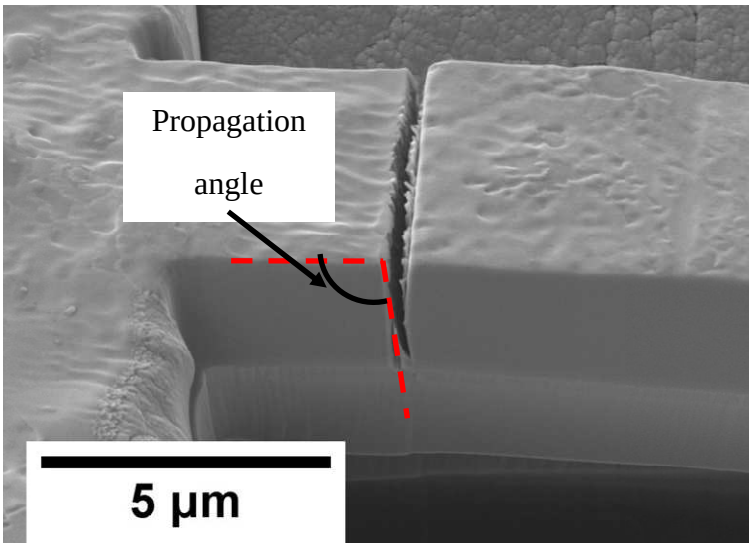

Figure 5.18 Schematic showing how the crack propagation angle was measured in cantilevers fractured in Ni Alloy exposed for 4500 h.

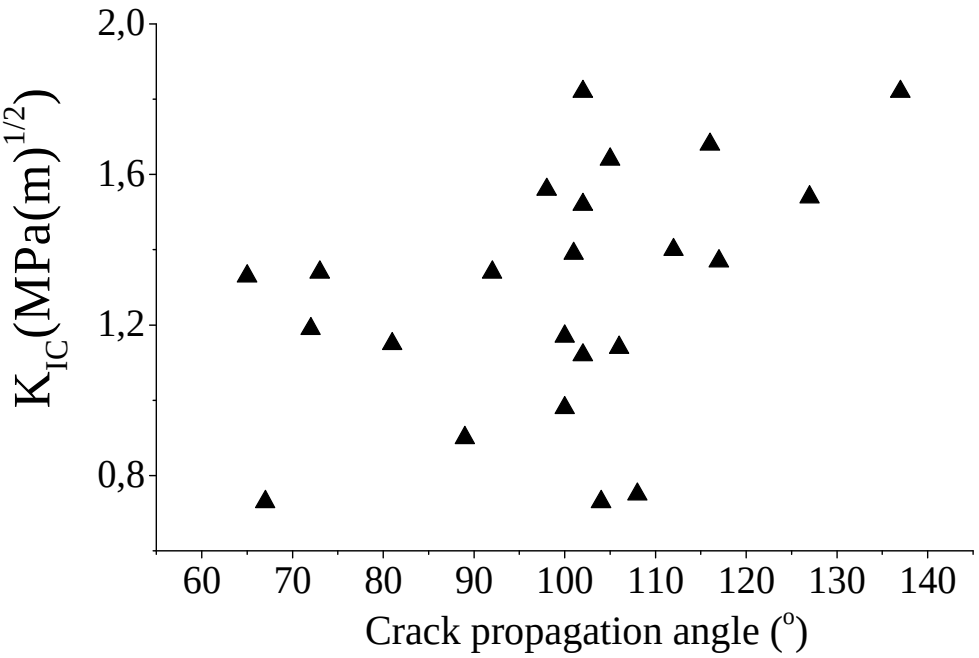

Figure 5.19 Calculated fracture toughness for the tested cantilevers in Ni Alloy exposed for 4500 h against the crack propagation angle.

5.5.6 Thickness and depth of the oxide

To further investigate the spread in the fracture toughness values, the thickness and the depth of the oxide were measured in each case. These measurements were performed using ImageJ from the SEM micrographs that were taken before the cantilevers were milled and were corrected for tilt. **Figure 5.20** shows how these measurements were performed. The variation of fracture toughness with the depth and the thickness of the oxide are shown in **Figure 5.21** and **Figure 5.22.**

There is no relation between the fracture toughness and the depth of the oxide. The average oxide depth for the tested cantilevers was approximately 3 μm. **Figure 5.22** shows little correlation between the fracture toughness values and the oxide thickness, in that the fracture toughness decreases with increasing of the oxide thickness up to approximately 0.12 μm. The average oxide thickness for the tested cantilevers was approximately 83 nm.

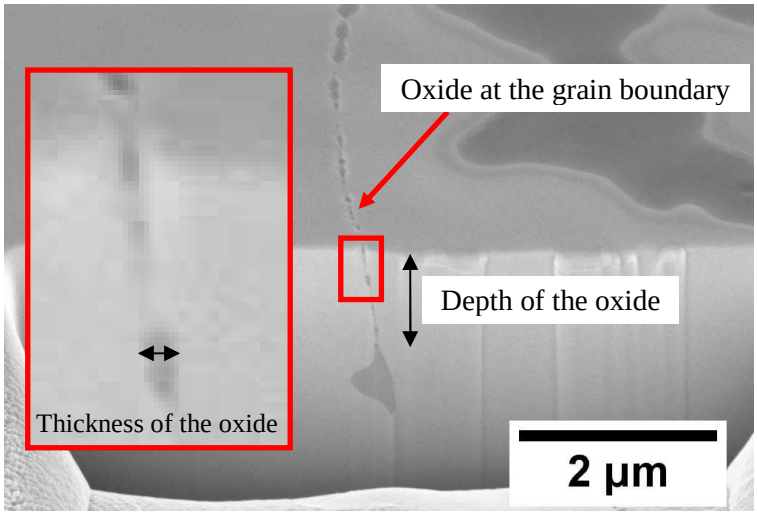

Figure 5.20 Schematic showing how the depth and thickness of the oxide were measured in Ni Alloy samples exposed for 4500 h.

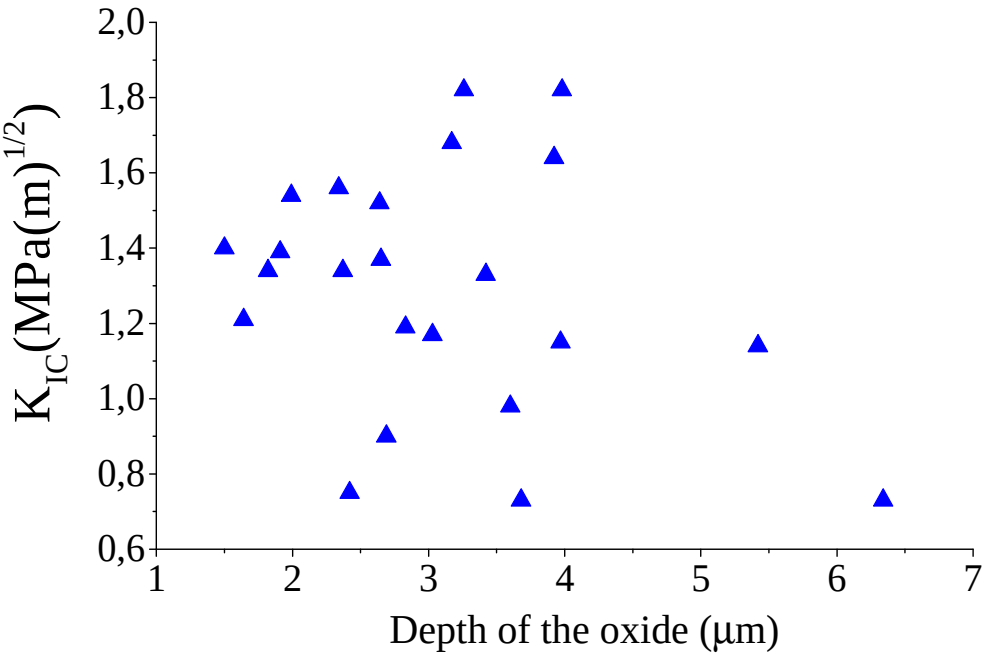

Figure 5.21 Calculated fracture toughness against the depth of the oxide for the 23 cantilevers fractured in Ni Alloy 600 sample exposed for 4500 h.

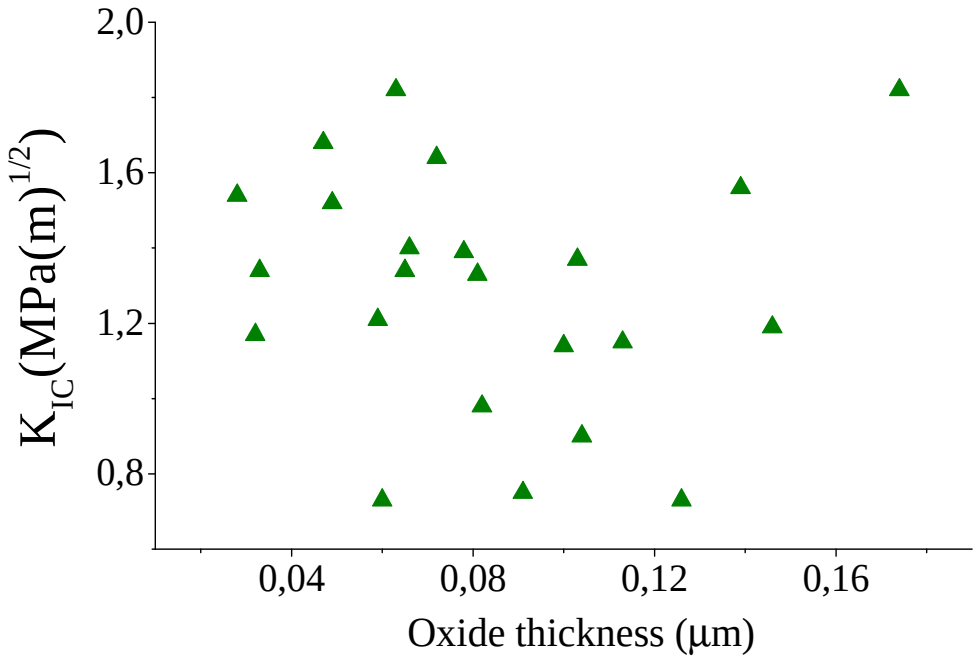

Figure 5.22 Calculated fracture toughness against the oxide thickness for the 23 cantilevers fractured in Ni Alloy 600 sample exposed for 4500 h.

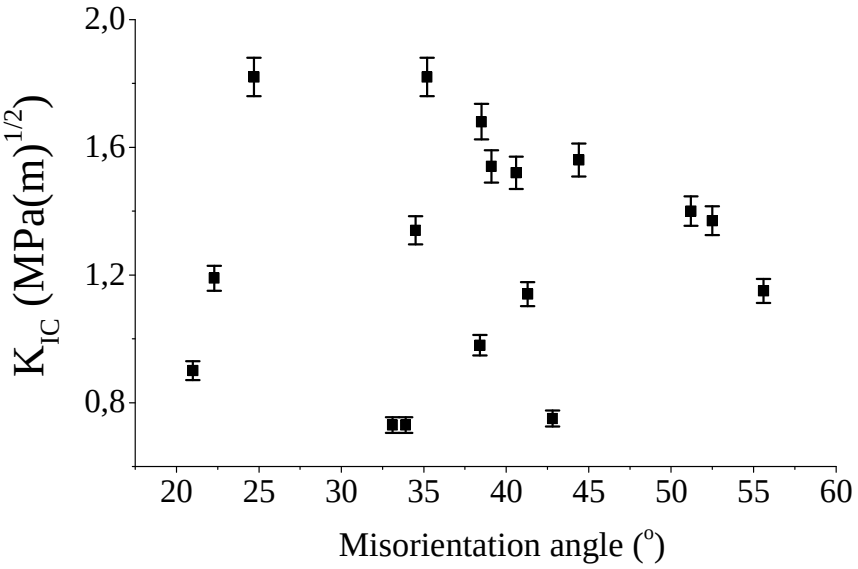

Figure 5.23 Fracture toughness as a function of the misorientation angle for cantilevers that fractured in Ni Alloy 600 sample exposed for 4500 h.

5.5.7 Influence of grain boundary misorientation on the fracture toughness

To determine whether the fracture toughness calculated for the oxidised boundaries in the 23 tested cantilevers depends on the misorientation of the grain boundaries, the misorientations were determined using EBSD. Because before testing the cantilevers the sample surface was not suitable for EBSD, this was performed after testing. The sample was repolished using colloidal silica, after all the post-test images were recorded. The misorientation in an angle/axis form for the tested cantilevers is presented in **Table 5.1** and a graph showing the fracture toughness values against the misorientation angle is shown in **Figure 5.23.** Out of the 23 cantilevers tested, the misorientation of the grain boundary could only be calculated for 17 because some of the cantilevers (7, 8, 12, 21, 22, 23) were destroyed in order to do the 3D reconstruction and the exposure of the fracture surface (see **Section 5.5.8**). As shown in **Figure 5.23** there is no direct correlation between the fracture toughness value of the tested cantilevers in Ni Alloy 600 sample exposed for 4500h and the misorientation angle.

5.5.8 3D FIB Reconstruction

To further investigate whether the fracture at the oxidised grain boundary separated the oxide from the oxide or the oxide from the metal, the method of 3D FIB reconstruction was implemented for one of the tested cantilevers. This method has been used successfully before, to study the evolution of residual stress and crack morphology in alumina [134]**.**

Table 5.1 Misorientation for the 23 oxidised grain boundaries given in an angle/axis form milled in Ni Alloy 600 sample exposed for 4500 h.

G.b. ID	K_{IC} (MPa(m)$^{1/2}$)	Angle (^{o})	Axis			Sigma	Plane 1			Plane 2		
			h	k	l		u	v	w	u	v	w
1	1.0	38.4	-5	6	5	7	-15	-19	16	0	-15	-8
2	1.7	38.5	-6	11	-14	-	-9	-20	10	-14	-9	9
3	0.9	21.0	1	-29	6	-	-16	17	-14	-20	-15	16
4	1.4	51.2	18	-5	24	-	-9	-25	-6	1	2	-2
5	0.7	33.9	-2	3	-4	-	1	-24	1	14	5	-5
6	1.8	24.7	13	-13	7	-	1	0	-30	-27	-9	-8
7	1.39	-	-	-	-	-	-	-	-	-	-	-
8	1.33	-	-	-	-	-	-	-	-	-	-	-
9	1.5	39.1	12	18	17	-	-24	1	7	-13	-19	17
10	1.2	55.6	16	12	15	3	-13	-2	-4	-2	-13	-18
11	1.1	41.3	-2	15	-26	-	5	10	16	-6	-17	-21
12	1.6	-	-	-	-	-	-	-	-	-	-	-
13	1.3	34.5	1	-25	-17	-	11	-10	-9	-21	-6	-16
14	0.8	42.8	26	7	-7	-	7	-10	-12	-1	-28	-5
15	1.5	40.6	14	5	-14	-	3	-25	-7	1	-1	-1
16	1.2	22.3	1	14	8	-	4	-11	7	12	-15	-7
17	0.7	33.1	-9	24	-10	33b	23	6	-12	14	1	-21
18	1.4	52.5	-14	10	11	-	15	-2	17	-16	-19	6
19	1.8	35.2	-2	-21	22	9	-18	-1	3	-10	-5	18
20	1.6	44.4	1	22	-3	-	-6	11	-16	17	-19	-10
21	1.2	-	-	-	-	-	-	-	-	-	-	-
22	1.2	-	-	-	-	-	-	-	-	-	-	-
23	1.3	-	-	-	-	-	-	-	-	-	-	-

The FIB slicing was performed using a Zeiss NVision 40 dual beam FIB instrument using 30 kV Ga^+ incident beam energy and a current of 150 pA. The sample was orientated so that the focused gallium ion beam was at normal incidence to the locally cross-sectional surface of the side of the cantilever. SEM secondary electron (SE) images were taken, using 2 kV electrons, of each sequential x-y 2D slice at a tilt angle of 54°. The dimensions of the milled volume for the cantilever were approximately x=40 μm, y=10 μm and z=10 μm, giving an approximately volume of 4000 μm^3. Before slicing the cantilever, a layer of C was deposited to protect the surface of the cantilever and to enhance the contrast of the top of the cantilever. The 2D SE images were automatically tilt corrected by the microscope software, so that all the final images used for 3D reconstruction were already tilt corrected. All the SE images were corrected for the drift using a cross-correlation algorithm of a feature that appeared in all the images [135]. Since this technique is based entirely on having a good contrast between the different composition elements, an optimal contrast-brightness level (such that the oxide and the carbides could be distinguished from the SE images) was set before taking the SE images. One of the 78 images that were collected during the FIB slicing is presented in **Figure 5.24**.

The area of interest was than selected in all the images and the new dimensions of the reconstructed volume were approximately x=36 μm, y=7 μm and z=7 μm. The voxel dimensions were 7x7x36 nm. The images were than arranged as a 3D set so that the top surface of the sample coincided with the top of the volume that was reconstructed. The reconstruction was performed using the Mercury Software's Avizo 6.1. During the reconstruction three different regions of interest were identified and marked as: opened crack, carbide and oxide. The oxide was present around the crack with a lower grey

level than the carbides. Both the ‘opened crack’ and the ‘carbide’ could be identified automatically using the grey level threshold.

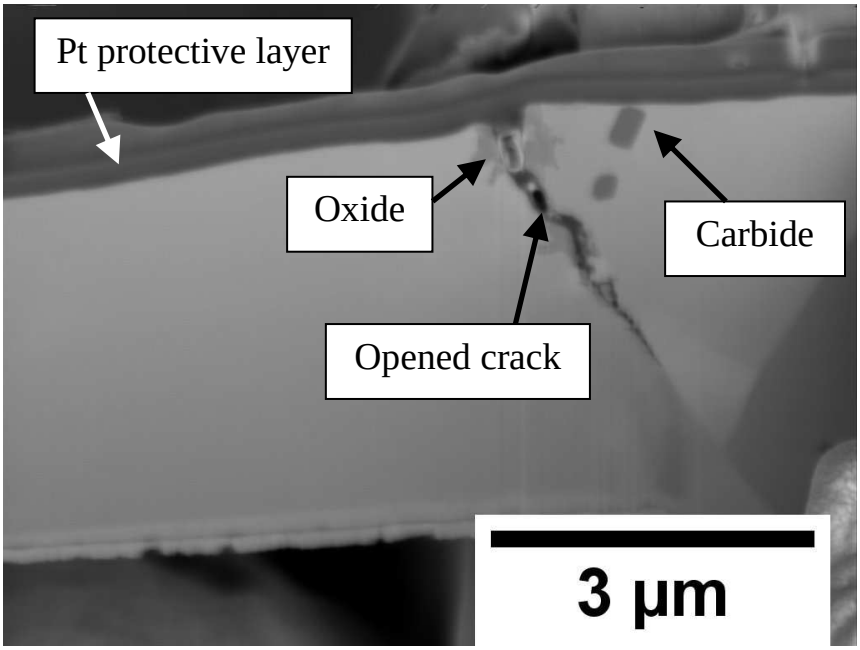

Figure 5.24 Typical 2D SE sample image that was used for the 3D reconstruction of a fractured cantilever milled in Ni Alloy sample exposed for 4500 h.

The ‘oxide’ was very difficult to identify automatically because it had similar grey level to the metal. The oxide was identified by manually selecting the areas where it was present, going through the whole volume by changing the slice number. After the elements were identified, the volume containing the crack was reconstructed. It could then be rotated in 3D so different areas of the volume could be analysed.

Figure 5.25 presents the 3D reconstruction looking at the surface perpendicular to the crack, viewed from each side.

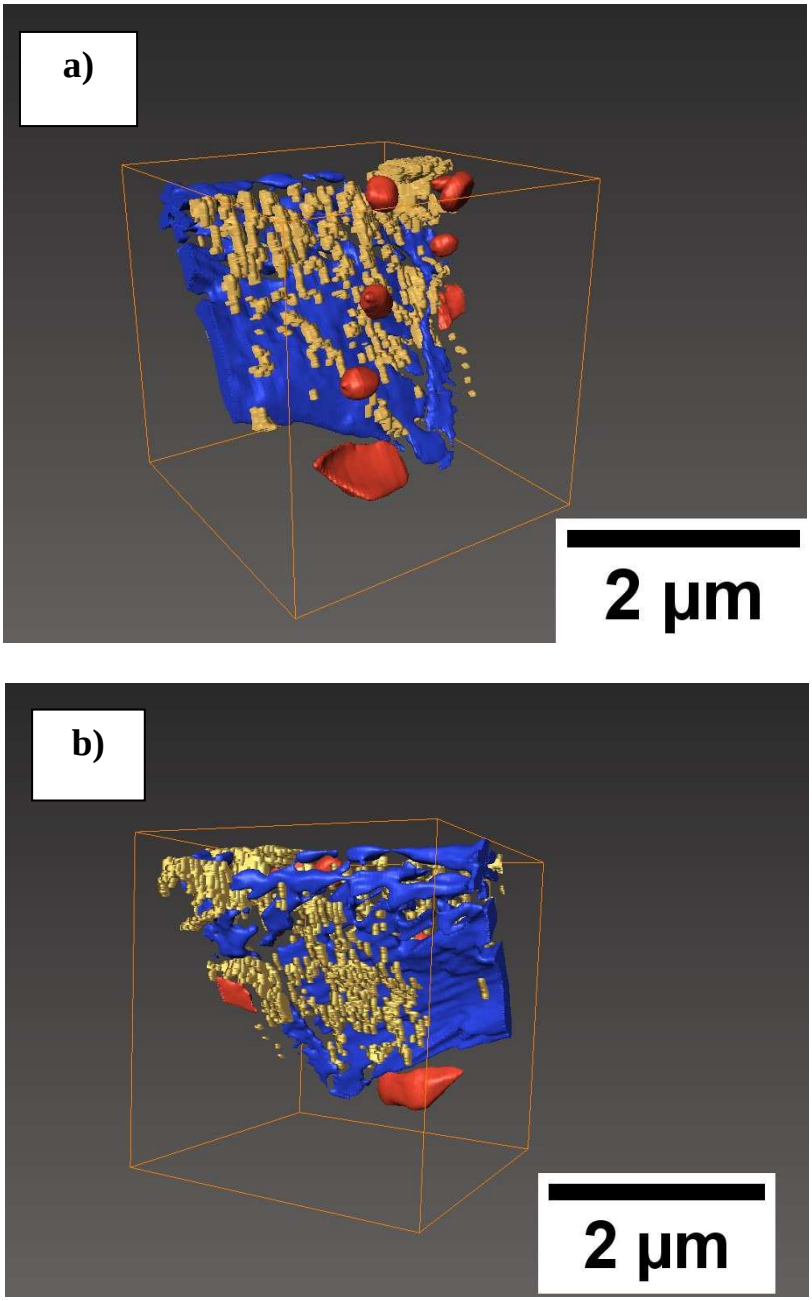

Figure 5.25 3D FIB reconstruction presenting the surface perpendicular to the crack: a) surface on the right and b) surface on the left of the crack. The oxide is depicted in yellow, the opened crack in blue and the carbide in red.

It can be observed that the oxide is present both to the left and to the right of the crack, which means that the crack is going through the oxide layer. In addition, the oxide layer thickness is not constant, so that there is more oxide present on one side of the cantilever than in the other. The oxide layer could, in reality, be more than the one shown in the reconstructed volume, but as mentioned above, the oxide was very sometimes difficult to identify precisely due to the contrast of the 2D SE images.

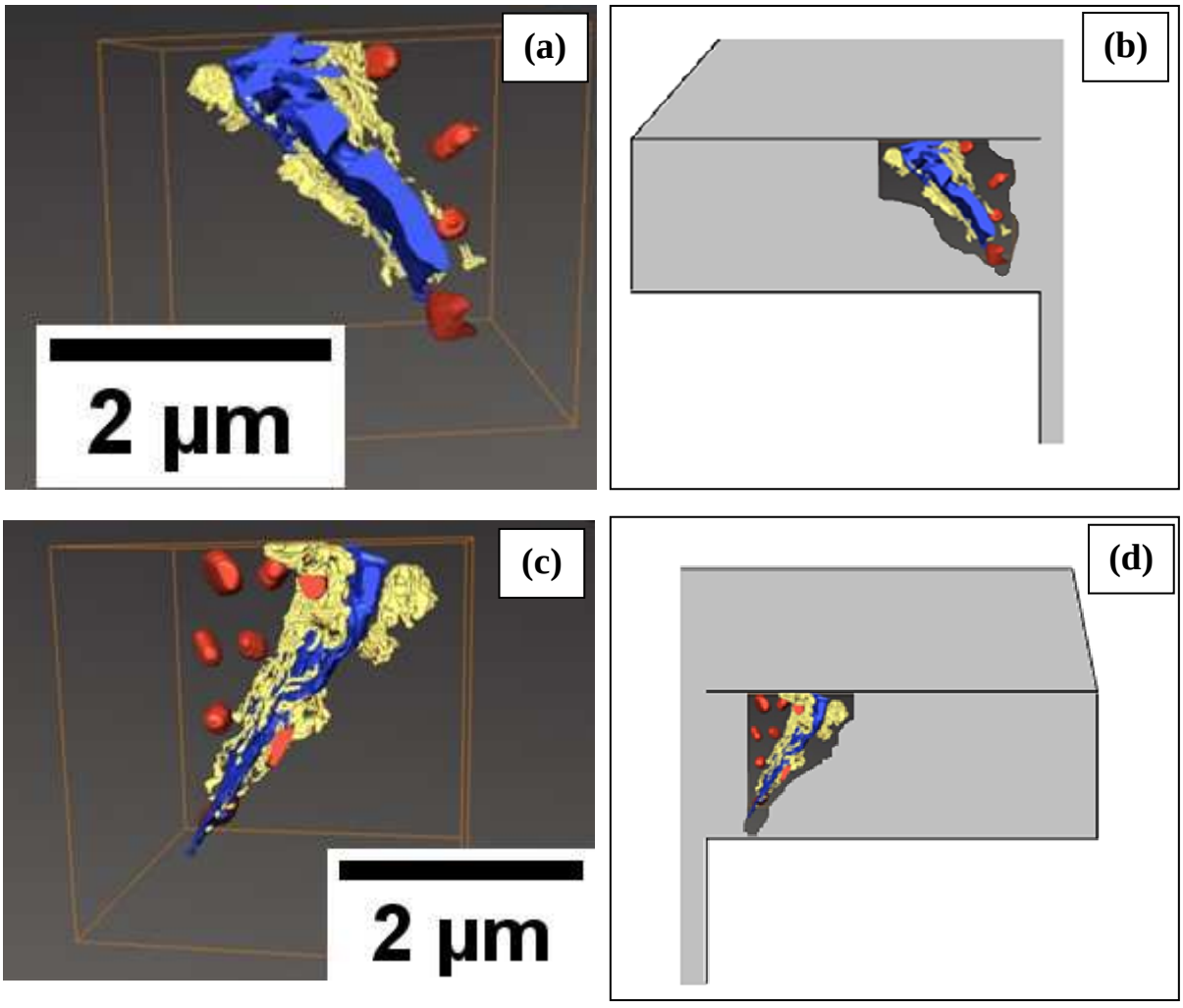

Figure 5.26 3D FIB reconstruction showing the lateral surface of the cantilever: (a) first side of the cantilever, (b) schematic of the cantilever showing the location of (a), (c) second side of the cantilever and (d) schematic of the cantilever showing the location of (c). The oxide is depicted in yellow, the opened crack in blue and the carbide in red.

Though most of the carbides that were detected during the reconstruction are intragranular, in one specimen there was an intergranular carbide present on one side of the cantilever, at the tip of the crack, as shown in **Figure 5.26**.

5.6 Ni-alloy 600 exposed for 1500 h

5.6.1 Sample preparation

Ni Alloy 600 sample was first polished down to a 1 µm diamond finish and then exposed in PWR primary water at 325 ^{o}C for 1500 h with a hydrogen partial pressure of 30 kPa which corresponds to 43 cc/Kg H_2. After exposure, the sample was polished with colloidal silica, to remove the major part of the oxide layer. After surface polishing, 255 nm of material has been removed. The final surface is shown in **Figure 5.27.**

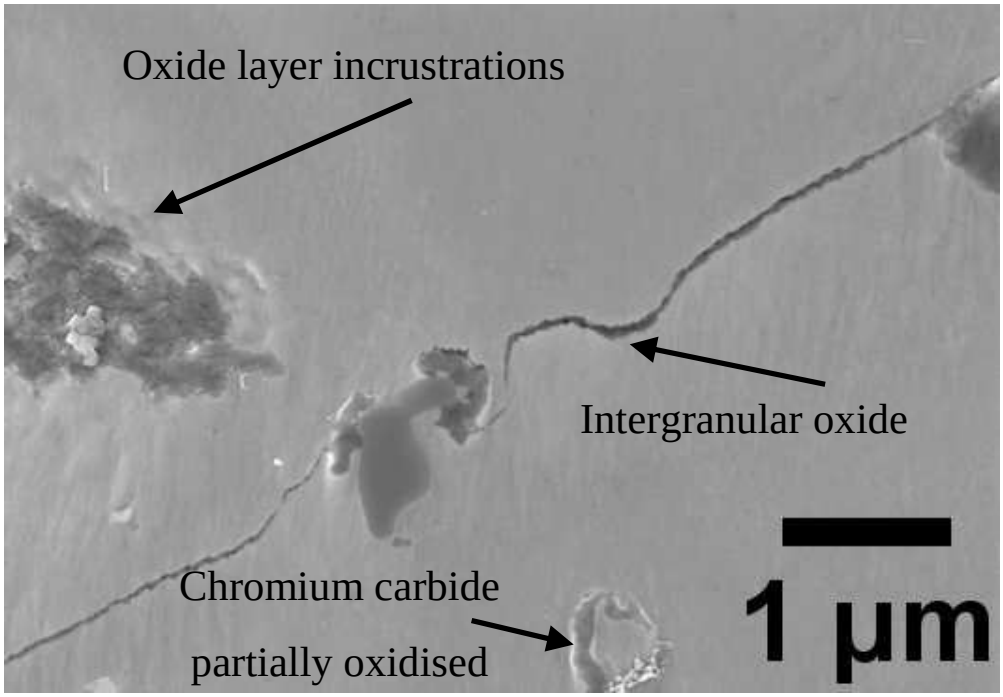

Figure 5.27 Final surface of the Ni Alloy 600 sample exposed for 1500 h showing the oxide layer incrustrations, the intergranular oxide and the chromium carbide that was partially oxidised.

5.6.2 Load vs. displacement curves

Three different cantilevers were tested in the Ni Alloy 600 sample that was exposed for 1500 h. The cantilevers were milled and tested as described in **Sections 5.2.2** and **Section 5.4**. The load vs. displacement curves for all the tested cantilevers are shown in **Figure 5.28.**

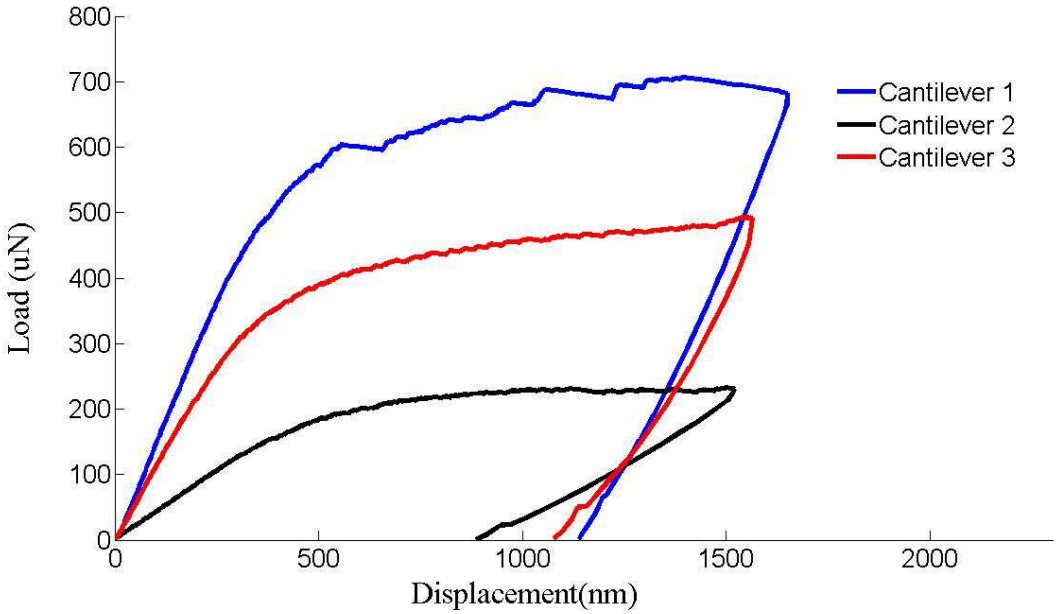

Figure 5.28 Load vs. displacement data for the oxidized cantilevers tested in Ni Alloy 600 sample exposed for 1500 h, showing no fracture.

The load vs. displacement curves for all the tested cantilevers indicate no fracture, but instead, the cantilevers yielded.

From the load vs. displacement curves shown in **Figure 5.28,** the yield stress that corresponds to each tested cantilever was calculated as described in **Section 5.3**. and are shown in **Table 5.2**.

Table 5.2 Yield stress values calculated for the cantilevers tested in Ni Alloy sample exposed for 1500 h.

Cantilever ID	Yield stress (MPa)
Low_oxidised_1	500
Low_oxidised_2	460
Low_oxidised_3	560
Average Yield stress for the tested cantilevers = 507 MPa	

The yield stress associated with the oxidised grain boundaries was in the range of 460-560 MPa, with an average value of 506 MPa.

5.6.3 Micrographs of tested cantilevers

For each of the tested cantilevers, images were recorded using the SEM before and after the tests. A comparison of the micrographs before and after the test of one cantilever is presented in **Figure 5.29** and **Figure 5.30.**

As the load vs. displacement curves indicate, none of the tested cantilevers fractured. Instead, as can be seen from **Figure 5.29b** and **Figure 5.30b**, the cantilevers yielded. SEM observations after the tests show slip bands on the surface as well as on the lateral surface of the cantilever.

5.6.4 Characterising oxidised and unoxidised grain boundaries in terms of misorientation for Ni Alloy 600 samples exposed for 1500 h

To determine which types of the grain boundaries in Ni Alloy 600 oxidise when exposed to the PWR environment, the misorientation of 19 additional oxidized and 19 un-oxidised boundaries was measured. The grain boundaries were selected such that they were from the same area of the sample. First, the oxidised grain boundaries were

selected using the SEM. As shown in **Figure 5.31,** an 'X' was milled using the FIB to mark the oxidized grain boundary.

Then, an EBSD pattern of the area marked with an 'X' was taken. Using the OIM Analysis software in the 'boundary mode', the misorientation as an Angle/Axis pair was determined. In this mode, the boundary normal is calculated to coincide with a vector that connects two predetermined points that belong to adjacent grains, as shown in **Figure 5.32. Table 5.3** presents the misorientation data of the 19 oxidised grain boundaries.

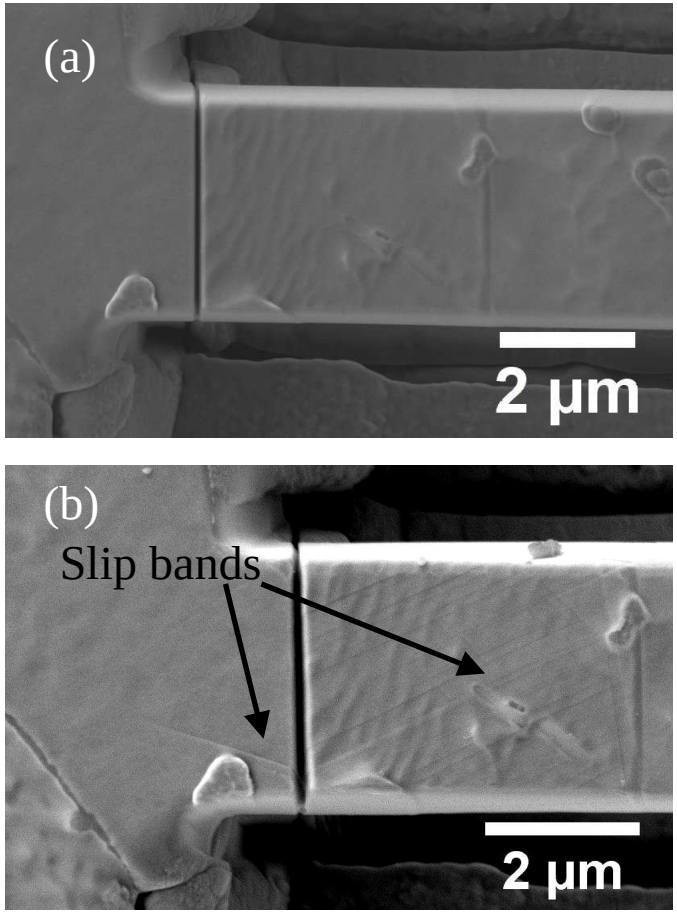

Figure 5.29. Top surface image of a cantilever milled in Ni Alloy 600 sample exposed for 1500 h: (a) before the test and (b) after the test. The arrows indicate the slip bands present after the test.

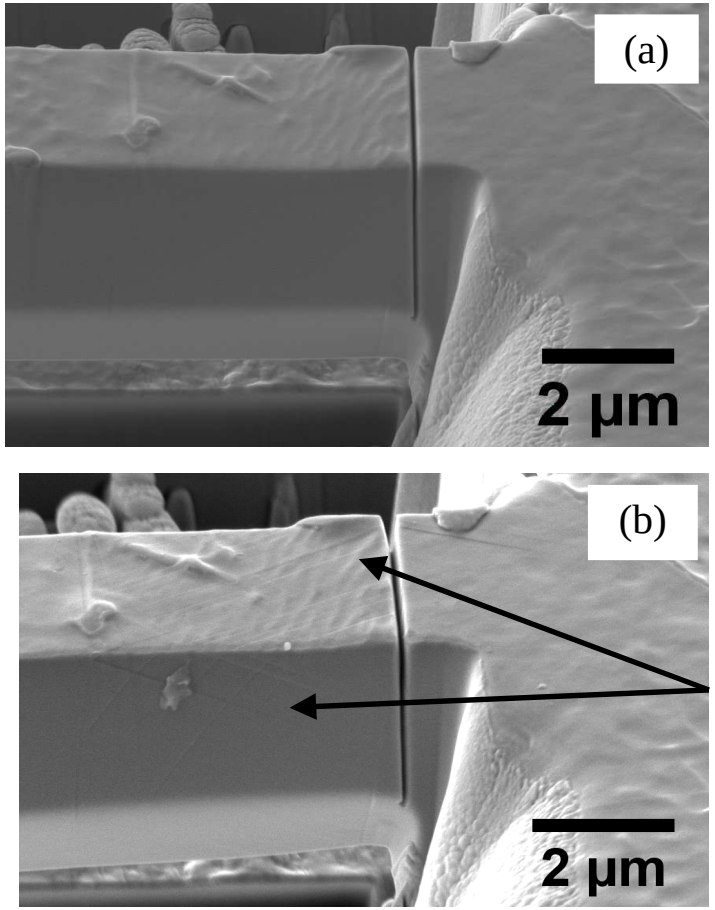

Figure 5.30 Side surface image of a cantilever milled in Ni Alloy 600 sample exposed for 1500 h: (a) before the test and (b) after the test. The arrows indicate the slip bands present after the test.

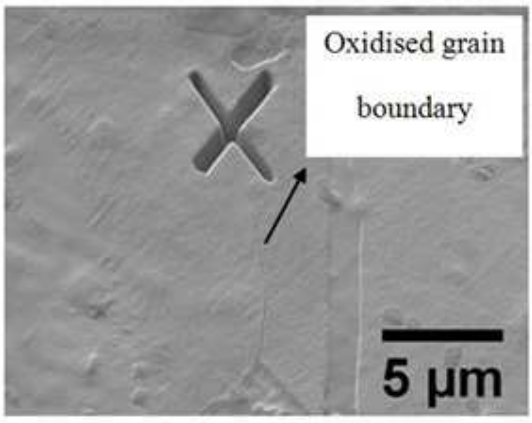

Figure 5.31 Image of an oxidised grain boundary marked with the FIB in Ni Alloy 600 exposed for 1500 h.

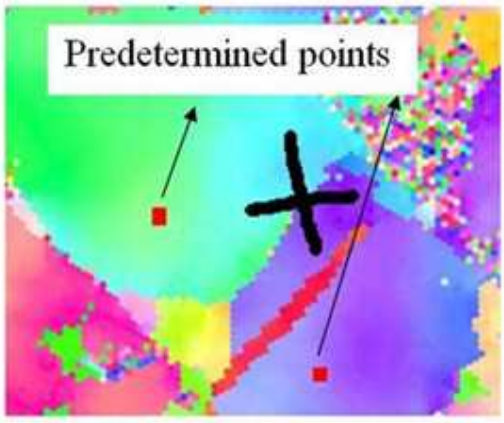

Figure 5.32 Image of the EBSD map of the marked grain boundary showing the points used to calculate the misorientation in Ni Alloy 600 exposed for 1500 h.

Though most of the oxidised grain boundaries for which the misorientation was measured are random grain boundaries, a few special boundaries, such as the ∑3, were oxidised as well. Similarly, the misorientation of the un-oxidised grain boundaries was measured and it is presented in **Table 5.4.**

In comparison to grain boundaries that are oxidised, more grain boundaries that do not oxidise are special boundaries (e.g. ∑3, ∑9).

5.6.5 Oxide depth

To further determine why the grain boundaries that were tested in the Ni Alloy 600 sample exposed for 1500 h did not fracture, the oxide depth was measured in the same way as described in **Section 5.5.6**. In contrast to the cantilevers milled in the Ni Alloy 600 sample exposed for 4500 h, in which the average oxide depth was 3 µm, the average oxide depth in the cantilevers in the Ni Alloy 600 sample exposed for 1500 h, was only 0.58 µm. To see how representative the tested grain boundaries were, the oxide depth for another 24 oxidised grain boundaries in the same sample was measured. The average oxide depth was only 0.67 µm.

Table 5.3 Misorientation for the 19 oxidised grain boundaries given in an angle/axis form.

G.b. ID	Angle (°)	Axis			Sigma	Plane 1			Plane 2		
		h	k	l		u	v	w	u	v	w
1	45.6	-18	19	9	29b	-17	-19	5	5	-15	21
2	14.3	27	4	1	1	5	-7	14	15	-13	7
3	43.6	9	-26	10	-	19	16	2	12	-13	-6
4	49.4	-6	-8	7	-	-1	29	-8	-10	-6	-19
5	46.8	13	-26	-7	-	13	-2	27	12	-25	8
6	18.1	-14	26	1	-	-19	-20	-9	-22	1	-21
7	31.3	-6	5	-26	-	-22	-15	13	-24	-16	1
8	50.2	-8	-7	5	-	-7	7	2	-15	-23	-8
9	49.3	-7	-15	-9	-	4	8	-25	4	15	-18
10	42.9	-20	22	-7	35b	2	-19	22	-9	-26	13
11	54.7	-14	-17	-16	3	4	10	5	-5	4	-2
12	45.4	-17	-19	-17	19b	5	11	-28	2	6	7
13	26.1	-1	-27	-10	-	-13	11	-17	-15	-4	26
14	58.0	-4	-2	-3	-	17	-20	16	29	1	-6
15	38.5	23	-6	-17	-	3	3	26	-6	-1	13
16	48.6	-22	11	6	-	-5	0	-23	-10	13	15
17	30.6	-21	-5	-16	-	13	9	-7	2	26	-13
18	47.6	8	-11	27	-	-20	23	-2	3	-13	2
19	46.1	-22	-15	14	-	-15	21	8	14	23	11

Table 5.4 Misorientation for the 19 un-oxidised grain boundaries given in an angle/axis form.

G.b. ID	Angle (^{o})	Axis			Sigma	Plane 1			Plane 2		
		h	k	l		u	v	w	u	v	w
1	59.8	-19	-17	-16	3	11	-9	7	27	-1	3
2	54.0	16	-21	12	-	15	-12	-4	-23	13	6
3	49.3	-17	1	-17	11	6	19	-16	1	13	-26
4	57.0	17	13	16	3	1	-25	9	-7	9	5
5	57.5	17	-17	12	-	-22	4	-1	-1	17	-22
6	40.4	-1	-17	-24	-	-11	22	1	1	-18	2
7	9.9	-2	-27	5	1	-19	-4	-12	21	6	19
8	60	-9	-10	9	3	13	-12	-4	-9	1	13
9	59.8	-17	17	18	3	-19	10	10	-20	19	8
10	59.7	13	17	13	3	-13	16	-19	-22	-7	3
11	59.6	-15	11	-11	-	-27	-8	4	-15	-12	-10
12	30.7	-9	22	8	-	-7	-12	-5	10	-1	-23
13	57.3	-14	-16	-15	3	-17	-8	-6	-3	-11	-10
14	37.8	-11	9	0	9	-7	-16	20	27	-3	-4
15	41.6	8	-22	5	-	-17	19	-15	16	18	7
16	48.3	-10	1	-10	11	-2	21	-18	5	-6	26
17	29.8	23	-17	-1	-	1	27	8	-3	-22	19
18	60.1	-18	13	-20	-	15	2	1	-5	-14	18
19	49.9	3	3	-4	-	17	3	-7	2	-19	17

5.7 Ni Alloy 600 without oxide

5.7.1 Sample preparation

The unoxidised Ni Alloy 600 sample was first polished down to a 1µm diamond finish and then exposed in PWR primary water at 325 ^{o}C for 4500 h with a hydrogen partial pressure of 30 kPa. After exposure, the sample was polished with colloidal silica, to fully remove the oxide. This sample preparation was performed by AREVA. The cantilevers were manufactured as presented in **Section 5.2.2** and pre-notched as described in **Section 5.2.3**.

5.7.2 Stress-strain curves

Load vs. displacement curves for all the four tested cantilevers made in un-oxidised Ni Alloy 600 are presented in **Figure 5.33**. The load vs. displacement curve is typical for a plastically deformed cantilever. The curve has initial elastic loading, yield and then plastic deformation. The yield stress was calculated from the four tested cantilevers. The results are shown in **Table 5.5**.

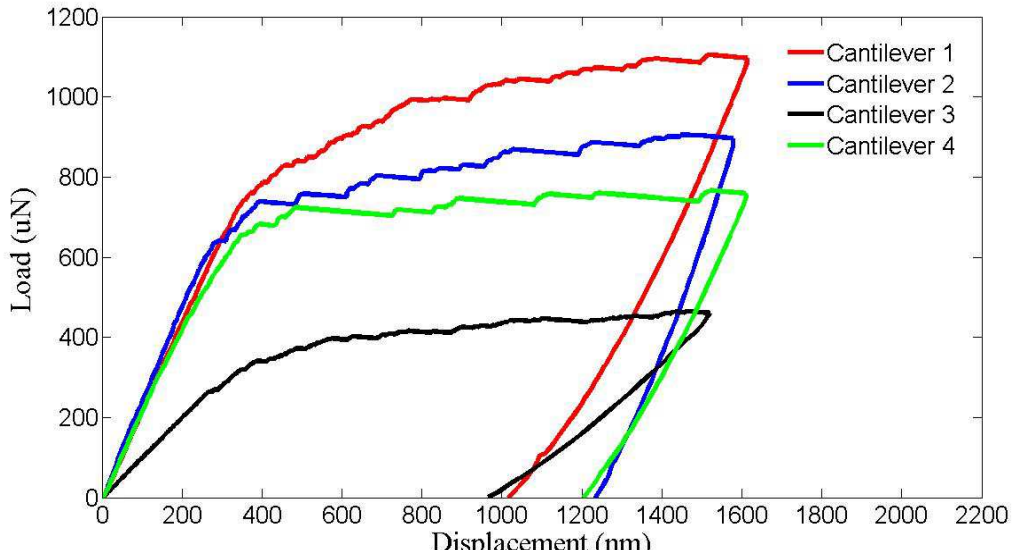

Figure 5.33 Load vs. displacement data for cantilevers tested in un-oxidised Ni Alloy 600, showing no fracture.

Table 5.5 Yield stress values calculated for the cantilevers tested in un-oxidised Ni Alloy 600.

Cantilever ID	Yield stress (MPa)
Unoxidised_1	650
Unoxidised_2	520
Unoxidised_3	510
Unoxidised_4	520
Average Yield stress for the tested cantilevers = 550 MPa	

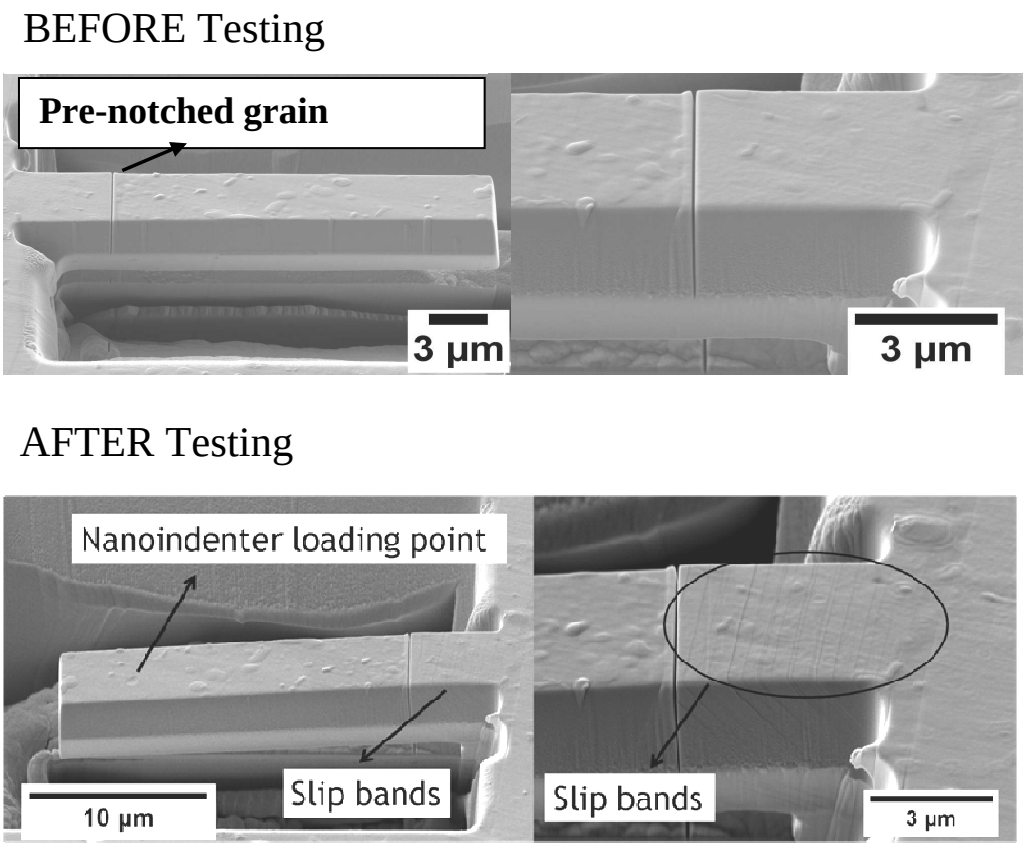

Figure 5.34 Cantilever in un-oxidised Ni Alloy 600 before and after testing. The image of the cantilever after testing shows slip bands (indicated by the arrow).

SEM micrographs were taken after the tests. All the cantilevers yielded and an example of a cantilever before and after the test is shown in **Figure 5.34**.

The cantilevers tested in the un-oxidised samples behaved similarly to the cantilevers tested in the Ni Alloy 600 sample exposed for 1500 h. The cantilevers did not fracture,

but instead, slip bands were present on the surface, as well as underneath the cantilever and on the lateral faces.

5.7.3 EBSD

EBSD maps such as **Figure 5.35** were taken for all the four cantilevers tested and the misorientation of the grain boundaries is shown in **Table 5.6.**

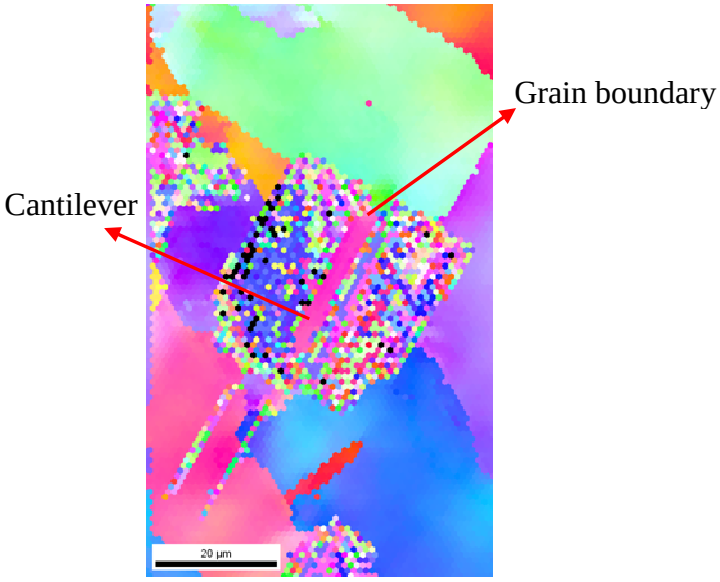

Figure 5.35 EBSD map of one cantilever tested in the un-oxidised Ni Alloy 600 sample showing that the cantilever was milled across a grain boundary.

Table 5. 6 Grain boundary misorientation for the four cantilevers tested in un-oxidised Ni Alloy 600.

Cantilever ID	Angle (°)	Axis			Sigma	Plane 1			Plane 2		
		h	k	l		u	v	w	u	v	w
1	46.1	8	19	-6	-	-1	21	-13	2	4	21
2	47.5	10	-23	14	-	-2	6	-27	13	-18	-9
3	14.3	9	-21	20	1	6	-1	6	-17	-24	-2
4	58.5	15	18	-19	3	21	15	-7	17	12	-5

In contrast to the cantilevers milled in the samples exposed for 4500 h, the cantilevers tested in the un-oxidised samples did not fracture, but instead deformed plastically showing the same behaviour as the cantilevers tested in samples oxidised for 1500 h. This was observed for all the four tested cantilever milled at grain boundaries with different orientations.

5.8 Summary

This study is believed to be the first that determines the fracture toughness of oxidised grain boundaries. The current work is in agreement with the previous study done by Lozano-Perez *et al.* [119] which observed the brittle character of the intergranular oxide. The method described is a valid testing method for determining grain boundary strength in SCC susceptible alloy. The fracture toughness associated with fracture of grain boundary oxide for tested cantilevers milled in the Ni Alloy 600 sample exposed for 4500 h was in the range of 0.73 – 1.82 MPa $(m)^{1/2}$, with an average value of 1.3 MPa $(m)^{1/2}$. The specimens containing oxidised grain boundaries in the Ni Alloy 600 sample exposed for 4500 h fractured at the boundary after small amounts of plasticity. SEM micrographs of the exposed fracture surfaces of the tested cantilevers revealed that the crack propagated down the oxidised grain boundary, starting at the notch. Not all the cracks propagated perpendicular to the surface; however, no correlation has been determined between the fracture toughness values and the crack propagation angle.

Cantilevers milled both in Ni Alloy 600 sample exposed for 1500 h and in the un-oxidised specimens yielded, and did not fracture. All the tested cantilevers showed slip bands either on the surface of the cantilever, on the lateral side or underneath the cantilever, close to the fixed end.

Oxide depth and thickness were measured in both Ni Alloy 600 samples that were exposed for 4500 h and 1500 h. The average oxide depth in samples exposed for 4500 h was approximately 3 µm and in samples exposed for 1500 h was 0.68 µm. The values of the oxide depth are much lower than the ones observed by Fujii et.al. [133] in a study that measured the strength of oxidized grain boundaries in Ni Alloy 600 exposed to the PWR water environment, where reported oxidation depth at the grain boundary were 2 µm in the samples exposed for 1500 h and 8 µm inthe samples that were exposed for 2700 h. The work reported here and Fujii's both show that the oxidation depth increases with the exposure time [133]. The experiments presented in this thesis determined no correlation between the oxide depth and the fracture toughness values when the oxide is deep. A weak correlation has been observed between the fracture toughness values and the oxide thickness, such that the fracture toughness decreases with the increase in the oxide thickness. The average oxide thickness observed in the samples exposed for 4500 h was 83 nm. These values compare to the ones obtained by Fujii *et al.*, where TEM measurements obtained a thickness of the oxide of approximately 100 nm for samples exposed for 1500 and 2700 h. The deeper oxide thickness measured by Fujii et al. is also due to the fact that the samples were under tension. Fujii *et al.* also determined that the fracture stress of oxidized grain boundaries in the samples exposed for 1500 h was higher than the fracture stress of oxidized grain boundaries in samples exposed for 2700 h. It can be concluded that while Fujii obtained fracture of the oxidised grain boundaries in the sample exposed for 1500 h, the samples exposed for 1500 h used during the experiments presented in this thesis were not oxidised enough to use fracture using micro-cantilevers. Also another reason for the fact that Fujii obtained fracture on the samples exposed for 1500 h is the size of the specimens. The large specimens used by Fujii [133] are easier to fracture (for larger specimens the plasticity

is reduced), while the small micro-cantilevers used in the present study are more difficult to fracture, fracture occurring only if the sample is very brittle.

From the measurements of the grain boundary misorientation it could be determined that only one out of 19 grain boundaries that get oxidised in the Ni Alloy sample exposed for 1500 h was a special (∑3) grain boundary. Out of the 19 grain boundaries that did not oxidise from the sample, seven of them were special boundaries such as ∑3 and ∑9.

The misorientation of the grain boundaries was tested for the cantilevers that fractured in Ni Alloy 600 sample exposed for 4500 h and the fracture toughness was plotted against the misorientation angle. From the plot, no direct correlation was observed.

3D FIB reconstruction of one of the cantilevers tested in sample that was exposed to 4500 h shows that the crack path goes through the oxide layer, so the fracture toughness values calculated in the study represent the fracture toughness of the oxide layer. In addition, the 3D reconstruction depicts a chromium carbide present at the end of the crack tip, which might have had the effect of stopping the crack from propagating further, though it this cannot be stated from only one observation. It has been observed before [168] that craks can also propagate around the oxide that surrounded intergranular carbides.

6 Characterisation of an IGSCC initiation site in 304 SS

6.1 Introduction

Predicting IGSCC in 304 SS is a very complex problem that is yet not fully understood. IGSCC combines a susceptible material, an applied stress and a corrosive environment but the influence of each on cracking has not been sufficiently quantified. In order to design resistant materials and predict IGSCC it is important to understand both the initiation (number of initiation sites, time to initiation, probability of initiation) as well as the propagation (propagation rate of an existing crack). The effect of several factors, such as: microstructure susceptibility, the temperature/composition of the environment and the level of stress or strain required needs to be understood [136]. It has been shown that the grain boundary orientation [55][137][138] makes a microstructure susceptible to IGSCC, but the exact definition has not been proposed and it might be that no general definition can be stated. Instead, specific definitions are needed for different material and environment combinations.

It has been observed in several studies that some of the parameters that control intergranular crack initiation are: the values of the Schmid factor in adjacent grains [139][140][141][142][143], the grain boundary inclination to the tensile axis [140][143] and the microstructure of grain boundaries [55][137][138][144]. However, no conclusion was reached into what the main factor is. What is more, the fact that the environment has an effect on the IGSCC is a limitation on applying this condition to all environments.

In addition, the level of sensitization of the grain boundaries in stainless steel is also correlated to the crack initiation, because after thermal sensitization, for example, chromium carbide precipitation causes depletion of Cr at the grain boundary. Austenitic stainless steels can also become sensitised after irradiation [145]. The most significant proposed parameters affecting crack initiation will be discussed in **Section 6.1.1**, **Section 6.1.2** and **Section 6.1.3**, and examples of models that have been proposed to predict crack initiation and to identify sites that are most probable for initiation will be discussed in more detail in **Section 6.2**.

6.1.1 Role of Schmid factor in predicting crack initiation

One parameter that characterises the deformation is the Schmid factor [146], which expresses the geometrical relationship between the direction of the force applied and the shear deformation mode. It therefore provides a measure of the tendency for plastic deformation of a grain. The relationship between the resolved shear stress, the area of the slip plane and the force applied is given in **Equation (14)**:

$$\tau_{CRSS} = \frac{F cos\lambda}{A/cos\varphi} = \frac{F}{A} cos\varphi cos\lambda \quad \textbf{(14)}$$

where F is the applied force, A is the cross sectional area, φ is the angle between the tensile axis and the slip normal and λ is the angle between the slip direction and tensile axis, as shown in **Figure 6.1.** Schmid's Law states that there is a constant value, τ_{CRSS}, named the critical resolved shear stress, for which slip occurs in any material. Since for each grain there is only one primary slip system, a single value can be assigned to a grain. The Schmid factor *m*, is calculated for a grain to be:

$$m = \cos\lambda \, cos\varphi \quad \textbf{(15)}$$

The uniaxial tensile stress to cause yield in the grain is thus:

$$\sigma_{y_g} = \frac{\tau_{CRSS}}{m} \quad \textbf{(16)}$$

where τ_{CRSS} is the critical resolved shear stress and m is the Schmid factor.

From inspection of **Equation (15)** the minimum uniaxial tensile stress to cause yield occurs when $\lambda=\varphi=45^{o}$, so that: $\sigma_{y_g} = 2\tau_{CRSS}$. For other grain orientations, a higher tensile stress is required for yield. The assumption that there is no constraint is made. In the case where constraint is present, the deformation of surrounding grains will affect (usually increase) the tensile stress required to cause yield.

The relationship between Schmid factor and intergranular cracking is seen in the following examples. For instance, in high temperature fatigue experiments that observed the properties of grain boundaries where cracking initiates, a strong correlation

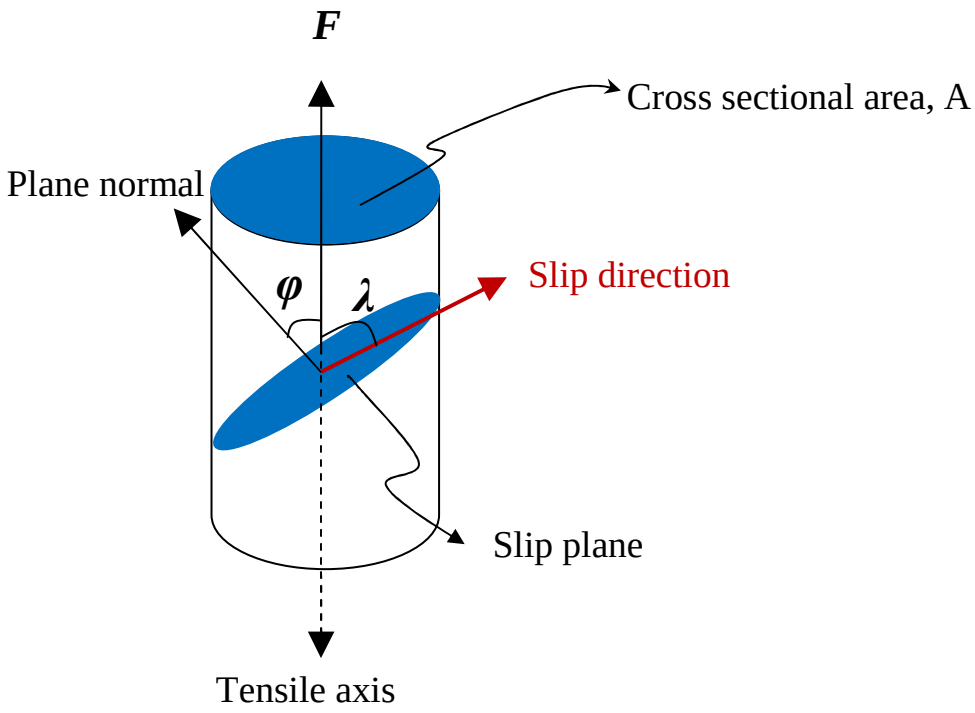

Figure 6.1 Schematic describing the Schmid's Law variables [Adapted from [147]].

was observed between the deformation parameters and the intergranular crack initiation. Rho *et al.* [139] studied intergranular cavitation in low cycle fatigue of Nb-A286 alloy at 650 ^{o}C, in connection to the Schmid factor. From eight different grain boundaries, it was concluded that cavitations are accelerated at high angle grain boundaries due to the strain incompatibility of adjacent grains. This is described by the difference in Schmid factor of the adjacent grains.

McMurtrey *et al.* [140] studied irradiation assisted stress corrosion cracking of Fe-13Cr-15Ni austenitic steel that was first irradiated using 2 MeV protons at a temperature of 360 ^{o}C to 5 dpa and then strained at 288 ^{o}C in a simulated BWR environment. It was concluded both experimentally and through simulations that crack initiation at the grain boundary depends on the slip continuity, such that the grain boundaries where cracking initiated were adjacent to a grain that was characterized by a low Schmid factor. For the simulations, the value of the Schmid factor was between 0.37 and 0.49, with the majority of the grains having a Schmid factor around 0.40. It can be deduced that, by comparison with the study of fatigue initiation described above, this could also be correlated with high Schmid factor mismatch since it occurred at boundaries adjacent to grains with a low Schmid factor.

Fukuya *et al.* [141] also studied the effect of the Schmid factor mismatch, looking at grain separation in cold worked SU2316 stainless steels irradiated to 73 dpa at a temperature of 300 ^{o}C, using a dose rate of $1.5x10^{-7}$ dpa/s and then strained at 320 ^{o}C in argon. In this study, 72 high angle grain boundaries were analysed and it was concluded that the tendency for grain boundary separation increased with the increase of Schmid factor mismatch. Looking at the fraction of the separated grain boundaries, 10% had a difference in the Schmid factor mismatch less than 0.05, 18% had a difference between 0.01 and 0.1, 33% had a difference between 0.1 and 0.15 and the rest had a difference

greater than 0.15, as shown in **Figure 6.2**. In addition, it can be observed that the separated boundaries tend to have a higher Schmid factor difference than the unseparated ones.

The same pattern was observed by West *et al.* [142][143] in a study of the intergranular cracking of 7 dpa proton-irradiated 316L steel in supercritical water that was strained at 400 ^{o}C. It was concluded that intergranular cracking is promoted by grains of higher Schmid factor adjacent to grains with a low Schmid factor; the results indicate a slight correlation to the Schmid factor mismatch as is indicated in **Figure 6.3**.

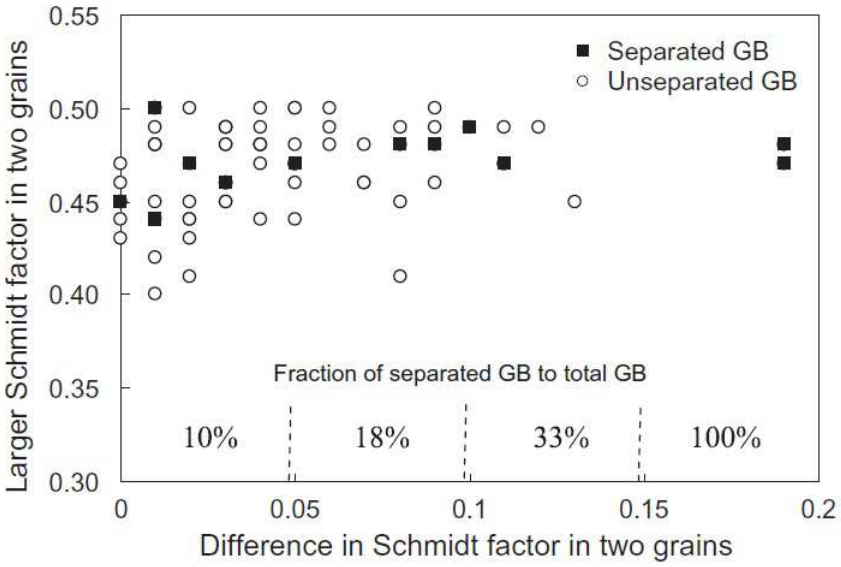

Figure 6.2 The role of Schmid factor and Schmid factor mismatch on the grain boundaries separation in cold worked SU2316 stainless steels irradiated to 73 dpa at a temperature of 300 ^{o}C and strained 320 ^{o}C.As the fraction of the separated grain boundaries increases from 10% to 39%, the Schmid factor mismatch increases from less than 0.05 to more than 0.15 [141].

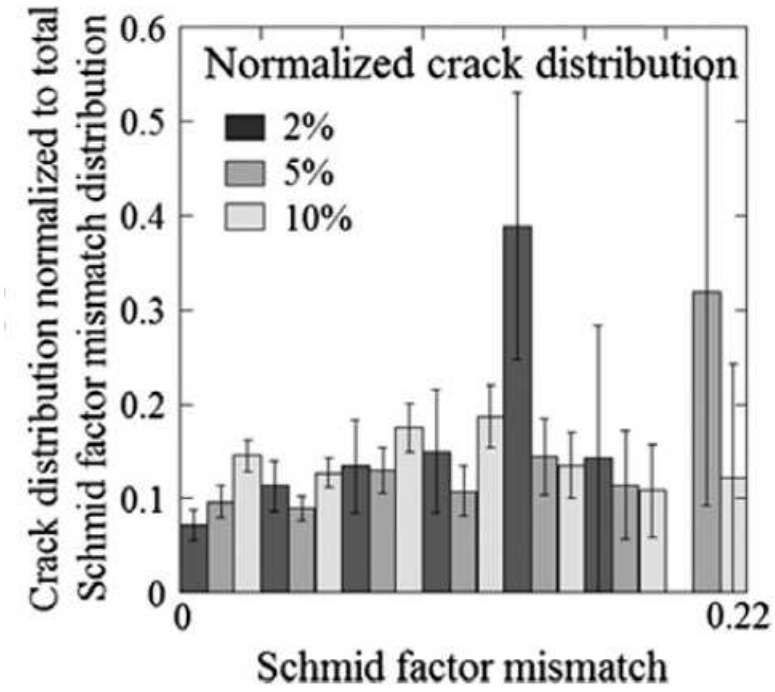

Figure 6.3 Role of Schmid factor mismatch on intergranular cracking of 7dpa proton irradiated 316L steel in supercritical water at 2%, 5% and 10% stain at 400 ^{o}C. In this distribution 39%, 30% and 27% of the grain boundaries that cracked had a Schmid factor mismatch greater than 0.07 for the three different strain levels [142].

These studies indicate that the Schmid factor mismatch is a parameter that influences cracking, however it has not been demonstrated that it is the dominant parameter. The Schmid factor mismatch is not sufficient to predict cracking by itself. For example, in **Figure 6.2** some of the separated grain boundaries have a Schmid factor mismatch of 0.05 or lower. Another parameter that influences cracking is the grain boundary inclination, which will be described next.

6.1.2 Role of grain boundary inclination to the tensile axis

The grain boundary inclination (also named the grain boundary trace angle) to the tensile axis, coupled with the Schmid factor mismatch, has been shown to play also an important role in predicting crack initiation [140][142][143]. McMurtrey *et al.*. [140] observed that most of the grain boundaries that experienced cracking in Fe-13Cr-15Ni

austenitic steel proton-irradiated at a temperature of 360 ^{o}C to 5 dpa and strained at 288 ^{o}C in simulated BWR environment, had surface trace angles of 70° or greater. West *et al.* [143] observed during an irradiation assisted stress corrosion cracking on austenitic steels that the majority of cracks formed at the grain boundaries that were perpendicular to the tensile direction. In addition, the cracks occurred at grain boundaries that had a boundary trace angle of 50° or greater.

6.1.3 Role of grain boundary misorientation and CSL value

It has been reported many times that the susceptibility to IGSCC of materials is determined by the crystallography of the grain boundaries (see for example [55][137][138]), and models have been created to predict intergranular degradation based on the distribution of "special" and "random" grain boundaries. The boundaries with $\sum \leq 29$ are often found to be more resistant to cavitation, sensitization, fracture, stress-corrosion cracking because they tend to have special chemical, mechanical, electronic, kinetic and energetic properties [149]. These grain boundaries also have lower energies as shown in **Figure 6.4.** If IGSCC would be determined only by the geometry of the grain boundary, then the resistance limit would be the one indicated in **Figure 6.4** [150]. Some examples of data that support this classification are presented in **Section 2.1.4**.

The most recent model that combines the effect of the Schmid factor and the grain boundary inclination to the tensile direction is the Schmid-modified grain boundary stress [142] model. This calculates the grain boundary normal stress and was used to study irradiated 316L stainless steel in supercritical water. The model and its validation by experimental data will be described further in **Section 6.2**.

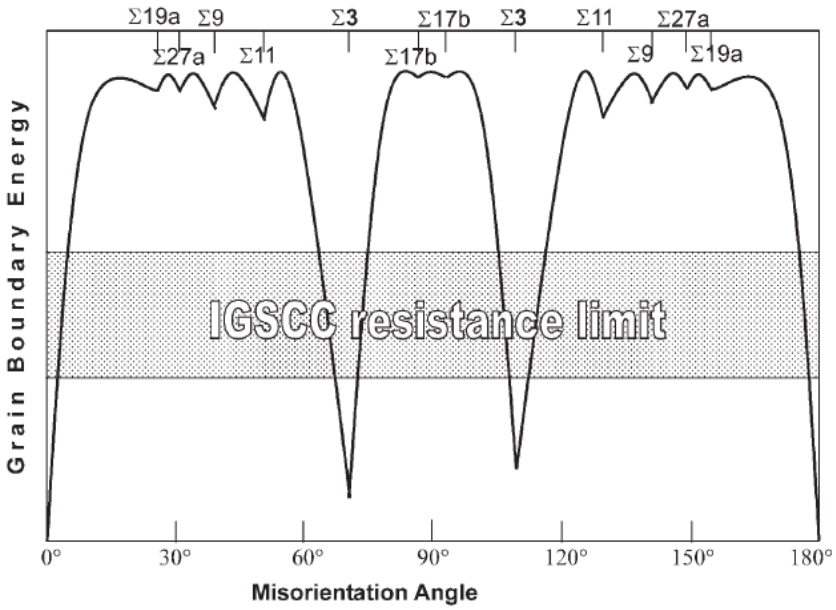

Figure 6.4 IGSCC resistance presented as a function of grain boundary energy and misorientation angle [150].

6.2 Schmid-Modified Grain Boundary Stress (SMGBS) model

This section presents the derivation of the SMGBS model, which is described in the literature; the model was previously used to study the intergranular cracking behaviour of irradiated 316L stainless steel at 400 ^{o}C in supercritical water [142]. The study concluded that the intergranular cracking depends on the value of the normal stress calculated for each grain boundary, such that intergranular crack nucleation is more likely to occur at grain boundaries that are highly stressed. The purpose of the study was not to calculate the value for the normal stress for each grain boundary, but to demonstrate that grain boundary to grain boundary variation in the local stress depends on the inclination of the grain relative to the tensile axis, as well as the likelihood of the grain to deform [142].

The normal stress acting on a grain boundary is calculated to be the perpendicular load on the grain boundary plane, divided by the area on which it is applied. The tensile stress acting on a grain is assumed to be the flow stress of the grain divided by the area of the grain, as illustrated in **Figure 6.5**.

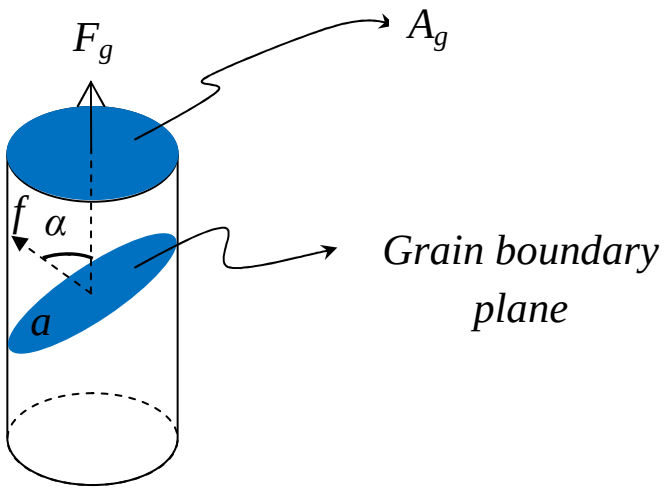

Figure 6.5 Schematic describing the relationship between the normal stress action on the grain boundary plane and the flow stress [Adapted from [142]].

The equations that calculate the normal stress acting on a grain boundary are presented below:

$$\sigma_N = \frac{f}{a} = \frac{F_g cos\alpha}{A_g/cos\alpha} \quad \textbf{(17)}$$

$$\sigma_{f_g} = \frac{F_g}{A_g} \quad \textbf{(18)}$$

From **Equation (17)** and **Equation (18)**, the normal stress on a grain boundary is:

$$\sigma_N = \sigma_{f_g}(cos\alpha)^2 \quad \textbf{(19)}$$

where α is the angle between the normal to the grain boundary plane and the tensile axis. To apply the model to two-dimensional data of a microstructure, the value of α was calculated as a function of the angle between the tensile direction and the grain boundary plane, φ, and the surface trace inclination of the grain boundary with respect to the tensile axis, θ. **Figure 6.6** shows a diagram defining the angles mentioned above.

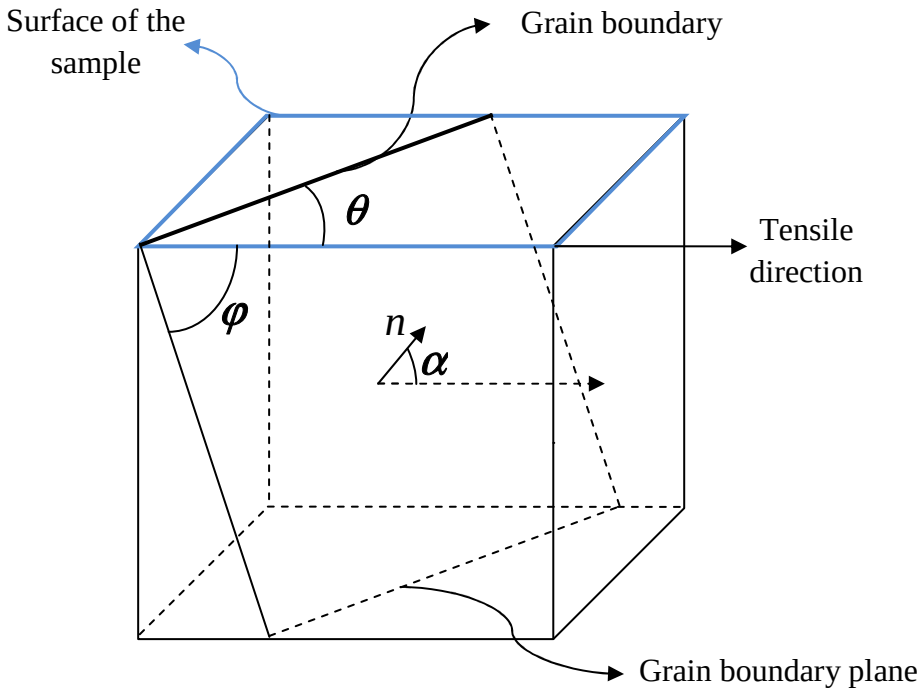

Figure 6.6 Diagram defining the variables used to express the normalized effective normal stress used in the SMBGS model [Adapted from [142]].

The derivation is presented by West *et al.* [142] and Alexandreanu [166] and the formula for α is given below:

$$\alpha = \arccos\left(\sqrt{\frac{1}{tan^2\varphi} + \frac{1}{tan^2\theta} + 1}\right)^{-1} \qquad \textbf{(20)}$$

The model assumes that the bulk yield stress and the flow stress of the polycrystalline material are related by the average Schmid factor of the material, such that:

$$\sigma_f = \sigma_y \propto \frac{1}{m_{avg}} \quad \textbf{(21)}$$

where m_{avg} is the average Schmid factor for the microstructure (this term thus allows texture effects to be considered). Using the same assumption, the flow stress of an individual grain σ_{f_g} is calculated as below; this is the tensile stress required to yield an individual grain.

$$\sigma_{f_g} = \sigma_f \frac{m_{avg}}{mg} \quad \textbf{(22)}$$

If the flow stress is set to be 1, so that the relative behaviours of grains may be considered, the normalized effective normal stress acting on a grain boundary is calculated from **Equation (19)** to be:

$$\sigma_N = \frac{m_{avg}}{mg}(cos\alpha)^2 \quad \textbf{(23)}$$

However, the normalized effective normal stress acting on a grain boundary should be a function that integrates the deformation properties of both grains. For this reason, the assumption made is that the tensile stress acting on a grain boundary depends on the average flow stress of the adjacent grains, so the final equation for the normalised effective normal stress is as presented below [142]:

$$\sigma_N = \frac{1}{2}\left(\frac{m_{avg}}{m_{g1}} + \frac{m_{avg}}{m_{g2}}\right)(cos\alpha)^2 \quad \textbf{(24)}$$

The model is used in the literature to look at the strain incompatibilities at grain boundaries [167] and it is applied to the crack distributions as a function of the Schmid factor and trace inclination. The author uses **Equation (23)** to generate the SMGBS curves, such that only one of the two grains is considered for the analysis. While the normal stress should really be calculated using **Equation (24)** instead of **Equation (23),**

the authors did not use it because it would involve more normalization to take into consideration the probability of adjacent grain boundaries that have the same Schmid factor [167]. When both the trace inclination and Schmid factor of one of the grains are measured, the angle between the tensile axis and the grain boundary plane is generated.

The final dependency of the normal stress as a function of the Schmid factor, trace inclination and boundary plane is shown in **Figure 6.7**. **Figure 6.7** shows that, as outlined at the beginning of this section, boundary to boundary variation in the local stress depends on the Schmid factor and trace inclination. The comparison between the normal stress that corresponds to a grain boundary with a low Schmid factor and a grain with a high Schmid factor is made as a function of the trace inclination angle. It can be observed that for the same values of β, the highest normal stress corresponds to the grain with the highest Schmid factor. In addition, the normal stress increases with both the inclination trace and β. Variable β is related to φ through the following expression:

$\varphi = arctan\sqrt{\frac{\frac{1}{cos^2\beta}-1}{\frac{1}{tan^2\beta}+1}}$ [167].

To increase the applicability of the model, the concept of a critical effective normal stress (CNS) was introduced by West *et al.* so that SMGBS curves (**Figure 6.8)** can be

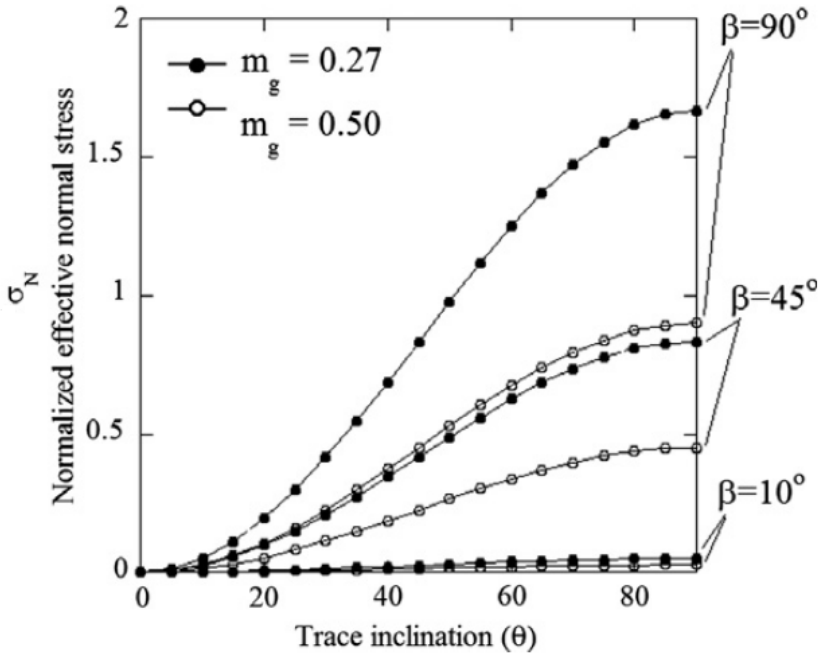

Figure 6.7 Final dependency of the normal stress on the Schmid factor, trace inclination and grain boundary plane [167].

generated for one specific parameter (the trace inclination, Schmid factor or grain boundary plane). Then, this curve can be compared to the distribution of cracked boundaries to determine if the curve predicts the data. One example, for 7 pda proton irradiated 316L steel tested in supercritical water (SCW) at different levels of strain, is presented in **Figure 6.9.** It can be observed that the generated SMBGS curve (shown in black) fits very well the experimental data.

The SMGBS model is used in this thesis to calculate the value of the (normalised) effective normal stress acting on selected grain boundaries and to determine whether this value explains the observed crack initiation site, when compared to the wider population of grain boundaries at which initiation did not occur. The Schmid factor was measured using the EBSD maps; the surface trace inclination, as well as the angle between the tensile direction and the grain boundary plane, were measured using image analysis software (ImageJ) applied to SEM images of a FIB-sectioned sample.

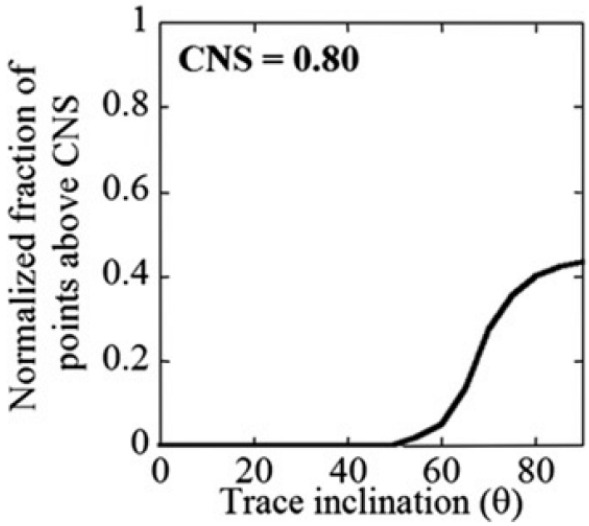

Figure 6.8 Example of a generated SMBGS curve for CNS=0.80. Since the CNS (critical effective normal stress) is normalized, the value will always be between 0 and 1[167].

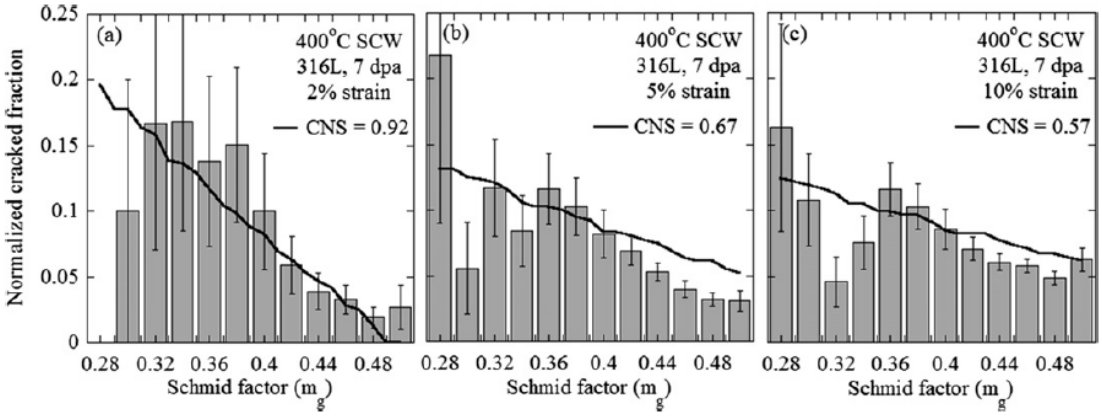

Figure 6.9 Distribution of the cracked grain boundaries for 316L,7 dpa, 400 ^{o}C in SCW (a) as a function of the trace inclination at 2% strain at a CNS=0.92 and (b) as a function of the Schmid factor at 5% strain at a CNS=0.67. The black SMGBS curve predicts very well the two distributions [142].

The SMGBS model described by West *et al.* [142] incorporates the effect of the Schmid factor and the grain boundary inclination, however, it does not take into consideration the role that sensitization plays in predicting IGSCC initiation. In addition, while the model looks at the orientation of the grain boundary plane, its structure is not taken into account. What is unique in applying this model to the current study is that the grain boundary plane was directly measured by sectioning the grain boundaries and also both of the adjacent grains are taken into consideration. The experiments and observations

conducted in this chapter aim to build on the SMGBS model by including in the effect of the grain boundary orientation on the normal stress of grain boundary calculation, and also by extending it to include sensitisation.

The SMGBS model is applied in this study such that the normalized stress is calculated using **Equation (24)** for different grain boundaries (both cracked and intact) as well as for the initiation site to determine whether the highest value for the normal stress corresponds to the initiation site. The initiation site was identified by *in-situ* observations performed at elevated temperature in oxygenated water, using an imaging autoclave at the University of Manchester, to test the SMBGS models application in this environment. The setup of the autoclave used will be described in more detail in **Section 6.4**. The sensitivity to each variable, such as the inclination of the grain boundary plane to the tensile axis, the Schmid factor and the angle between the grain boundary plane and the tensile direction, are individually analysed to see how they influence the normalized stress at the crack initiation site. These results will be presented in **Section 6.6.2.2**. The effect of sensitisation and grain boundary structure are considered in **Section 6.6.2.3** and **Section 6.6.2.4**. Lastly, in **Section 6.6.2.5** experimental characterization for different grain boundaries, including the stress corrosion initiation site was performed by HR-EBSD.

6.3 IGSCC Initiation in High-Temperature Oxygenated Water

The sample preparation and the digital image correlation (DIC) observations were performed at the University of Manchester. Prior to testing, the heat-treated 304 SS sample was machined to final dimensions of approximately 90mm x 10mm x 7 mm (LxWxT) and the surface was electro-polished in a 92% acetic acid and 8% perchloric acid mix at a voltage of 42 V for 60 s, and electro-etched in the same solution at a

voltage of 13 V for 20s. The sample was stressed above the yield point, at approximately 200 MPa, in oxygenated water at 250 ^{o}C for 30 days, in a windowed autoclave (described below) [154]. The experimental conditions mentioned above were used to accelerate the corrosion process, but might activate some mechanisms that might not be the same as the ones in real plant conditions. The experiment and the data analysis were conducted by Dr Jonathan Duff (with Prof. James Marrow) at the University of Manchester. The analysed data, in the form of identification of initiation sites by DIC and the sample itself, were provided to this project to perform the further analysis presented in this chapter.

6.4 Autoclave description and DIC technique

The “imaging autoclave” has been customized by the requirements given by The University of Manchester and produced by Cormet Testing Systems (Finland). A schematic of the autoclave is shown in **Figure 6.10**.

It consists of a push rod (1) and the loading jig that can be used for either bi-axial bend samples or uniaxial four-point bend samples. The main autoclave seal (2) prevents the steam from leaking while the loading road moves freely. The specimen can be observed through a sapphire window 40 mm in diameter by 8 mm in thickness (4) that is located at the base of the autoclave.

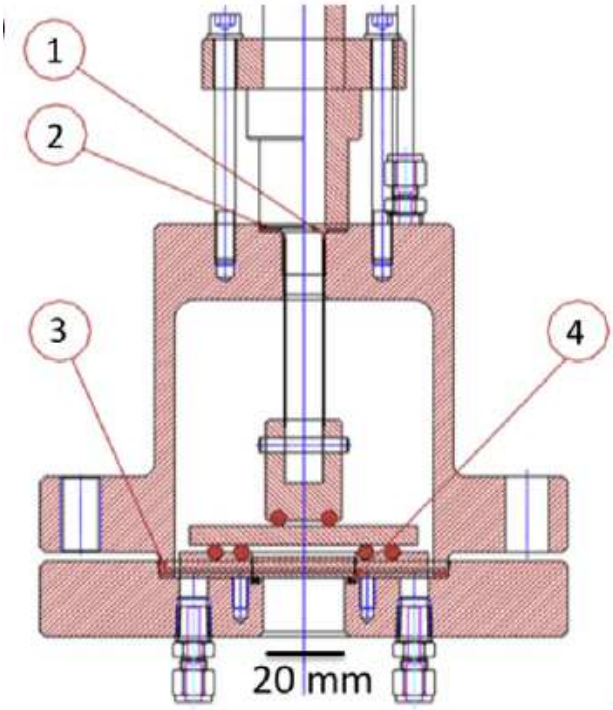

Figure 6.10 Cross-section of the "imaging autoclave": (1) push rod; (2) autoclave seal; (3) sapphire window; (4) optical system [154].

The optical system (3) contains a high specification camera used for acquiring DIC images. The optical microscope has lenses with a long working distance that vary from 21 mm in air to 32.5 mm in water. The 0.9 litre autoclave is used for slow strain rate (10 kN) testing; for the tests in this study, a temperature of 250 ^{o}C and a pressure of 50 bar were used [154].

DIC is a technique that calculates the displacement vector from successive images by using the surface features. The vectors are combined to produce a displacement map and by differentiation strain can be calculated as shown in **Figure 6.11**. Using the described setup, the size of the pixel is 0.23 μm and the field of view is approximately 450 μm by 450 μm at a X20 magnification. By looking at the change in displacement, cracks can

be detected. The cracks of these dimensions cannot be seen in an optical microscope, DIC technique offering a much better resolution. The noise in determining the displacement in the described setup is approximately 0.05 to 0.07 μm and depends on the window size [155] .

An optical image showing the sample after the experiment is shown in **Figure 6.12** and the analysed data showing the strain maps at different time intervals is presented in **Figure 6.13**. In **Figure 6.13.**, the strain maps are superimposed on an optical image of the crack, at the end of the test. This strain represents the change in displacement field, which is caused by the opening of the surface cracks, and which is measured using DIC.

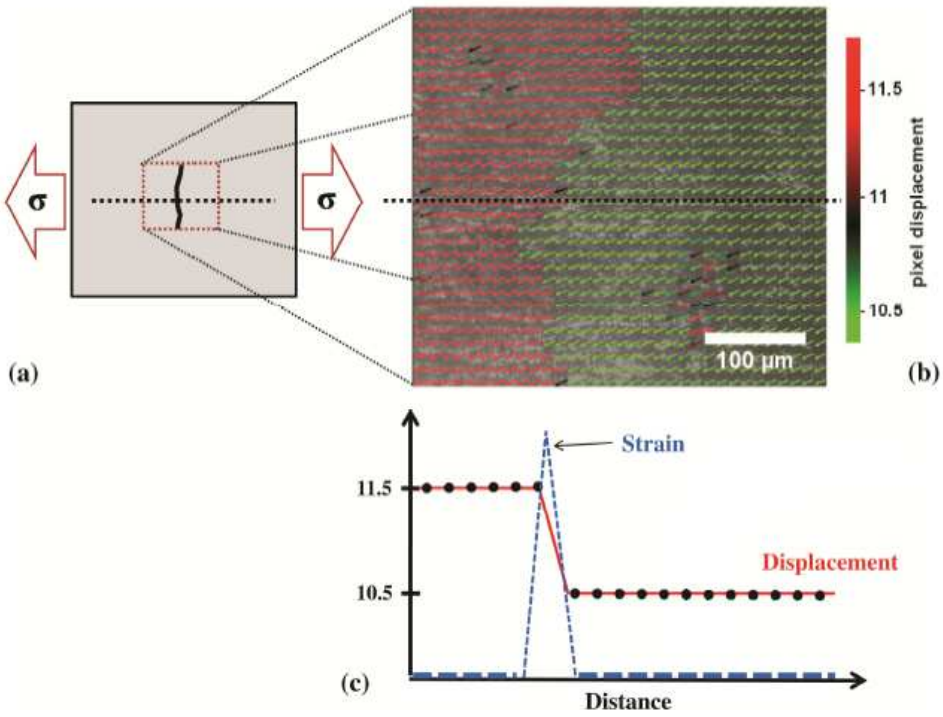

Figure 6.11: Detecting crack initiation using DIC: a) loaded sample containing a crack, b) displacement vectors (the different colours correspond to different displacement magnitudes) and c) strain derivation from the displacement (the highest strain corresponds to the highest change in displacement) [44].

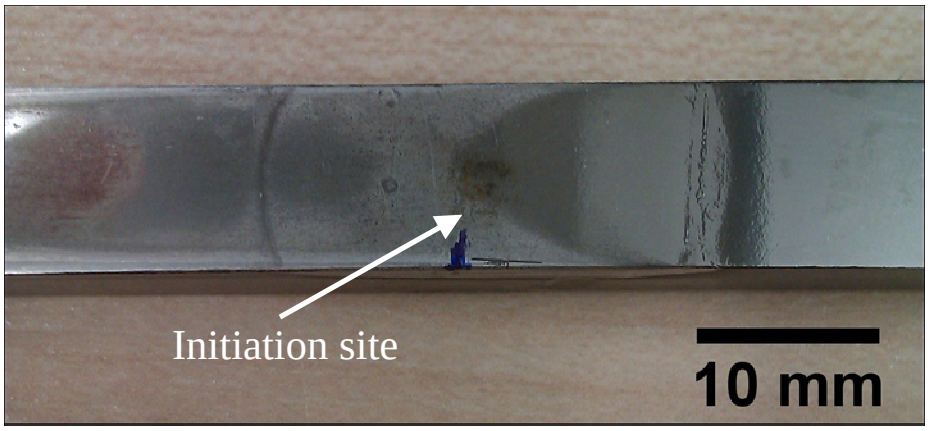

Figure 6.12 Optical image of the 304 SS sample after the test. The initiation site marked (Image from J. Duff).

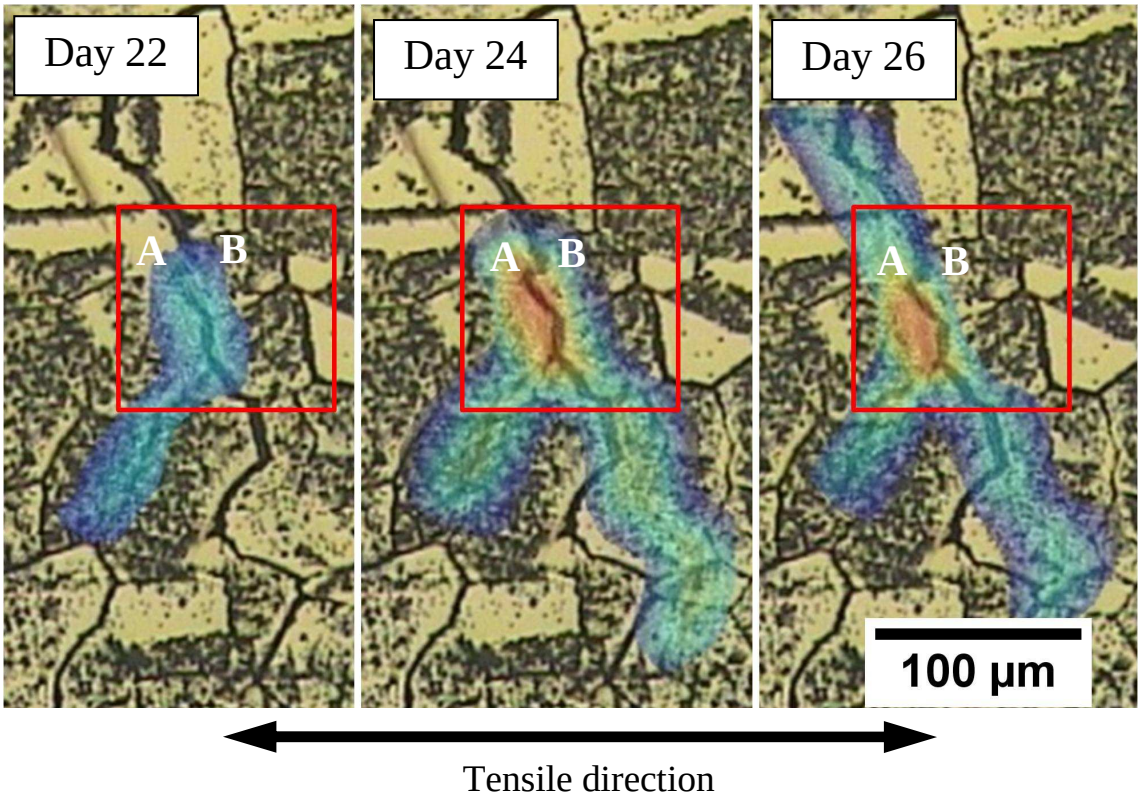

Figure 6.13 Micrographs showing DIC results (strain map) at different time intervals. The crack initiation site is marked by the red rectangle. On a coloured scale, the dark blue represents a low strain while red represents a high level strain (Image from J. Duff).

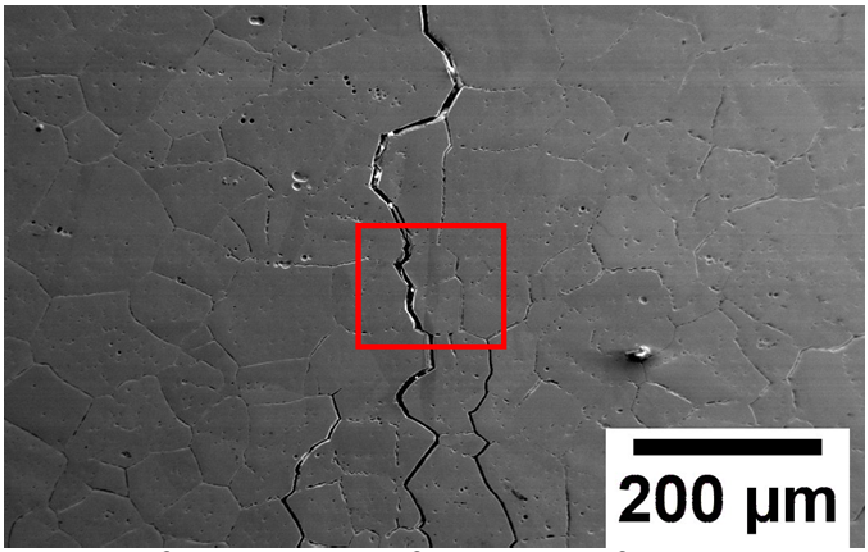

Figure 6.14 Final surface preparation of the sample before EBSD. Crack initiation site is marked with the red rectangle.

At the end of the bending test, the surface of the sample was not suitable for EBSD. To prepare the surface for EBSD, the sample was further polished with colloidal silica until a final mirror surface was obtained. Approximately 5 µm of material was removed (micro indents were placed before polishing, to quantify the amount of the material that was polished through). A micrograph of the initiation site after the final polishing is presented in **Figure 6.14**.

6.5 High Resolution Electron Back Scatter Diffraction (HR-EBSD)

HR-EBSD is a cross-correlation based analysis method of EBSD patterns that can be used to study the crystal lattice misorientation within grains and in the vicinity of grain boundaries with a very high precision. These misorientation concentrations represent the dislocations that piled up during the deformation [156]. This method was developed by Wilkinson *et al.* [157] and it offers an angular resolution of 4.3×10^{-5} radians, which is approximately 100 times better than the resolution of the Hough Transform analysis (4.3×10^{-3} rad) which is conventionally used to detect the orientation or the

misorientation [158]. Conventional Hough based analysis was previously used to determine the orientation gradients and the geometrically necessary dislocation (GND) density. However, because of the poor sensitivity, the relatively high noise in the GND measurements obscured the important features of the structure [157][160].

The HR-EBSD technique is based on correlating very small shifts of the entire diffraction pattern to the variation in the elastic strain and lattice rotations. A reference pattern is usually picked from a point on the sample where the strain is known or assumed to be zero, and all the calculations are made with respect to this reference [159]. A more detailed description of the method is presented by Wilkinson *et al.* [157][160]. High resolution EBSD patterns similar to the one shown in **Figure 6.15** are collected and are further analysed off-line using the X-EBSD code. Examples of the application of this technique include micro-scale studies to observe the dislocation content of a macrozone in hot-rolled Ti-6Al-4V alloy [156], analysis of the dislocations near grain boundaries in deformed copper [161], observations of the deformation due to nanoindentation around grain boundaries in α-Ti [162] by looking at the GND density.

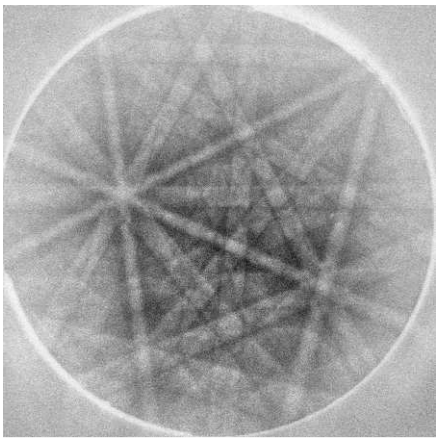

Figure 6.15 EBSD pattern used for HR-EBSD.

In this thesis, the HR-EBSD technique was used to analyse the GND density in different areas of the 304 SS sample and to investigate correlations between GND density distribution and crack initiation. The distribution of GNDs was obtained from the lattice curvatures using the methods developed by Nye [163] and Kroner [164].

While the role of localized deformation in SCC susceptibility is not yet fully understood, it has been shown that it is correlated with the nucleation of IGSCC in different irradiated materials (stainless steels and Ni Alloys) [165]. It has been shown by Was *et al.* [165] that in irradiated materials cracks tend to occur at boundaries that are perpendicular to the direction of the applied stress, a parameter that is also included in the Schmid-modified grain boundary stress (SMGBS) [142] model.

Even though localised deformation is found mainly in irradiated materials, the same concept might apply to unirradiated materials. No study has previously been done to analyze the GNDs of boundaries where IGSCC initiates. The current study looks at the GND of grains or grain boundaries where IGSCC occurs and analyses them in the context of the normal stress obtained using the SMGBS and the Schmid factor.

EBSD data was collected using a JOEL-6500F SEM and the TSL OIM DC v4 software using standard parameters. For acquiring the maps, a voltage of 20 kV and a probe current of approximately 1 nA were used. The binning used with the camera was 2x2 and the exposure time was approximately 0.5 s. The exposure time is the one that controls the contrast of the acquired patterns and the time chosen gave the best contrast. A ‘square’ grid with a step size of 0.3 μm was used. The step size chosen gave a good resolution for the EBSD patterns and its value is determined in correlation with the size of the map and the time that it needs for an EBSD map to be acquired.

6.6 Testing the SMGBS Model

6.6.1 Methodology

6.6.1.1 Determining the Schmid factor

The Schmid factor was individually calculated for each grain. First, a low resolution EBSD map of approximately 600 μm by 1400 μm was taken using 4x4 binning for the camera and a 'hexagonal' grid with a step size of 1 μm. A Schmid factor map was generated using the OIM Analysis software and the Schmid factor was extracted for each individual grain using the 'Point' option of the OIM Analysis software. To check whether the value obtained from one single point was representative, the Schmid factor for one grain was measured in 5 or 6 different locations within the grain and the standard deviation was of ±0.01 which is sufficient for the purpose of the model.

6.6.1.2 Determining the trace boundary angle

The trace boundary angle was measured for each grain boundary to which the SMGBS model was applied. The channelling contrast made grain boundary detection easier and the angle was directly measured using the ImageJ and the SEM images that were recorded for each individual grain boundary. The boundaries measured were straight and the error in the angle measurement was approximately 3° (this error comes from determining the angle using ImageJ and was estimated by measuring the angle several times).

6.6.1.3 Determining the grain boundary plane

A FIB cut-out was milled across each individual grain boundary of interest with the sample tilted at 54°, so that the ion beam was perpendicular to the surface of the sample. The cut-outs had similar dimensions of approximately 15 μm by 2 μm and were milled using the Auriga FIB, at a current of 1 nA. Then, the cut-outs were cleaned using a

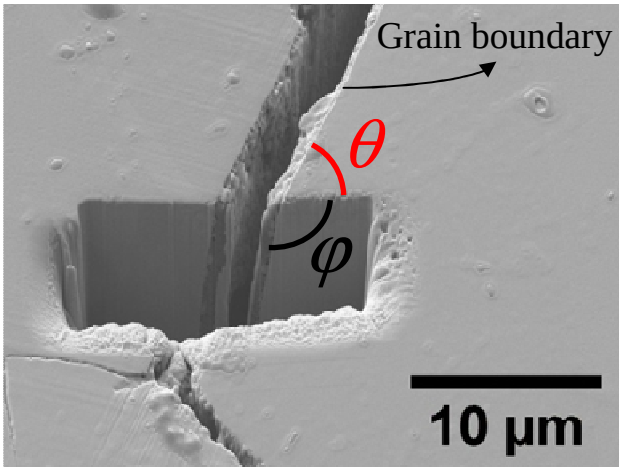

Figure 6.16 FIB cut-out revealing a grain boundary angle. The grain boundary, the grain boundary angle (φ), and the trace angle (θ) are labelled.

current of 600 pA. SEM images were collected and the channelling contrast allowed identification of the grain boundary, as shown in **Figure 6.16**. The grain boundary angle was measured using ImageJ from the recorded SEM images that were previously corrected for tilt and as before the error was approximately 3°.

6.6.2 Results

6.6.2.1 Simple 2D characterisation

First, the data were analysed in two dimensions to determine the values of the Schmid factor and to look at the CSL boundaries of an area of the sample that included the crack initiation site. The Schmid factor map of a larger area of the specimen which included the initiation site (clearly marked between grains A and B) is presented in **Figure 6.17**. In addition, the distribution of the Schmid factor for the same grains is shown in **Figure 6.18**. It can be observed that the Schmid factors range between 0.27 and 0.5, with the majority of the grains having a value close to the upper end. The distribution is similar to the one observed by West *et al.* [167] in 316L stainless steel, presented in **Figure 6.19**. It can be observed from the Schmid factor map that the initiation site

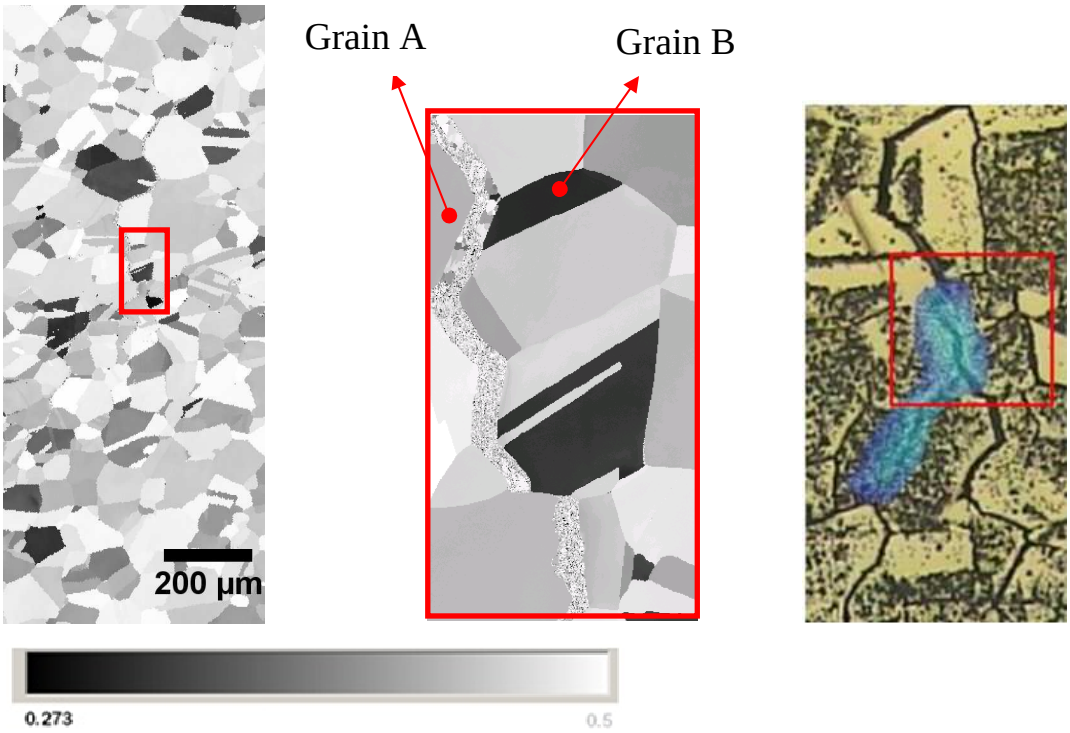

Figure 6.17 The Schmid factor map of the 304 SS sample, including the crack initiation site, which is between grains A and B.

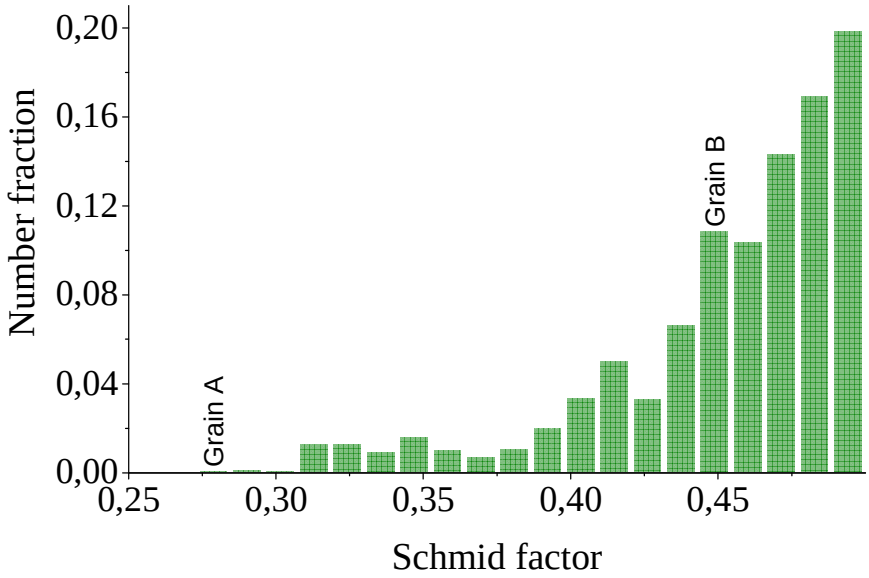

Figure 6.18 The Schmid factor distribution of an area of the 304 SS sample including the crack initiation site. The Schmid value that corresponds to grain A is 0.28 and the one that corresponds to grain B is 0.45.

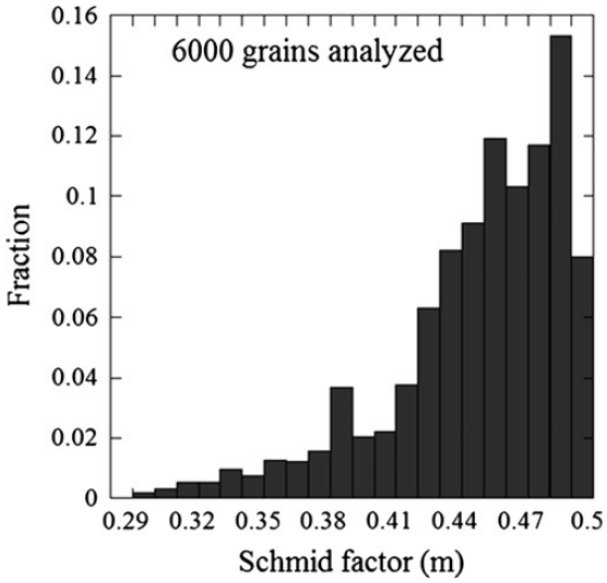

Figure 6.19 Schmid factor distribution for 316L stainless steel [167].

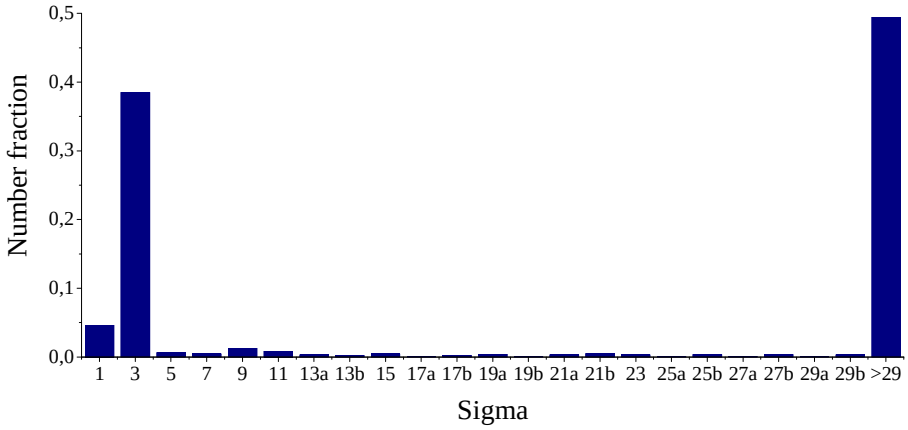

Figure 6.20 Sigma distribution for the grain boundaries including the crack initiation site.

(AB – see **Figure 6.13**) is next to a to a relatively "soft" (high Schmid factor) grain (A), next to a"hard" (lowest Schmid factor) grain (B).The distribution of the CSL boundaries is presented in **Figure 6.20**. As expected, the majority of the grain boundaries have a CSL ∑3 (approximately 39%), ∑9 and ∑27 together are approximately 2%, while the other ∑ values are less common. Rahimi *et al.* [45] observed a similar distribution in the same material, such that the number fraction of the ∑3 was approximately 30%, ∑9 and∑27 together were 3% and the number fraction of the 'random grain boundaries'

was approximately 56%. The grain boundary where crack initiated is a 'random' boundary; this is expected since such boundaries tend to sensitise [45].

6.6.2.2 SMGBS analysis for intact and cracked boundaries

The SMGBS model was applied for a total of 50 randomly selected grain boundaries from three different areas of the sample that were all located 5-10 grains apart from the initiation site. These will be referred to as "intact boundaries." The model was also applied for a total number of 25 grains that were along the crack path, which therefore included the grain boundary where the crack initiated. These will be referred to as "cracked boundaries."

The normal stress, as described in **Section 6.5,** depends on the input parameters of Schmid factor, trace inclination and the grain boundary angle. All these parameters were analysed and further compared for both the intact and cracked boundaries, and they will be described next.

The Schmid factor values from randomly-chosen intact boundaries were compared to the Schmid factor values from a larger distribution of approximately 2000 grains (obtained from the map presented in **Figure 6.17**) and both distributions are plotted in **Figure 6.21,** where P represents the percentage of grain boundaries that have a particular Schmid factor value. The Kolmogorov-Smirnov test from the MATLAB Statistics toolbox was applied and it indicated that the distributions are similar, which means that the randomly selected grain boundaries chosen are sufficiently representative of the Schmid factor distribution for this material.

The Schmid factor mismatch distribution for both intact and cracked boundaries is shown in **Figure 6.22**. For the intact boundaries, the values range between 0.01 (which is the resolution limit of the Schmid factor mismatch) and 0.13, with the maximum

value corresponding to only two grain boundaries. For the cracked boundaries, the values range between 0.01 and 0.17, with the maximum value corresponding only to the grain boundary where crack initiated.

The data for the trace angle for both intact and cracked boundaries are presented in **Figure 6.23** and have a normal distribution, judging that the distribution looks Gaussian**.** For the intact boundaries, the maximum values was 83° and the majority of the grain boundaries have a grain boundary trace angle greater than 40°, only 3 grain boundaries have values between 20 and 40°.

For the cracked boundaries, the majority of the boundaries had a trace angle of 68° and no grain boundary had a trace angle less than 30°. The maximum trace angle had a value of 88°. The value that corresponds to the boundary where crack initiated had a value of 68° and is not at any extreme of the distribution. The data obtained for cracked boundaries show no significant difference with the data for the randomly selected intact boundaries.

The distribution of the angle between the grain boundary plane and the direction of the tensile direction (φ) for both intact and cracked boundaries is presented in **Figure 6.24.** For the intact boundaries, the range is between 43 and 89° and the maximum value corresponds to only one grain boundary. The majority of the grain boundaries have values for (φ) of 63° and 87°. For the cracked boundaries, the angle that corresponds to the grain boundary where the crack initiated had a value of 87° and this was the highest value obtained on the crack path. From the distribution graph, this is the closest to 90°. Again, the distributions show no significant difference between the cracked and the intact boundaries.

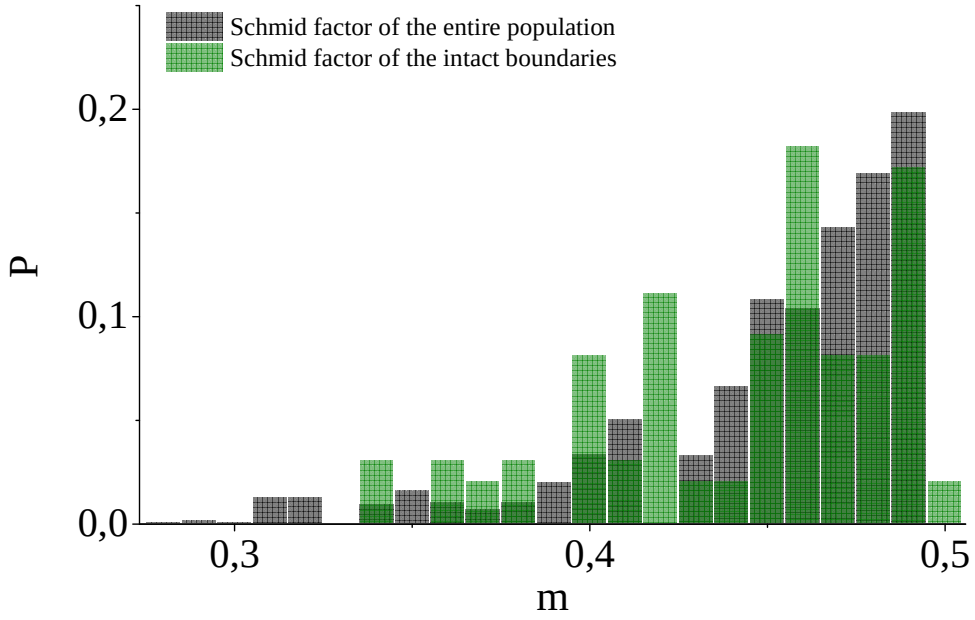

Figure 6.21 Distribution of the Schmid factor for the entire population of grains and the random selected population of grain boundaries that did not fail (for which 3D data on grain boundary plane were also measured).

The distribution for $\sigma_N$that is obtained for both the intact and cracked boundaries is shown in **Figure 6.25**. For the intact boundaries, the values obtained for σ_N range between 0.12 and 1.08. Both the maximum value and the second largest (σ_N=1.05) correspond to only one grain boundary. For the cracked boundaries, that values for σ_N range between 0.04 and 1.12 with the highest value corresponding to only one grain boundary, which is the initiation site. The Kolmogorov-Smirnov test from the MATLAB Statistics toolbox was used to check whether the two sets of data (intact and cracked boundaries) are from the same continuous distribution and the result confirms that they are not statistically different. The hypothesis is accepted because the p-value=0.178 is greater than the value of the set level of significance which is 0.05.

In summary, the initiation site has the highest Schmid factor mismatch of 0.17 and the highest value for normal stress of 1.12. Also, the value for φ that corresponds to the initiation site is 87 ^{o}; this value was the highest obtained for the cracked boundaries.

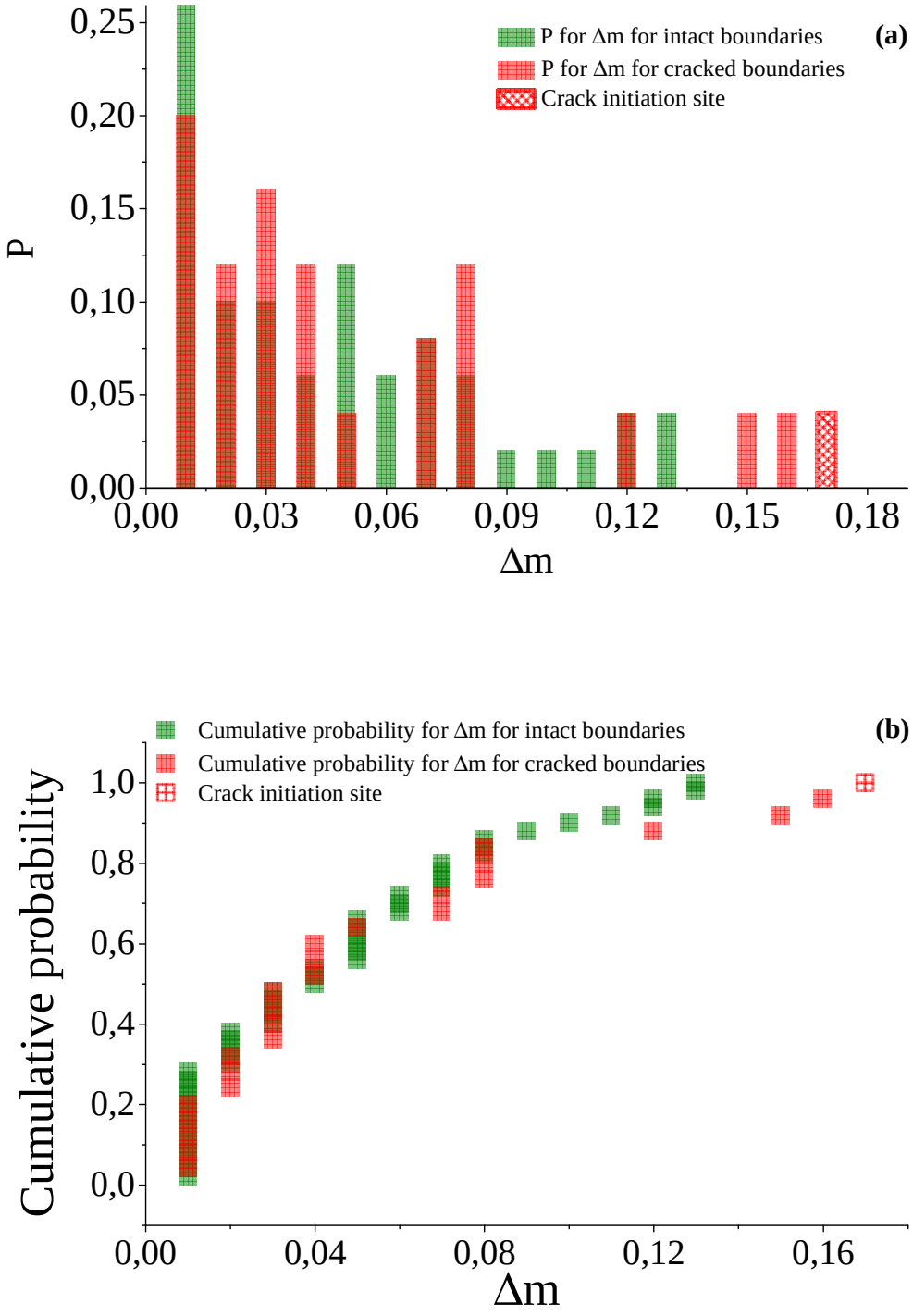

Figure 6.22 Schmid factor mismatch for intact and cracked boundaries shown as: (a) normalised frequency distribution and (b) cumulative probability.

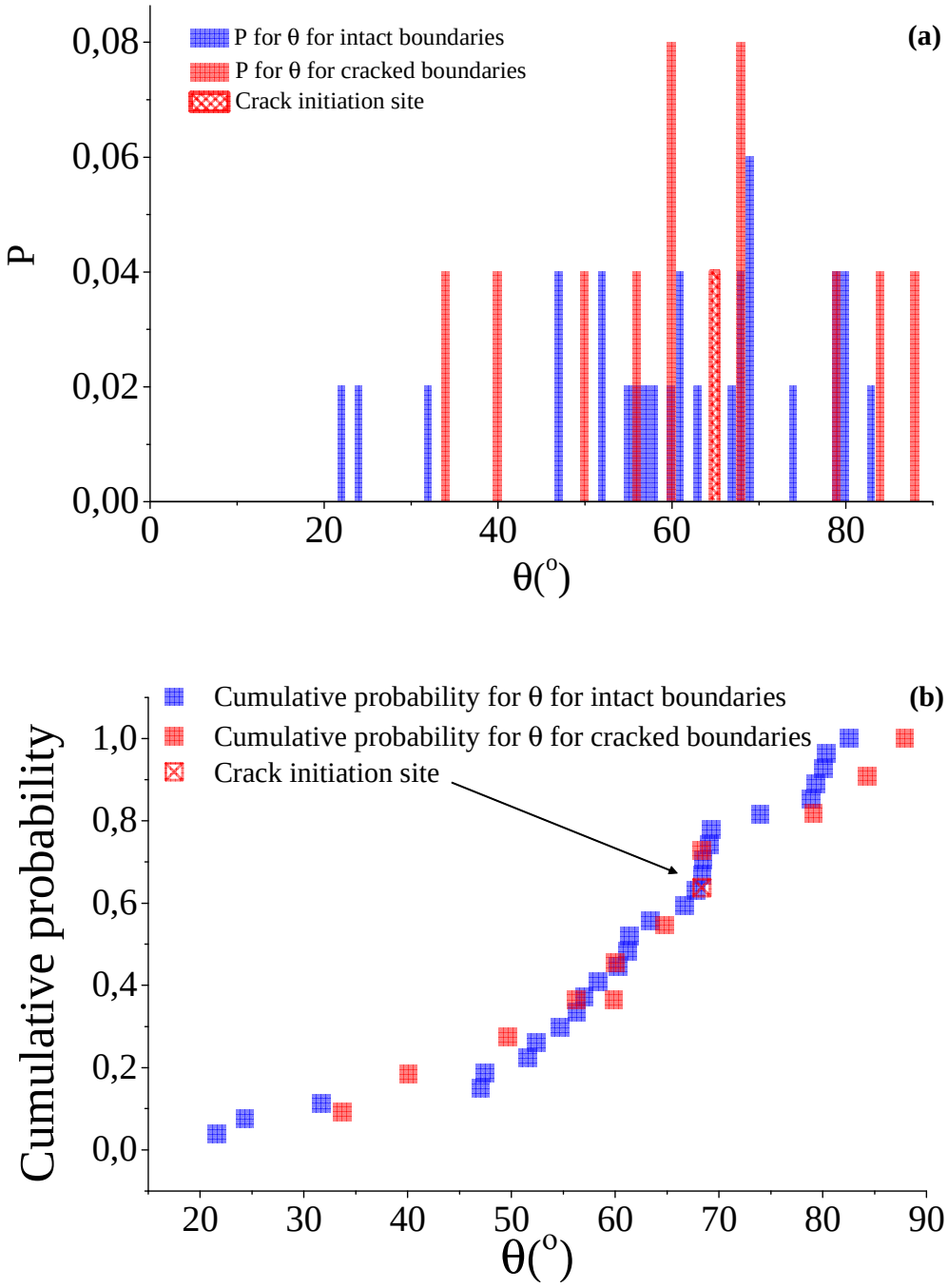

Figure 6.23 Values of *θ* for intact and cracked boundaries shown as: (a) distribution and (b) cumulative probability.

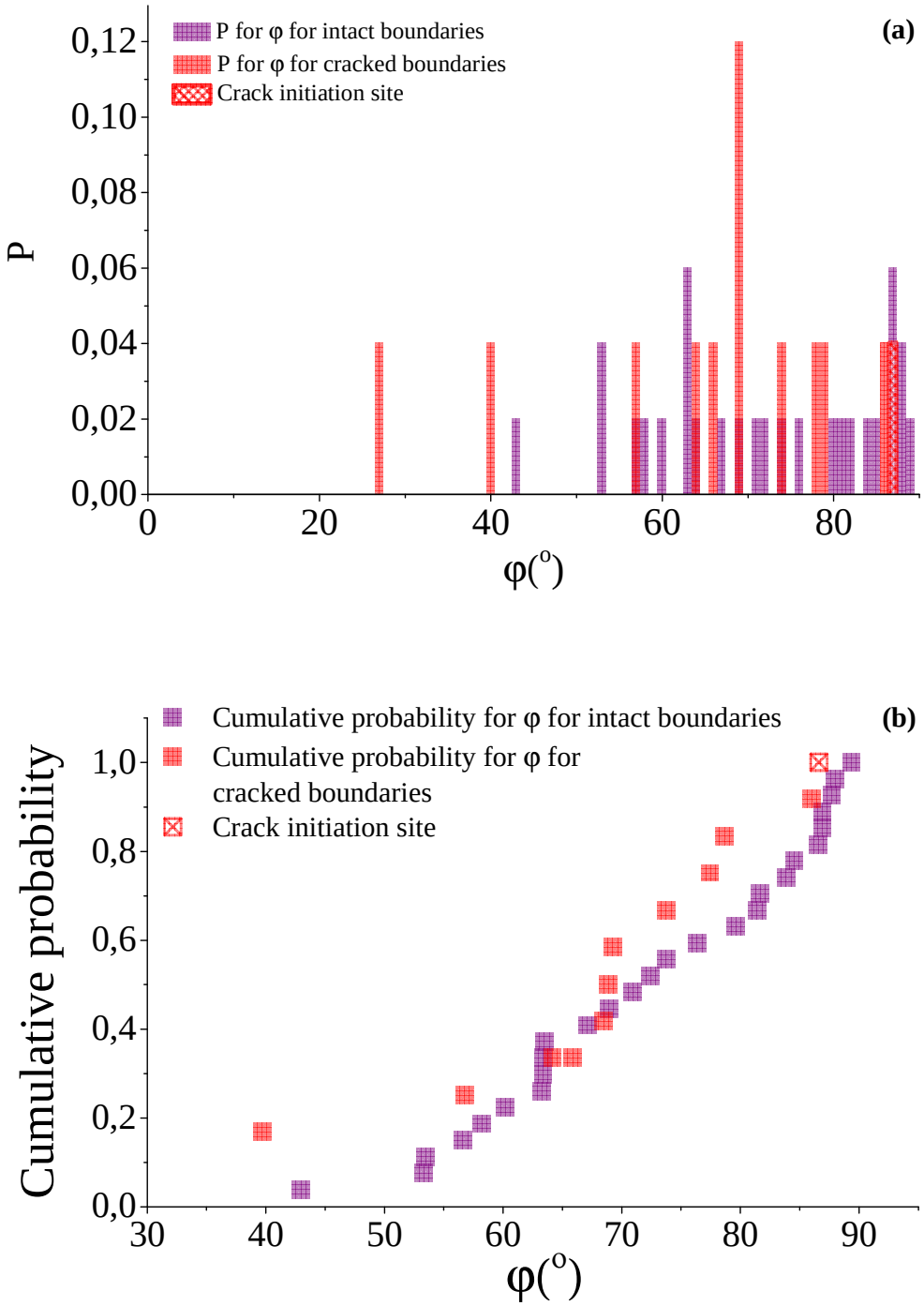

Figure 6.24 Values of φ for intact and cracked boundaries shown as: (a) distribution and (b) cumulative probability.

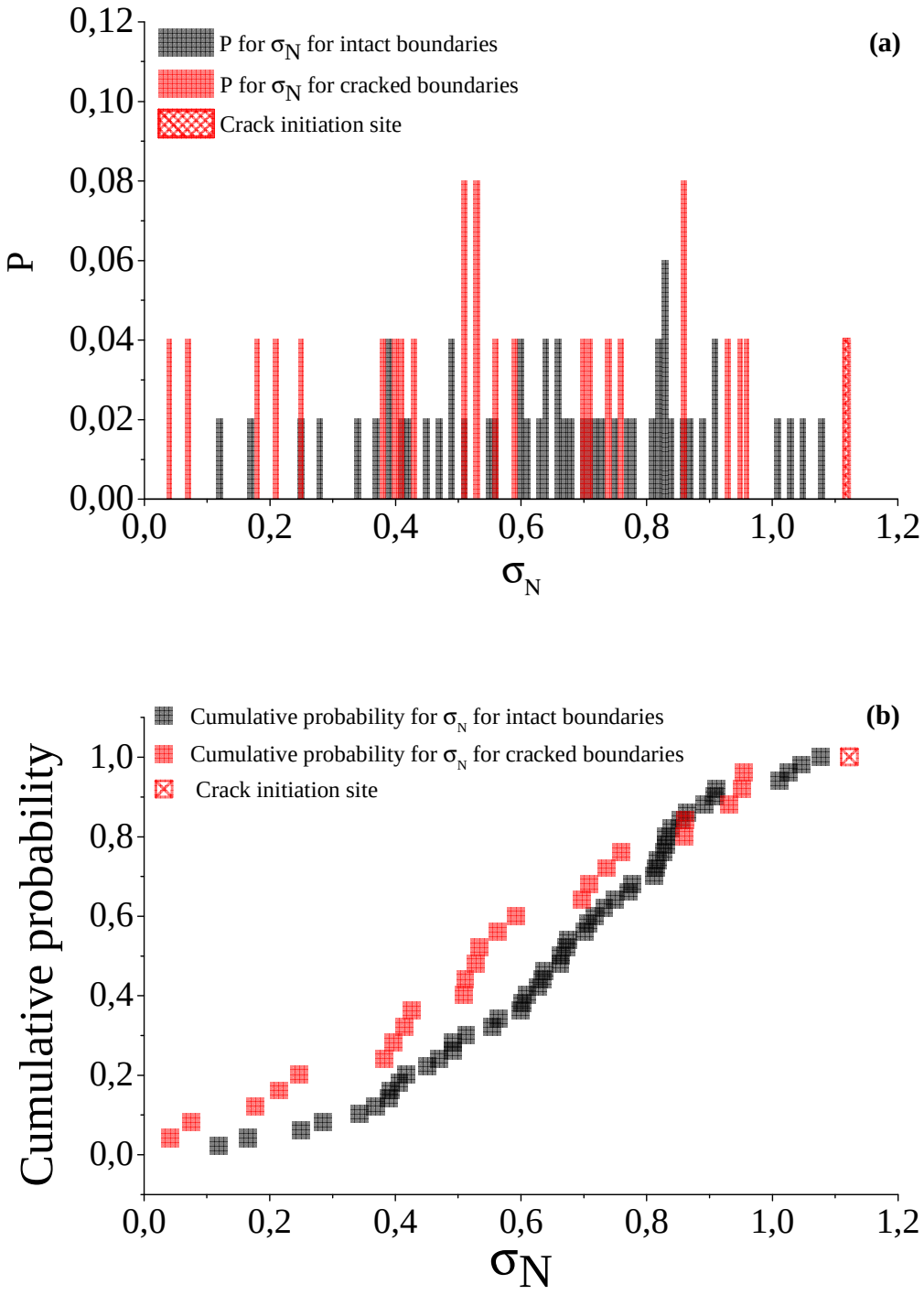

Figure 6.25 Values of σ_N for intact and cracked boundaries shown as: (a) distribution and (b) cumulative probability.

6.6.2.3 CSL values of the grain boundaries

While the SMGBS model seems to differentiate the grain boundaries that are susceptible from the grain boundaries that are resistant to IGSCC in terms of the mechanical loading, looking at the importance of sensitization as well as the CSL information of the grain boundaries could provide more insights into further predicting crack initiation. To determine how the SMGBS model can be extended, the CSL ∑ values of all grain boundaries on which the SMGBS model was applied was calculated and is presented in **Figure 6.26**. It can be observed that 68% of the total intact grain boundaries had a random orientation, 16% were ∑3, while the rest had ∑ values of 1, 5, 9, 11, 13a, 21a or 39b. Regarding the boundaries that cracked, 84% had a random orientation. The other 16% had ∑ values of 7, 25b, 41b or 43b. The grain boundary where crack initiated had a random orientation. No ∑3 boundaries were observed to crack.

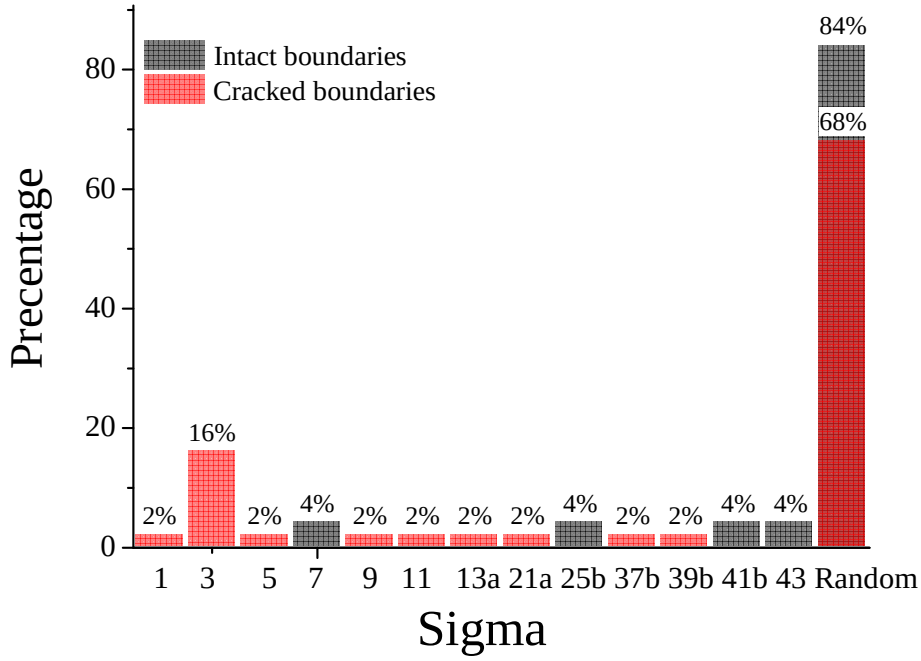

Figure 6.26 CSL information for the intact and cracked grain boundaries.

As shown in the above distributions, some of the intact grain boundaries have a CSL value that is known to be less susceptible to IGSCC (e.g. ∑3, ∑9).

To investigate sensitivity to the ∑ value, the grain boundaries that have a CSL value less or equal to ∑29 will be excluded from the analysis. This is an approximation, since some of the cracked grain boundaries had low CSL ∑ value. The plot of the cumulative probability for σ_N after filtering out the grain boundaries that are less susceptible to IGSCC, is shown in **Figure 6.27**.

From **Figure 6.27** it can be observed that two grain boundaries with the largest σ_N values from the intact boundaries were filtered out using the CSL criterion. The ∑ values of these two grain boundaries were ∑9 and ∑13a. The grain boundary where the crack initiated still has that greatest σ_N value out of all the grain boundaries analysed.

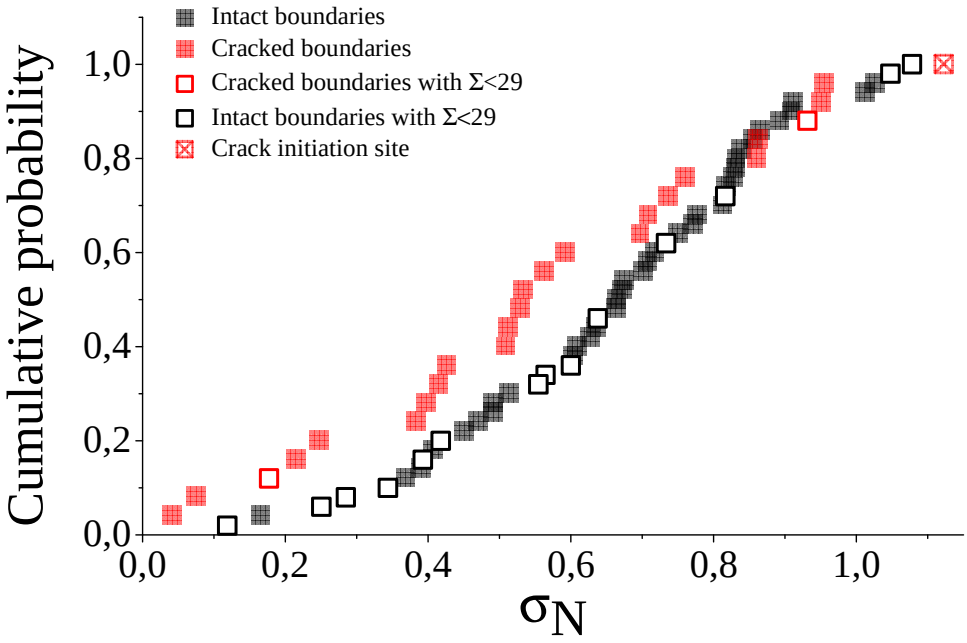

Figure 6.27 Cumulative probability for $\sigma_N$values for intact and cracked boundaries, after the grain boundaries with CSL values less than ∑ 29 were filtered out.

6.6.2.4 Misorientation and relationship between grain boundaries and low indexed reference planes

As mentioned in **Section 6.1.3,** low {hkl} indexed boundary planes are also considered to be resistant to cracking. In order to determine which tested grain boundaries are close to a low indexed plane the misorientation of grain boundaries was calculated using the OIM Analysis software in the form of angle and axis misorientation. Then, to determine how close the analysed grain boundaries are to the low indexed planes, the dot product was used to calculate the angle between the grain boundaries and the indexed planes, up to {hkl}={332}. Then, the minimum angle was recorded and the results are shown in the **Appendix**. It can be observed from the **Appendix** that some of the grain boundaries are close to a low indexed plane. A grain boundary is defined to be close to a low indexed plane if it is within 6° of the plane (this value was chosen because it represents the error in the angle measurement). A “low indexed plane” is defined to be less than

{322}. The grain boundaries that are close to a low indexed plane were excluded from the analysis, as before in **Section 6.6.2.3**. The new plot of the cumulative probability for σ_N, after filtering the data using grain boundary plane criterion is shown in **Figure 6.28**. The boundary with the highest value of the normal stress that was filtered out was close to a (100) plane. This means that even though the corresponding normal stress value was high, the boundary did not crack because it was a resistant boundary.

From **Figure 6.28** it can be observed that no extra grain boundaries with a large σ_N value were filtered out using the low indexed plane criterion. The grain boundary where the crack initiated has still that greatest σ_N value out of all the grain boundaries analysed.

The uncertainty in the σ_N was calculated to be approximately 2%. If we remove the σ_N values of the boundaries that have been filtered out using the two criteria, than the threshold for σ_N required for cracking is between 1.03±0.02 (highest value for the intact boundaries) and 1.12±0.02 (value of the initiation site).

To see whether the grain boundaries that are close to a low indexed plane are also low CSL, the plot of the cumulative probability for σ_N marking these boundaries is shown in **Figure 6.29.** It can be observed that only six intact boundaries are in this category. The boundary that was filtered out and is closest to the initiation site in terms of the normal stress value is close to (100) plane and is a ∑13a.The grain boundary where crack initiated is closest to (3 -3 1) plane.

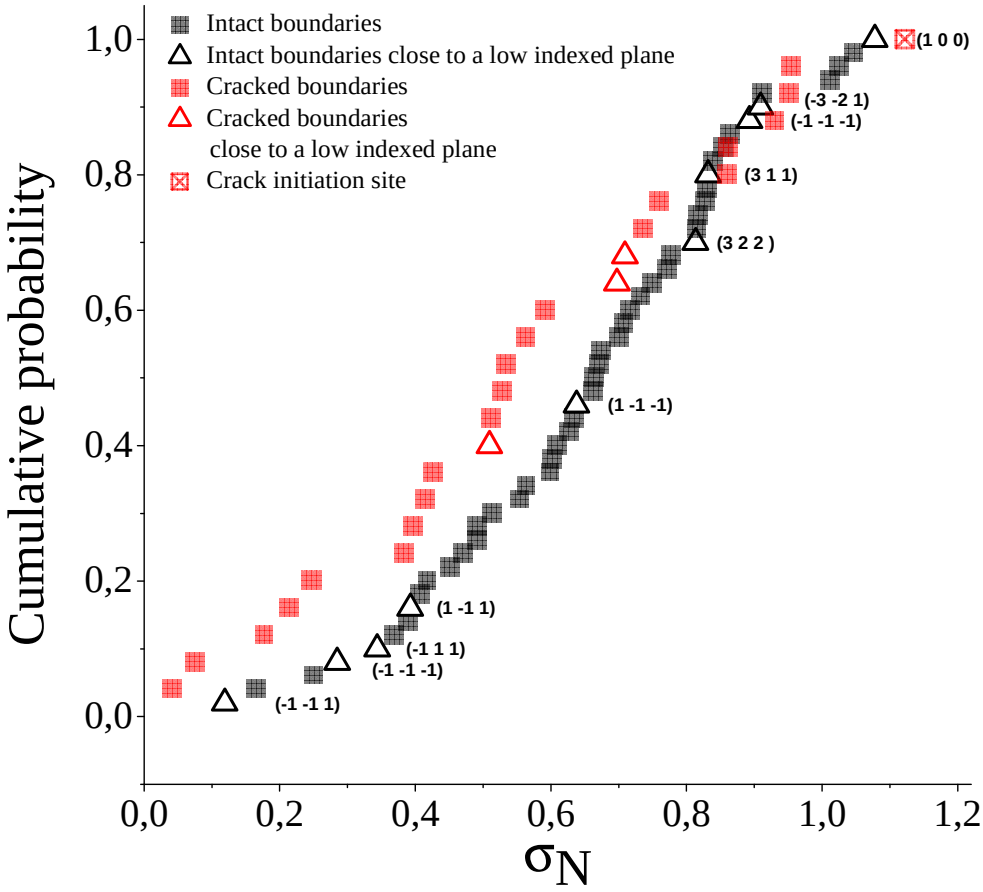

Figure 6.28 Cumulative probability for $\sigma_N$values for intact and cracked boundaries after the grain boundaries that were close to a low indexed plane were filtered out. The corresponding low indexed planes of boundaries that were filtered out are marked.

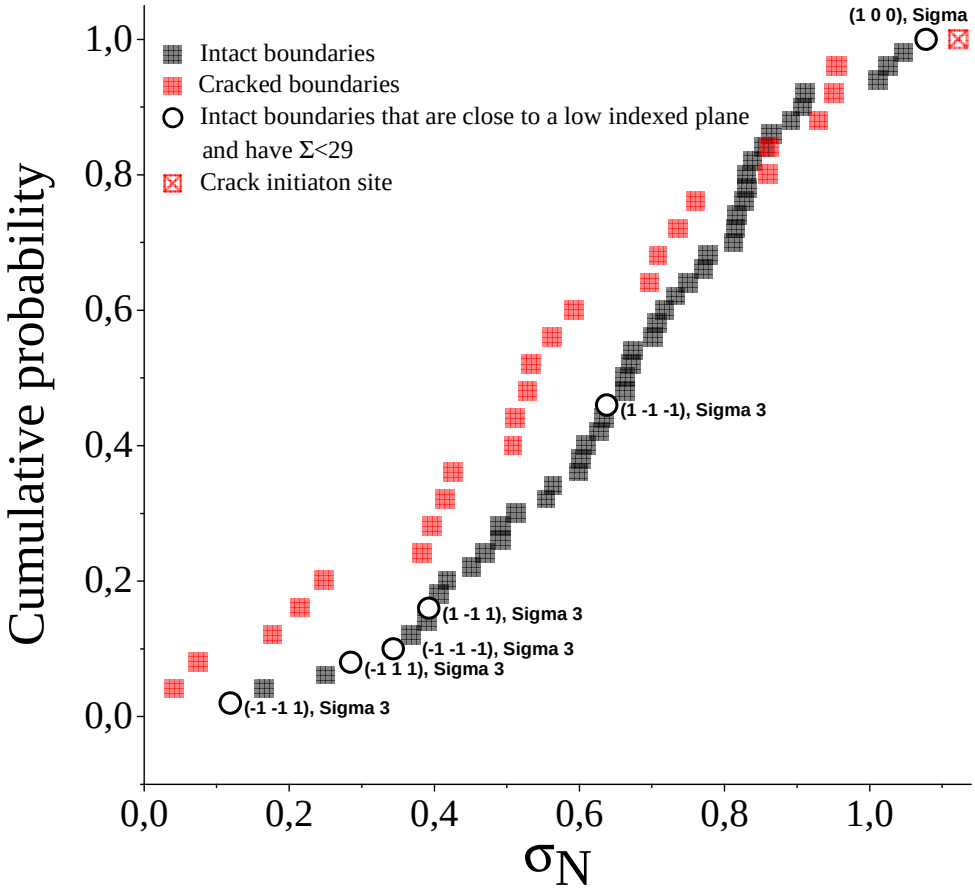

Figure 6.29 Cumulative probability for $\sigma_N$values for intact and cracked boundaries showing the grain boundaries that are both close to a low indexed plane and have ∑<29.

6.6.2.5 HR-EBSD analysis

To investigate the crack initiation site for evidence of the effects of localized deformation, and also to compare it to other grain boundaries where cracks did not initiate, three different areas of the sample were analysed using the X-EBSD code, applied to HR-EBSD maps. The locations of the three maps are shown in a low magnification micrograph in **Figure 6.30**.

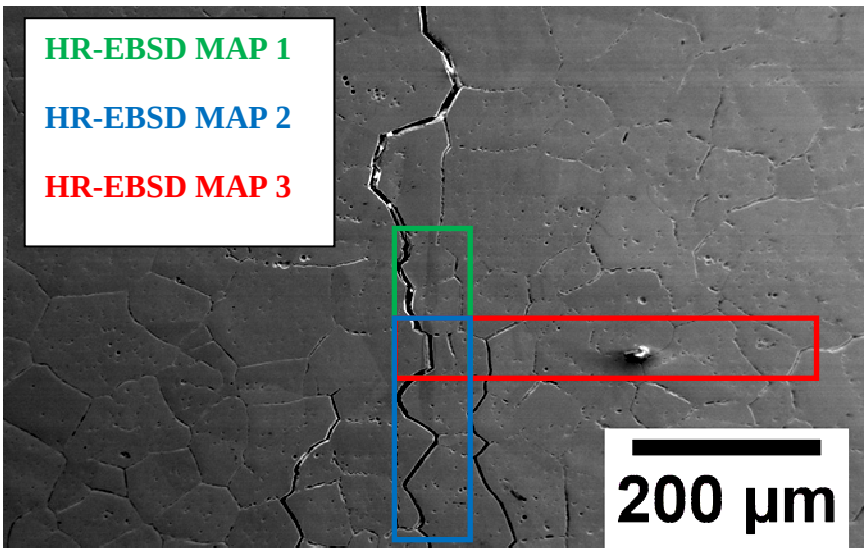

Figure 6.30 Micrographs showing the location of the three HR-EBSD maps.

The micrographs showing the total GNDs for MAP 1, MAP2 and MAP 3 are presented in a collage shown in **Figure 6.31.** MAP 1 included the crack initiation site, as determined using the DIC. It can be observed that the areas with high GNDs densities are around the grain boundaries that cracked. In addition, an area with high GNDs density is in the interior of the smaller grain, at the bottom of the micrograph. Also, the higher GNDs are located at triple junction points, an observation that has been also made by Jiang et.al [161].

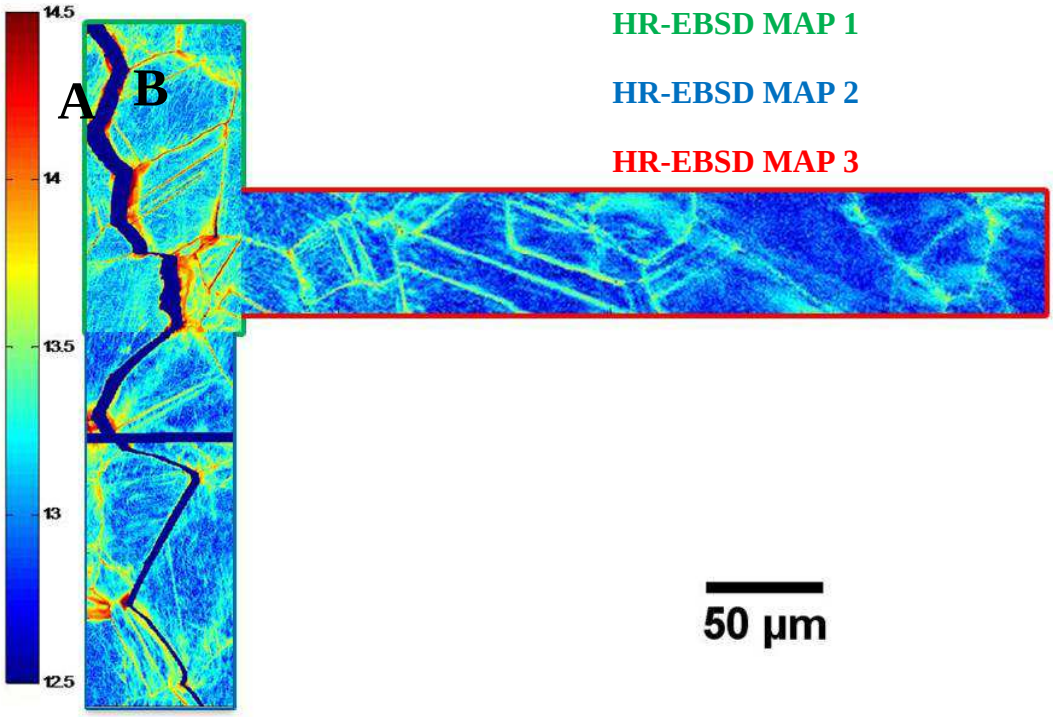

Figure 6.31 MAP 1, 2 and 3 analysed using the XEBSD code, showing the GNDs map of crack initiation site. The grain boundary where crack initiated (AB) that also has the highest value of σ_N is labeled. The units of the GNDs are $\log_{10}(\rho_{GND})$ where ρ_{GND} is measured in m^{-2}.

The second area (MAP 2) contained the crack path that propagated from the initiation site. The highest GNDs values are still around the cracked grain boundaries and some of the values are close to the ones that corresponded to the initiation site. For the middle region of the micrograph, where the black line is, no data could be collected because the beam of the microscope was lost during the mapping.

The area of MAP 3 was selected as having no cracks present. The chosen area (MAP 3) was perpendicular to the crack. As before, the highest GNDs densities could still be determined near the cracked grain boundaries. The GND values that will be presented for the three different maps were normalised with respect to MAP 3 since there is a

slight difference in the GND value for the same common grain that is in all three maps. The normalization was done using the absolute GND value of the common grain. In MAP 1 and MAP 2, the log of the GND is 0.8% higher and 0.4% lower than in MAP 3, respectively. This is most likely due to a combination of factors: the current of the microscope, the position of the sample or the settings of the camera.

From the HR-EBSD observations, the high GND values are around the cracked boundaries and the lowest values are at grain intact boundaries. This cannot be a sample preparation artifact because, as can be observed, the GND is not uniformly distributed along the cracks; there are areas around cracks where there are no accumulations of GNDs. The GNDs may be higher along the grain boundaries that cracked because the dislocations accumulate at the stress intensification of the tip of the crack and are then left behind as the crack grows [9]. This can also be due to some local plasticity associated with cracking. The deformation might be affected by the relative orientation of the crack to the slip systems in the grain, so would not be symmetric about the crack [9].

To test whether the GND in the vicinity of a grain boundary varies as a function of the Schmid factor mismatch of the two adjacent grains, the average GND was calculated for the cracked boundaries (MAP 1, 2) and intact boundaries (MAP 3). The average GND for one grain boundary was calculated using a MATLAB code available in the group, by averaging the absolute GND values of one grain with the adjacent grain. The GND value that corresponds to one grain was calculated to be the average GND value taken from the edge of a crack to 2 pixels (approximately 0.6 μm) away from the grain boundary. Both average grain boundary GND as well as individual GND average for one side of the boundary only will be examined, as appropriate. A grain boundary is defined to be the region between two grains that have different indexes. The data were

then compared with the grain boundary parameters of Schmid factor, Schmid factor mismatch and the normal stress.

The average GND for several grains (adjacent to both cracked and intact boundaries) was plotted against the corresponding Schmid factor and the graph is shown in **Figure 6.32**. No correlation could be determined between the average GND and the Schmid factor.

The average GND of grain boundaries against the Schmid factor mismatch is shown in **Figure 6.33**. It can be observed that there is no correlation between the average GND of grain boundaries and the Schmid factor mismatch. However, the initiation site has one of the highest averages. **Figure 6.34** shows the plot of the maximum GND value adjacent to the grain boundary versus the Schmid factor that corresponds to that particular grain. Again, there is no correlation between the GND value and the Schmid factor.

The GND average of grain boundaries was plotted against the σ_N for the cracked boundaries and the graph is shown in **Figure 6.35**. It can be observed that there is no correlation between the average GND and the σ_N.

From the GND analyses presented above there is no correlation between the grain average GNDs and the Schmid factor, or the boundary average GNDs and the Schmid factor mismatch.

Also, there is no correlation between the GNDs of boundaries and σ_N. However, the cracked boundaries tend to have a higher grain average GND than intact boundaries.

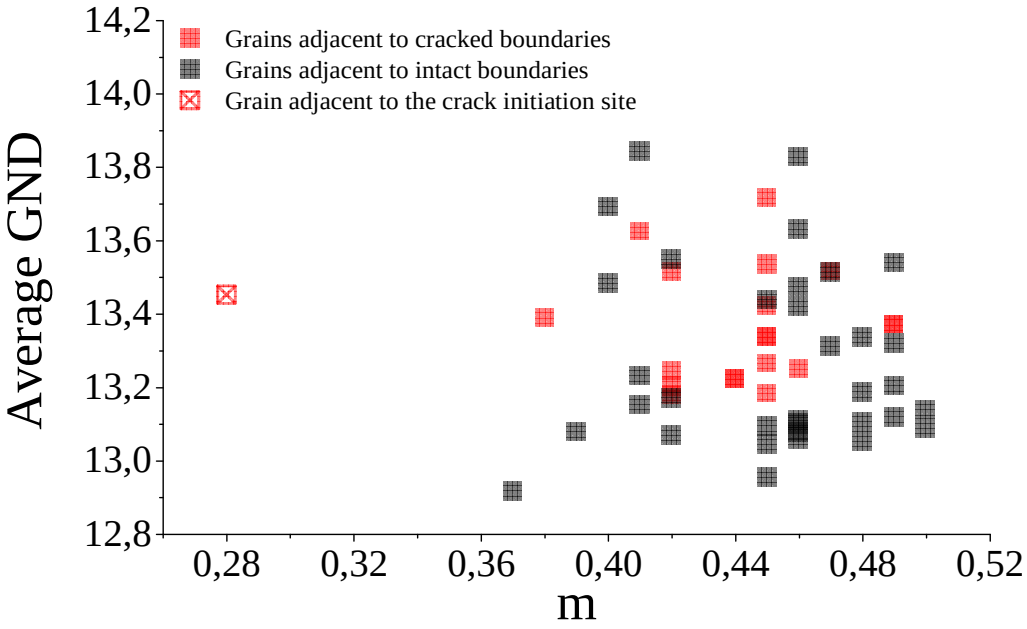

Figure 6.32 Average GND calculated for each grain as a function of the corresponding Schmid factor for grains that are adjacent to both cracked and intact boundaries.

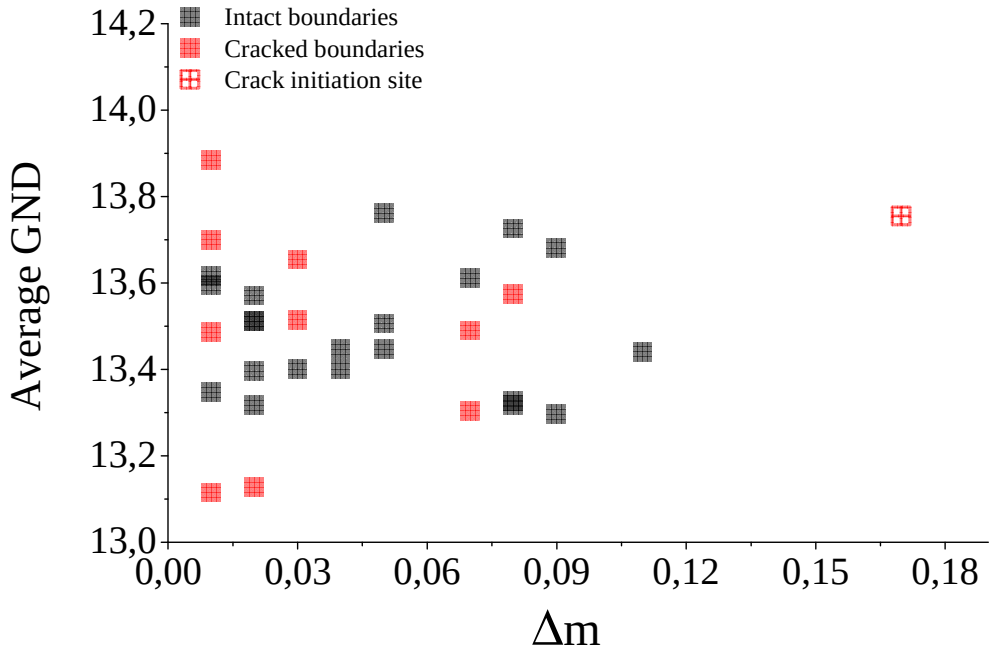

Figure 6.33 Average GND calculated for each grain boundary as a function of Schmid factor mismatch of the adjacent grains for both cracked and intact boundaries. The lowest and highest GND value for each boundary is indicated.

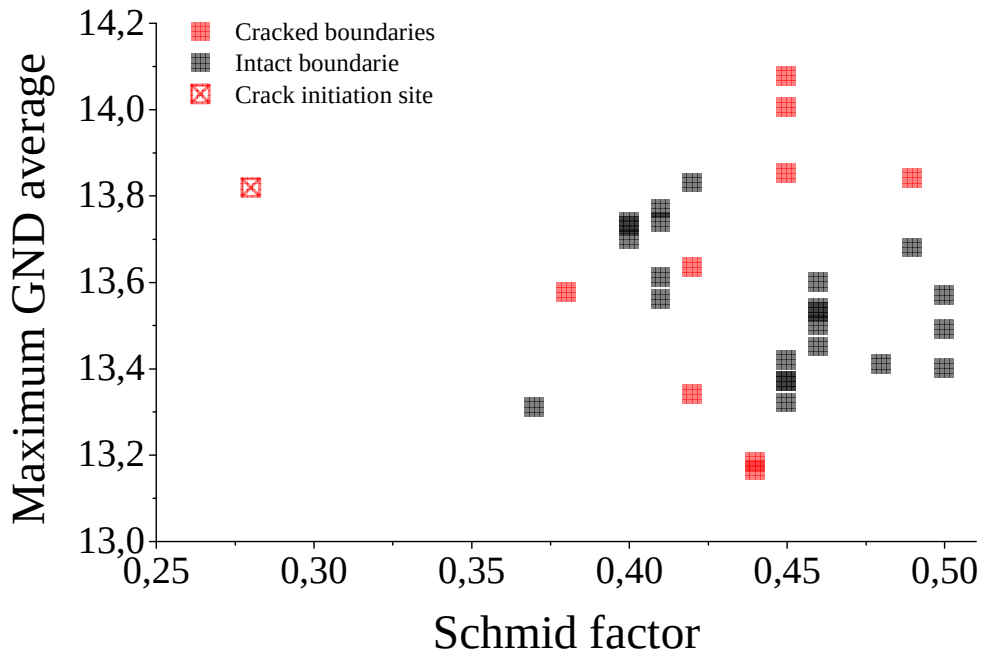

Figure 6.34 Maximum value of the GND adjacent to the boundary versus the Schmid factor that corresponds to that grain.

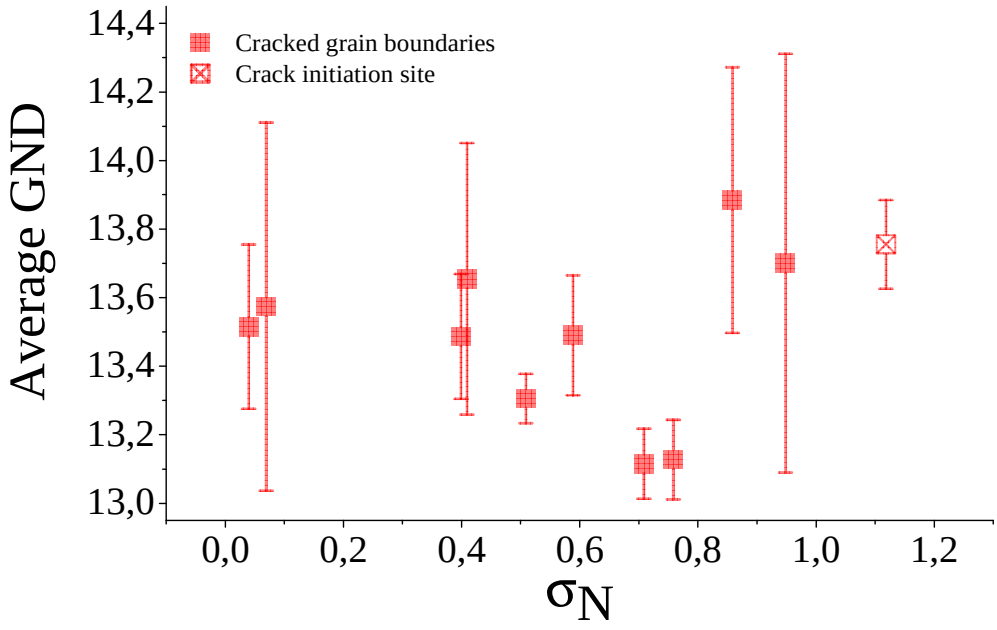

Figure 6.35 Average GND calculated for each grain boundary as a function of σ_N cracked grain boundaries.The maximum and minimum values of the two grains adjacent to the boundary are marked.

6.7 Discussion

The purpose of this study was to apply the SMGBS model to interpret an observation of IGSCC initiation in 304 SS, to extend it by including sensitisation and to apply the HR-EBSD technique to see how the plasticity around the initiation site is different from the others.

The crack trace angle (θ), the angle formed between the tensile direction and the grain boundary plane (φ) and the Schmid factor mismatch (Δm) were analysed. These variable are used by the SMGBS model to calculate σ_N and, as presented in the beginning of the chapter, they have been observed in different studies to influence crack initiation.

No direct correlation could be determined between only the trace angle and the crack initiation site. However, this would not be expected, especially since the trace inclination is not representative in a 3D analysis. Also, no direct correlation could be determined between only φ and the susceptibility to cracking. While the grain boundary that corresponds to the initiation had a value for φ of 87°, it was not the only grain boundary with this value nor is it the highest value found. From these parameters that influence the normal stress it seems that none of them is dominating the normal stress, instead the highest normal stress value comes from combining together all these factors.

The Schmid factor mismatch was the greatest for the grain boundary where crack initiated. The plot of σ_N versus the Schmid factor mismatch is shown in **Figure 6.36**. It can be observed that the initiation site is the grain boundary with the highest value of both Schmid factor mismatch and σ_N. Also, there is a general but scattered trend for σ_N to increase with the increase in the Schmid factor mismatch. This also comes from

Equation (24) that uses the average of the two values of the Schmid factor for the two grains in calculating the normalized stress.

To illustrate this, the σ_N was plotted against a constant φ (the angle formed between the tensile direction and the grain boundary plane) value for three different combinations of grains of different Schmid factor mismatch, denoted as: hard-hard (Δm =0), soft-soft (Δm =0) and hard-soft (Δm =0.23). The graph is shown in **Figure 6.37.** The normal stress increases as the tensile stress becomes more normal to the grain boundary plane for all combinations, but the magnitude is sensitive to the Schmid factor mismatch. For the hard-hard combination (low Schmid factor mismatch, high resistance to slip) the boundary has the highest normal stress; for the soft-soft combination (low Schmid factor mismatch, low resistance to slip) the boundary has the lowest normal stress and for the hard-soft combination (high Schmid factor mismatch) the boundary has a high normal stress. This explains the scatter in the values plotted in **Figure 6.36**, such that for the same Schmid factor mismatch, the value of the normal stress varies, depending on the relative orientation of the grain boundary plane to the tensile direction.

The highest value of the cracked boundaries for σ_N was 1.12 and it corresponds to the crack initiation site. The other boundaries that cracked and are around the initiation boundary all have values for σ_N between 0.04 and 0.95, which are lower than the initiation boundary. The SMBGS was also applied for three random areas of the sample where no cracks were present. Though the maximum values calculated for the grain boundaries that did not crack are not far off from the value that corresponds to the crack initiation site, they are still lower (**Figure 6.25**), indicating that none of the grain boundary that was analysed failed because the value of σ_N was not high enough or it was

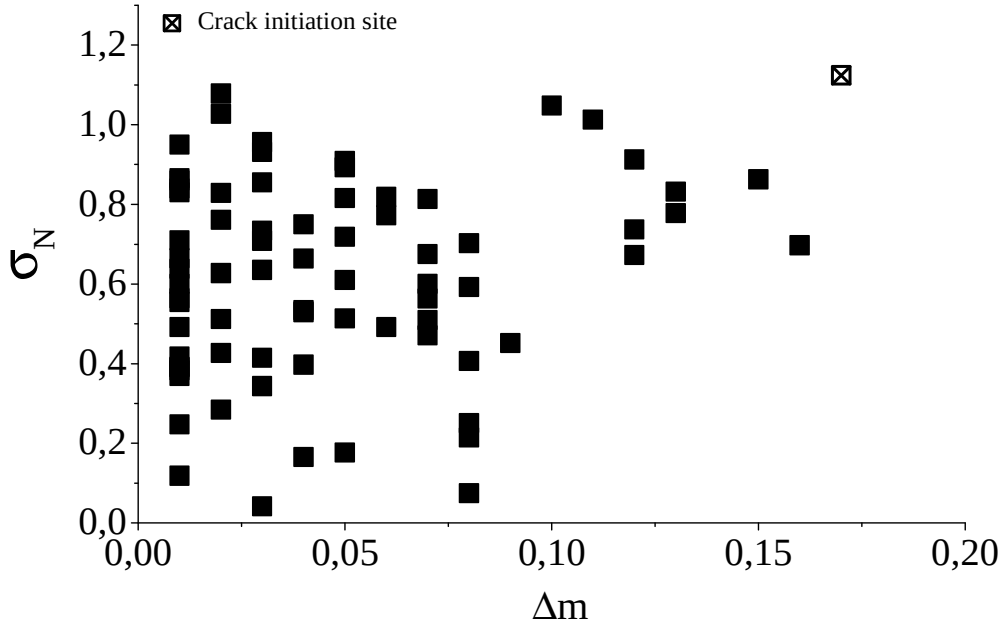

Figure 6.36 Plot of σ_N versus the Schmid factor mismatch for the grain boundaries that were analysed using the SMGBS model.

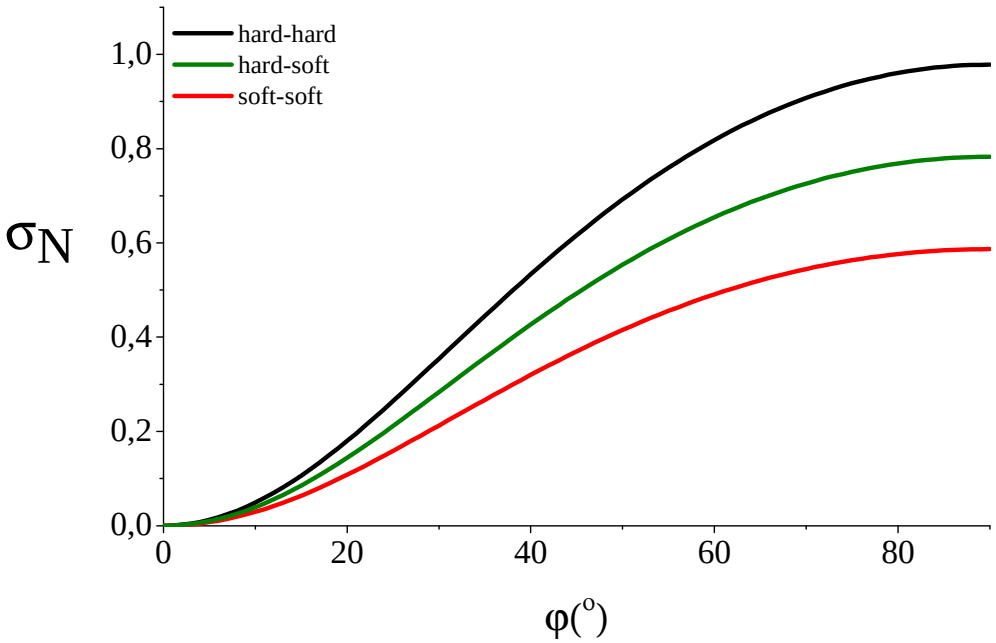

Figure 6.37 Variation of σ_N with φ for three different combinations of grains: hard-hard, soft-soft and hard-soft.

not the highest. Another reason why these grain boundaries did not fail is that they might not have been sensitised.

To further look into what makes a grain boundary susceptible, the CSL boundaries as well as the closest low indexed plane was calculated for all the grain boundaries for which the SMBGS model was applied. By applying the CSL criterion and the low indexed plane one, two of the grain boundaries that had high stress but did not crack (σ_N equal to 1.05 and 1.08, these being the highest calculated for the grain boundaries where no cracks initiated) were found to be excluded due to their structure. While more data would be needed to draw a firm conclusion, it can be noted that, even though the effect of the sensitisation presented in this chapter cannot be extended easily to PWR conditions, the SMBGS model is not complete unless sensitisation is taken into consideration. The analysis of the CSL $\sum$ and the low indexed plane of grain boundaries accurately described the reason why some grain boundaries did not crack. Two of the grain boundaries that had high normal stress values and were excluded by the CSL criterion were $\sum$9 and $\sum$13a. The grain boundary that was the closest in stress to the initiation site was $\sum$13a and was close to (100) plane. The grain boundary where crack initiated had a random orientation, was closest to (3 -3 1) plane and had a σ_N equal to 1.12. The other boundaries that cracked and are around the initiation had all random orientation and were not close to a low indexed plane.

HR-EBSD was used to determine the GNDs density for three different areas: the area where the crack initiated, an area perpendicular to the initiation site and an area along the propagated crack. As shown in **Figure 6.33**, the boundary average GNDs tend to be higher for the cracked boundaries than for the intact boundaries, the initiation boundary having one of the highest value.

An improved SMBGS model that will take into consideration both the CSL boundary information as well as the closest low indexed plane is a valid model that has the potential to accurately predict IGSCC in stainless steel. The SMBGS model identified the crack initiation boundary to be of random orientation, not close to a low indexed plane, with the highest value of σ_N out of both cracked and intact boundaries which was located between a “soft” and a “hard” grain. According to the observations presented in this chapter, the grain boundary that is less resistant to cracking is the one with the highest normalised stress, which is sensitised.

To improve the model future work would include applying the data for other samples that have been tested in the same environment as the one presented in this chapter to see how well the model can predict crack initiation. Also, in order to clearly state how the GNDs can predict crack initiation, more data need to be gathered.

7 Final conclusions

The research presented in this thesis focused on developing micro-mechanical testing techniques to study IGSCC at individual grain boundaries in two different materials and environments: 304 SS in 0.1 M potassium tetrathionate and Ni Alloy 600 in PWR environment. In addition, to gain a better understanding of the initiation step of IGSCC, larger-scale experiments were used to assess and extend a model for prediction of crack initiation in 304 SS.

FIB manufactured cantilevers were milled in 304 SS and Ni Alloy 600 to test the crack growth rate and fracture toughness of individual grain boundaries fractured during micro-mechanical testing. This technique was applied *in-situ* on 304 SS as described in **Chapter 4**. Different parameters (e.g. testing time, pH, counter electrode) that influence IGSCC were varied during several experiments to control the crack growth rate. However, the different combinations of variables did not produce a controllable crack growth rate. Though controllable crack growth rate can be produced at the macro-scale, by using a platinum counter electrode [14], this was not the case in the micro-specimens. Fracture at the grain boundary could be obtained only when the sample was polarised using a 6 V battery. In this case, the crack growth rate was very rapid (approximately 40 μm/s and 120 μm/s) and it was a few orders of magnitude higher than IGSCC crack growth rate reported for macro-scale specimens that range between 10^{-9}-10^{-8} μm/s and 10^{-2}-10^{-1} μm/s [35]. However, since the tests were performed for single grain boundaries, the crack growth rate should be compared to the one of a single crystal. In single crystal silicon, the crack growth rate was reported to be 10^{-4}-10^{2} μm/s [131], values that are comparable with the results obtained in the current study for the crack growth rate determined using micro-mechanical testing.The same

technique was used to test micro-cantilevers in Ni Alloy 600, work that was presented in **Chapter 5**. In this case, the samples had already been exposed to a PWR environment for three different conditions (4500 h, 1500 h and no exposure). Grain boundary fracture occurred in all specimens that had been exposed for 4500 h while only plastic deformation could be observed in the samples that were exposed for 1500 h or were un-oxidised. The misorientation of the grain boundaries was also measured for the boundaries tested. No correlation could be determined between the grain boundary fracture toughness values and the misorientation. It was also observed that only one out of the 19 oxidised grain boundaries was a special boundary ($\sum 3$), while seven out of the 19 un-oxidised boundaries were either $\sum 3$ or $\sum 9$. This method of testing embrittlement at grain boundaries coupled with the characterisation of misorientation of grain boundaries is a technique that could bring more insight into what makes grain boundaries resistant or susceptible to IGSCC.

While the method of study IGSCC at individual grain boundaries proved to be more challenging in the case of 304 SS, it gave very good results when applied to Ni Alloy 600. The method has a high potential to be applied in similar study of grain boundary embrittlement for materials with application in the nuclear industry. The environment in which 304 SS was tested proved to be rather complex and in order for more results to be obtained in this environment, further research needs to be performed to determine the difference between the SCC at the macro-scale and SCC at the micro-scale. While SCC is relatively easy to control at a greater scale, it proved to be quite challenging to be applied similarly at a smaller scale.

Chapter 6 tested the Schmid-modified grain boundary stress (SMGBS) model to see whether it could predict crack initiation in 304 SS. The model was applied to two different sets of boundaries: cracked and intact boundaries. The value for normal stress $\sigma_N$was calculated for all these boundaries, including the initiation site. The model identified the boundary where crack initiated as being the one with the highest value for the normal stress. Next, the grain boundaries that are known to be resistant to IGSCC in 304 SS were identified. It was observed that some of these grains had values for σ_N equal to 1.05 and 1.08, values that were very close to the σ_N of the initiation site (1.12). This shows that, in order for the model to accurately describe the initiation in 304 SS, the resistant boundaries need to be taken into account.

HR-EBSD was also applied to determine geometrically-necessary dislocation (GND) densities near the intact and cracked boundaries, as well as to the boundary where crack initiated. The modelled used, coupled with sensitisation as well as HR-EBSD technique could successfully identify the initiation site. While more data will need to be collected for different samples, the model has the potential to accurately predict IGSCC initiation in 304 SS.

The observations made in this study can be incorporated in the future into a model that could predict IGSCC in 304 stainless steel. For this, a threshold of the normalised stress needs to be established to determine the value that corresponds to a susceptible boundary. Also, HR-EBSD needs to be applied to several samples to determine the correlation between the GND values and the initiation site.

The micro-mechanical testing technique can be used in the future to compare the grain boundary resistance of Ni Alloys and Stainless Steel. For example, for a given exposure time and environmental conditions, a specific grain boundary of known orientation (that

can be determined using EBSD) can be tested and the fracture toughness values can be compared. As suggested by AREVA, some of these families can be: Alloy 600 MA (mill annealed, with intergranular carbides and few intergranular carbides), Alloy 600 TT (with carbides at the grain boundaries which are known to increase resistance), 304 SS, Alloy 690 TT (in as received conditions) and Alloy 690 MA.

8 Appendix: Misorientation data for each grain boundary – AREA 1

G.B. ID {hkl}	1	2	3	4	5	6	7	8	9	10	11	12	13	14	15	16	17	18	19	20	21	22	23
(1 1 1)	69	71	174	75	105	76	43	65	12	86	70	66	70	128	109	67	87	120	163	102	100	71	145
(-1 1 1)	109	109	106	85	134	99	29	90	83	112	100	103	108	160	71	108	154	134	124	147	111	0	92
(-1 -1 1)	178	178	72	151	143	165	91	58	113	59	62	69	70	95	0	177	132	129	71	83	148	71	92
(-1 -1 -1)	111	109	6	105	75	104	137	115	168	94	110	114	110	52	71	113	93	60	17	78	80	109	35
(-1 1 -1)	71	69	65	46	68	56	80	160	117	164	170	174	178	104	109	72	107	64	85	139	48	71	35
(1 -1 1)	109	111	115	134	112	124	100	20	63	16	10	6	2	76	71	108	73	116	95	41	132	109	145
(1 -1 -1)	71	71	74	95	46	81	151	90	97	68	80	77	72	20	109	72	26	46	56	33	69	180	88
(1 0 0)	54	56	129	81	68	70	97	69	43	67	63	57	56	74	125	53	35	81	111	56	81	125	133
(-1 0 0)	126	124	51	99	112	110	83	111	137	113	117	123	124	106	55	127	145	99	69	124	99	55	47
(1 1 0)	34	36	143	46	71	42	62	94	33	106	94	89	90	109	145	32	64	86	142	101	66	90	119
(-1 1 0)	90	89	85	61	101	76	50	125	102	145	135	139	143	136	90	90	136	99	107	168	79	35	61
(-1 -1 0)	146	144	37	134	109	138	118	86	147	74	86	91	90	71	35	148	116	94	38	79	114	90	61
(1 -1 0)	90	91	95	119	79	104	130	55	78	35	45	41	37	44	90	90	44	81	73	12	101	145	119
(2 1 0)	38	41	142	59	68	51	76	83	31	90	81	75	75	95	141	37	50	83	131	83	71	105	127
(-2 1 0)	105	103	70	76	107	90	63	122	117	133	131	136	139	126	75	106	146	100	91	150	87	39	53
(-2 -1 0)	142	139	38	121	112	129	104	97	149	90	99	105	105	85	39	143	130	97	49	97	109	75	53
(2 -1 0)	75	77	110	104	73	90	117	58	63	47	49	44	41	54	105	74	34	80	89	30	93	141	127
(2 2 1)	53	56	162	61	90	60	50	78	16	95	80	76	78	121	125	52	77	105	157	102	85	79	134

G.B. ID {hkl}	1	2	3	4	5	6	7	8	9	10	11	12	13	14	15	16	17	18	19	20	21	22	23
(-2 -2 1)	166	163	56	147	128	155	103	71	128	65	72	79	78	84	16	167	126	114	56	81	133	79	78
(-2 -2 -1)	127	124	18	119	90	120	130	102	164	85	100	104	102	59	55	128	103	75	23	78	95	101	46
(-2 2 -1)	79	77	73	51	83	64	67	145	111	160	154	158	163	119	101	80	120	79	95	154	61	55	46
(2 -2 1)	101	103	107	129	97	116	113	35	69	20	26	22	17	61	79	100	60	101	85	26	119	125	134
(2 -2 -1)	79	80	84	106	60	91	144	74	89	53	64	61	56	28	101	80	30	62	63	19	83	164	102
(2 1 1)	60	63	164	76	92	71	62	64	8	78	65	59	62	109	118	59	68	107	145	85	94	90	149
(-2 1 1)	118	117	86	90	130	105	48	99	102	115	108	113	117	141	62	117	166	124	104	145	108	19	75
(-2 -1 1)	161	159	62	133	136	146	88	77	125	78	82	88	89	100	19	162	144	121	68	98	132	62	75
(-2 -1 -1)	120	117	16	104	88	109	118	116	172	102	115	121	118	71	62	121	112	73	35	95	86	90	31
(-2 1 -1)	91	88	56	64	83	75	80	144	128	147	152	158	160	107	90	92	122	76	78	140	66	62	31
(2 -1 1)	89	92	124	116	97	105	100	36	52	33	28	22	20	73	90	88	58	104	102	40	114	118	149
(2 -1 -1)	62	63	94	90	50	75	132	81	78	65	72	67	63	39	118	63	14	56	76	35	72	161	105
(3 1 1)	57	60	154	77	85	70	72	64	18	74	63	57	59	99	121	56	59	99	135	77	90	100	147
(-3 1 1)	121	120	76	93	126	107	58	103	112	115	111	117	120	131	59	121	165	118	94	141	106	29	67
(-3 -1 1)	151	149	57	123	130	136	86	87	130	88	92	98	99	102	29	152	147	115	68	106	123	59	67
(-3 -1 -1)	123	120	26	103	95	110	108	116	162	106	117	123	121	81	59	124	121	81	45	103	90	80	33
(-3 1 -1)	101	98	53	74	92	85	81	135	133	137	142	148	150	107	80	102	130	82	75	137	75	59	33
(3 -1 1)	79	82	127	106	88	95	99	45	47	43	38	32	30	73	100	78	50	98	105	43	105	121	147
(3 -1 -1)	59	60	104	87	54	73	122	77	68	65	69	63	60	49	121	59	15	62	86	39	74	151	113
(3 3 1)	47	49	156	56	84	55	54	83	21	98	85	80	82	117	131	45	72	99	153	102	79	82	129
(-3 3 1)	97	96	93	70	114	84	40	112	94	133	122	125	130	148	82	97	146	112	114	165	91	22	73
(-3 -3 1)	160	157	50	143	122	150	108	76	134	68	77	83	82	80	22	161	123	108	51	80	127	82	73
(-3 -3 -1)	133	131	24	124	96	125	126	97	159	82	95	100	98	63	49	135	108	81	27	78	101	98	51

G.B. ID {hkl}	1	2	3	4	5	6	7	8	9	10	11	12	13	14	15	16	17	18	19	20	21	22	23
(3 -3 1)	97	99	103	126	91	113	119	42	72	24	32	28	24	56	82	97	54	94	81	21	113	131	129
(3 1 0)	42	45	139	66	68	56	83	78	33	83	75	69	69	88	137	41	44	82	125	75	74	111	130
(-3 1 0)	112	110	64	83	109	96	69	119	124	127	127	133	136	120	69	112	147	100	85	142	91	43	50
(-3 -1 0)	138	135	41	114	112	124	97	102	147	97	105	111	111	92	43	139	136	98	55	105	106	69	50
(3 -1 0)	68	70	116	97	71	84	111	61	56	53	53	47	44	60	111	68	33	80	95	38	89	137	130
(3 2 1)	50	53	158	65	84	61	61	75	15	88	75	70	72	110	128	49	66	99	146	91	83	90	138
(-3 2 1)	108	107	85	79	120	94	47	108	102	126	118	123	127	142	72	108	156	115	106	155	98	22	70
(-3 -2 1)	159	156	52	135	126	145	99	80	134	76	83	89	89	89	22	160	134	111	57	91	126	72	70
(-3 -2 -1)	130	127	22	115	96	119	119	105	165	92	105	110	108	70	52	131	114	81	34	89	97	90	42
(-3 2 -1)	91	88	67	62	90	75	69	139	119	149	148	153	156	117	90	91	129	84	88	150	70	52	42
(3 -2 1)	89	92	113	118	90	105	111	41	61	31	32	27	24	63	90	89	51	96	92	30	110	128	138
(3 -2 -1)	72	73	95	101	60	86	133	72	78	54	62	57	53	38	108	72	24	65	74	25	82	158	110
(3 3 2)	59	61	167	66	96	66	47	73	13	92	76	72	75	124	119	57	80	110	161	102	90	76	138
(-3 3 2)	104	103	100	78	125	92	33	100	88	121	110	113	118	156	76	103	152	124	120	156	102	10	83
(-3 -3 2)	172	169	62	149	134	160	99	66	123	62	69	75	75	88	10	173	128	119	62	82	139	76	83
(-3 -3 -2)	121	119	13	114	84	114	133	107	167	88	104	108	105	56	61	123	100	70	19	78	90	104	42
(-3 3 -2)	76	74	70	48	77	61	72	150	113	163	160	164	168	113	104	77	115	74	91	149	56	61	42
(3 -3 2)	104	106	110	132	103	119	108	30	67	17	20	16	12	67	76	103	65	106	89	31	124	119	138
(3 -3 -2)	76	77	80	102	55	88	147	80	92	59	70	67	62	24	104	77	28	56	60	24	78	170	97
(3 2 0)	35	38	143	54	69	47	71	87	31	96	86	80	81	100	143	34	55	84	135	90	69	99	124
(-3 2 0)	99	98	76	70	105	84	58	124	111	138	133	138	142	130	81	100	143	100	97	157	84	37	56
(-3 -2 0)	145	142	37	126	111	133	109	93	149	84	94	100	99	80	37	146	125	96	45	90	111	81	56
(3 -2 0)	81	82	104	110	75	96	122	56	69	42	47	42	38	50	99	80	37	80	83	23	96	143	124

G.B. ID {hkl}	1	2	3	4	5	6	7	8	9	10	11	12	13	14	15	16	17	18	19	20	21	22	23
(3 2 2)	64	66	171	75	98	73	54	64	2	81	66	62	65	117	115	62	76	113	153	92	96	82	148
(-3 2 2)	114	114	94	88	132	103	40	95	94	114	105	109	113	149	65	114	163	129	112	147	110	11	82
(-3 -2 2)	169	167	66	141	140	154	89	69	120	70	74	80	81	98	11	170	139	125	69	92	139	65	82
(-3 2 -2)	83	80	60	57	77	67	80	151	124	154	159	166	168	106	98	84	116	71	81	141	58	65	32
(3 -2 2)	97	100	120	123	103	113	100	29	56	26	21	14	12	74	82	96	64	109	99	39	122	115	148
(3 -2 -2)	66	66	86	92	48	77	140	85	86	66	75	71	67	31	115	66	17	51	68	33	70	169	98

The cell highlighted in grey represents the angle closest to the {hkl} plane and the column highlighted in grey identifies a grain boundary that is close to a low indexed plane

AREA 1 – the 23 grain boundaries are identified

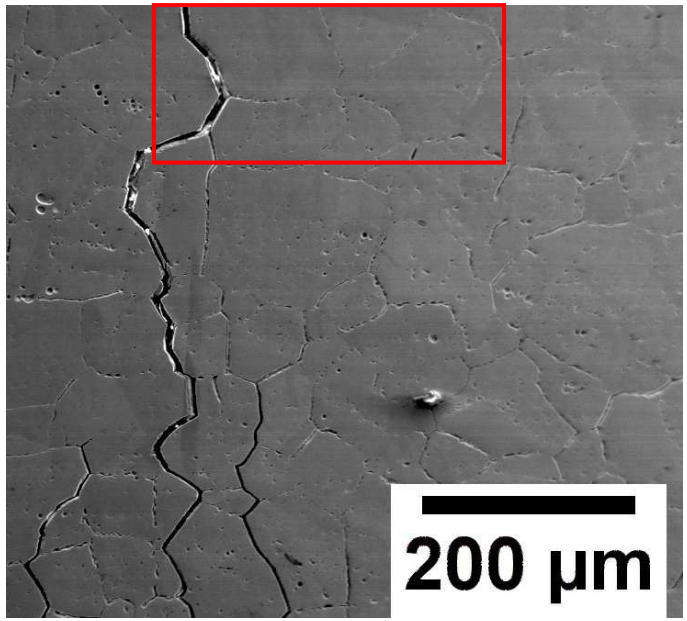

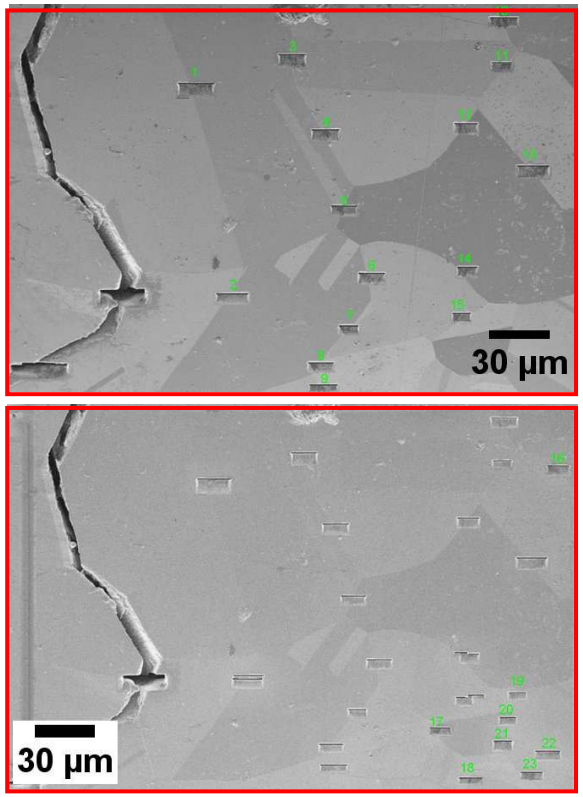

Misorientation data for each grain boundary – AREA 2

G.B. ID {hkl}	1	2	3	4	5	6	7	8	9	10	11	12	13	14	15
(1 1 1)	29	111	91	178	59	127	43	75	45	45	120	108	49	97	54
(-1 1 1)	99	167	82	110	129	70	72	105	108	66	80	56	114	74	70
(-1 -1 1)	117	97	137	72	129	22	70	62	99	135	107	17	105	16	141
(-1 -1 -1)	151	69	89	2	121	53	137	105	135	135	60	72	131	83	126
(-1 1 -1)	126	119	28	70	121	89	140	172	149	66	11	95	145	125	58
(1 -1 1)	54	61	152	110	59	91	40	8	31	114	169	85	35	55	122
(1 -1 -1)	81	13	98	70	51	110	108	75	72	114	100	124	66	106	110
(1 0 0)	26	58	98	124	6	145	69	63	30	74	126	139	22	110	78
(-1 0 0)	154	122	82	56	174	35	111	117	150	106	54	41	158	70	102
(1 1 0)	36	99	64	143	45	159	76	97	59	29	97	141	56	132	34
(-1 1 0)	117	153	51	90	135	77	106	140	135	61	45	73	138	100	58
(-1 -1 0)	144	81	116	37	135	21	104	83	121	151	83	39	124	48	146
(1 -1 0)	63	27	129	90	45	103	74	40	45	119	135	107	42	80	122
(2 1 0)	24	82	78	139	27	163	72	83	44	48	110	146	40	125	52
(-2 1 0)	134	143	63	75	153	59	110	134	147	79	45	59	153	88	76
(-2 -1 0)	156	98	102	41	153	17	108	97	136	132	70	34	140	55	128
(2 -1 0)	46	37	117	105	27	121	70	46	33	101	135	121	27	92	104
(2 2 1)	28	106	79	163	51	142	58	85	49	35	110	123	50	113	43
(-2 2 1)	47	147	78	134	49	129	62	84	53	47	111	121	51	111	51
(-2 -2 1)	130	90	129	56	134	13	85	71	109	145	97	24	114	30	147
(-2 2 -1)	124	135	36	78	129	83	125	159	146	62	26	85	145	114	56

G.B. ID {hkl}	1	2	3	4	5	6	7	8	9	10	11	12	13	14	15
(2 -2 -1)	72	10	112	78	46	108	93	59	60	118	116	118	54	94	116
(2 1 1)	11	92	94	160	39	139	48	68	32	52	126	121	32	103	60
(-2 1 1)	119	155	81	91	149	54	86	112	125	80	68	45	132	71	81
(-2 -1 1)	133	108	117	63	149	9	85	82	117	128	88	10	124	35	129
(-2 -1 -1)	169	88	86	20	141	41	132	112	148	128	54	59	148	77	120
(-2 1 -1)	142	124	47	62	141	70	134	152	163	80	21	76	163	105	73
(2 -1 1)	38	56	133	118	39	110	46	28	17	100	159	104	17	75	107
(2 -1 -1)	61	25	99	89	31	126	94	68	55	100	112	135	48	109	99
(3 1 1)	5	83	95	150	30	144	53	66	27	58	128	128	25	106	64
(-3 1 1)	129	146	81	81	158	47	93	114	133	87	63	42	140	70	87
(-3 -1 1)	141	112	107	60	158	12	92	92	127	122	79	18	134	45	122
(-3 -1 -1)	175	97	85	30	150	36	127	114	153	122	52	52	155	74	116
(-3 1 -1)	148	125	57	59	150	60	128	142	166	87	30	66	170	95	82
(3 -1 1)	32	55	123	121	30	120	52	38	14	93	150	114	10	85	98
(3 -1 -1)	51	34	99	99	22	133	87	66	47	93	117	138	40	110	93
(3 3 1)	30	104	74	156	49	147	64	88	52	32	106	128	51	119	39
(-3 3 1)	111	165	63	98	135	73	93	127	125	61	58	66	130	91	61
(-3 -3 1)	135	87	125	50	135	14	91	75	113	148	92	28	118	36	148
(-3 -3 -1)	150	76	106	24	131	33	116	92	128	148	74	52	129	61	141
(-3 3 -1)	122	141	41	82	131	81	119	153	143	61	32	81	144	110	56
(3 -3 1)	58	39	139	98	49	99	61	27	37	119	148	99	36	70	124
(3 -3 -1)	69	15	117	82	45	107	87	53	55	119	122	114	50	89	119
(3 1 0)	22	75	84	136	19	159	70	76	38	56	115	145	33	121	59

G.B. ID {hkl}	1	2	3	4	5	6	7	8	9	10	11	12	13	14	15
(-3 -1 0)	158	105	96	44	161	21	110	104	142	124	65	35	147	59	121
(3 -1 0)	39	43	111	111	19	128	69	51	30	93	134	127	23	98	96
(3 2 1)	18	95	83	156	40	148	58	79	41	43	116	129	40	114	50
(-3 2 1)	119	158	70	91	146	62	94	122	130	73	59	55	136	81	73
(-3 -2 1)	139	98	118	53	146	2	92	82	120	137	86	21	125	38	137
(-3 -2 -1)	162	85	97	24	140	32	122	101	139	137	64	51	140	66	130
(-3 2 -1)	133	135	47	72	140	72	124	151	153	73	28	74	155	104	67
(3 -2 1)	47	45	133	108	40	108	56	29	27	107	152	106	25	76	113
(3 -2 -1)	61	22	110	89	34	118	86	58	50	107	121	125	44	99	107
(3 3 2)	27	108	83	168	54	136	52	81	47	38	114	117	49	107	47
(-3 3 2)	105	171	73	105	133	71	82	115	116	64	70	60	122	82	66
(-3 -3 2)	125	93	132	62	133	15	79	68	106	142	101	20	111	25	145
(-3 -3 -2)	153	72	97	12	126	44	128	99	133	142	66	63	131	73	133
(-3 3 -2)	125	129	33	75	126	85	131	164	147	64	20	89	146	118	57
(3 -3 2)	55	51	147	105	54	95	49	16	33	116	160	91	34	62	123
(3 -3 -2)	75	9	107	75	47	109	98	65	64	116	110	120	58	98	114
(3 2 0)	28	88	72	142	34	163	73	88	49	41	105	145	46	128	45
(-3 2 0)	128	148	58	81	146	66	109	137	143	72	44	64	148	93	69
(-3 -2 0)	152	92	108	38	146	17	107	92	131	139	75	35	134	52	135
(3 -2 0)	52	32	122	99	34	114	71	43	37	108	136	116	32	87	111
(-3 2 2)	111	161	81	99	141	61	80	109	118	74	73	49	125	72	76
(-3 -2 2)	126	103	125	67	141	13	78	74	110	132	96	10	116	27	135
(-3 -2 -2)	162	80	87	12	133	46	135	109	143	132	56	64	141	79	123

G.B. ID {hkl}	1	2	3	4	5	6	7	8	9	10	11	12	13	14	15
(3 -2 2)	45	58	141	115	47	102	43	19	22	106	165	96	25	67	113
(3 -2 -2)	69	19	99	81	39	119	100	71	62	106	107	131	55	108	104

The cell highlighted in grey represents the angle closest to the {hkl} plane and the column highlighted in grey identifies a grain boundary that is close to a low indexed plane

AREA 2 – the 15 grain boundaries are identified

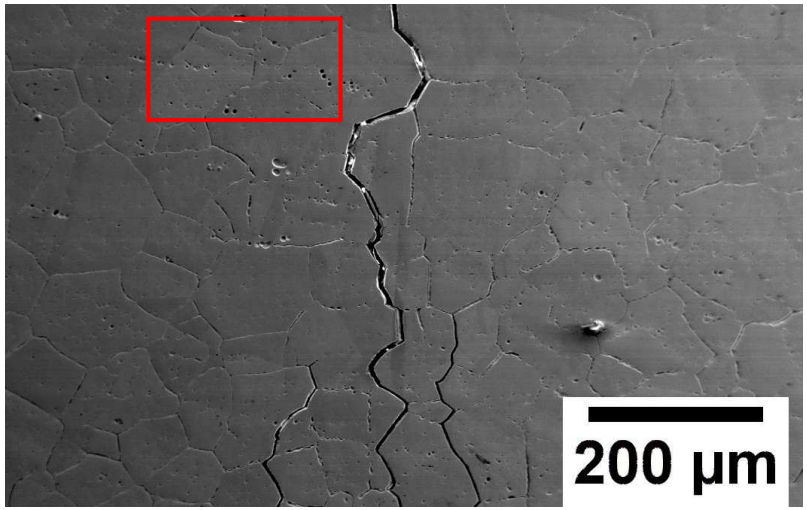

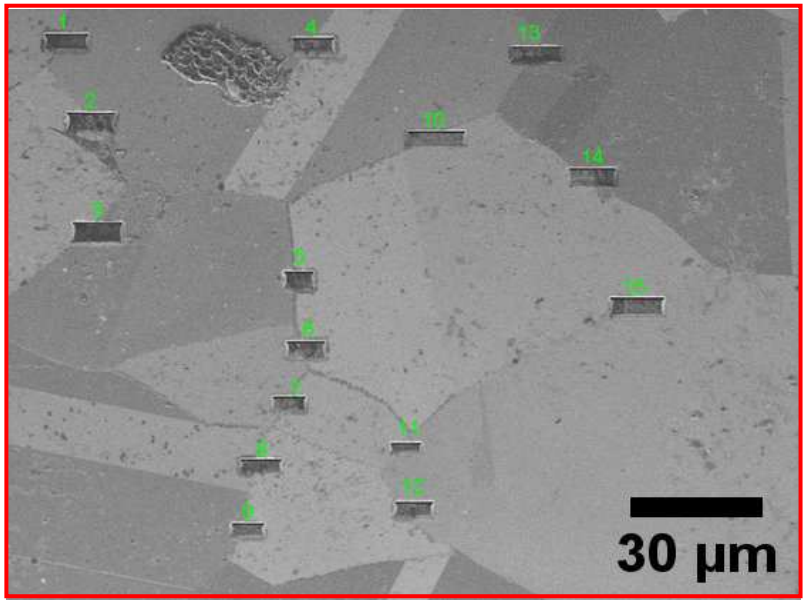

Misorientation data for each grain boundary – AREA 3

G.B. ID {hkl}	1	2	3	4	5	6	7	8	9	10	11	12
(1 1 1)	24	110	22	60	120	62	129	56	150	87	81	65
(-1 1 1)	79	178	55	86	50	107	122	68	138	99	31	63
(-1 -1 1)	93	108	88	156	47	76	51	139	94	155	93	132
(-1 -1 -1)	156	70	158	120	60	118	51	124	30	93	99	115
(-1 1 -1)	132	110	113	60	63	172	122	56	79	46	41	45
(1 -1 1)	48	70	67	120	117	8	58	124	101	134	139	135
(1 -1 -1)	101	2	125	94	130	73	58	112	42	81	149	117
(1 0 0)	51	56	72	69	171	50	95	81	96	79	127	92
(-1 0 0)	129	124	108	111	9	130	85	99	84	101	53	88
(1 1 0)	54	91	57	30	137	82	140	37	119	54	82	48
(-1 1 0)	107	145	84	69	48	141	130	55	110	71	9	44
(-1 -1 0)	126	89	123	150	43	98	40	143	61	126	98	132
(1 -1 0)	73	35	96	111	132	39	50	125	70	109	171	136
(2 1 0)	49	76	61	45	154	68	122	55	111	63	101	66
(-2 1 0)	118	141	94	87	30	142	111	73	100	83	27	62
(-2 -1 0)	131	104	119	135	26	112	58	125	69	117	79	114
(2 -1 0)	62	39	86	93	150	38	69	107	80	97	153	118
(2 2 1)	36	102	37	46	129	71	136	45	137	72	81	56
(-2 2 1)	51	129	49	55	131	69	132	51	132	73	61	55
(-2 -2 1)	108	100	104	159	43	86	44	144	79	143	95	134
(-2 -2 -1)	144	78	143	134	51	109	44	135	43	108	99	124

G.B. ID {hkl}	1	2	3	4	5	6	7	8	9	10	11	12
(-2 2 -1)	122	126	100	63	55	160	127	54	93	56	26	42
(2 -2 1)	58	54	80	117	125	20	53	126	87	124	154	138
(2 -2 -1)	88	15	112	102	133	58	53	119	54	94	164	127
(2 1 1)	25	91	39	60	139	54	119	62	131	83	98	74
(-2 1 1)	97	160	74	95	31	118	109	79	119	101	31	70
(-2 -1 1)	107	117	96	143	28	95	61	127	90	136	78	117
(-2 -1 -1)	155	89	141	120	41	126	61	118	49	97	82	106
(-2 1 -1)	137	118	114	78	44	165	109	71	80	65	39	59
(2 -1 1)	43	62	66	102	136	15	71	109	100	115	141	121
(2 -1 -1)	83	20	106	85	149	62	71	101	61	79	149	110
(3 1 1)	31	81	48	61	149	51	112	67	121	82	106	79
(-3 1 1)	106	150	84	100	22	123	103	84	109	101	36	75
(-3 -1 1)	114	120	100	134	18	105	68	119	88	126	70	109
(-3 -1 -1)	149	99	132	119	31	129	68	113	59	98	74	101
(-3 1 -1)	137	121	113	88	34	155	103	79	81	75	41	67
(3 -1 1)	43	59	67	92	146	25	77	101	99	105	139	113
(3 -1 -1)	74	30	96	80	158	57	77	96	71	79	144	105
(3 3 1)	42	99	44	41	132	74	138	42	131	66	81	53
(-3 3 1)	97	159	73	75	47	128	129	59	121	81	11	50
(-3 -3 1)	114	96	110	157	42	89	42	145	73	138	96	134
(-3 -3 -1)	138	81	136	139	48	106	42	138	49	114	99	127
(-3 3 -1)	117	132	95	65	52	154	129	53	98	61	20	42
(3 -3 1)	63	48	85	115	128	26	51	127	82	119	160	138

G.B. ID {hkl}	1	2	3	4	5	6	7	8	9	10	11	12
(3 -3 -1)	83	21	107	105	133	52	51	121	59	99	169	130
(-3 1 0)	122	137	98	94	23	139	103	81	95	88	35	70
(-3 -1 0)	131	110	116	128	18	118	66	117	73	112	71	106
(3 -1 0)	58	43	82	86	157	41	77	99	85	92	145	110
(3 2 1)	35	91	44	49	140	64	127	53	128	73	92	64
(-3 2 1)	101	158	77	86	36	127	117	70	116	90	21	60
(-3 -2 1)	114	107	106	148	31	96	53	134	79	134	85	123
(-3 -2 -1)	145	89	136	131	40	116	53	127	52	107	88	116
(-3 2 -1)	126	129	103	75	43	158	117	64	91	67	28	53
(3 -2 1)	54	51	77	105	137	22	63	116	89	113	152	127
(3 -2 -1)	79	22	103	94	144	53	63	110	64	90	159	120
(3 3 2)	31	105	32	51	126	68	134	49	142	77	81	59
(-3 3 2)	87	171	63	81	48	117	125	63	131	91	21	56
(-3 -3 2)	102	103	98	159	44	82	46	143	84	148	95	134
(-3 -3 -2)	149	75	148	129	54	112	46	131	38	103	99	121
(-3 3 -2)	126	120	105	62	57	165	125	54	88	52	31	42
(3 -3 2)	54	60	75	118	123	15	55	126	92	128	149	138
(3 -3 -2)	93	9	117	99	132	63	55	117	49	89	159	124
(3 2 0)	50	82	59	39	147	73	129	48	115	59	94	59
(-3 2 0)	114	143	90	80	37	142	118	66	104	78	20	55
(-3 -2 0)	130	98	121	141	33	107	51	132	65	121	86	121
(3 -2 0)	66	37	90	100	143	38	62	114	76	102	160	125
(3 2 2)	23	99	31	60	131	57	123	59	139	85	91	70

G.B. ID {hkl}	1	2	3	4	5	6	7	8	9	10	11	12
(-3 2 2)	89	168	66	91	39	113	115	74	127	100	30	67
(-3 -2 -2)	157	81	149	120	49	123	57	121	41	95	89	110
(-3 2 -2)	136	115	114	71	52	171	115	64	80	57	39	53
(3 -2 2)	44	65	66	109	128	9	65	116	100	123	141	127
(3 -2 -2)	91	12	114	89	141	67	65	106	53	80	150	113

The cell highlighted in grey represents the angle closest to the {hkl} plane and the column highlighted in grey identifies a grain boundary that is close to a low indexed plane

AREA 3 – the 12 grain boundaries are identified

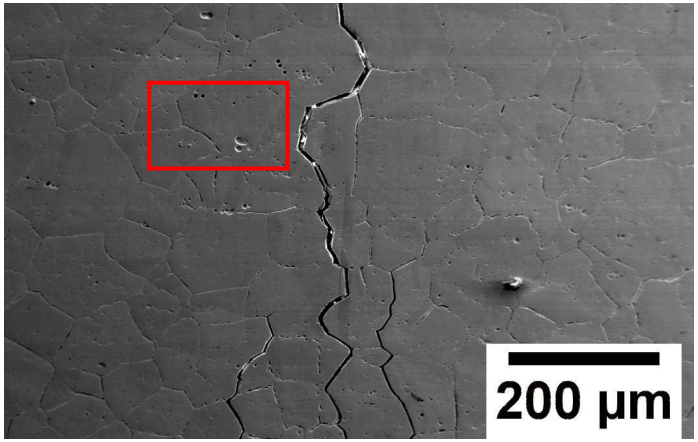

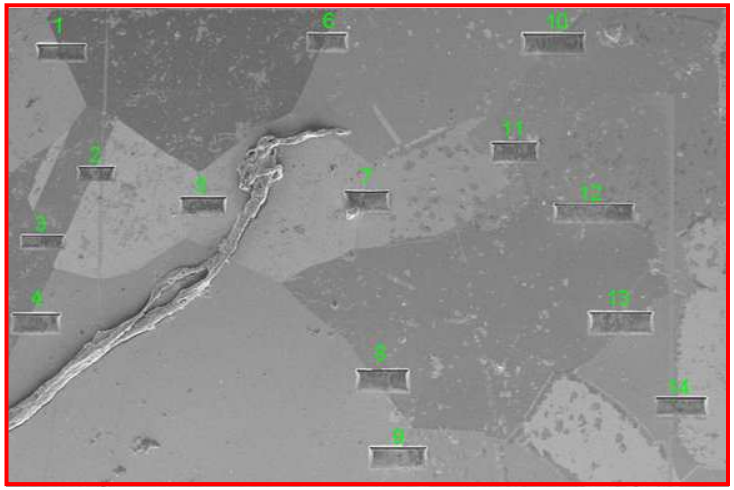

Misorientation data for each grain boundary – Initiation site

G.B. ID {hkl}	1	2	3	4	5	6	7	8	9	10	11	12	13	14	15	16	17	18	19	20	21	22	23	24	25
(1 1 1)	123	129	83	138	52	146	154	90	46	91	129	101	137	110	94	136	55	131	63	76	12	93	126	158	126
(-1 1 1)	88	155	40	151	118	138	105	136	73	135	139	151	71	115	26	77	102	159	105	141	79	25	80	127	159
(-1 -1 1)	18	86	33	90	144	76	47	81	68	153	120	137	73	48	71	86	165	101	73	104	105	51	16	71	110
(-1 -1 -1)	57	51	97	42	128	34	26	90	134	89	51	79	43	70	86	44	125	49	117	104	168	87	54	22	54
(-1 1 -1)	112	110	101	97	106	100	92	152	141	78	69	87	39	139	50	29	80	95	173	141	121	70	102	90	90
(1 -1 1)	68	70	79	83	74	80	88	28	39	102	111	93	141	41	130	151	100	85	7	39	59	110	78	90	90
(1 -1 -1)	92	25	140	29	62	42	75	44	107	45	41	29	109	65	154	103	78	21	75	39	101	155	100	53	21
(1 0 0)	120	76	124	84	20	94	124	51	70	54	84	53	157	86	148	145	47	76	53	28	47	147	131	106	72
(-1 0 0)	60	104	56	96	160	86	56	129	110	126	96	127	23	94	32	35	133	104	127	152	133	33	49	74	108
(1 1 0)	156	115	116	117	29	131	165	96	79	58	95	70	129	129	105	119	20	107	85	73	41	115	161	140	98
(-1 1 0)	102	140	70	128	117	124	101	170	107	108	104	120	47	137	20	48	91	129	140	163	102	40	91	112	125
(-1 -1 0)	24	65	64	63	151	49	15	84	101	122	85	110	51	51	75	61	160	73	95	107	139	65	19	40	82
(1 -1 0)	78	40	110	52	63	56	79	10	73	72	76	60	133	43	160	132	89	51	40	17	78	140	89	68	55
(2 1 0)	143	99	122	104	14	117	149	77	74	53	90	61	144	111	122	132	26	94	71	55	39	130	153	128	87
(-2 1 0)	84	126	62	116	135	109	82	155	110	117	102	126	33	119	13	38	109	120	139	178	115	31	74	96	120
(-2 -1 0)	37	81	58	76	166	63	31	103	106	127	90	119	36	69	58	48	154	86	109	125	141	50	27	52	93
(2 -1 0)	96	54	118	64	45	71	98	25	70	63	78	54	147	61	167	142	71	60	41	2	65	149	106	84	60
(2 2 1)	138	124	98	130	40	142	166	93	60	76	113	87	136	120	99	130	39	121	72	74	23	103	142	154	114
(-2 2 1)	127	140	100	137	49	138	135	96	64	74	115	85	130	122	121	126	52	133	71	58	47	116	128	137	124
(-2 -2 1)	12	76	46	78	152	63	32	82	83	140	104	126	63	47	72	74	179	88	83	106	121	56	2	57	98

G.B. ID {hkl}	1	2	3	4	5	6	7	8	9	10	11	12	13	14	15	16	17	18	19	20	21	22	23	24	25
(-2 2 -1)	108	124	87	111	112	111	96	167	126	92	84	102	40	141	35	35	85	110	159	155	113	56	98	100	106
(2 -2 1)	72	56	93	69	68	69	84	13	54	88	96	78	140	39	145	145	95	70	21	25	67	124	82	80	74
(2 -2 -1)	86	28	127	38	61	46	76	28	92	56	57	42	121	54	164	116	82	34	60	25	91	152	95	58	36
(2 1 1)	126	110	99	119	35	128	149	75	50	77	113	83	153	103	114	148	47	111	56	58	15	112	133	141	107
(-2 1 1)	76	137	40	131	136	120	87	140	86	138	125	149	52	109	12	61	116	139	115	156	98	11	67	108	142
(-2 -1 1)	29	93	35	93	164	78	45	98	83	151	113	140	55	63	55	67	164	103	92	122	117	39	19	70	112
(-2 -1 -1)	54	70	81	61	145	52	31	105	130	103	67	97	27	77	66	32	133	69	124	122	165	68	47	39	73
(-2 1 -1)	93	110	85	98	125	95	79	152	134	96	78	102	22	124	37	18	99	99	162	156	130	54	83	83	97
(2 -1 1)	87	70	95	82	55	85	101	28	46	84	102	78	158	56	143	162	81	81	18	24	50	126	97	97	83
(2 -1 -1)	104	43	140	49	44	60	93	40	94	42	55	31	128	71	168	119	64	41	65	24	82	169	113	72	38
(3 1 1)	126	100	106	109	28	118	143	68	55	70	105	75	160	98	123	150	45	101	53	49	23	122	134	131	97
(-3 1 1)	71	128	43	121	145	110	78	139	93	137	117	145	43	105	12	52	122	129	120	160	108	12	61	98	132
(-3 -1 1)	37	96	39	94	173	80	46	107	91	145	109	138	45	72	47	58	156	104	102	131	123	34	27	70	111
(-3 -1 -1)	54	80	74	71	152	62	37	112	125	110	75	105	20	82	57	30	135	79	127	131	157	58	46	49	83
(-3 1 -1)	84	109	76	97	135	92	72	147	128	104	83	110	16	116	32	19	109	101	152	160	133	47	74	80	101
(3 -1 1)	96	71	104	83	45	88	108	33	52	76	97	70	164	64	148	161	71	79	28	20	47	133	106	100	79
(3 -1 -1)	109	52	137	59	35	70	102	41	87	43	63	35	137	75	168	128	58	51	60	20	72	168	119	82	48
(3 3 1)	144	122	104	126	36	139	169	94	66	70	107	82	134	123	101	127	33	116	76	74	28	107	148	150	109
(-3 3 1)	97	149	58	138	119	131	103	158	94	119	117	132	55	130	15	58	96	141	127	159	93	31	87	119	138
(-3 -3 1)	14	72	52	73	153	58	26	83	89	134	98	121	59	48	73	70	173	84	87	106	127	59	6	51	93
(-3 -3 -1)	36	58	76	54	144	41	11	86	114	110	73	98	46	57	79	53	147	64	104	106	152	73	32	30	71
(-3 3 -1)	106	129	81	116	114	115	98	172	120	97	90	108	41	141	30	39	87	116	153	159	110	51	96	104	112
(3 -3 1)	74	51	99	64	66	65	82	8	60	83	90	72	139	39	150	141	93	64	27	21	70	129	84	76	68

G.B. ID {hkl}	1	2	3	4	5	6	7	8	9	10	11	12	13	14	15	16	17	18	19	20	21	22	23	24	25
(3 1 0)	136	92	124	98	10	110	141	69	72	52	88	58	150	104	130	137	32	89	65	47	40	136	147	121	83
(-3 -1 0)	44	88	56	82	170	70	39	111	108	128	92	122	30	76	50	43	148	91	115	133	140	44	33	59	97
(3 -1 0)	103	60	121	70	37	78	106	33	69	59	80	53	153	68	163	145	64	64	44	10	59	150	114	91	63
(3 2 1)	137	113	105	119	30	131	158	83	61	70	107	78	145	112	111	137	37	110	66	63	23	114	143	143	104
(-3 2 1)	86	141	51	132	130	122	92	151	94	127	118	139	49	119	4	55	107	137	125	164	100	21	76	110	137
(-3 -2 1)	23	83	45	82	163	67	34	93	89	140	103	129	52	58	62	64	170	92	94	117	126	48	13	59	101
(-3 -2 -1)	43	67	75	61	150	49	22	97	119	110	73	102	35	68	69	43	143	70	114	117	157	66	37	37	76
(-3 2 -1)	97	121	79	108	123	106	87	162	124	100	87	109	30	130	29	29	96	110	155	164	120	48	86	94	107
(3 -2 1)	83	59	101	72	57	74	93	18	56	80	93	71	150	50	151	151	84	70	25	16	60	132	94	86	73
(3 -2 -1)	94	39	129	48	50	58	88	29	86	53	62	41	131	61	176	125	73	43	55	16	80	159	104	70	43
(3 3 2)	132	126	93	134	44	144	162	92	55	82	119	92	137	116	98	133	45	125	69	75	18	100	136	157	118
(-3 3 2)	92	154	48	146	119	136	104	146	82	128	129	143	63	122	19	68	100	151	115	150	85	26	83	124	149
(-3 -3 2)	12	80	41	82	150	68	37	81	77	145	110	130	66	47	71	78	175	93	79	105	115	54	6	62	102
(-3 -3 -2)	48	54	87	46	136	36	18	88	125	98	61	88	43	64	82	47	135	55	111	105	162	80	44	23	62
(-3 3 -2)	110	119	92	106	110	107	95	162	132	87	79	97	39	141	41	32	83	105	164	150	116	61	99	96	100
(3 -3 2)	70	61	88	74	70	73	85	18	48	93	101	83	141	39	139	148	97	75	16	30	64	119	81	84	80
(3 -3 -2)	88	26	132	34	61	44	76	34	98	52	51	37	117	58	161	112	80	29	65	30	95	154	97	56	31
(3 2 0)	149	105	120	109	19	123	156	84	76	55	92	65	138	118	116	128	22	99	76	62	39	124	157	133	92
(-3 2 0)	91	132	65	121	128	115	89	161	109	114	103	124	38	126	13	41	102	124	140	175	110	34	81	102	122
(-3 -2 0)	31	75	60	71	161	57	24	96	104	125	88	115	42	62	64	52	158	81	104	118	141	56	23	47	88
(3 -2 0)	89	48	115	59	52	65	91	19	71	66	77	56	142	54	167	139	78	56	40	5	70	146	99	78	58
(3 2 2)	125	118	92	127	42	136	152	81	48	83	120	91	147	106	106	144	50	119	58	66	10	104	130	148	115
(-3 2 2)	81	145	39	139	129	128	95	140	80	138	131	151	60	112	17	67	110	147	111	151	90	15	73	116	149

G.B. ID {hkl}	1	2	3	4	5	6	7	8	9	10	11	12	13	14	15	16	17	18	19	20	21	22	23	24	25
(-3 -2 2)	23	90	33	91	156	77	45	91	76	153	116	140	62	57	61	75	167	102	84	114	113	43	15	70	112
(-3 -2 -2)	55	62	88	53	138	44	28	99	132	97	60	89	33	74	74	36	130	61	122	114	170	76	50	32	65
(-3 2 -2)	101	111	91	98	117	97	84	154	138	88	74	96	29	131	42	22	91	98	169	151	127	61	91	86	94
(3 -2 -2)	99	35	141	41	51	52	85	40	100	42	49	29	120	68	163	113	70	33	69	29	90	165	107	64	31

The cell highlighted in grey represents the angle closest to the {hkl} plane and the column highlighted in grey identifies a grain boundary that is close to a low indexed plane

9 References

[1] Thomas S. Energ Policy 2010;38:4903.

[2] Coombs C. Hinckley J Polit 2010;11(1).

[3] Lee BW. Prog Nucl Energ 2002;40(3):327-333.

[4] Sertyesilisik B, Melaine Y. Environ Qual Manag 2010;19(3):55-56.

[5] Van Leeuwen JWS, Smith P. From ore to electricity, energy production and uranium resources, 6th revision in: Nuclear Energy: The Energy Balance 2005.

[6] Nifenecker H. Comparison of the energy structure between Denmark, France and Sweden 2003.

[7] Cattant F, Crusset D, Feron D. Mater Today 2008;11(10):32-37.

[8] Scott PM. Corrosion 2000;56(8):771-782.

[9] Hull D, Bacon DJ. Introduction to Dislocations. Butterworth-Heinemann 2001.

[10] Singley WJ, Welinsky IH, Whirl SF, Klein HA. Stress Corrosion of Stainless Steel and Boiler Water Treatment in Shippingport Atomic Power Station: Proceeding from American Power Conference 1959;21:748.

[11] Jones RL. Corrosion experience in US light water reactions: NACE 50th anniversary perspective. Corrosion 1993;93.

[12] Raquet O, Herms E, Vaillant F, Couvant T, Boursier JM. SCC of Cold-Worked Austenitic Stainless Steels in PWR Conditions:T R Allen, P J King, and L Nelson, editors, Proceedings of 12th International Conference on Environmental Degradation of Materials in Nuclear Power Systems - Water Reactors 2005.

[13] Marcus P, Oudar J. Corrosion Mechanisms in Theory and Practice. New York 1995.

[14] Marrow TJ, Babout L, Jivkov AP, Wood P, Engelberg D, Stevens N, Withers PJ, Newman RC. J Nucl Mater 2006; 352(1):62-74.

[15] Fontana MG. Corrosion Engineering. McGraw-Hill, New York 1986.

[16] Sedriks AJ. Electrochemical Society: Corrosion of Stainless Steels. Wiley, New York 1996.

[17] Marshall P. Austenitic Stainless Steels - Microstructure and Mechanical Properties. Springer 1984.

[18] Lacombe P, Baroux B, Béranger G, Colombier L, Hochmann J. Stainless Steels. Les Editions de Physique, Les Ulis, France 1993.

[19] Avner SH. Introduction to Physical Metallurgy. McGraw-Hill, New York 1964.

[20] Trethewey KR, Chamberlain J, Trethewey KR. Corrosion for Science and Engineering, 2nd ed.. Longman Scientific & Technical, Harlow 1995.

[21] Logan HL. The Stress Corrosion of Metals. Wiley, New York 1996.

[22] Staehle RW. Proceedings of conference on Fundamental Aspects of Stress Corrosion Cracking and Hydrogen Embrittlement of Iron Base Alloys 1973.

[23] Combrade P. INL Seminar on SCC in LWRs, Idaho Falls, Idaho, USA 2013 .

[24] American Society for Testing and Materials. Stress Corrosion Cracking of Metals--a State of the Art. American Society for Testing and Materials, Philadelphia 1972.

[25] Engelberg DL. Grain boundary engineering for intergranular stress corrosion resistance in austenitic stainless steel. Ph.D. Thesis, University of Manchester 2006.

[26] Milne I, Ritchie RO, Karihaloo BL. Comprehensive Structural Integrity, Elsevier 2003.

[27] Llewellyn DT. Steels : Metallurgy and Applications. Butterworth-Heinemann, Oxford 1992.

[28] Shreir LL, Jarman RA, Burstein GT. Corrosion, 3rd ed. Butterworth Heinemann, Oxford 1994.

[29] Ford FP. Current understanding of the mechanisms of stress corrosion cracking and corrosion fatigue, ASTM STP 821 1984;32.

[30] Staehle RW. Critical Analysis of "Tight Cracks": Proceeding 13th Int. Symp on Environmental Degradation of Materials in Nuclear Power Systems- Water Reactos 2007.

[31] Logan HL. J Res Nat Bur Stand 1952;48(2):99-105.

[32] Leffler B. Stainless – Stainless Steels and Their Properties 1996.

[33] Jones RL.Corrosion 1990; 30:70.

[34] Jones RL, Gordon GM, Neils GH. Environmental degradation of materials in boiling water reactors: Proceedings of the 4th Int. Symp. on Environmental Degradation of Materials in Nuclear Power Systems-Water Reactors August 1989.

[35] Scott PM. Int J Pressure Vessels Piping 1996;65(3):255-264.

[36] Scott PM. INL Seminar on SCC in LWRs. Idaho Falls, Idaho, USA 2013.

[37] Staehle RW, Hochmann J, McCright RD, Slater JE. Stress corrosion cracking and hydrogen embrittlement of iron base alloys: NACE 1977.

[38] Truman JE. Stainless steels 1969;101.

[39] Hubner W, Johansson BJE. Rev High Temp Mat 1972; 2:159.

[40] Clarke WL, Gordon EM. Corrosion 1973;29:1.

[41] Berry WE, White EL, Boyd WK. Corrosion 1973:29(12):451-469.

[42] Pickett AE, Sim RG. Corrosion 1973;73:105.

[43] Speidel MO. Corrosion 1977;33(6):199-203.

[44] Rahimi S. Behaviour of short intergranular stress corrosion crack in type 304 austenitic stainless steel. Ph.D. Thesis, The University of Manchester 2009.

[45] Rahimi S, Engelberg D, Duff J, Marrow T. J Microsc 2009;233(3):423-431.

[46] Danko JC, Smith RE, Gandy DW. Effect of surface preparation on crack initiation in welded austenitic stainless steel piping: Proceeding of the 5th Int. Symp. on Environmental Degradation of Materials in Nuclear Power Systems-Water Reactors August 1991.

[47] Kuniya J, Masaoka I, Sasalii R, Kirihara S. J Mat for Energy Systems 1980;1:30.

[48] Matsushima S, Ishihara T, Ito G. Corrosion Eng 1977; 27:367.

[49] Solomon HD. Corrosion 1980;38:53.

[50] Acharyya S, Khandelwal A, Kain V, Kumar A, Samajdar I. Mater Charact 2012;72:68.

[51] Bain EC, Aborn RH, Rutherford JJB. Trans Am Soc Steel Treating 1933; 21:481.

[52] Newell HD. Trans Am Soc Steel Treatment 1932;19:673.

[53] Cihal V. Prot Mat 1966;2:127.

[54] Stainless Steel 1950. US Pat. 2531 155.

[55] Watanabe T. Res Mechanica 1984;11:47.

[56] Essam JW. Rep Prog Phys 1980;43:833.

[57] Stauffer D, Aharony A. Introduction to Percolation Theory 1992. Taylor & Francis, London, 1992.

[58] Wells DB, Stewart J, Herbert AW, Scott PM, Williams DE. Corrosion 1989;45:649.

[59] Jivkov AP, Stevens NPC, Marrow TJ. Comp Mater Sci 2006;38:442.

[60] Palumbo G, King PJ, Aust KT, Erb U, Lichtenberger PC. Scripta Metall Mater 1991;25:1775.

[61] British Standards 2000. BS EN 10020.

[62] British Standards 2005. BS EN 10088-1.

[63] British Standards 2009. BS EN 10088-4.

[64] Lewis HM, Hattersley B. Acta Metall Mater 1965;13:1159.

[65] Thorvaldsson T, Salwén A. Scripta Metall Mater 1984;18:739.

[66] http://www.thomas-sourmail.org/stainless/index.html).

[67] Etienne CF. CEGB informal meetings on creep in stainless steels 1977.

[68] Honeycombe RWK. Steels : Microstructure and Properties 1981. Edward Arnold, London.

[69] ASTM A262 2001,

[70] Cihal V. Intergranular Corrosion of Steels and Alloys 1984. Elsevier.

[71] Ahmedabadi PM, Kain V, Dangi BK, Samajdar I. Corros Sci 2012;66:242.

[72] Streicher MA. ASTM Bulletin 1958;77.

[73] Streicher MA.Corrosion 1964;20:57.

[74] Streicher MA. ASTM STP 1978:656:3.

[75] ASTM G108 1999.

[76] Majidi AP, Streicher MA. Corrosion 1984;40:584.

[77] Buzzanca G, Caretta E, Meini L, Pascali R, Ronchetti C. Corros Sci 1985;25:805.

[78] Trillo EA, Murr LE. Acta Mater 1998;47:235.

[79] Trillo E, Beltran R, Maldonado J, Romero R, Murr L, Fisher W, Advani A. Mater Charact 1995:35:99.

[80] Rahimi S, Engelberg D, Duff J, Marrow T. J Microsc 2009; 233:423.

[81] Turnbull A. Corros Sci 1993;34:921.

[82] West JM. Basic corrosion and oxidation 1986.J. Wiley & Sons, New York.

[83] Newman R, Procter R. Brit Coros J 1990;25:259.

[84] Lacombe P, Aucouturier M, Chene J, Gibala R, Hehemann R. ASM Publication 1984;79.

[85] Sieradzki K, Newman R. J Phys Chem Solids 1987;48:1101.

[86] Shreir LL. Corrosion 1976. Butterworth & Co.Ltd.

[87] Patel SJ.JOM 2006;58:18.

[88] INCONEL Alloy 600 2013.

[89] Panter J, Viguier B, Cloué JM, Foucault M, Combrade P, Andrieu E. J Nucl Mater2006;348:213.

[90] IAEA Nuclear Energy Series NP-T-2.5 2011.

[91] Pressurized Water Reactors 2013.

[92] Capell BM, Was GS. Metall Mater Trans A 2007;38:343.

[93] Ford F. Int J Pressure Vessels Piping 1989;40:343.

[94] Hall M. Corros Sci 2008;50:2902.

[95] Magnin T, Chieragatti R, Oltra R. Acta Metall Mater 1990;38:1313.

[96] Scott P. An overview of internal oxidation as a possible explanation of intergranular stress corrosion cracking of alloy 600 in PWRs: Ninth International Symposium on Environmental Degradation of Materials in Nuclear Power Systems-Water Reactors 1999.

[97] Mohanty S, Majumdar S, Natesan K. A Review of Stress Corrosion Cracking/Fatigue Modeling for Light Water Reactor Cooling System Components 2012.

[98] Laghoutaris P, Chêne J, Guerre C, Raquet O, Sennour M, Molins R, Vaillant F, Scott P. Mater Sci Eng Energy Systems 2008;3:119.

[99] Combrade P, Scott P, Foucault M, Andrieu E, Marcus P. Oxidation of Ni base alloys in PWR water: oxide layers and associated damage to the base metal: Proceedings of the Twelfth International Conference on Environmental Degradation of Materials in Nuclear Power Systems-Water Reactors 2005.

[100] Leonard F. Study of Stress Corrosion Cracking of Alloy 600 in High Temperature High Pressure water 2010. Ph. D. Thesis, University of Manchester.

[101] Sennour M, Laghoutaris P, Guerre C, Molins R. J Nucl Mater 2009;393:254.

[102] Aguilar A, Albarran J, Lopez H, Martinez L. Mater Lett 2007;61:274.

[103] Bulischeck T, Van Rooyen D. Corrosion 1981;37:597.

[104] Staehle R, Gorman J. Corrosion 2004;60:115.

[105] Alexandreanu B, Capell B, Was GS. Mater Sci Eng A 2001;300:94.

[106] Weihs T, Hong S, Bravman J, Nix W. J Mater Res 1988;3:931.

[107] Johansson S, Schweitz J, Tenerz L, Tiren J. Appl Phys 1988;63:4799.

[108] Armstrong DEJ. Measuring Elastic, Plastic and Fracture Properties using Micro-Cantilever Testing 2009. Ph.D. Thesis, University of Oxford.

[109] Baek C, Kim Y, Ahn Y, Kim Y. Sensor Actuat Phys A 2005;117:17.

[110] Comella B, Scanlon M, J Mater Sci 2000;35:567.

[111] Cardinale G, Howitt D, Clift W, McCarty K, Medlin D, Mirkarimi P. Thin Solid Films 1996;287:214.

[112] Ericson F, Schweitz J, J Appl Phys 1990;68:5840.

[113] Wilson C, Ormeggi A, Narbutovskih M. J Appl Phys 1996;79:2386.

[114] Terada T, Komai K. Fatigue Fract Eng M 2000; 23:33.

[115] McCarthy J, Pei Z, Becker M, Atteridge D. Thin Solid Films 2000;358:146.

[116] Di Maio D, Roberts S. J Mater Res 2005;20:299.

[117] Armstrong D, Haseeb A, Roberts S, Wilkinson A, Bade K. Thin Solid Films 2012;520:4369.

[118] Armstrong D, Wilkinson A, Roberts S. Phil Mag Lett 2011;91:394.

[119] Lozano-Perez S, Dugdale H, Armstrong DEJ, Terachi T, Yamada T, Tarleton E, Roberts SG. MRS Proceedins 2013;1519.

[120] TestWorks 4 Software for Nanoindentation System, 1999.

[121] Agilent Continuous Stiffness Measurement (CSM) Option 2013.

[122] Schwartz AJ, Kumar M, Adams BL, Field DP. Electron Backscatter Diffraction in Materials Science 2009. Springer.

[123] Hughes G. Introduction to FIB 2010.

[124] Stevie F, Giannuzzi L, Prenitzer B. The focused ion beam instrument, Introduction to Focused Ion Beams 2005. Springer.

[125] Rogers ME. Micromechanical Investigations of Stress Corrosion Cracking 2008. Part II Thesis, University of Oxford.

[126] Herbert W. Micromechanical Testing of Stress-Corrosion Cracking 2009. Part II Thesis, University of Oxford.

[127] Armstrong DEJ, Rogers ME, Roberts SG. Scr Mater 2009;61:741.

[128] Herbert FW, Roberts SG. IFHTSE 2010;4:70.

[129] Knott JF. Fundamentals of Fracture Mechanics 1973. Butterworths.

[130] Kumar M, King WE, Schwartz AJ. Acta Mater 2000;48:2081.

[131] Fitzgerald A, Iyer R, Dauskardt R, Kenny T. J Mater Res Pittsburgh 2002;17:683.

[132] Fujii K, Fukuya K. Mater Trans 2011;52:20.

[133] Fujii K, Miura T, FukuyaK. Measurement of GB Strength - Oxidized GBs in Ni-base alloys, QMM-2, Idaho 2011.

[134] Elfallagh F, Inkson B. J Microsc 2008;230:240.

[135] Schaffer B, Grogger W, Kothleitner G. Ultramicroscopy 2004;102:27.

[136] Frankel G, Corrosion Science in the 21 st Century. J Corros Sci Eng 2003:6 (2003).

[137] Palumbo G, King P, Lichtenberger P, Aust K, Erb U. Scripta Metal Mater 1991;25:1775.

[138] Lehockey EM, Brennenstuhl AM, Thompson I. Corros Sci 2004;46:2383.

[139] Rho BS, Hong HU, Nam SW. Scr Mater 2000;43:167.

[140] McMurtrey M, Was G, Patrick L, Farkas D. Materi Sci Eng 2011;528:3730.

[141] Fukuya K, Nishioka H, Fujii K, Miura T, Torimaru T. J Nucl Mater 2011;417:958.

[142] West E, Was G. J Nucl Mater 2011;408:142.

[143] West EA, McMurtrey MD, Jiao Z, Was GS. Metall Mater Trans A 2012;43:136.

[144] Gertsman V, Bruemmer SM. Acta Mater 2001;49:1589.

[145] Stoller RE, Kumar AS, Gelles DS. Effects of radiation on materials: 15th international symposium 1992.

[146] Schmid E, Boas W. Plasticity of crystals 1950. F. A. Hughes and Co. Limited.

[147] Slip in Single Crystals, http://www.doitpoms.ac.uk/tlplib/slip/printall.php 2013.

[148] Randle V. The Measurement of Grain Boundary Geometry 1993. Institute of Physics Pub.

[149] Palumbo G, Lehockey E, Lin P. J Mater 1998;50:40.

[150] Gertsman V, Bruemmer SM. Acta Mater 2001;49:1589.

[151] Randle V. Acta Mater 2004;52:4067.

[152] King A, Johnson G, Engelberg D, Ludwig W, Marrow J, Science 2008;321:382.

[153] Jones R, Randle V, Owen G. Mater Sci Eng 2008;496:256.

[154] Duff J, Marrow T. Corros Sci 2012;68:34.

[155] Wood P, Duff J, Marrow T. Imaging Autoclave Development for In-Situ Optical Measurement of High Temperature Aqueous Corrosion Processes 2009: ICF12, Ottawa.

[156] Britton TB, Birosca S, Preuss M, Wilkinson AJ. Scr Mater 2010;62:639.

[157] Wilkinson A, Meaden G, Dingley D. Mater Sci Tech Ser 2006;22:1271.

[158] Humphreys F. Scr Mater 2004;51:771.

[159] Wilkinson A, Clarke E, Britton T, Littlewood P, Karamched P. J Strain Anal Eng Des 2010;45:365.

[160] Britton T, Wilkinson A. Ultramicroscopy 2011;111:1395.

[161] Jiang J, Britton TB, Wilkinson AJ. Philos Mag Lett 2012;92:580.

[162] Britton T, Liang H, Dunne F, Wilkinson A. The effect of crystal orientation on the indentation response of commercially pure titanium: experiments and simulations: Proceedings of the Royal Society A: Mathematical, Physical and Engineering Science 2010;466:695.

[163] Nye J. Acta Metall 1953;1:153.

[164] Kroner E. Continuum theory of dislocations and self stresses, Defense Technical Information Center 1971.

[165] Was GS, Farkas D, Robertson IM. Curr Opin Solid State Mater Sci 2012;16:134.

[166] Alexandreanu B. Corrosion 2002;59:705.

[167] West E, Was GS. J Nucl Mater 2012.

[168] Dugdale et al. Acta Mater 2013;61(13):4707.

[169] Garcia et al. Corrosion Science 2001;43(8):1519.

[170] Andresen et al J Nucl Mater 2008;383(1):97.